UNIVERSITÀ DI PARMA

UNIVERSITÀ DEGLI STUDI DI PARMA
Dottorato di Ricerca in Ingegneria Civile e Architettura
Ciclo XXXII

Fracture processes
in indentation and cutting of soft biomaterials

PhD Dissertation

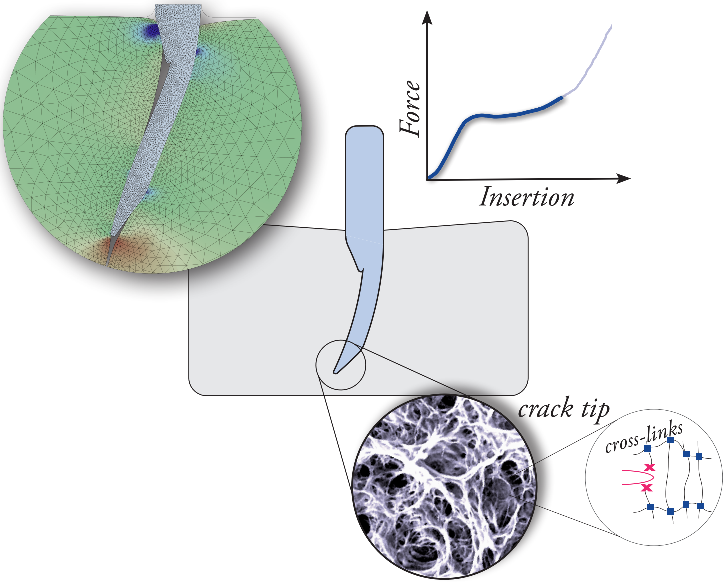

Coordinatore: Prof. Andrea Carpinteri
Tutor: Prof. Andrea Spagnoli
Co-tutor: Prof. Daniele Dini

Candidato: Michele Terzano

Anni 2016/2019

UNIVERSITÀ DI PARMA

UNIVERSITÀ DEGLI STUDI DI PARMA
Dottorato di Ricerca in Ingegneria Civile e Architettura
Ciclo XXXII

Fracture processes

in indentation and cutting of soft biomaterials

PhD Dissertation

Coordinatore:	Prof. Andrea Carpinteri
Tutor:	Prof. Andrea Spagnoli
Co-tutor:	Prof. Daniele Dini

Candidato: Michele Terzano

Anni 2016/2019

To my father
the harshest mentor yet a wise guide
whose footsteps I have been following in all along
without even knowing it

Michele Terzano

Contents

Abstract

Understanding the mechanics lying behind the behaviour of biological materials is not only vital to the current knowledge of living systems but also a keystone of the design of new materials, with relevant applications in engineering and related areas. This thesis is dedicated to the fracture process during cutting of soft biomaterials, specifically those with a porous microstructure such as the brain tissue.

Various aspects are considered, including (i) the interaction between cutting tools and crack propagation; (ii) the effect of cracks in soft elastic solids exposed to large deformations; (iii) the role of rate-dependent energy dissipation during crack propagation. Each point is treated separately, in order to tackle the complexity of the material behaviour and propose theoretical models based on simplifying assumptions.

The mechanics of cutting is analysed in depth combining analytical, numerical and experimental data. Focusing on some peculiar aspects of cutting, our investigation is centred on the stage of cut propagation in elastic materials and carried out borrowing the classical concepts of fracture mechanics. In particular, the mechanism of propagation during cutting is found to depend on a tool sharpness parameter, whose influence is considered analytically and with respect to experimental data.

The behaviour of soft biomaterials is analysed taking into account their large strain elastic response and the presence of rate-dependent effects, associated to various dissipative processes. Numerical simulations of fracture in soft materials are performed, adopting different models to describe the behaviour of biological materials. Hyperelastic incompressible models with strain hardening are adopted to investigate the role of large deformations. Viscoelasticity and poroelasticity are included in the bulk material separately, combined with the hyperelastic behaviour and with a cohesive model of the crack-tip process zone.

The ultimate goal of our work is to develop efficient and reliable computational tools to simulate cutting in soft biomaterials, with possible applications in the fields of healthcare, bioengineering, food industry and robotics. A finite element based algorithm is presented, which can be applied to different cutting tools or needles, providing detailed analyses of the tool-tissue interactions, damage and fracture process in soft materials, and replicating specific features of the insertion process, including needle steering.

Sommario

Comprendere il comportamento meccanico dei tessuti biologici è un aspetto essenziale, non soltanto per espandere l'attuale conoscenza dei sistemi viventi ma anche per lo sviluppo di nuovi materiali, con importanti risvolti applicativi. Questa tesi è incentrata sul processo di frattura durante il taglio (o *cutting*) di materiali biologici soffici, caratterizzati da una microstruttura porosa, di cui un esempio rilevante è il tessuto cerebrale umano.

Diversi aspetti sono presi in considerazione, tra i quali (i) l'interazione dello strumento di taglio nella fase di propagazione della frattura; (ii) il comportamento di fessure in materiali soffici con grandi deformazioni; (iii) l'influenza della dissipazione di energia dovuta a fenomeni dipendenti dal tempo. Ogni punto viene affrontato separatamente, per indagare il complesso comportamento dei materiali e formulare modelli analitici basati su ipotesi semplificative.

La meccanica del cutting è analizzata in dettaglio attraverso la combinazione di modelli teorici, analisi numeriche e dati sperimentali. L'analisi della fase di propagazione del taglio in materiali elastici viene affrontata applicando concetti classici della meccanica della frattura, ma tenendo anche in conto di alcuni aspetti peculiari del cutting. In particolare, il meccanismo di propagazione dipende da un parametro di *sharpness* dello strumento di taglio, la cui influenza è stata motivata sia analiticamente che rispetto a dati sperimentali.

Per studiare il comportamento dei materiali biologici soffici, abbiamo preso in considerazione la risposta elastica in grandi deformazioni ed alcuni processi dissipativi che determinano l'insorgenza di fenomeni dipendenti dal tempo. Per valutare l'effetto delle grandi deformazioni, le simulazioni numeriche del processo di frattura hanno adottato modelli iperelastici incomprimibili con strain hardening. A questo è stato aggiunto, separatamente, un comportamento viscoelastico e poroelastico, unitamente ad un modello coesivo per simulare la zona di processo all'apice della fessura.

L'obiettivo finale è giungere allo sviluppo di una tecnica computazionale affidabile ed efficiente, in grado di simulare il cutting di materiali biologici soffici, orientata al settore della medicina, della bio-ingegneria, del food processing e della robotica. Nella tesi viene presentato un algoritmo agli elementi finiti, in grado di simulare dettagliatamente le interazioni tra strumento di taglio e materiale, il processo di danneggiamento e frattura, e capace di replicare aspetti peculiari, quali ad esempio lo *steering* di aghi chirurgici.

Acknowledgements

This dissertation is the result of a three-year research work carried out with enthusiasm and dedication, that could not have been possible without the support of various people.

Foremost, I would like to thank my tutor and supervisor, Prof. Andrea Spagnoli. I am feeling grateful not only for his scientific expertise, which was invaluable in the development of my research, but also for the empathy, patience and trust that he has showed me in all the time of my work.

I would also like to thank my co-tutor, Prof. Daniele Dini, who introduced me to the fascinating world of biological materials and welcomed me in his research group at the Imperial College. With his advice he helped me to direct the potential of my work towards new compelling applications.

A profound feeling of gratitude goes to Prof. Per Ståhle for his precious collaboration and the pleasant discussions that we had together: his expertise and rigorous approach to research have been inspiring. I am also deeply grateful to Prof. James Barber, whose immense knowledge guided me at the beginning of my doctoral studies and will be an example in the future.

Last but not the least, I owe a debt of gratitude to the people and colleagues that I met during my PhD studies, both at the University of Parma and at the Imperial College in London. A sincere thank you to Dr. Antonio Forte and Dr. Matthew Oldfield, for their help when I began facing unfamiliar topics, and to my friend Dr. Federico Artoni, for the countless hours spent with me in the laboratory.

1

Introduction

The Earth is a living body. Its soul is its ability to grow. Its flesh is the soil, its bones are the strata of rock, its cartilage is the tufa, its blood is the underground streams, the reservoir of blood around its heart is the ocean, the systole and diastole of the blood in the arteries and veins appear on the Earth as the rising and sinking of the oceans.

Leonardo Da Vinci

In nature, many constituents of living beings can be classified as soft biological materials. Besides bones and teeth, almost any other part of the human body, such as skin, muscles, tendons, cartilage, blood vessels and organs presents a soft mechanical nature. These are by no means ordinary materials: thanks to a hierarchical structure that spans multiple length scales, they are able to react to a variety of external stimuli, absolving to complex biological functions and ensuring exceptional mechanical properties. For this reason, research on biomaterials has always attracted the attention of scholars[1–4]. Nowadays, materials scientists are putting significant efforts in replicating some of the mechanical properties of natural tissues with synthetically made materials, for applications in tissue engineering, healthcare, regenerative medicine and smart materials[5–14].

In particular, the mechanics of damage and fracture of natural tissues is a fascinating and puzzling subject. Each of us might have personally experienced the consequence of a bad injure or a surgical intervention, in which tissues get damaged and recover. Even the toughest natural tissue can break if subjected to an excessive force, like any other material. Compared to the classical fracture mechanics of brittle and ductile hard solids, which is grounded on solid foundations built in the first half of the last century, fracture of biological materials is still at the centre of the scientific debate. How these materials get damaged and break, what is the origin of their strength, what happens when we pierce or cut them with a sharp tool: these are only a few of the multiple questions which have been sparking the interest of materials scientists, biologists and bioengineers[15]. The purpose of this introductory chapter is to present the motivation and aims of our research and how this thesis is structured.

1.1. What are soft biomaterials?

In the common sense, soft is any material capable of deforming consistently without applying an excessive force, so that its deformation can be felt by hand or seen with the naked eye. This simple assessment does not capture the whole of soft matter features, which go far beyond a highly compliant behaviour. Natural systems rely on the ability of soft materials to accommodate large deformations with minimal damage and provide protection to vital parts. Skin, for instance, is the armour of many living beings, but differently from the heavy stiff metallic armours of medieval knights, it consists of a complex multi-scale network resulting in a tough yet compliant layer[16]. If we wished to tear apart a small stripe of rabbit skin, the task would prove to be almost impossible, to an extent that a small pre-made cut would not propagate but only deform. By contrast, we know by experience that even a small flaw in a glass slab can lead to a catastrophic failure of the component. Glass elastic modulus is orders of magnitude larger than that of skin, so that the response observed might appear surprising. It is because of this and other unique mechanical properties that natural tissues are among the most studied, yet less understood materials. Let us consider their properties more in detail.

Skin and other elastic tissues

Soft elastic tissues, such as skin or blood vessels, are often described as incompressible materials with large deformations, resulting from their molecular structure and elastic restoring forces, mostly of entropic origin. A sparse population of strong bonds connects molecules together and prevents macroscopic flow, allowing some molecular motion at the microscopic scale[17]. Skin, for instance, derives its remarkable tearing resistance from the structure of its outer layer, the dermis, which consists of a tangled network of collagen fibrils and elastin[16,18].

Elastic tissues can be considered similar to rubber-like polymers, with a non-linear elastic stress-strain relationship described by the same models developed for elastomers. Yet, there are also relevant differences. Unlike most rubbers, the stress-strain curve of biological tissues has a peculiar J shape, displaying a severe strain hardening which prevents large deformations that could threaten the tissue integrity[19]. This stiffening effect is related to the stretching of fibres along the direction of load application, which leads to a characteristic anisotropic response[17]. In terms of fracture, the exceptional tearing resistance might be related to the initial horizontal part of the stress-strain curve. In fact, it has been observed that the low shear modulus results in an increased resistance to the transmission of energy to crack tips[20–22].

Brain tissue and porous biomaterials

Many biomaterials are composed of an organic matrix swollen by water, forming a solid which is porous, permeable and deformable. One example is articular cartilage, consisting of an organic matrix of collagen fibrils with variable diameters, which make about the 20-30% of the total wet weight, and the larger remaining part occupied by fluid[23]. The role of cartilage is to carry loads and serve as a damper to absorb shocks, with a remarkable resistance to fracture deriving from the interactions within its microstructure[24].

Another example of a soft and porous material is the brain tissue. Human brain is suspended inside the skull, floating on the cerebrospinal fluid, a clear and colourless liquid not much different from water. Its structure is composed of two main constituents: the grey matter, which contains the nerve cell bodies and accounts for almost the 30% of the total volume; and the white matter, characterised by a large proportion of myelinated axons[25]. In particular, the grey matter numerous junctions result in a denser material with respect to the white matter, which therefore is less permeable to drainage of the cerebrospinal fluid.

The brain is the most complex organ of the human body, not only for its biological functions. Owing to the different microstructure of its components, brain tissue is an inhomogeneous material and its mechanical response has been the subject of extensive studies[26–30]. Below we summarise some of the main features that need to be considered when studying the mechanical behaviour of brain:

- the instantaneous response is non-linear elastic, similar to an elastomer with a very low elastic modulus (average values of the instantaneous shear modulus fall below 1 kPa);
- the brain tissue has a different response in tension versus compression, and during loading-unloading cycles it shows evidences of a Mullins-like effect;
- the cerebrospinal fluid might interact with brain deformation, resulting in a volumetric shrinking observed, for instance, during the administration of hyper-osmotic drugs or in the brain-shift phenomenon[31];
- human brain shows viscoelastic relaxation, which is assumed to influence the deformation in particular situations, such as in response to shocks or traumatic injuries.

Although the response of brain to compression-relaxation, cyclic indentation and rheometric tests has been explored extensively, not much can be found on the topic of brain fracture. Most results are obtained from compression tests, where brain displays a fracture behaviour typical of fibrous materials with rate-dependent ultimate properties[28]. However, the fracture stress or strain measured from the experiments only reflect the materials ability of sustaining mechanical loads, whereas an appropriate definition of toughness for such materials need to be based on the fracture energy[32].

Hydrogels and mimicking materials for soft tissues

Dealing with real tissues presents several critical aspects, connected to the availability, costs, ethical issues and difficulties in the collection of repeatable experimental data because of the variable microstructure of biological materials. For these reasons, synthetic phantoms mimicking the behaviour of natural tissues are used extensively in testing and simulations, for training purposes, design of robotic aided surgery systems and bio-implants[8]. There are multiple factors to consider when choosing a mimicking material, not least the biocompatibility if the artificial compound has to be implanted in the human body.

Countless alternatives of mimicking materials can be found in the literature. Focusing on the elastic nature displayed by soft biomaterials, rubber-like polymers are among the most common options. Silicone rubber, in particular, has been proposed to replace human skin in tensile and tearing experiments, because the toughness and constitutive response of silicone and skin are similar[33,34]. Throughout this research, we have extensively used different types of silicones in experiments, to investigate the non-linear elastic response and the large strain fracture behaviour observed in soft biomaterials. Silicones have been proposed to mimic the brain tissue as well, although hydrogels might offer a more appropriate choice for tissues with a porous network.

From the materials point of view, hydrogels are polymer networks highly swollen with a liquid, ranging from ten up to thousands of times their dry weight. Actually, we can think of a simple single-phase gel as a dilute rubber: when the water content is increased, the effect is analogous to expose a polymer to a temperature surge, so that gels behave as very soft rubbers[7]. Hydrogels can be classified in terms of the type of cross-links joining the polymeric chains together[8]:

- reversible or *physical* gels: the polymer networks are held together by molecular entanglements, and/or secondary forces including ionic, H-bonding or hydrophobic forces. All of these interactions are reversible, and can be disrupted by changes in physical conditions such as ionic strength, pH and temperature. Gelatines are one of such examples, often used in food and pharmaceutical industries because they are able to melt in the mouth or in the stomach;

- permanent or *chemical* gels, whose networks contain strong covalent cross-links so that the chemical structure resembles that of elastomers.

It is the role of fluid the most peculiar aspect of the mechanical response of gels. When they are compressed, water is expelled from the solid network, whereas fluid is taken up in tension, and the mechanical properties are affected by rate. Certain hydrogels display another type of rate-dependent behaviour, related to the breaking and re-forming of the cross-links, which result in a viscous relaxation. It is important to notice that the stress relaxation, as well as the fracture behaviour, depends on the type of gel[35]. Gelatines, for instance, are brittle compounds showing little or no rate-dependent behaviour at small to medium strains. On the contrary, parameters like the ultimate stress and the fracture energy depend on the rate of deformation[36–38]. In particular, the fracture energy of biopolymeric gelatines has been found to vary linearly with the crack velocity, and the rate sensitivity increases with the amount of physical cross-linking[39–42]. The local process leading to macroscopic fracture is different for the two classes: fracture in physical gels is dominated by a viscoplastic mechanism leading to the pull-out of the polymeric chains[39], whereas chemical gels fail by scission of the stretched chains, similarly to rubber-like polymers[43].

Various physical and chemical gels have been proposed to replicate the time-dependent behaviour of the human brain and other porous biomaterials, including gelatines and composite hydrogels. We have considered more in detail the mechanical response of a biopolymeric gelatine and a soft hydrogel[44–46]. The latter, thanks to a multicomponent composition, ensures superior performances in reproducing the mechanics of brain during different loading scenarios, including fracture tests, and is also suitable to mimic other porous organs[47].

1.2. Fracture and strength of soft materials

Irrespectively of the material considered, fracture is a matter of large strains at small scale lengths[48]. However, the fracture process in a soft material is qualitatively different from what is observed in metals, rocks, glass and other hard materials[49–51]. Large strains, energy dissipation, rate-dependent behaviour: these are the main points affecting the fracture process and toughness of soft biomaterials.

Fracture of gels is, in this sense, archetypical. Intrinsically, they are very brittle due to the large water content which results in a scattered distribution of molecules, with high propensity to damage and failure because of the low number of highly stretched polymeric chains[52]. However, the amount of dissipated energy due to various mechanisms has the power to increase their fracture resistance by several orders of magnitude[53,54]. Materials experts have devised techniques to build up energy dissipation in the microstructure of artificial materials, in order to develop new compounds with outstanding fracture properties[55–58]. Instead of considering the specific failure mechanisms at the micro-scale, we might acquire instructive information by analysing the typical length scales involved in fracture mechanics.

Length scales of fracture mechanics

Rupture or fracture always starts from a pre-existing crack or flaw, the presence of which, when not introduced deliberately, should be considered as inevitable. Therefore we can focus on the situation of a propagating crack in an infinite body to distinguish three main regions[50] (Fig.1.1):

- the *process zone* (A). This is the region very close to the crack tip, where local damage and molecular fracture occur, and in which the stress is determined by the tension required to break individual bonds;

- the *crack-tip region* (B). This is where the material is affected by the vicinity of the crack tip, which in general causes stress concentration, and potentially where energy dissipation is connected to the propagating crack;

- the *far-field region* (C). Far away from the crack tip, the material behaviour is unaffected by the crack and depends on far-field loading: energy dissipation, if relevant, is due to bulk processes which are independent on the presence of the crack.

Let us begin by considering materials whose bulk behaviour is elastic and energy dissipation is confined to the process zone, that is assumed much smaller than any other relevant size of the problem. This is the well-known small scale yielding assumption, which is the founding hypothesis of linear elastic fracture mechanics (LEFM). Being the dissipative zone indefinitely small, the crack-tip region is dominated by the elastic fields controlled by a stress intensity factor.

It is the conventional approach adopted in hard materials such as rocks, bones or glassy polymers, but need to be revised for soft and highly deformable solids.

The definition of soft in fracture mechanics is made on a relative basis: that is, we need to consider the competition between the elastic strain energy and the effective surface energy for fracture. A length scale is derived, which in the literature has been given various names, such as the crack-tip radius ρ (Fig.1.1) or the length of flaw sensitive failure[50,59]. Regardless of the interpretation, it characterises a region of large strains outside of which the LEFM assumptions remain valid. While in most hard solids such a region is very small, usually in the order of the molecular distances, in soft materials it might become larger than any other significant dimension involved in the problem. As a result, fracture of soft materials cannot be studied without first addressing the role of large deformations.

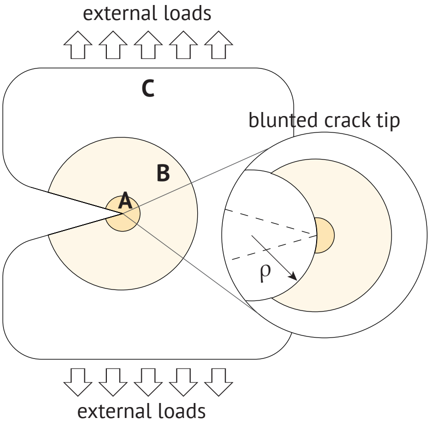

Figure 1.1 Sketch of the crack-tip region and the various length scales involved in fracture mechanics. The inset shows the crack tip in a soft material, where ρ is the tip radius characterising the size of the large strain zone

The scenario is further complicated if energy dissipation occurs on a large scale. The small-scale yielding assumption does not hold and the amount of dissipated energy has a primary effect on the available energy for fracture. In such cases, the very existence of a fracture energy as a material parameter needs to be reconsidered[50].

1.3. The importance of cutting

During their lifetime, living beings are exposed to numerous external actions, as part of the natural course of events or coming from unexpected situations. During surgeries, for instance, the affected biological tissue is subjected to unusual forces by means of tools, which stretch and cut causing a temporary injure or damage[60]. Incisions by means of scalpels, dissections using surgical scissors, needle insertions: in the healthcare sector, the range of techniques involving cutting processes is vast. Another field in which cutting has a central role is the food processing industry. Automated machines perform cutting operations on a broad variety of foodstuff, many of them characterised by being soft and viscous, such as cheese, gelatine etc. Cutting is also employed as an alternative technique to test the mechanical properties of soft materials, whose low elastic modulus and inherent complex behaviour make the traditional methods problematic[61].

Any action causing separation in a material through the application of forces by means of an external tool – be it a wedge, a pair of scissors or a surgical needle – is the object of the mechanics of cutting[62]. The science of cutting was firstly investigated in relation to metals, applying the traditional slip-line model of the plasticity theory to wedge indentation[63], and in brittle materials considering a Coulomb-Mohr criterion[64]. With respect to these mechanisms, the novelty in cutting elastic materials is related to the central role played by fracture mechanics[65,66], and this might explain why a large part of this thesis is centred on fracture and crack propagation.

However, there is one fundamental difference between cutting and fracture, that we wish to clarify through an intuitive example. Let us consider a soft and extensible piece of material, for instance a large rubber band with a small cut. If we try to separate this piece by stretching it by hand, we will soon find out that a considerable amount of force is required. By contrast, we know that with a sharp blade we can easily cut through it. In more rigorous terms, it is when we attempt to feed energy to a crack from remotely loaded regions that tearing is difficult, whereas with blades or other sharp objects the deformation is extremely localised[21]. This is the peculiarity of fracture during cutting: that is, the way in which the external work is provided and converted in surface energy to feed crack propagation.

1.4. Motivation and aim

From this introduction it can be seen that the analysis of cutting in soft biomaterials requires a multidisciplinary approach, dealing with physics, contact, fracture mechanics and materials science. While we do not pretend to address all the topics discussed above, these represented the starting point which arose our interest in the subject of soft biomaterials. The need to provide an exhaustive answer to the implications of cutting in several fields, from materials science to bioengineering, was a more practical reason that suggested us to pursuit the investigation presented in this thesis.

The mechanics of indentation and cutting plays an important role during mechanical testing of soft materials. Specifically, in order to measure the fracture toughness of very compliant solids, cutting-based techniques are becoming of widespread use. Recently, wire cutting has been applied to characterise the ultimate behaviour of the human brain tissue and soft mimicking hydrogels, which show a complex response affected by non-linearity and rate effects. Wire cutting is adopted as a model technique in many parts of this work, as it allowed us to study the cutting process in its entirety with an amenable geometry for numerical simulations.

Among the various cutting techniques adopted in surgery, needle insertions have become popular for minimally invasive surgeries, which in some cases offer relevant benefits for the patients. The development of a new type of flexible needles, which are controlled by robots and can steer inside the target biological tissues, requires a detailed investigation in the mechanics of needle penetration. The peculiar steering observed in experiments depends on a complex mechanism of crack propagation, for which accurate and efficient numerical simulations are needed. Among the main purposes of our work was the development of a refined numerical algorithm, capable of describing the tool-tissue interaction and predict the process of needle steering. The insight gained from the analyses constitute an essential tool supporting the production of the surgical needle, and can also be used for training purposes.

An additional difficulty in testing soft biomaterials and their synthetic counterparts is represented by energy dissipation. Besides the well-known viscoelastic relaxation showed by elastomers, in soft porous materials rate-dependence might be caused by the process of fluid draining. The human brain tissue, behaving like a soft hydrogel, show a remarkable effect of the rate of insertion during wire cutting and needle penetration experiments, the cause of which are still not completely understood. This last point motivated us to investigate the role played by fluid draining and viscoelastic relaxation in the crack-tip region of a soft solid, through a combined analytical and numerical approach.

1.5. Thesis outline

This thesis is structured in four main chapters, closed by a chapter of conclusions and appendices. Single chapters address a specific topic of our research and are, to a certain extent, self-contained. For this reason, we have included an introductory section to the chapters, in order to concentrate the readers attention on the contents presented and provide a dedicated literature review. The full list of the chapters is presented below.

- Chapter 2 is about the mechanics of cutting in elastic materials. It provides the background of the governing equations and introduce an important definition of sharpness. Experimental results, as well as numerical simulations, are presented and discussed with respect to the analytical models;
- Chapter 3 is centred on the effect of large deformations in non-linear elastic materials, as this is an essential step to understand the mechanics of cutting in soft biomaterials. Although cutting begins with an initial stage of contact and indentation, the main source of the behaviour observed in the experiments occurs during crack propagation: therefore, the fracture is what this chapter is centred on. Specifically, the fracture process in cutting is discussed in terms of the near-tip fields and the role of crack blunting;
- Chapter 4 considers the role of rate-dissipation in fracture, in particular with respect to the human brain and similar soft porous materials, which are treated as soft non-linear elastic solids with rate-dependent behaviour. Both the role of fluid interaction and of viscoelastic dissipation are examined;
- Chapter 5 is dedicated to the numerical modelling of the cutting process in soft materials. An advanced finite element algorithm is presented and applied to simulations of wire cutting and flexible needles insertion;
- Chapter 6 presents the conclusions. The main results are synthetically presented in the form of bullet points, trying to establish a link among the chapters;
- Appendices close the thesis, containing the main theoretical background of non-linear elasticity, viscoelasticity and poroelasticity, with most of the equations that are recalled throughout the chapters.

2

The mechanics of cutting in elastic materials

Sharp knives, of course, are the secret of a successful restaurant.

George Orwell

Most cutting processes essentially consist of two stages, in which the material is initially deformed until an appropriate failure mechanism is activated, and then is separated. When a cutting tool is pushed into the material, it causes a deformation that may be either reversible or irreversible depending on the nature of the material itself. Not only the material but also the tool geometry plays an important role in the type of deformation, a fact that can be understood if one thinks of the differences between splitting a rock with a thick wedge and perforating a rubber sheet with a thin needle. In the present thesis, we confine our attention to soft materials, such as rubber, skin or gels, whose behaviour can be assumed elastic until the occurrence of failure identified by fracture initiation[62]. The first stage of indentation in elastic materials can be treated as a contact problem. For instance, surgical blades have a wedge-like tip profile and the indentation can be studied adopting a plane contact geometry, whereas needle indentation might be treated as an axisymmetric problem. A comprehensive discussion of the contact solutions for wedge and cone indenters in plane strain or axisymmetric conditions is provided in Truman et al.[67]. While the classical contact mechanics solutions are attractive, we should carefully consider their limits in relation to the specific nature of the material. For instance, the singular state of stress predicted by the sharp wedge solution does not exist in practice, because of the effect of edge rounding and plastic flow[68]. Moreover, when soft solids are compressed, their deformation is extensive and goes beyond the small strain framework in which most contact solutions are derived[69–71].

The mechanics of cutting in elastic brittle materials is different from that in ductile solids, such as metals. One of the peculiarities is related to the failure mechanism, which in the former occurs by formation of a crack while in the latter is connected to plastic flow[34]. Focusing on the separation stage following failure, a cut or crack propagates under the action exerted by the cutting force until a so-called steady-state may be established. A viable approach is to consider separation as a process of energy conversion: the work done by the external force applied through the cutting tool is converted into elastic strain energy, surface energy to propagate a crack and dissipated energy due to friction[72]. It might be convenient to employ the energetic equation of cutting as the starting point of analytical models and equations. Section 2.1 presents an extensive discussion on the energetic balances in cutting. A simplified analytical model of the steady-state propagation in a linear elastic material with an elliptical wedge is also included[73].

Although the mechanisms of propagation during steady-state cutting and tearing are similar, the way in which bulk energy is converted into surface energy available for crack propagation is different. More specifically, the crack driving energy during cutting is the result of a local conversion of the external work performed with the tool, as opposed to a remote source in conventional fracture tests. A fundamental parameter controlling the mechanism of propagation is the tool sharpness, whose role is analogous to the critical crack-tip radius in fracture tests[74]. Several authors have proposed metrics to measure the tool sharpness, and observed how it affects the cutting forces: for instance, blunt tools require a higher force and the cut surfaces are more irregular if compared to sharper tools[75,76]. This is an undesired consequence in the medical field[77] and in the food processing industry[78], for instance. Moreover, the tip shape has also an important effect on the geometry of the resulting cut[33]. In §2.2, a definition of sharpness is derived from the analytical model proposed, and then compared with results of numerical analyses where the effect of different tool profiles is explored. Experimental cutting tests on polystyrene, an example of a hard material which can be studied according to linear elastic fracture mechanics, confirm the implications of tool sharpness and show good agreement with the forecasts of the analytical model.

In Section 2.3 we show the results of an experimental investigation in cutting of soft elastic materials. In addition to measuring the cutting force, we have employed the Digital Image Correlation technique to examine in detail the deformations within the crack-tip region. The results confirm that crack propagation occurs with a mechanism that is typical of soft matter. These analyses, suggesting that the role of sharpness is coupled with fracture at large deformations, are introductory to the study of the crack-tip zone in soft materials, which is the subject of Chapter 3.

While a large part of cutting mechanics in elastic materials is related to crack propagation, there are certainly other factors that need to be considered. One of them is the role played by friction. Soft solids, such as food and biological tissues, often have a negligible bending stiffness but exert a high frictional resistance when cut. Methods to minimise the frictional effects are sought out in practical applications in order to reduce the cutting force, with the positive implications already discussed. An infamous example was devised as early as the Middle Age with the guillotine. The principle upon which it was ideated is known as oblique cutting[62], where the blade inclination produces a slice-push effect causing a reduction of the cutting force. A similar phenomenon is experienced in the daily life when cutting food: beside using a sharp knife, the addition of a sliding action to the push greatly reduces our effort[79,80]. Moreover, the effect of friction is to give an apparent enhancement of the fracture resistance, which has to be separated from the real material toughness[81]. In §2.4 we discuss the role of blade inclination and friction with an application to cutting experiments on thin samples of silicone rubber.

2.1. Models of indentation and cutting

2.1.1. Energetic balance of cutting

A versatile description of a cutting process is provided by an energy balance, in which the external work performed by a cutting tool pushed into the material is consumed by various contributions. In elastic cutting by means of a rigid tool the general incremental form of the energy balance is[72]

$$\mathrm{d}W_{\mathrm{ext}} = \mathrm{d}U_s + \mathrm{d}U_f + \mathrm{d}U_G, \tag{2.1}$$

where $\mathrm{d}W_{\mathrm{ext}}$ is the external work input, $\mathrm{d}U_s$ is the strain energy variation in the solid, $\mathrm{d}U_f$ is the energy dissipated due to friction and $\mathrm{d}U_G$ is the fracture energy required to separate the material. When the tool is pushed into the material for an infinitesimal length $\mathrm{d}D$ (Fig.2.1), the work done by the cutting force F is

$$\mathrm{d}W_{\mathrm{ext}} = F\mathrm{d}D. \tag{2.2}$$

Any type of cutting begins with indentation, in which the material is deformed without the creation of new cutting surfaces, until the insertion depth D reaches a critical value D_c. From Eqs.(2.1)-(2.2), taking $\mathrm{d}U_G = 0$, we obtain

$$F\mathrm{d}D = \mathrm{d}U_s + \mathrm{d}U_f. \tag{2.3}$$

In most cases, the frictional dissipation $\mathrm{d}U_f$ is also neglected until the beginning of separation. Notice that the condition $\mathrm{d}U_G = 0$ can also describe the insertion of a cutting tool in an open cut, for instance when a blade is inserted for the second time in an already cut material. In such a case, however, the frictional term in Eq.(2.3) must be included.

When $D = D_c$ a crack is initiated and the tool starts to separate the material. There is a transient stage, generally characterised by a sudden drop in the cutting force, which eventually leads to a steady-state. A required condition of steady-state cutting is that the rate of creation of new surfaces is equivalent to the rate of insertion of the tool[76]. In other terms, the displacement increment dD must equal the increase in cut length da (Fig.2.1). Notice that such a condition does not ensure the steadiness of the cutting force. More specifically, when the finite dimension of the tool, measured in the direction of insertion, is small compared to the size of the substrate, crack propagation occurs at constant force right after fracture initiation. On the contrary, when both tool and sample have comparable sizes, a crack is propagated for some time before the steady-state is attained. The motivation is connected to the length of the contact region, which increases while the tool is inserted in the material. As a consequence, both the strain energy and the frictional term on the right-hand side of Eq.(2.1) increase.

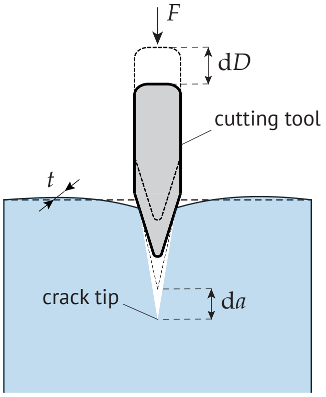

Figure 2.1 Two-dimensional sketch of crack propagation during cutting of an elastic material

The energy balance in the stage of crack propagation can be written as

$$F\mathrm{d}a = \mathrm{d}U_s + \mathrm{d}U_f + \mathrm{d}U_G. \tag{2.4}$$

In a two-dimensional framework, the increment in work of fracture $\mathrm{d}U_G$ represents the energy required to open a new surface of area $A = t\mathrm{d}a$, where t is the out-of-plane thickness of the material. We can write

$$\mathrm{d}U_G = Gt\mathrm{d}a \tag{2.5}$$

and, from Eq.(2.4), we obtain

$$G = \frac{F}{t} - \left(\frac{\mathrm{d}U_s}{t\mathrm{d}a} + \frac{\mathrm{d}U_f}{t\mathrm{d}a}\right), \tag{2.6}$$

where G is known as the energy release rate in fracture mechanics.

In the term $T = \mathrm{d}U_s/(t\mathrm{d}a)$ we recognise the so-called tearing energy of soft materials[82], which represents the fracture energy per unit area in the absence of an external force input. Methods to derive this energy are considered in detail in §3.1. The condition to create new crack surfaces requires that the left-hand side term G attains a critical value Γ, denoted as the fracture toughness of the material. If the bulk behaviour of the material is assumed linear elastic, the fracture energy can be expressed by means of the relation $G = K^2/E$, where K is the stress intensity factor and E is the Young modulus of the material. In a more general scenario, Γ includes dissipative terms due to inelastic effects and rate-dependence.

In steady-state cutting of soft solids, the contribution of friction is often the dominating term, whereas the strain energy term $\mathrm{d}U_s$ may be neglected. This simplifying assumption comes from considering the offcuts of soft materials being ineffective in storing relevant strain energy. However, if a pre-strain or a transverse state of compression is induced, for instance due to the clamping system of an experimental setup, the contribution of strain energy may have to be included. In particular, a tensile strain applied during the insertion reduces the cutting force by increasing the available energy for fracture, at the same time minimising frictional effects[83].

2.1.2. A two-dimensional model of steady-state cutting

The energetic balance of cutting, Eq.(2.1), is suitable for applications in a range of different materials and geometries. In the case of a linear elastic solid we have developed an alternative description of the cutting process in the steady-state, by solving a two-dimensional boundary value problem for the stress and displacement fields in an infinite body indented by a rigid tool[73]. In particular, the following assumptions are introduced:

- the material is linear elastic and the small strain assumption is retained;
- the contact between blade and material is assumed frictionless;
- the blade cross-section consists of an ellipse, with an aspect ratio that is kept constant during the insertion;
- a quasi-static insertion is considered, so that we can neglect inertia

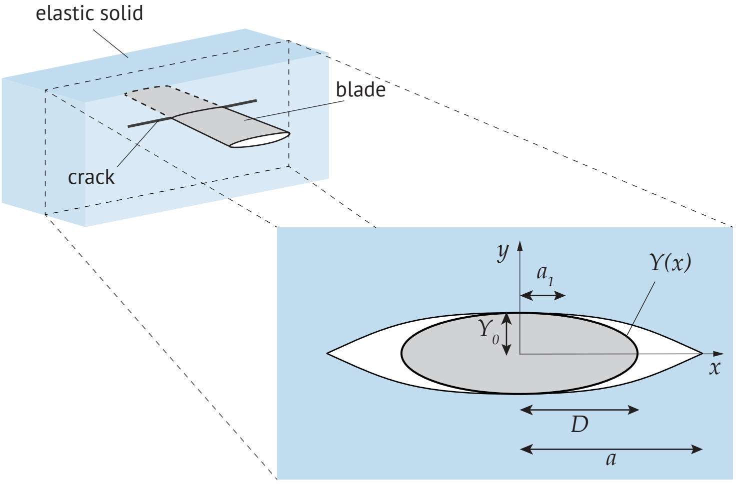

Figure 2.2 Schematic of the analytic model of cutting, with an elliptic blade inserted in a crack of length $2a$. The enlarged figure shows the blade cross section, where $Y(x)$ is the elliptic profile and a_1 is the contact length between blade and material

Let us consider an infinite solid with a centred cut of length $2a$. The cross-section of a rigid blade is represented by an ellipse with semi-axes D and $Y_0 \leq D$ (Fig.2.2). As specified in the hypotheses, we can change the relative length of the major semi-axis with respect to the crack semi-length but not the aspect ratio, i.e., D/Y_0 = const. While this assumption is a simplification of the cutting indentation with commercial blades, it is essential for the solution of the mathematical problem. In practical terms, a situation described by this model is the insertion of an elliptic conical blade, with a gradually increasing cross section, along a direction parallel to the blade axis. The equation of the ellipse is written as

$$Y(x) = \frac{Y_0}{2D}\sqrt{D^2 - x^2}. \tag{2.7}$$

The radius of curvature at a generic point of the ellipse is given by

$$\rho(x, Y) = (Y_0 D)^2 \left(\frac{x^2}{D^4} + \frac{Y^2}{{Y_0}^4} \right)^{3/2}, \tag{2.8}$$

which at the wedge tips $|x| = D$ is equal to

$$\rho(x = \pm D, Y = 0) = \frac{{Y_0}^2}{D}. \tag{2.9}$$

Formulation of the problem

Because of the double symmetry, only a quarter of the model needs to be considered. The crack initially extends in the region $|x| \leq a$, $y = 0$, while the ellipse is assumed to be shorter or equal to the cut, i.e. $D \leq a$. Furthermore, let $x \leq a_1$ denote the length along which the ellipse is in frictionless contact with the material. In this region we impose unilateral contact conditions by means of the following set of equations

$$y(x) = Y(x), \quad \sigma_{yy}(x) \leq 0 \quad \text{for } x \leq a_1, \tag{2.10}$$

where $y(x)$ represents the deformed profile of the crack.

Along the free edge of the crack the normal stresses must be null, while in terms of displacement we have two different conditions. We can write

$$\sigma_{yy}(x) = 0, \quad y(x) > Y(x) \qquad \text{for } a_1 < x < D; \tag{2.11a}$$

$$\sigma_{yy}(x) = 0, \quad y(x) > 0 \qquad \text{for } D \leq x < a. \tag{2.11b}$$

Ahead of the crack, continuity and symmetry bring the displacements unconditionally to zero, while no condition on the normal tractions can be established

$$y(x) = 0 \quad \text{for } x \geq a. \tag{2.12}$$

Finally, shear stresses are null everywhere along the crack plane as a result of the frictionless contact assumption

$$\sigma_{xy}(x) = 0 \quad \text{for } y = 0. \tag{2.13}$$

Equations (2.10)-(2.13) represent a boundary value problem to be solved for the stresses $\sigma_{yy}(x)$ and the displacements $y(x)$. The problem is decomposed in two cases which are solved separately (Fig.2.3). We begin by considering an elliptic displacement profile which derives from a well-known solution of fracture mechanics in which a crack is subjected to a uniform stress σ_0[84] (Fig.2.3a). Assuming the crack length equal to $2D$, in plane stress conditions we obtain

$$y(x) = \frac{2\sigma_0}{E}\sqrt{D^2 - x^2} \quad \text{for} \quad x \leq D, \tag{2.14}$$

from which we can find the normal stresses as

$$\sigma_{yy}(x) = -\sigma_0 \quad \text{for } x \leq D; \tag{2.15a}$$

$$\sigma_{yy}(x) = \sigma_0 \left(\frac{x}{\sqrt{x^2 - D^2}} - 1 \right) \text{for } x > D. \tag{2.15b}$$

Now we observe that the normal stress satisfies Eq.(2.10) if we take

$$\sigma_0 = \frac{EY_0}{2D}, \tag{2.16}$$

but in the open part of the crack, i.e. for $a_1 < x < a$, the solution needs to be modified, so that the conditions specified in Eq.(2.11) are respected. In order to equilibrate the normal stresses in the open part, a superimposed different problem is solved. We can consider a crack of length $(a - a_1)$ (Fig. 2.3b). The following tractions are applied on its surface

$$\sigma_{yy}(x) = \sigma_0 \quad \text{for } a_1 < x \leq D; \tag{2.17a}$$

$$\sigma_{yy}(x) = \sigma_0 \left(1 - \frac{x}{\sqrt{x^2 - D^2}}\right) \quad \text{for } D < x < a. \tag{2.17b}$$

In terms of displacements we prescribe that

$$y(x) = 0 \quad \text{for} \quad x > a \text{ and for } x < a_1\,. \tag{2.18}$$

To solve this second part of the boundary value problem, we observe that in general a stress singularity is expected at both ends $x = a_1$ and $x = a$. We immediately rule out the former by invoking the unilateral contact conditions (Eq.2.10), which prevent negative or positive stress intensity factors for any internal point. We expect the following conditions

$$K_{I,a_1} = 0, \quad K_{I,a} \geq 0, \tag{2.19}$$

where K_I is the mode-I stress intensity factor (SIF).

The weight function method for SIF computation

There are several available numerical methods to compute SIFs in linear elastic fracture mechanics, including the weight function method, the boundary collocation approach, the distributed dislocation technique and the finite element method[85]. Here we show how to derive the expression of $K_{I,a}$ of Eq.(2.19) through a specific application of the weight function method.

The method of weight functions is based on the application of Green's functions to express the stress state in a system subjected to a generic loading, combined with Betti's reciprocal theorem and the principle of superposition by Bueckner[86]. The latter is invoked to find the stress state in a cracked body subjected to generic external loading by following two steps: firstly, stresses in the uncracked body are found, in particular their distribution along the original crack line. Then, the system is subjected to equilibrating tractions along the crack, and the global solution is obtained from the sum of the two steps. A Green function can be used in the second step to find the stress intensity factor for the equilibrating internal tractions.

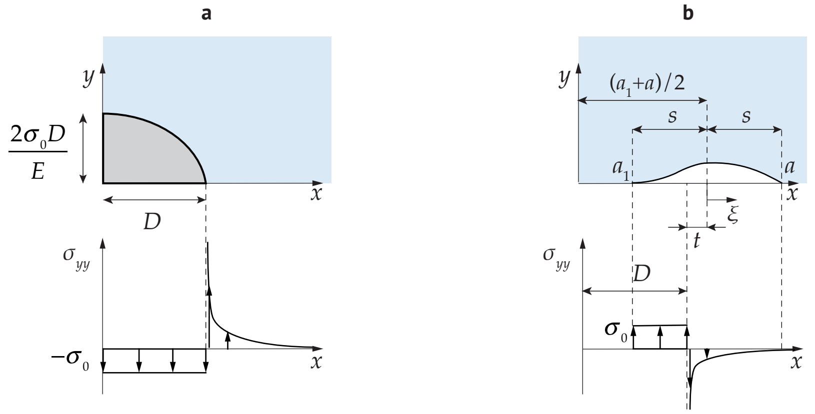

Figure 2.3 Displacement and stresses in the boundary value problem. **a** Equivalence between the elliptic profile and a crack of length $2D$ with an applied constant stress σ_0. **b** A crack of length $2s$, with prescribed stresses on its surface (derived from equilibrium). Notice the discontinuity in the displacement derivative at $x = a$

Let us consider two arbitrary loading systems, both resulting in a pure mode-I condition, and suppose that we know the resulting SIF for the first system. The SIF for the unknown loading is related to the first by[84]

$$K_I^{(2)} = \frac{1}{K_I^{(1)}} \frac{2\mu}{\kappa + 1} \int_C t_y^{(2)} \frac{\partial u_y^{(1)}}{\partial a} \mathrm{d}C, \tag{2.20}$$

where t_y are normal tractions applied on the outer boundary C of the system, kept fixed during an infinitesimal crack advance da, and u_y are the normal opening displacements of the crack. Notice that we have employed the shear modulus μ and Kolosov's constant κ to retain general validity. In plane stress, for instance, $\kappa = (3 - \nu)/(1 + \nu)$ and Eq.(2.20) can be written as

$$K_I^{(2)} = \frac{1}{K_I^{(1)}} \frac{E}{4} \int_C t_y^{(2)} \frac{\partial u_y^{(1)}}{\partial a} \mathrm{d}C. \tag{2.21}$$

Invoking the principle of superposition, we can relate the SIF to normal opening stresses σ_{yy} applied directly on the crack face

$$K_I^{(2)} = \int_c \sigma_{yy}^{(2)}(x) h(x) \mathrm{d}x, \tag{2.22}$$

where c is the crack perimeter and

$$h(x) = \frac{2\mu}{\kappa + 1} \frac{1}{K_I^{(1)}} \frac{\partial u_y{}^{(1)}(x)}{\partial a} \tag{2.23}$$

is referred to as the *weight function*. Given the arbitrary of the loading systems, $h(x)$ depends only on the body geometry and can be interpreted as the SIF generated by a unit force applied to the crack face at a point x.

Notice that we can use any arbitrary loading system to obtain $K_I^{(1)}$ in Eq.(2.23), provided that it results in pure mode-I loading on the crack faces and the body is assumed infinite. For instance, the SIF in an infinite body containing a crack of half-length a, centred on $x = 0$ and subjected to uniform tension σ_0, is

$$K_I^{(1)} = \sigma_0\sqrt{\pi a}, \tag{2.24}$$

and the normal displacement is given by

$$u_y^{(1)} = \frac{\kappa+1}{4\mu}\sigma_0\sqrt{x^2-a^2}, \tag{2.25}$$

with $x = 0$ corresponding to the centre of the crack.

Replacing Eqs.(2.24)-(2.25) in Eq.(2.23), the required SIF in Eq.(2.22) becomes

$$K_I^{(2)} = \frac{1}{\sqrt{\pi a}}\int\limits_{-a}^{a} \sigma_{yy}^{(2)}\sqrt{\frac{x+a}{x-a}}dx. \tag{2.26}$$

Solution of the elliptic wedge problem

Back to the specific problem shown in Fig.2.3b, we consider a crack of half-length $s = (a - a_1)/2$ and introduce a new variable ξ, such that the crack is centred at $\xi = 0$. Equation (2.26) is transformed in

$$K_\mathrm{I} = -\frac{1}{\sqrt{\pi s}}\int_{-s}^{s}\sigma_{yy}(\xi)\sqrt{\frac{s+m\xi}{s-m\xi}}\mathrm{d}\xi \tag{2.27}$$

by taking $x = \xi + (a_1 + a)/2$. The factor m is equal to -1 for the crack tip at $x = a_1$ and to +1 for the crack tip at $x = a_2$. Notice that the condition on the SIF at $x = a_1$, which has to be zero, will be used to find the position of a_1. Along the crack of length $2s$ the normal stress is discontinuous, as specified by Eq.(2.17), and it is therefore convenient to split the integral of Eq.(2.27) as follows

$$K_I^{(A)} = -\frac{\sigma_0}{\sqrt{\pi s}}\int_{-s}^{t}\sqrt{\frac{s+m\xi}{s-m\xi}}\mathrm{d}\xi = -\sigma_0\sqrt{\pi s}; \tag{2.28a}$$

$$K_I^{(B)} = \frac{\sigma_0}{\sqrt{\pi s}}\int_{t}^{s}\frac{D-t+\xi}{\sqrt{(\xi-t)(2D-t+\xi)}}\sqrt{\frac{s+m\xi}{s-m\xi}}\mathrm{d}\xi, \tag{2.28b}$$

where $t = D - (a_1 + a)/2$. Introducing the normalised variables $\hat{\xi} = \xi/s$, $\hat{t} = t/s$ and $\hat{D} = D/s$, the resulting SIF is given by

$$K_I = K_I^{(A)} + K_I^{(B)} = -\sigma_0\sqrt{\pi} + \frac{\sigma_0}{\sqrt{\pi}}\int_{\hat{t}}^{1}\frac{\hat{D}-\hat{t}+\hat{\xi}}{\sqrt{(\hat{\xi}-\hat{t})(2\hat{D}+\hat{\xi}-\hat{t})}}\sqrt{\frac{1+m\hat{\xi}}{1-m\hat{\xi}}}\mathrm{d}\hat{\xi}. \tag{2.29}$$

Taking $m = -1$ we have the expression for the stress intensity factor in $x = a_1$, and imposing the first condition of Eq.(2.19) we find that

$$K_{I,a_1} = K_{I,a_1}{}^{(A)} + K_{I,a_1}{}^{(B)} = 0 \Rightarrow \int_{\hat{t}}^{1}\frac{\hat{D}-\hat{t}+\hat{\xi}}{\sqrt{(\hat{\xi}-\hat{t})(2\hat{D}+\hat{\xi}-\hat{t})}}\sqrt{\frac{1-\hat{\xi}}{1+\hat{\xi}}}\mathrm{d}\hat{\xi} = \pi. \tag{2.30}$$

The integral of Eq.(2.30) is solved with a numerical recursive method which proceeds until a converged result is obtained after N cycles. At the generic cycle i we solve the following integral

$$k_i = \left(\frac{1}{\pi} \int_{\hat{t}}^{1} \frac{1+(\hat{\xi}-\hat{t})k_{i-1}}{\sqrt{(\hat{\xi}-\hat{t})(2+(\hat{\xi}-\hat{t})k_{i-1})}} \sqrt{\frac{1-\hat{\xi}}{1+\hat{\xi}}}\,\mathrm{d}\hat{\xi} \right)^{2}, \quad \text{with} \quad k_0 = 0, \tag{2.31}$$

where $k_i = s/D = 1/\hat{D}$. For $i = N$ we obtain $s = k_N D$ and hence a_1/a for any value of the ellipse semi-axis D.

Taking $m = +1$ in Eq.(2.28) we have the expression for the stress intensity factor in $x = a$

$$K_{I,a} = K_{I,a}{}^{(A)} + K_{I,a}{}^{(B)} = \sigma_o\sqrt{\pi} \left(\int_{\hat{t}}^{1} \frac{\hat{D}-\hat{t}+\hat{\xi}}{\sqrt{(\hat{\xi}-\hat{t})(2\hat{D}+\hat{\xi}-\hat{t})}} \sqrt{\frac{1+\hat{\xi}}{1-\hat{\xi}}}\,\mathrm{d}\hat{\xi} - 1 \right), \tag{2.32}$$

where the integral is solved as described above.

The results obtained from Eq.(2.30) and Eq.(2.32) are illustrated in Fig.2.4a as a function of the normalised length D/a. The ratio D/a represents the part of the initial crack of half-length a that is filled by the blade. Following a more common definition in cutting, we denote D/a as the relative insertion of the wedge, keeping in mind that, according to the present model, increasing D results in an increase of the other semi-axis. The SIF $K_{I,a}$ is normalised with respect to K_R, the stress intensity factor that would develop if the wedge filled the entire crack, i.e. $D = a$, defined as

$$K_R = \sigma_0\sqrt{\pi a} = \frac{EY_0}{2}\sqrt{\frac{\pi}{a}}. \tag{2.33}$$

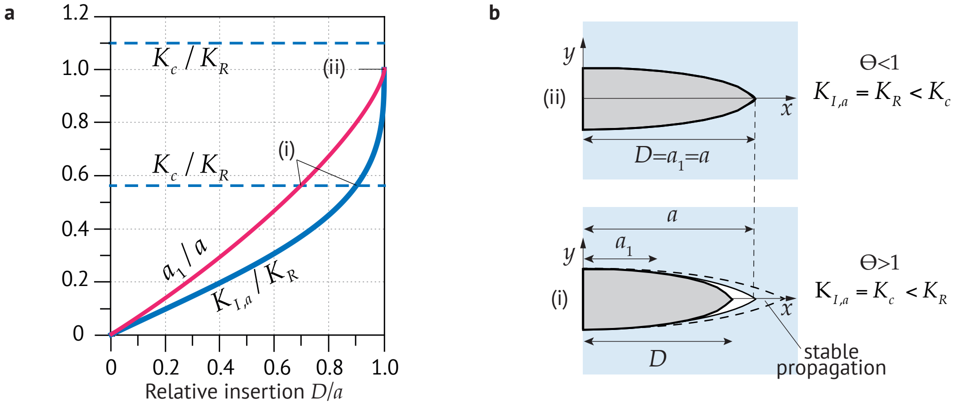

Figure 2.4 a Analytic results for the elliptic wedge. The dimensionless stress intensity factor $K_{I,a}/K_R$ and the position of the separation point a_1/a are plotted as a function of the normalised length D/a. **b** Crack propagation during the blade insertion is shown with respect to two different critical conditions (when $K_{I,a} = K_c$), with (i) related to a blunt wedge ($\Theta > 1$) and (ii) to a sharp wedge ($\Theta < 1$)

2.2. The role of blade sharpness

The model presented in the previous section is instrumental in exploring the role of the blade sharpness on the fracture process, specifically at critical conditions for crack propagation. In practical terms, sharper tools require less force to be pushed into the material, reduce the deformations and result in smoother cut surfaces. Firstly, we propose a definition of sharpness for the elliptic wedge problem, which considers the geometry and the material properties. With the aid of numerical analyses, we explore the influence of different tool profiles on the condition for crack propagation and compare them to the reference case of the elliptic blade. Finally, we show an application of the proposed model to cutting of a glassy polymer, which we assume to behave according to linear elastic fracture mechanics. The results obtained from experiments seem to confirm the role of sharpness in crack propagation during the steady-state cutting[72].

2.2.1. A definition of sharpness

In a linear elastic material we can express the critical condition for crack propagation as $K_{I,a} = K_c$, where K_c is the fracture toughness. A sharpness parameter can be introduced if we express the condition for propagation in terms of a critical radius ρ_c, to be compared with the radius of curvature ρ at the tip. In the elliptic wedge, we can combine Eq.(2.16) and Eq.(2.33) in Eq.(2.9) to obtain

$$\rho = \frac{4}{\pi}\left(\frac{K_R}{E}\right)^2 , \tag{2.34}$$

where we have assumed $D = a$. The critical radius ρ_c is consistently defined as

$$\rho_c = \frac{4}{\pi}\left(\frac{K_c}{E}\right)^2 . \tag{2.35}$$

Then we can introduce a sharpness parameter Θ from the ratio

$$\Theta = \frac{\rho}{\rho_c} = \left(\frac{K_R}{K_c}\right)^2 , \tag{2.36}$$

with $\Theta < 1$ identifying a sharp and $\Theta \geq 1$ a blunt wedge.

The critical condition for crack propagation is different according to this distinction, as illustrated in Fig.2.4b. With the help of the SIF plots (Fig.2.4a) we can discuss the implications of the sharpness parameter Θ on crack propagation. As the elliptic wedge is inserted in the crack, the SIF increases with the normalised length D/a: depending on the wedge sharpness, there are two different ways in which crack propagation might happen. For the case of blunt wedges with $\Theta > 1$, $K_{I,a}$ increases until the limit imposed by the material toughness K_c is attained. Then, the crack starts to propagate in a stable manner, so that the distance between the current crack tip and the wedge tip remains constant and equal to $a - D$. Consequently, the wedge tip never reaches the crack tip. For $\Theta < 1$, the sharp wedge is inserted completely into the crack and the SIF rises up to the value $K_{I,a} = K_R$, but the critical condition cannot be attained. In order to propagate the crack and cut through the material, the wedge is pushed against the crack tip and further energy is required.

Neglecting friction and the compression of the material caused by the wedge, according to Eq.(2.6), the increment of cutting force to be provided to the system is

$$\Delta F = \frac{\left(K_c^2 - K_R^2\right)}{E} t. \tag{2.37}$$

2.2.2. Influence of tool geometry

The major outcome of the proposed analytical model is the role played by the wedge sharpness on crack propagation. Still, there are many limitations that need to be addressed if the discussion has to be applied to cutting with commercial blades.

One of them is related to the material behaviour, which until now we have assumed linear elastic. In fact, the region where the blade is inserted is affected by high stresses, and it is therefore obvious to expect some material damaging and inelasticity. For instance, it was found that a small plastic zone near the crack tip resulted in a visible decrease of $K_{I,a}/K_R$, the more relevant the more the wedge was inserted into the material, i.e. for $D/a \to 1$[73]. On the contrary, the position of the contact point a_1/a was not significantly altered by plasticity. Since this material behaviour is not common in the soft elastic tissues considered throughout the thesis, we are not taking it into account here. Rather, it is the effect of large deformations that needs to be considered in soft materials. The role of blade sharpness in soft hyperelastic tissues is explored in the chapter dedicated to large deformations (§3.4).

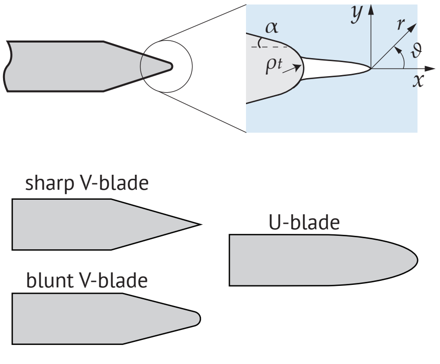

Figure 2.5 Blades with different profiles, characterised by the wedge angle α and the tip radius ρ_t

Another limitation in our analytic model is related to the elliptic shape of the blade, which is far from the features of a commercial blade. We have explored the impact of the tool geometry on crack propagation with the help of finite element (FE) analyses. Instead of modelling the whole propagation process, we have considered the contact problem between the rigid blade and a semi-infinite body with an edge-crack of length a. The material is linear elastic and plane stress conditions are assumed, as in the analytical model. Unilateral contact constraints are enforced by means of no-tension springs (i.e., springs with zero stiffness if the interface stresses are tensile) and additional boundary conditions are imposed to take advantage of the symmetry. The tool geometry is defined by the wedge opening angle α and the wedge tip radius ρ_t. In particular, we have considered three geometries (Fig 2.5): a sharp V-blade, with an angle $\alpha = 25^\circ$ and $\rho_t \simeq 0$, a blunt V-blade, with an angle $\alpha = 25^\circ$, and a blunt U-blade with a wedge angle $\alpha = 0^\circ$. Blunt blades are characterised by a non-zero value of the tip radius ρ_t, which in commercial tools is often in the order of a few micrometres. However, the grade of mesh refinement attainable in our FE model was not enough to capture the effect of such a small radius. In the analyses, we have considered $\rho_t = 100 h_{\mathrm{el}}$, where h_{el} is the smallest element near the crack tip, in the order of 10^{-3}mm (the crack length is $a = 1$mm).

The results are shown in Fig.2.6, in terms of $K_{I,a}/K_{I,D=a}$ and a_1/a as a function of the relative insertion D/a. Notice that we have used $K_{I,D=a}$ to normalise the results, which is the SIF obtained from the numerical analyses for each profile when $D = a$. For the elliptic wedge this is also equal to K_R. The stress intensity factors are obtained from the opening displacements u_y of nodes located behind the crack tip through the following relationship

$$K_{I,a} = \lim_{r \to 0} u_y(r) \frac{E}{4} \sqrt{\frac{2\pi}{r}}, \tag{2.38}$$

where r is the distance measured from the crack tip. To ensure the best possible accuracy, the displacements were taken from nodes at a certain distance from the tip and then the SIF was obtained through a linear extrapolation. A careful design of the mesh in the crack-tip region was also essential. Additional details on finite elements and mesh specifications for fracture mechanics analyses are reported in the Appendix A.4.

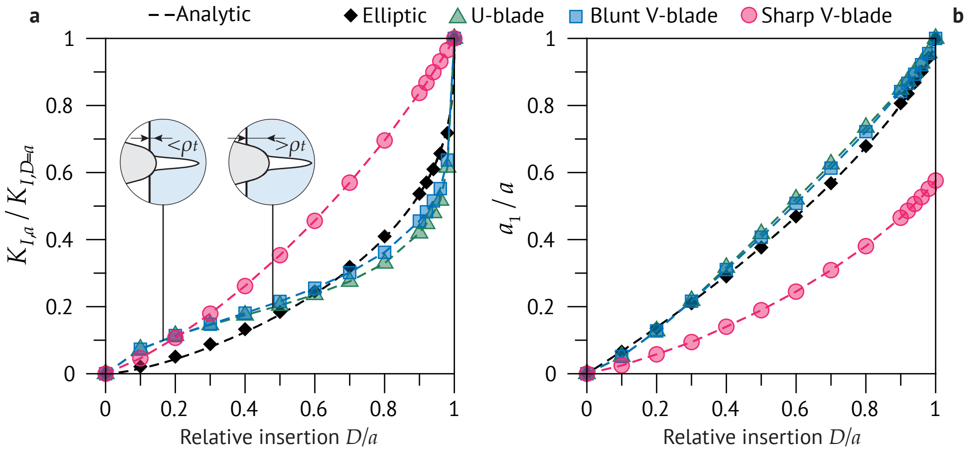

Figure 2.6 The dimensionless stress intensity factor $K_{I,a}/K_{I,D=a}$ (**a**) and the position of the separation point a_1/a (**b**) are plotted as a function of the normalised length D/a. Points are obtained from FE analyses whereas the black dashed line comes from the analytic solution of an elliptic wedge. The insets show the initial insertion of blunt blade with tip radius ρ_t

The black dashed lines in Fig.2.6 come from the analytical solution of the elliptic wedge. The black diamonds are obtained from FE analyses that reproduced the geometry of the elliptic wedge and show excellent agreement with the analytic solution. With respect to the influence of different tool geometries, it might be noticed that the main role is played by the tip radius ρ_t, while the effect of the opening angle α seems to be more limited. Notice that ρ_t is a constant radius of curvature, whereas in the elliptic wedge the tip radius ρ changes with the insertion length D. Since the aspect ratio of the ellipse is kept constant, from Eq.(2.9) we notice that the radius gets larger when D increases.

In Fig.2.6a we observe that the stress intensity factor produced by a sharp V-blade is noticeably larger than in the other blades, for the same length D/a. In other terms, the condition for crack propagation is anticipated and the required cutting force is smaller than in the other blade profiles. In addition, Fig.2.6b shows that, for a given insertion length, the extension of the traction-free zone $(a_1 - a)$ is larger for sharp than for blunt blades. Observing the trends in Fig.2.6a for the blunt blades, it should be noticed that the blade shape is fully described by a circular arc during the initial penetration stage ($D/a \lesssim 0.2$). On the other hand, in the subsequent stage the blade profile is composed by a circular arc and a straight segment, as shown in the enlarged figures. This might help to appreciate the peculiar trends of those curves.

2.2.3. Experimental investigation of a glassy polymer

Tool sharpness plays an important role in cutting elastic materials. We have shown how sharper blades result in higher stress intensity factors and what the different nature of crack propagation with a sharp tool is. Now we are ready to test the predictions of our analytical model on a case of real cutting. The combined results of experiments and numerical analyses are illustrated in this paragraph.

The material that we have chosen is polystyrene, a thermoplastic glassy polymer with a rather stiff and brittle behaviour, which we assume to conform to the assumptions of the model. Fracture of glassy polymers is characterised by the formation of crazes, planar crack-like defects near the crack tip, which might result in a toughening effect and an increase in the fracture resistance of the material[87]. In order to apply linear elastic fracture mechanics, we need to take the maximum care in avoiding the formations of such crazes. Tensile tests on a dog-bone shaped specimen allowed us to measure the main mechanical properties, such as the Young modulus E, the tensile strength σ_{max} and the ultimate strain ϵ_{max}. Poisson's ratio is taken from the literature[88]. The fracture toughness K_c was measured on a single-edge notched specimen, containing an initial crack made with a razor blade. The mechanical properties of polystyrene are summarised in Table 2.1.

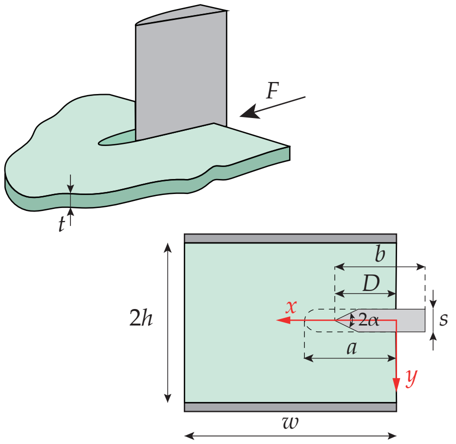

Figure 2.7 Sketch of the specimen used in the cutting tests, with details of the blade shape. The blade is inserted in control of displacements for a length D and the cutting force F is measured. A crack of length a is propagated in the material following the initial indentation

A sketch of the cutting test geometry is shown in Fig. 2.7. Thin plate specimens of width w, height $2h$ and thickness t are cut with a blade held orthogonally to the plate and pushed into it along the x axis in control of displacements. We have used a commercial, stainless steel cutter blade, whose profile has the following measures: thickness $s = 0,5$mm, width $b = 18$mm, opening angle $\alpha = 20°$. The samples are clamped with a proper system that minimises the risk of unwanted slips and the blade is changed after each test, in order to avoid any alteration of the tip sharpness. All the tests are performed at room temperature. Displacements are imposed to the blade at rates ranging from 8 to 100 μm/s, with the lower rates corresponding to quasi-static testing conditions. Records of the cutting force F against the imposed displacement D are acquired for each test.

In Fig.2.8a we show the results obtained from a typical cutting test, where the force per unit thickness F/t is plotted as a function of the insertion displacement D. The relevant dimensions are included in the plots. The force-displacement curves are characterised by a first stage (i), up to $D = D_c \approx 3$ mm, which corresponds to the initial indentation. The external work done by the tool is mainly consumed by strain energy, according to the equation of cutting shown in Eq.(2.3). A linear dependence of the penetration force with the displacement is noticed, with a slope of F/t versus D of about 30 N/mm^2. Increasing the applied displacement results in a small drop in the penetration force, due to the dissipation of strain energy in crack initiation. The second stage of the curves (ii), up to a penetration depth $D \approx D_C + b$, describes the part of separation occurring with increasing force. A crack of length a propagates ahead of the cutting tool, with the force that increases due to the contribution of friction along the blade surfaces in contact with the material. The slope of the penetration force versus the displacement is about 1.5 N/mm^2. In the third stage (iii), the steady-state is reached because the blade has penetrated completely, so that the force tends to become constant. Also shown in Fig.2.8a is the curve obtained from a blunt blade, where blunting was achieved by manually scratching the tip with emery paper. Although the effect is minimal, we notice that there is no difference until crack propagation begins, which happen at a slightly higher force with respect to the sharp case.

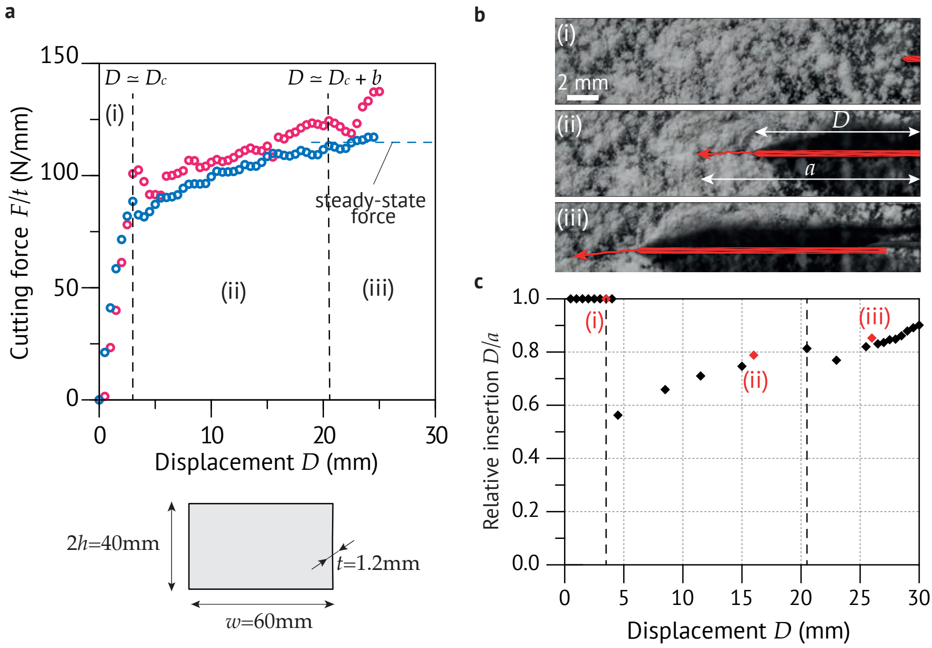

Figure 2.8 **a** Experimental force-displacement curve from cutting tests on the polystyrene specimens, showing (i) the initial stage of indentation, (ii) the stage of propagation with increasing F and (iii) the steady-state (iii) (blue points). Points shown in red are related to the same geometry but with a manually blunted blade tip. **b** High-definition images of the blade insertion, taken at points representative of the three different stages of the force-displacement curve. The blade cross-section is highlighted in red, with the small arrows showing the crack paths. **c** The relative insertion D/a as a function of the displacement D, where a identifies the instantaneous position of the crack tip (red diamonds are those shown in the images)

Focusing on the state of crack propagation with increasing force, the energy balance of cutting is given by Eq.(2.4), where both the contributions due to the strain energy and the frictional dissipation coexist. In the absence of applied stretches, the material is compressed due to the blade and the clamping system of the test (Fig.2.7). Following elementary calculations, we consider uniaxial compression by the blade in the affected region, of volume $V = hDt$. The strain energy density derivative is independent of the displacement D

$$\frac{\mathrm{d}U_s}{\mathrm{d}D} = Et\frac{s^2}{4h}, \tag{2.39}$$

where $s = 0.5$mm is the blade thickness.

Considering Coulomb friction along the contact surface, of area $A = 2Dt$, the derivative of the frictional work increases with D, according to

$$\frac{\mathrm{d}U_f}{\mathrm{d}D} = \frac{Es}{h}ftD. \tag{2.40}$$

With respect to the material parameters (Table 2.1) and the geometry used in the experiments ($h = 20$mm, $t = 1.2$mm and $s = 0.5$mm), we can work out values of $\mathrm{d}U_s/\mathrm{d}Dt \simeq 1$N/mm and of $\mathrm{d}U_f/\mathrm{d}Dt \simeq 10$N/mm, assuming a coefficient of friction $f = 0.3$. We believe that the strain energy contribution might therefore be neglected with reasonable approximation.

In the light of the discussion on the role of tip sharpness on the condition for propagation, we show in Fig.2.8b three high-definition images taken during the tests. At the same time, we report in Fig.2.8c the relative position D/a as a function of the blade insertion D, where a is the length of the crack initiated and propagated by the blade. At the very beginning (i) there is no crack propagation, therefore we find all the points aligned at $D/a = 1$. Following fracture initiation, a sudden increase in the crack length a occurs, which takes a while to stabilise in the steady-state cutting, and the ratio D/a drops. This means that the crack is advancing ahead of the blade tip. Increasing the displacement D, it seems that the blade tip gets a little closer to the crack without ever reaching it. The observed behaviour is typical of what we have defined as blunt propagation.

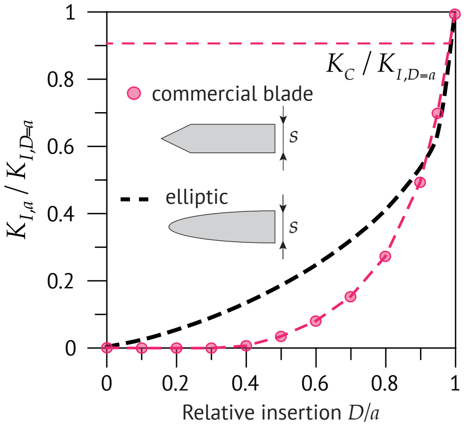

Figure 2.9 Results of FE analyses. Normalised stress intensity factor $K_{I,D}/K_{I,D=a}$ for the commercial blade, compared to the elliptic wedge. The horizontal dashed line corresponds to the ratio $K_c/K_{I,D=a}$ pertaining to the polystyrene

But can we compute a value of the sharpness parameter Θ? Since Θ was derived for an elliptical wedge, we can obtain an equivalent tip radius for the commercial blade used in the experiments from Eq.(2.34)

$$\rho_{eq} = \frac{4}{\pi}\left(\frac{K_{I,D=a}}{E}\right)^2, \tag{2.41}$$

where the SIF $K_{I,D=a}$ has been computed through FE analyses with the profile of the commercial blade, when $D = a$. The results are illustrated by the red dashed line in Fig.2.9, compared to the

Table 2.1 Mechanical parameters of the polymeric materials used in the cutting experiments

Variable	Polystyrene	Silicone
Young's modulus E (Pa)	$1.30 \cdot 10^9$	$1.36 \cdot 10^6$
Poisson's ratio ν	0.35	0.42
Fracture toughness K_c(Pa m$^{1/2}$)	$2.44 \cdot 10^6$	-
Fracture toughness Γ (Pa m)	-	$1.02 \cdot 10^3$

elliptic wedge solution. Using the fracture toughness K_c of polystyrene and $\rho_{eq} \simeq 5 \cdot 10^{-3}$mm for the commercial blade, from Eq.(2.36) we find $\Theta \simeq 1.22$. Indeed, the ratio $K_c/K_{I,D=a} \simeq 0.91$ corresponds to D/a less than unity on the plot. This is in good agreement with the experimental plot shown in Fig.2.8c, where an average value of D/a in the steady-state is in the range 0.8–0.9.

2.3. Experimental cutting of soft materials

Until now we have considered a linear elastic solid, providing an ideal framework to develop our model of cutting. In particular, within the hypothesis of small scale yielding adopted in linear elastic fracture mechanics, the region of large strains surrounding the crack tip is replaced with a K-dominated region, in which the material elastic properties become irrelevant. However, most biological tissues considered in the thesis are soft and behave quite differently from this picture. For this reason, we have organised a large experimental campaign on cutting of soft materials. The results also provide a good comparison to check the implications and limits of the linear elastic model.

Given the limitations in the supply of biological tissues for the experimental tests, we have employed silicone rubbers, characterised by a stress-strain curve similar to that of skin[72]. We have chosen a commercial silicone (Elite Double 32 by Zhermack Dental) and prepared in-house several specimens. Matrix and curing agents were thoroughly mixed according to the ratios suggested by the producer. The mixture was spread onto a custom-made aluminium mould where it rested for at least 24 hours. Then the specimens were extracted from the mould and cut in rectangular plates with razor blades.

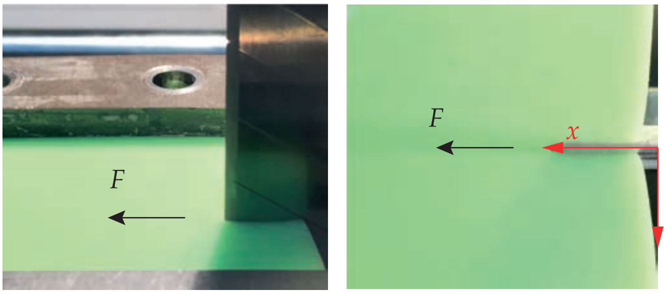

Figure 2.10 Pictures taken during the cutting tests on silicone, showing the direction of load application and the reference system (left, side view; right, top view)

Before beginning the cutting tests, the material was characterised through mechanical tests to determine the Young modulus and the fracture toughness. The instantaneous stress-strain curve obtained from tensile tests is typical of a rubber-like material with reduced strain hardening, and at low-to-moderate stretches it is fitted equivalently well by a neo-Hookean or Ogden's hyperelastic incompressible law (see Chapter 3), from which the Young's modulus can be derived. The fracture toughness of soft materials cannot be measured with the traditional linear elastic fracture mechanics approach followed on polystyrene. Instead, it is possible to derive the toughness of rubber-like materials from the tearing energy, following one of the available methods among those described in §3.1. In this specific case, we have used the so-called single-edge notch test and obtained the fracture energy Γ of the silicone rubber. The mechanical parameters of the material are summarised in Table 2.1.

The cutting tests have adopted the same experimental set-up described for polystyrene and illustrated in Fig.2.7 and Fig.2.10. Since the effect of rate is significant for rubber-like materials, displacements were imposed to the blade at various rates, ranging from 8 to 100 μm/s, with the lower values corresponding to quasi-static testing conditions. Records of the cutting force F against the imposed displacement D were acquired for each test.

Figure 2.11a illustrates the experimental curves obtained from a group of tests performed at different blade insertion velocities v. The relevant dimensions are included in the plots. The force per unit thickness F/t is plotted as a function of the insertion displacement D, at two different rates of blade insertion v. For $v = 0.03$mm/s we show the average and standard deviation from different tests, where the dispersion observed is ascribed to small temperature fluctuations between the tests. We have also computed the slope of the force-displacement curve (dashed line in the figure) as a moving average of the tangent at each point. This usually provides a clearer view of the different stages of cutting: in particular, the beginning of the steady-state is identified by the stiffness curve dropping to zero[76]. The force-displacement plots are qualitatively similar to those obtained from analogous tests on polystyrene (Fig.2.8a), although the forces are noticeably lower due to the reduced stiffness of silicone. The three different stages of indentation-cutting of soft materials are illustrated in the sketches below the plot. The curves initially rise in a non-linear manner, up to the critical depth of fracture initiation D_c, characterised by a significant drop in the stiffness. This point is not clearly visible in the curve for $v = 0.1$mm/s. In the following stage, the blade advances in the material under increasing force, with the stiffness showing some fluctuations around a mean value. Finally, for a displacement $D \simeq D_c + b$ the blade has fully penetrated the specimen, and the force stabilises at a constant, slightly decreasing value.

We have also performed some tests on specimens containing pre-cracks of length a_0, made with a razor blade (Fig.2.11b). The first evident difference in the force-displacement curve is the lack of the initial indentation. According to Eq.(2.3), when the blade is advanced into an open cut the work of fracture dU_G is null. Moreover, in soft materials the cumulated strain energy is also small and the only contribution left is due to frictional dissipation. The force rises almost linearly until the tip of the pre-crack is reached, which occurs when $D \simeq a_0$, where we notice a sudden rise in the cutting force. Since the tool touches the crack tip, an additional amount of energy has to be provided in order to further propagate the crack. Although we cannot use Eq.(2.37) for linear elastic materials to compute the force jump, we can assume that the energy for crack propagation is related to the fracture energy Γ of the material. The final stage of the curves corresponds to the steady state, where the penetration force is approximately constant. Changing the length a_0 of the pre-crack does not modify the main stages observed but inverts the order in which they occur. When $a_0 < b$ (yellow line in the plot), the blade hits the tip of the pre-crack before being

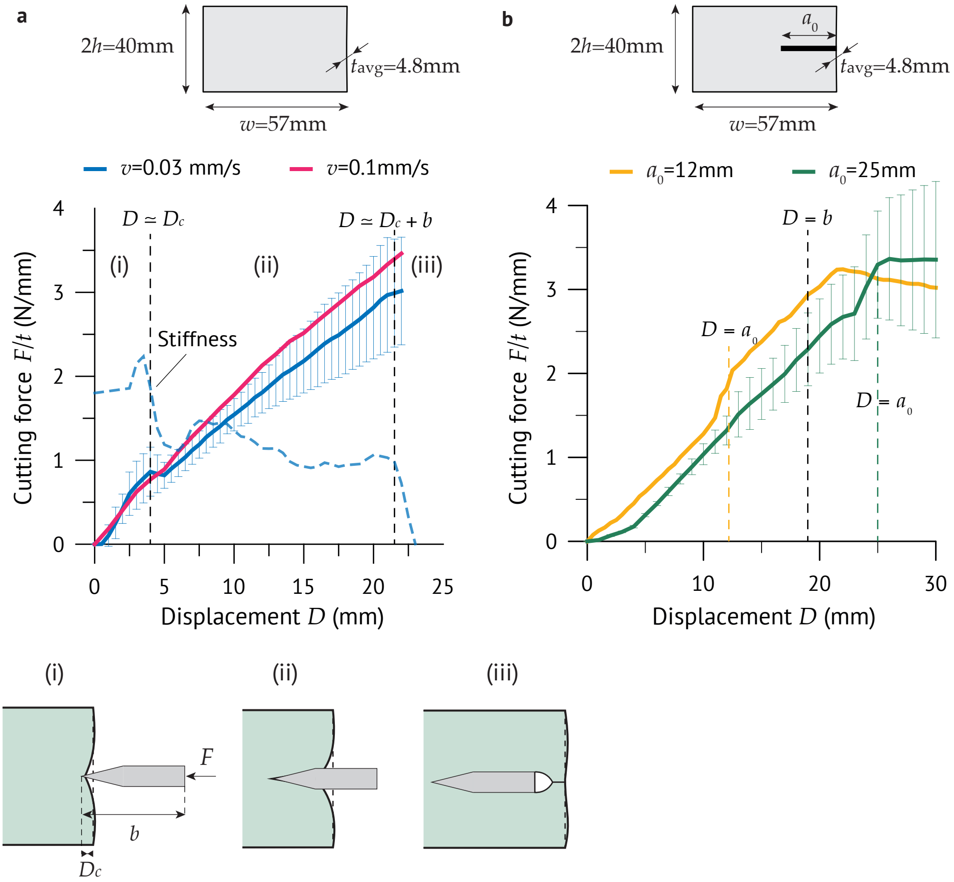

Figure 2.11 Experimental curves from cutting tests on silicone rubber. Average values with standard deviation are shown for multiple tests with the same parameters. **a** Force-displacement curves at two different displacement rates v. The dashed line is the stiffness at the lowest rate. **b** Results for specimens with pre-crack of different lengths a_0, at a displacement rate of 0.03 mm/s

completely penetrated into the material. After the sudden jump, the force resumes the increasing trend with the same initial slope until it is pushed completely into the material. On the opposite, if $a_0 > b$ (green line in the plot), the force increases constantly until $D \simeq b$ and then seems to stabilise because the contact area has become constant. Later comes the force jump, when $D \simeq a_0$.

DIC strain and displacement maps

As anticipated, the more relevant feature of cutting soft materials is the large deformation surrounding the blade tip. Before considering the stress fields in hyperelastic materials more in detail (Chapter 3), we offer a preliminary insight through the strain and displacement maps obtained by means of a Digital Image Correlation (DIC) technique. Images were acquired with a high-resolution digital camera (maximum resolution of 5184 × 3456 pixels) mounted on a tripod, and lights were used to ensure a uniform illumination of the specimens, which have been covered with

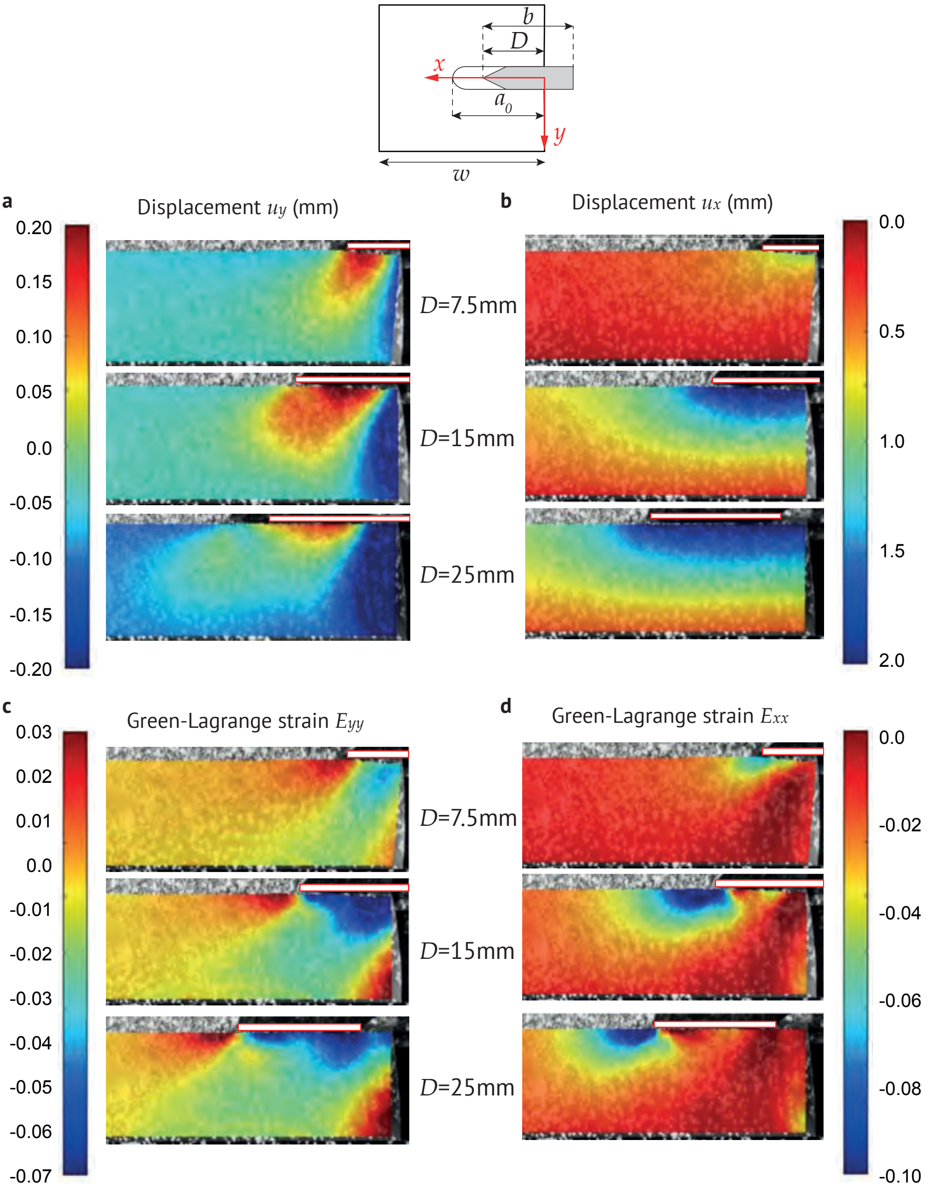

Figure 2.12 DIC maps of the displacements and strains during cutting of a silicone sample, at three different insertion lengths D of the blade. **a** Displacements u_y and **b** u_x. **c** Green-Lagrange strains E_{yy} and **d** E_{xx}

speckle patterns before beginning the tests. The raw data were then analysed by means of the freeware software Ncorr[89] to extract the displacement and strain fields within the samples.

The results shown in this section are related to a specimen with an initial crack of length $a_0 = 12\text{mm} < b$ and an insertion velocity $v = 8\mu\text{m/s}$. The full-field maps of the displacements u_y and u_x, and the Green-Lagrange strains E_{yy} and E_{xx} are shown in Fig.2.12. For each plot we have considered three different stages of the blade insertion: in particular we are showing the results for $D = 7.5\text{mm} < a_0$, $a_0 < D = 15\text{mm} < b$ and $D = 25\text{mm} > b$. The latter is the only one within the region of steady-state cutting. The values are also plotted as a function of the normalised distance x/w in four different charts displayed in Fig.2.13. The reference system is shown in Fig.2.12.

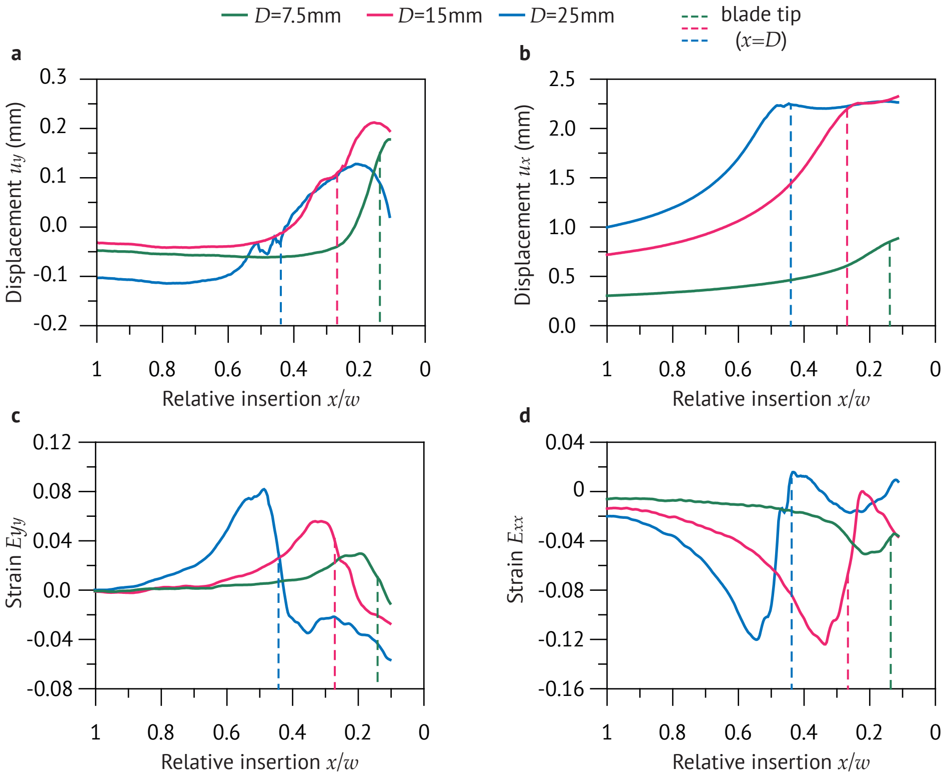

Figure 2.13 Plots of **a** the displacements u_y and **b** u_x, and of **c** the Green-Lagrange strains E_{yy} and **d** E_{xx}, as a function of the normalised distance x/w. The curves correspond to three different insertion lengths D, and the dashed lines mark the position of the blade tip $x = D$ in each case

When the blade is pushed into the material, points are displaced normally to its travelling direction. The displacement u_y illustrated in Figs.2.12-2.13a shows a maximum corresponding to the thicker part of the blade section, which should approximately be equal to half of the thickness $s = 0.5\text{mm}$. Consistently, the strain E_{yy} (Figs.2.12-2.13c) is negative in the same region, whereas it is positive ahead of the blade tip. The phenomenon of crack-tip touching is observable in the plots related to $D = 15\text{mm}$ and $D = 25\text{mm}$. Figure 2.13b shows a remarkable increase in the displacement u_x caused by the blade pushing against the tip of the pre-crack, with respect to the green curve for $D = 15$mm, when the crack tip has not been touched yet. At the same time, a localised region of negative strains appears in the strain maps of E_{xx} (Fig.2.12-2.13d).

The results of DIC, combined with the force-displacement curves, offer a compelling picture of cutting in soft elastic materials, whose peculiarities might be appreciated if compared to the same process in hard materials (§2.2.3). When a compliant solid is indented and cut by means of a rigid blade, a region of large strain surrounds the tool tip. However, this area is small if compared to the size of the sample, which remains largely undeformed. Provided that the cutting tool is sufficiently sharp, crack propagation does not happen as an autonomous process under symmetric mode-I, as in hard and brittle materials. An external amount of energy is required, which is directly input at the crack tip, so that the cutting tool is pushed against the material. The result is the development of a compressed region which moves as the blade cuts through the solid. It is also evident that a definition of sharpness cannot be made a-priori without considering both the features of the cutting tool and the material properties. In particular, the same commercial blade that was considered 'blunt' in the polystyrene samples, behaves like a 'sharp' blade when cutting silicone. This arises an important question: what exactly is the material parameter controlling the influence of sharpness on crack propagation? The fracture mechanics at large deformation and the crack-tip region in soft materials need to be investigated before we can attempt to answer to that question.

2.4. On the effect of friction

When a material is separated under the action of a cutting tool, the surfaces of the newly formed crack slide against the blade dissipating energy through friction. Frictional dissipation is often the main contribution to the energy balance of cutting in soft elastic materials, making up a large part of the cutting force. In this section, we show how frictional effects can be minimised through the addition of a fictitious slicing action during the insertion, obtained by inclining the cutting tool. The technique is commonly known as oblique cutting.

Cutting with slicing is notoriously easier than simply pushing into the material. In oblique cutting, a slice-push effect is induced because of a component of the tool velocity parallel to the edge, which reduces the frictional force. One can find an optimum blade angle corresponding to the minimum cutting force, considering the reduction of the frictional force and the increase of the work due to the out-of-plane deflection which occurs at larger angles. Adopting the basic model of oblique cutting proposed by Atkins et al.[79], we have performed experimental tests on silicone thin samples cut by a rigid blade with different inclination angles[81]. The samples are rectangular plates containing a pre-crack of length a_0, identical to those used in the other cutting experiments (see §2.3). A sketch of the experimental set-up, showing the variables employed in the analytical formulation, is presented in Fig 2.14. The material properties have been described previously (Table 2.1) but here we need to spend a few more words on which frictional model is the most suitable for soft solids.

Coulomb's frictional law is the most common model, owing to its simplicity. It is a pressure-dependent frictional model, in the sense that the frictional force is proportional to the normal force acting on the contact surface. In practice, Coulomb's law states that slips are initiated when the tangential contact stress exceeds the normal stress σ_n multiplied by the coefficient of friction f. When soft solids come into contact with hard surfaces, such as the steel blade of the experiments, relevant frictional dissipation is observed despite little contact stress against the blade. Pressure-dependent laws seems therefore inappropriate in this case. Instead, we can represent friction by a constant adhesive stress τ_f acting over the whole contact length between blade and material. Therefore we simply have

$$\sigma_{xy} = \tau_f, \tag{2.42}$$

irrespective of the contact pressure.

Let us focus on the steady-state, when the blade is inserted into the material for a length $D \geq b$, which we also assume longer than the pre-crack a_0. The reason why we have employed pre-cracked samples is because we want to isolate the effect of oblique cutting during crack propagation from that connected to the indentation. The energy dissipation due to friction, per increment of insertion length, is

$$\mathrm{d}U_f = F_f \mathrm{d}D, \tag{2.43}$$

where $F_f = 2bt\tau_f$ is the frictional force and the factor 2 is added to account for both sides of the blade-material contact. Inserted in the energy balance of cutting, Eq.(2.4), we obtain

$$F\mathrm{d}a = \mathrm{d}U_s + F_f \mathrm{d}a + Gt\mathrm{d}a, \tag{2.44}$$

with $\mathrm{d}a = \mathrm{d}D$ from the steady-state condition.

2.4.1. A model of oblique cutting

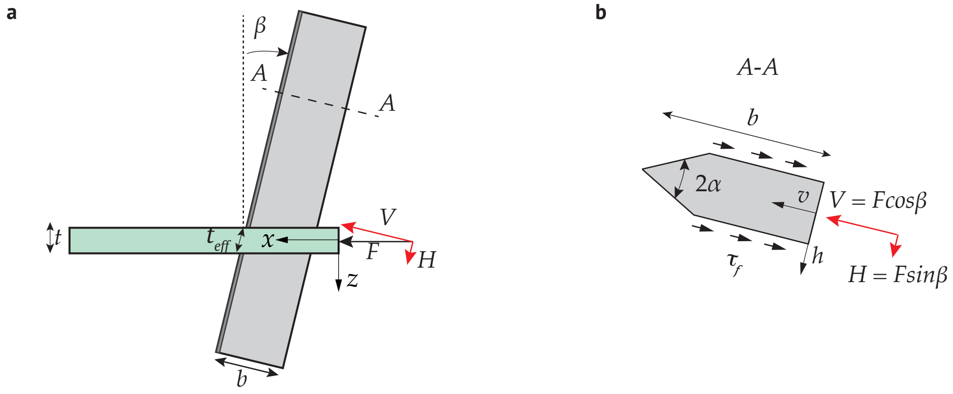

Figure 2.14 **a** Sketch of oblique cutting of silicone samples. The blade is inclined at an angle β with respect to the normal direction to the sample. **b** Enlarged view of the blade cross-section, with the local reference axes and the adhesive shear stress τ_f

If we consider an inclined blade whose normal forms an angle β with the motion direction, the cutting force F might be split in two components, one normal and one parallel to the edge of the blade. Such components are (Fig.2.14)

$$V = F\cos\beta \quad \text{and} \quad H = F\sin\beta, \tag{2.45}$$

where ξ is the slice-push ratio defined by

$$\xi = \frac{H}{V} = \tan\beta. \tag{2.46}$$

Similarly, the components of the frictional force F_f are

$$V_f = 2bt_{\text{eff}}\tau_f\frac{1}{\sqrt{1+\xi^2}} \quad \text{and} \quad H_f = 2bt_{\text{eff}}\tau_f\frac{\xi}{\sqrt{1+\xi^2}}, \tag{2.47}$$

where $t_{\text{eff}} = t/cos\beta$ indicates the effective thickness of the specimen in the inclined direction.

Rewriting the energy balance of cutting, Eq.(2.44), in terms of the force components, and neglecting the strain energy contribution, we find

$$(V - V_f)\mathrm{d}v + (H - H_f)\mathrm{d}h = Gt_{\text{eff}}\mathrm{d}v, \tag{2.48}$$

where $\mathrm{d}v$ and $\mathrm{d}h$ denote, respectively, the normal and parallel displacement components to the cutting edge. The resultant cutting force F, acting along the direction $\mathrm{d}x = (\mathrm{d}v^2 + \mathrm{d}h^2)^{1/2}$, can be written as

$$\frac{F}{\Gamma t_{\text{eff}}} = \frac{\sqrt{(V-V_f)^2 + (H-H_f)^2}}{\Gamma t_{\text{eff}}} = M + \frac{1}{\sqrt{1+\xi^2}}, \tag{2.49}$$

where we have assumed $G = \Gamma$, the fracture resistance of the material. The variable M, given by

$$M = \frac{2b\tau_f}{\Gamma}, \tag{2.50}$$

represents the ratio between the frictional force per unit thickness and the fracture resistance.

The components of the normalised cutting force are

$$\frac{V}{\Gamma t_{\text{eff}}} = \frac{M}{\sqrt{1+\xi^2}} + \frac{1}{1+\xi^2}, \tag{2.51a}$$

$$\frac{H}{\Gamma t_{\text{eff}}} = \xi\left(\frac{M}{\sqrt{1+\xi^2}} + \frac{1}{1+\xi^2}\right). \tag{2.51b}$$

A slight modification of Eq.(2.49) has been proposed to account for the wedge opening angle α[90], which does not affect much the results of the commercial blade considered in our examples. The cutting force may is written as

$$\frac{F}{\Gamma t_{\text{eff}}} = \frac{1}{\sqrt{1+\xi^2}}\left(1 + M\sqrt{\sec^2\alpha + \xi^2}\right). \tag{2.52}$$

When $M = 0$ we are in the case of frictionless cutting, where the blade angle has no effect on the cutting force. Indeed, from Eq.(2.49), we find

$$F = \Gamma t_{\text{eff}}/\sqrt{1+\xi^2} = \Gamma t. \tag{2.53}$$

The ratio M increases in contacts with higher friction: the result is an increase of the cutting force, that is, it appears that the cutting resistance of the material is enhanced by friction.

Experimental results

We have considered four different values of the blade inclination angle, specifically $\beta = 0, 10, 20, 30^\circ$, with the orthogonal configuration $\beta = 0^\circ$ taken as the reference case. Notice that the sign of the inclination angle has no effect on the magnitude of the forces. In order to compute the ratio M, we had to measure the adhesive shear stress τ_f. To this purpose, we have performed a specific cutting test with a double run of the orthogonal blade in an originally sound specimen, where the second run is made following the open crack. According to Eq.(2.3), and neglecting the strain energy contribution $\mathrm{d}U_s$, we find

$$\tau_f = \frac{F}{2tb}, \tag{2.54}$$

where F is the average value of the steady-state force, which is assumed to be due to friction only. From the average of repeated tests, we have found an adhesive shear stress falling within the range 70-80 kPa. Using this value, and the fracture resistance of the silicone rubber $\Gamma = 1.02\mathrm{kPa\,m}$, from Eq.(2.50) we have obtained $M \approx 3$.

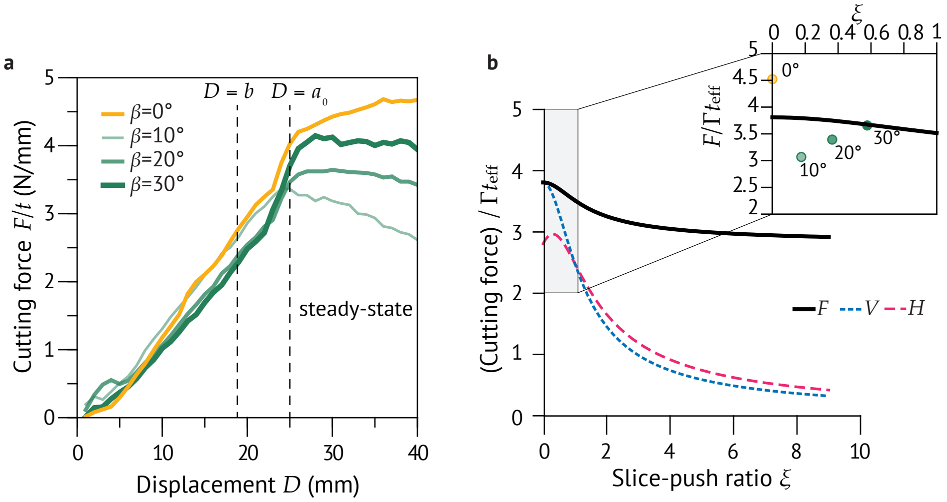

Figure 2.15 **a** Cutting force F/t as a function of the displacement D, for different values of the blade angle β. **b** Analytical steady-state cutting forces versus the applied slice-push ratio, Eq.(2.49) and Eq.(2.51), with $M \approx 3$. In the enlarged view, the experimental steady-state force $F/\Gamma t_{\mathrm{eff}}$ is compared to the analytical curve

The results are illustrated in Fig.2.15a, where the resultant cutting force F/t is plotted against the applied displacement D. The general trends are similar to those already observed for the orthogonal cutting of a sample containing a pre-crack $a_0 > b$. The effect of the blade inclination is more evident in the steady-state, when $D \geq a_0$. Focusing on the resultant cutting force F, we can work out the average values at the steady-state corresponding to the four different inclinations and compare them with the prediction of the analytical model. This is shown in Fig.2.15b as a function of the slice-push ratio ξ. The black curve plots the analytic cutting force F, Eq.(2.49), which seems to decrease with an increasing slice-push ratio. The other curves refer to the normal/pushing force V (dotted blue line) and the parallel/slicing force H (dashed red line), Eq.(2.51): while the former decreases constantly, the latter seems to peak at a critical ratio, and then decreases[79]. Notice that the range of slice-push ratios that are achievable with oblique cutting is limited, generally between ξ=0 (corresponding to $\beta = 0°$) and ξ=1 (for $\beta = 45°$). Larger ratios are attainable by adding a slicing motion of the cutting tool. In the enlarged plot of Fig.2.15b, the normalised resultant force $F/\Gamma t_{\text{eff}}$, predicted by the analytical model, is compared to the results of the experiments. Specifically, the force is taken as the average of the steady-state cutting (when $D \geq a_0$), for the four inclination angles corresponding to $\xi = 0$, $\xi = 0.18$, $\xi = 0.36$ and $\xi = 0.58$.

It seems that inclining the blade from the orthogonal position has the effect of reducing the cutting force for inclinations below $\beta = 10 - 20°$. However, at larger angles the force seems to increase again, probably due to the out-of-plane deformation occurring in the sample. In fact, large inclination angles induce a non-negligible deflection of the thin sample, so that a relevant part of external work is consumed by the bending energy. The experimental results might be corrected taking into account such contributions, although an exact quantification is not trivial, depending not only on the elastic properties of the material but also on the geometry and the boundary conditions of the sample. Notwithstanding the limitations, model and experimental results combined together effectively captured the importance of friction in oblique cutting, at least in the steady-state stage when the material is being separated. While the interest in frictional effects is oriented towards the minimisation of the cutting force, we should not overlook the contribution to cutting resistance coming from friction. In particular, it seems that the frictional force results in a fictitious enhancement of the fracture toughness of the material. The advantages of slicing in cutting are not limited to the stage of crack propagation: in our daily lives we experience the benefits of cutting food with an angled blade, or adding a small slicing action, even before the beginning of separation. In other terms, there is an effect during the indentation stage leading to failure which might not depend on friction, if we assume, as we did, that frictional effects are negligible before separation. In particular, indentation of an elastic solid involves strong global deformation and leads to material damage, eventually resulting in fracture initiation. Adding a small slicing action, or cutting with an angled blade, creates a critical local tension at the surface which anticipates fracture with a reduced global compression of the material[70].

3

The crack-tip zone in soft elastic tissues

The little reed, bending to the force of the wind,
soon stood upright again when the storm had passed over.

Aesop

In the *Introduction* we have provided a concise discussion of how the differences in molecular structure with respect to hard solids might explain the peculiar rupture process of soft materials. Contrary to common hard materials, such as rocks, glass or metals, a stretched soft matter specimen can deform multiple times its original length before failing. Moreover, even in the presence of small flaws these materials preserve their integrity and resist catastrophic failure. In order to understand the origin of such unique features, this chapter adopts a macroscopic approach to fracture of soft materials, borrowing concepts from the field of non-linear elasticity and fracture mechanics at large deformations. The theoretical background of this chapter, concerning finite strain elasticity and hyperelasticity, is provided in the Appendix A.1.

Linear elastic fracture mechanics (LEFM) is established on the hypothesis that all dissipative mechanisms of rupture are confined to an infinitesimal crack-tip process zone, with the additional assumption that the large strain zone is sufficiently small so that a linear elastic behaviour is retained both in the crack-tip region and in the bulk (see §1.2). While the former hypothesis remains valid for any elastic material, the latter breaks down for very deformable bodies, in which the region dominated by large strains is extensive, making linear elasticity inappropriate to describe the strain and stress fields near the crack tip[48,50]. The energy-based description of fracture, pioneered by Griffith's famous criterion[91], is a statement of a plain conversion of bulk elastic energy to surface energy to feed the crack growth. Without considering the stress state in the material, it is reasonable to assume that such a description, and specifically the concept of the energy release rate G, holds its validity for any material where dissipation is negligible. Early studies by Rivlin and co-workers introduced the concept of a critical energy for tearing, which was formulated in the line of Griffith's theory[82,92]. Their experiments on pre-cut rubber specimens showed that the rupture process could be considered completely elastic up to the point of catastrophic rupture, save for the strain crystallisation in a highly deformed region near to the cut tip and some negligible hysteresis in the material[82]. Their energetic approach paved the way to the standardisation of several testing procedures for soft materials[49], which replace the common fracture tests on notched specimens in hard solids. Moreover, techniques involving cutting[83,93], including puncture[94–97] and wire cutting tests[98,99], are often employed to measure the fracture toughness of soft materials. A survey of these methods, with a few applicative examples on the silicone rubber used in the experiments, is provided in §3.1.

The fact that an energetic approach to fracture worked well not only for traditional engineering materials but also for elastomers, and to some extent for biological tissues, has allowed scholars to overlook an equivalent field description in terms of stresses for many years. Within the LEFM framework, Irwin reconciled long time ago the two approaches[100], showing that Griffith's energetic criterion is perfectly equivalent to a stress-based one, derived from the asymptotic singular fields in the neighbourhood of the crack tip. The stress intensity factor (SIF) is the only parameter which controls the magnitude of the local fields in a linear elastic material, as a function of geometry and external loading. To reconcile stress and energy-based criteria in non-linear elastic materials, the amplitudes of the singular terms can be related to a path-independent integral surrounding the crack-tip, known as the J-integral[101]. For purely elastic solids, and under the assumption of self-similar crack propagation, that is, the crack grows along its direction, the J-integral is equal to the energy release rate[49]. However, the J-integral was initially defined without considering the large deformations. A complete solution of the strain and stress fields within the framework of finite strain elasticity arrived years later and remained for years confined to the experts of elasticity. The first systematic analysis of near-tip fields dates back to Knowles and

Sternberg, who derived an analytic solution of stress and displacements for a mode-I plane strain crack in a hyperelastic compressible material[102,103]. A few years later came the solution for an incompressible generalised neo-Hookean solid[104], then extended to mode-II cracks[105] and plane stress conditions[106,107]. The purpose of §3.2 is to illustrate the peculiarities of the crack-tip fields in soft biological tissues. After a review of the analytical solutions, we present a detailed numerical investigation on the crack-tip stress singularities and the deformed crack profiles. To model the behaviour of biological tissues, we have chosen some incompressible hyperelastic models with strain hardening. We also attempt to reconcile stress- and energy-based approaches by exploring the meaning of a SIF-like parameter to identify the condition of crack propagation.

A distinctive feature of the crack-tip region in a soft material is the transition from a sharp crack to a blunted rounded notch before propagation. An illuminating study by Hui et al.[108] identified the elastic blunting before propagation as a consequence of large deformations, which become relevant when the cohesive stress of the material exceeds its elastic modulus. Blunting plays the role of a limiting factor in the stress concentration caused by cracks, thereby preventing further increases in the maximum stress in front of the crack tip. As a consequence, rubbers and biological tissues such as skin, blood vessels and cartilage, are able to resist to cracks up to a few millimetres long (in contrast to the typical nanometre scale for hard brittle solids). This remarkable flaw tolerance[59,109,110] is one of the reason that brought the scientific community to emulate the structure of soft tissues[111,112]. The stress concentration of a blunted notch has been known since the studies of Inglis and Creager and Paris[113,114], who derived a simple expression of the stress concentration factor in an elliptic notch embedded in a linear elastic material. In §3.3 we present a simplified model to describe elastic blunting based on the measure of a local crack-tip radius. The model has been applied to analyse thin elastomeric specimens containing various cracks and subjected to uniaxial tension, and provided meaningful insights into the correlation between blunting and flaw tolerance[115].

One last point to complete this chapter on the effect of large strains is related to the role of crack blunting during cutting. Based on the definition of an intrinsic length scale in fracture of elastic materials, that is, the natural tip radius of an elastically blunted crack[50], we speculate that propagating a crack during cutting adds an additional length connected to the finite geometry of the tool. A hint came from the study by Hui et al.[108], who observed that during "cutting with a sharp knife, the elastic blunting effect may be limited by the fact that the crack opening displacement is determined by the knife geometry ". In §3.4, we address this point by considering refined numerical analyses of wire cutting, a well-known technique in which a rigid wire is inserted in a sample material. By considering wires of various diameters, we are able to detect a critical interaction between the intrinsic fracture length and the wire diameter. More in general, we can define a critical length in the cutting process establishing a transition from autonomous crack propagation to a constrained mechanism. This is believed to generalise the concept of tool sharpness presented in §2.2 to non-linear elastic materials.

3.1. Fracture toughness of soft matter

An essential step in the characterisation of the fracture behaviour of materials is the experimental measure of their toughness, defined as the ability to resist crack growth. Ultimately, the goal is to derive a material-based parameter which can be compared with a quantity connected to the crack driving force. In linear elastic materials, such a quantity is the stress intensity factor K which controls the amplitude of the singular fields surrounding the crack tip, and the fracture criterion is given by

$$K = K_c, \tag{3.1}$$

where K_c (dimensions $FL^{-3/2}$) is defined as the fracture toughness in terms of the critical value of the stress intensity factor. The measurement of K_c through standardised methods is performed in hard materials, such as rocks, concrete, glassy polymers and metals[84].

Testing methods for highly deformable materials are derived following the energetic approach to fracture. As long as the zone of inelasticity remains small, the elastic energy release rate G is correctly defined in linear and non-linear materials as well, and the fracture criterion is given by

$$G = \Gamma, \tag{3.2}$$

where Γ (dimensions FL^{-1}) is the fracture toughness defined as the critical energy per unit area of crack growth.

In this section, we illustrate the most common procedures used to measure the fracture resistance of soft materials experimentally, two of which are described more in detail and applied to measure the fracture toughness of a commercial silicone rubber. All the methods proposed were developed for testing rubber and other common elastomers above the glass transition temperature, where the energy required to propagate a crack is correctly estimated as the strain energy needed to break the covalent bonds of polymer chains at the crack tip[43]. When part of the energy is dissipated, for instance because of viscous flow, only a fraction of the strain energy is effectively converted in surface energy for crack propagation and test results are incorrect[116]. Furthermore, some authors raised concerns over the applicability of the testing procedures to soft elastic biomaterials, which typically show a steep J-shaped stress-strain curve with relevant strain hardening[22].

Pure shear, simple extension and trousers test

The first and probably most used procedure is the so-called Pure Shear (PS) test, which employs a long thin specimen of height $2h$ and width $w \gg 2h$, containing an edge crack $a > 2h$. The top and bottom edges are clamped and pulled apart by a uniform displacement Δ in the direction parallel to the short edges (see Fig.3.6 below). In a state of pure shear, the specimen is stretched parallelly to the direction of loading while it is undeformed along the other in-plane principal direction (see §A.1). A pure shear deformation possesses other amenable features for experimental testing: for instance, the stress state does not change with respect to a reference system centred on the crack tip as the tip is shifted during deformation. Moreover, regions far away from the crack tip are either fully relaxed or uniformly stretched in the direction parallel to the displacement imposed. Crack propagation can be regarded as the transition of a uniformly deformed region, of width da, into a fully relaxed region with the same width[32]. The change in the stored elastic strain energy is then written as

$$\mathrm{d}U_s = -2W(\lambda)ht\,\mathrm{d}a, \tag{3.3}$$

where $W(\lambda)$ is the strain energy density of the material at the current stretch, defined by $\lambda = 1 + \Delta/h$. Therefore the energy release rate is given by[82]

$$G = -\frac{\mathrm{d}U_s}{t\mathrm{d}a} = 2W(\lambda)h. \tag{3.4}$$

Typical rupture of rubber-like materials under constant displacement begins as a progressive tearing in the early stages and then turns into catastrophic rupture once that the applied stretch reaches a critical value λ_c. In a pure shear configuration, the energy release rate at rupture is independent of the crack length, and the strain energy density $W(\lambda_c)$ can be computed from the stress-strain curve of an uncracked PS sample stretched at $\lambda = \lambda_c$. The PS configuration is also employed advantageously in tests where the rate effect should be considered, because a crack propagates at constant velocity as a result of G being independent of the crack length[49].

The simple extension test employs a specimen of height $2h$ and thickness t, with an edge crack $a \gg h$, which is peeled apart from the two ends at the cracked edge. In this configuration, neglecting stretching in the clamped ends, the energy release rate is given as[82]

$$G = 2F/t, \tag{3.5}$$

where F is the force applied at the clamped ends.

The trousers test[117], also known as tearing test, consists of a specimen similar to the one used in the simple extension test, containing an edge crack a parallel to its longitudinal dimension. The crack is deformed out-of-plane by imposing opposite forces at the two clamped legs, bent at 90° with respect to the longitudinal plane. Neglecting three-dimensional effects, the energy release rate is given by the same expression of Eq.(3.5), provided that the strain in the legs is small.

3.1.1. The single edge notch test

The Single Edge Notch (SEN) test consists of a long thin strip of height $2h$ and width $w < h$, with an edge-crack of length $a \ll w$, subjected to uniaxial tension (Fig.3.1a). Because the crack is short, the specimen is under uniaxial strain except for a zone close to the crack tip, and the stress-strain curve is almost uninfluenced by the notch. Rivlin's analysis for pure shear configuration[82] needs to be modified accordingly, yielding the following expression of the energy release rate[118]

$$G = 2aW(\lambda)k(\lambda), \tag{3.6}$$

where $k(\lambda)$, derived by experimental work, is approximately equal to $k(\lambda) = 3/\sqrt{\lambda}$. Differently from the PS test, the energy release rate in a SEN test increases linearly with the crack length before the catastrophic rupture. Although widely employed because of its easy implementation, this method has been validated for vulcanised rubbers and its applicability to conditions other than plane stress state is questionable[119].

Fracture toughness of silicone rubber

We have employed the SEN test to measure the fracture resistance of the commercial silicone rubber used in the experiments presented in Chapter 2. Silicone was moulded in thin stripes of height $2h \simeq 75$mm, width $w \simeq 25$mm and thickness $t \ll w$. Specimens containing edge notches of various lengths a, cut with a sharp razor blade, were tested under displacement control up to complete rupture, measuring the reaction force through a load cell. A sound specimen was also tested to obtain the load-displacement curve, whose area is also equal to the strain energy density W. According to Eq.(3.6), the fracture energy is obtained from the strain energy density of the uncracked sample, at a stretch equal to the stretch at rupture λ_c

$$\Gamma = \frac{6aW(\lambda_c)}{\sqrt{\lambda_c}}. \tag{3.7}$$

In general, λ_c decreases with the length of the initial notch, following a trend which is approximately linear. In Fig.3.1b we show the variation of the nominal stress against the applied stretch

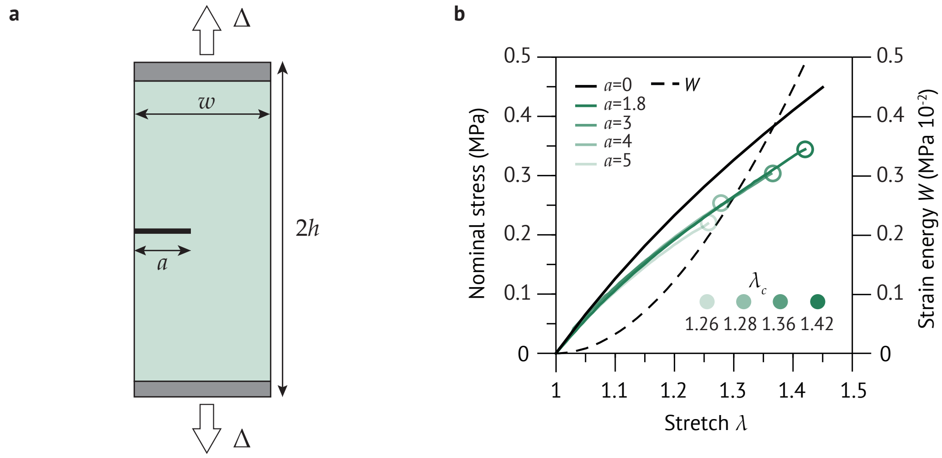

Figure 3.1 **a** Schematic representation of the SEN test. **b** Experimental curves of nominal stress-stretch, and strain energy density W (dashed line) versus stretch in the sound specimen. Circles mark the point of rupture of specimens with different initial cut lengths a (in mm), at the critical stretch λ_c reported in the plot

λ, with circles marking the points of catastrophic rupture. The values obtained from each test are consistent and yielded fracture energies in the order of 1kPa m.

3.1.2. Toughness measures from indentation and cutting

Alternative methods to measure the fracture toughness have been sought, mainly because of the limitations connected to traditional fracture tests when dealing with extremely deformable materials or biological tissues. Cutting and indentation tests have been proposed and applied extensively to test the toughness of biological materials and foodstuffs. Beside overcoming intrinsic limitations of traditional procedures, such as the difficulties in realising a correct clamping of the specimen, during cutting the work of loading is transferred into crack growth directly, so that material deformation is more localised in the vicinity of the blades and high strains are avoided. However, frictional dissipation between blades and material should be accounted for to obtain the net work done by the force in extending the cut.

One of the proposed procedures is the so-called scissors test[120], which is particularly suitable to test strain hardening tissues, such as the mammalian skin. A thin sound specimen, mounted between the open blades of a pair of scissors, is cut by applying a constant displacement to the blades in the normal plane. The fracture energy is obtained from the net work done by the cutting force, after a compensation for frictional effects through a second pass in the open cut. Similar approaches use a surgical cutting blade[94] or a needle[95] inserted and advanced under steady-state conditions in a thin strip of material. From the energetic balance of steady-state cutting, Eq.(2.6), the fracture toughness is given by

$$\Gamma = \frac{F\mathrm{d}a - \mathrm{d}U_s - \mathrm{d}U_f}{\mathrm{d}A}, \tag{3.8}$$

where F is the force acting on the blade, $\mathrm{d}D$ is the increment of displacement, $\mathrm{d}U_s$ is the strain energy variation in the solid and $\mathrm{d}U_f$ is the energy dissipated due to friction. Under steady-state conditions we assume that the increment in crack area is given by $\mathrm{d}A = t\mathrm{d}D$.

The blade is firstly inserted in the sound specimen, and the cutting force F is measured and plotted against the blade displacement D. A second pass in the open cut is carried out, where the measured force F_f is due to friction alone, if we neglect the contribution of the strain energy after crack initiation. Rewriting Eq.(3.8) as

$$\Gamma = \frac{(F - F_f)\mathrm{d}D}{\mathrm{d}A}, \tag{3.9}$$

the terms in brackets can be determined by integrating numerically the load–displacement curve obtained from the difference of the cutting force between the two passes of the blade. The fracture toughness Γ is obtained from the slope of the best-fit line to the curve $(F - F_f)\mathrm{d}D$ vs $\mathrm{d}A$, in the region of steady-state cutting[94]. An application of the method is illustrated in Fig.3.2, from an experimental test on the commercial silicone rubber used in other experiments. The value obtained is $\Gamma \simeq 0.53\mathrm{kPa\,m}$, which is approximately half the fracture toughness determined from the SEN test. The discrepancy, save for unpredictable differences in the specimens and small temperature fluctuations between the tests, can be ascribed to the omission of the strain energy contribution.

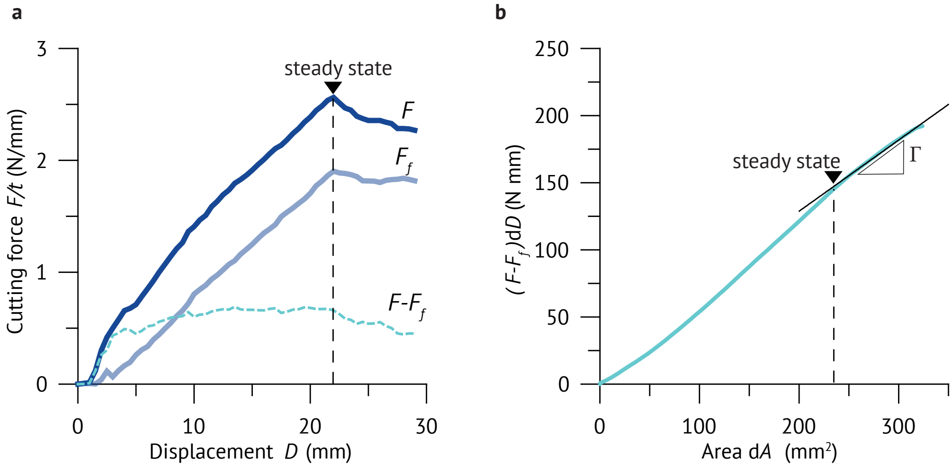

Figure 3.2 **a** Load-displacement curves for the cutting pass, the free pass and the difference $(F - F_f)$. **b** The term $(F - F_f)\mathrm{d}D$ as a function of the area $\mathrm{d}A$, with Γ obtained from the slope of the linear fit in the steady-state stage

Wire cutting test

Wire cutting is a recurring technique in the food processing industry and it has been also proposed to measure the mechanical parameters of soft materials. Here we describe the original model for cutting of cheese[98] and the main variables that are used throughout this thesis (see §3.4 and §5.2).

Let us consider a rigid wire of diameter d_w inserted in a sample of thickness t (Fig.3.3a). Focusing on the steady-state of cut propagation, we assume that there is a flow zone around the bottom half of the wire which also produces a circumferential frictional stress (whereas friction around the wire is neglected). From the energetic balance of steady-state cutting, Eq.(2.6), we may write

$$F\mathrm{d}D = \Gamma t \mathrm{d}D + \mathrm{d}U_P \tag{3.10}$$

where F is the steady-state force, $\mathrm{d}D$ is the increment of displacement and of cut length and $\mathrm{d}U_P$ is the energy dissipated in the flow zone by yielding and friction. From the equilibrium in the direction of wire penetration we find that[98]

$$\mathrm{d}U_P = t d_w \int_0^{\pi/2} \left(\sigma_{\max} \cos\vartheta + f\sigma_{\max} \sin\vartheta\right) \mathrm{d}\vartheta \; \mathrm{d}D \tag{3.11}$$

where $\sigma_{\max}$ is a characteristic stress of the material and f is the coefficient of friction. Then the force per unit thickness is

$$\frac{F}{t} = \Gamma + \left(1 + f\right) \sigma_c d_w \tag{3.12}$$

Equation (3.12) shows that the cutting force increases linearly with the wire diameter d_w and can be used to derive the fracture toughness Γ from experimental results. The typical force-displacement curve of a wire cutting test is shown in Fig.3.3b. In order to compute Γ, several tests with different wire diameters are performed, so that the steady-state force can be plotted as a function of the wire diameter. A linear extrapolation at zero diameter gives the value of Γ.

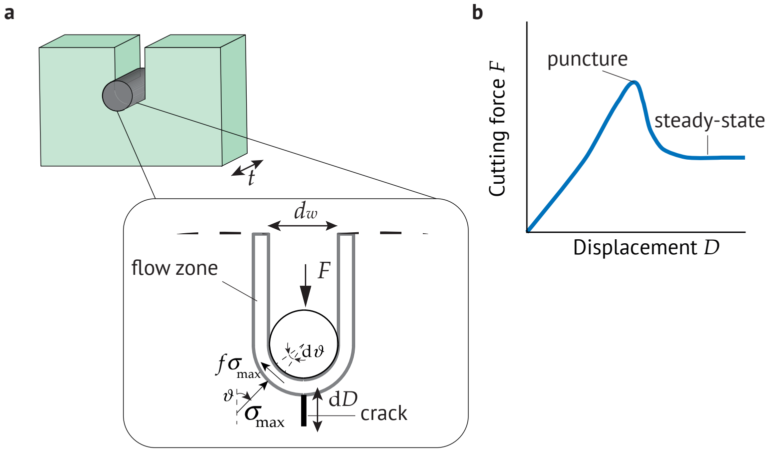

Figure 3.3 **a** Schematic of the wire-cutting tests with an enlarged view of the rupture process. **b** Typical force-displacement curve in wire cutting of soft materials

3.2. Crack-tip singularities in strain-hardening soft materials

As mentioned in the *Introduction*, many biological tissues are known to undergo strain hardening when stretched, often much earlier than rubber-like solids. Since this section is centred on the crack-tip zone in strain hardening materials, we need to begin with a short summary of the most common strain hardening models before moving on to the analysis of the crack-tip fields. Other basic hyperelastic models are presented in the Appendix A.1. In this section, we have adopted a slightly different notation with respect to the rectangular coordinates: specifically, we use the index $i = 1, 2, 3$ in place of x, y, z adopted in the rest of the thesis.

3.2.1. Strain hardening models for soft tissues

Suitable Strain Energy Density (SED) functions to describe the strain hardening behaviour might be those presenting an exponential dependence on the strain invariants[22]. Widely used in biomechanics for skin and similar materials is the exponential Fung-Demiray (FD) model[121,122]

$$W(I_1) = \frac{\mu}{2b}\left[e^{b(I_1-3)} - 1\right], \tag{3.13}$$

where I_1 is the first strain invariant and the non-dimensional constant b is the strain hardening parameter (in the limit of $b \to 0$ the neo-Hookean model is recovered). A subsequent development, including the dependence on the second invariant I_2, is the three-parameter Vito model[123]

$$W(I_1, I_2) = \frac{\mu}{2b}\left[e^{b[\alpha(I_1-3)+(1-\alpha)(I_2-3)]} - 1\right], \tag{3.14}$$

where b and α are the strain-hardening parameters. The parameter $\alpha \leq 1$ accounts for the influence of the second invariant: smaller values of α correspond to a greater dependence on I_2 (in the limit of $\alpha = 1$, one recovers the FD model).

Further models have been proposed to deal with the anisotropic nature of biological tissues. It is out of the scope of this work to directly consider anisotropy in the formulation of the constitutive model; however, an accurate isotropic formulation which fits excellently to experimental data on human skin has been proposed by Gambarotta et al.[124], based on the anisotropic Tong-Fung model[125]. The SED function presents both a linear and an exponential dependence on the Green-Lagrange strain invariants $\hat{I}_1(\mathbf{E}), \hat{I}_2(\mathbf{E})$

$$W(\hat{I}_1(\mathbf{E}), \hat{I}_2(\mathbf{E})) = g_1(\gamma_1, \mu_1, \hat{I}_1, \hat{I}_2) + c e^{g_2(\gamma_2, \mu_2, \hat{I}_1, \hat{I}_2)}, \tag{3.15}$$

where $\gamma_1, \mu_1, \gamma_2, \mu_2, c$ are five material constants to be determined experimentally and the functions g_i are given by

$$g_i = \frac{\gamma_i}{2}(\mathrm{tr}\mathbf{E})^2 + \mu_i \mathrm{tr}(\mathbf{E}^2), \quad i = 1, 2. \tag{3.16}$$

Rewriting Eq.(3.16) in terms of the invariants of the left Cauchy-Green strain tensor $\mathbf{b}$, the expression is

$$g_i(I_1(\mathbf{b}), I_2(\mathbf{b})) = \frac{\gamma_i}{8}(I_1 - 3)^2 + \frac{\mu_i}{4}(I_1^2 - 2(I_1 + I_2) + 3). \tag{3.17}$$

The difference between hyperelastic models for rubbers and strain hardening materials can be appreciated in Fig.3.4, where the Cauchy stress is plotted as a function of stretch in uniaxial extension. In Fig.3.4a, the dots are related to the silicone rubber considered in §3.1.1 and in the experiments of Chapter 2. Different hyperelastic SED functions, namely the neo-Hookean (NH), the Mooney-Rivlin (MR) and the Ogden functions are considered (refer to the Appendix A.1.2 for the formulation of such models). Within the limited stretch range considered, different models provide a similar approximation, suggesting that for stretches below approximately 1.3 simple strain energy functions that require fewer calibration parameters can be used. Included is also the

Ogden curve for a vulcanised rubber with similar initial shear modulus (the fitting parameters are taken from the literature[126]), which is an example of the so-called S-shaped stress-strain response. On the contrary, silicone has a different behaviour, resembling the J-shaped stress-strain curves of biological elastic tissues, although with reduced strain hardening. The difference in the shape of the stress-strain curve is fundamental: as explained by Gordon in his brilliant book[20], biological tissues, such as blood vessels, would fail catastrophically if they had the S-shape of natural rubber.

In Fig.3.4b we illustrate some of the strain-hardening models for soft tissues. The calibration parameters are average values for human skin taken from the literature[34], with the initial shear modulus approximately equal to $\mu = 0.11\text{MPa}$. With respect to the classical models for rubber-like materials (Fig.3.4a), the striking difference is the much larger strain hardening displayed at relatively low stretches. In the two-parameter model by Fung-Demiray, b controls the degree of strain-hardening, with typical values comprised in the range $b = 1 - 5$ reflecting the variability among individuals and age[127]. The effect of the second invariant in the formulation of Vito's model becomes larger in problems involving multiaxial states of deformation[128]. We have also included the Generalised Neo-Hookean model (GNH), which offers a reasonable approximation of the exponential models by taking a specific combination of the parameters (in particular, choosing a high value of the strain hardening exponent n).

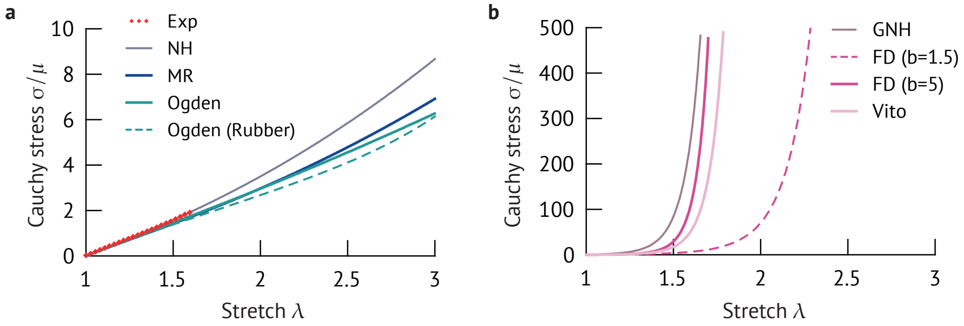

Figure 3.4 Comparison of uniaxial stress-strain response in different hyperelastic materials. **a** Experimental data from a silicone rubber. Fitting models parameters: NH: $\mu = 450\text{kPa}$; MR: $\mu = 490\text{kPa}$, $\alpha = 0.7$; Ogden: $\mu_1 = \mu_2 = 334\text{kPa}$, $\mu_3 = 3\text{Pa}, \alpha_1 = \alpha_2 = 1.48$, $\alpha_3 = 0.09$. Dashed line is related to a vulcanised rubber (Ogden: $\mu_1 = 161\text{Pa}$, $\mu_2 = -1.83\text{kPa}$, $\mu_3 = 781\text{kPa}$, $\alpha_1 = 7.3$, $\alpha_2 = -2.7$, $\alpha_3 = 1.1$). **b** Exponential strain-hardening functions for soft biological tissues. Model parameters: GNH: $\mu = 110\text{kPa}, b = 5, n = 20$; FD: $\mu = 110\text{kPa}$, $b = 5$ and $b = 1.5$ (dashed line); Vito: $\mu = 110\text{kPa}$, $b = 5, \alpha = 0.5$

3.2.2. Analytical solution of the crack-tip fields

In this section we briefly review the analytic method to derive the asymptotic stress and displacement at the tip of a crack in an incompressible hyperelastic material. The classical solution of linear elastic fracture mechanics is introduced as a comparison.

The *K*-fields in linear elastic materials

The crack tip fields in linear elastic materials are derived with the assumption of infinitesimal strain, so that the reference and deformed configurations are interchangeable[129,130]. In the vicinity of the crack tip, the leading order terms of the stress components have the following separable form, with respect to the radial distance from the tip r and the angle ϑ (refer to Fig.3.5 for the symbols)

$$\sigma_{ij} = \frac{K_I}{\sqrt{2\pi}} r^{-1/2} f_{ij}(\vartheta), \tag{3.18}$$

where K_I is the stress intensity factor in mode-I loading conditions, which is a function of geometry and remote loads, and $f_{ij}(\vartheta)$ are the angular functions. The complete expressions can be written as

$$\left(\begin{array}{c} \sigma_{11} \\ \sigma_{22} \\ \sigma_{12} \end{array}\right) = \frac{K_I}{\sqrt{2\pi}} r^{-1/2} \cos(\theta/2) \left\{\begin{array}{c} 1 - \sin(\vartheta/2)\sin(3\vartheta/2) \\ 1 + \sin(\vartheta/2)\sin(3\vartheta/2) \\ \sin(\vartheta/2)\cos(3\vartheta/2) \end{array}\right\}, \tag{3.19}$$

which are valid both in plane strain and plane stress. Similar equations are also obtainable for mode-II and mode-III loading.

It can be noticed that each component shows the same -1/2 singularity with respect to the distance from the tip r, implying that a point close to the tip is in a state of hydrostatic tension. The near-tip displacements present the following separable form

$$u_i = \frac{K_I}{2\mu\sqrt{2\pi}} r^{1/2} g_i(\vartheta), \tag{3.20}$$

where $g_i(\vartheta)$ are the angular functions, which are different in plane stress or plane strain. On the crack surfaces, i.e. for $\vartheta = \pm\pi$, the angular functions are $g_1(\pm\pi) = 0$, $g_2(\pm\pi) = \pm 1$, so that the profile of the crack is parabolic.

Plane stress solution in GNH materials

The analytic solution of stress and displacements at the tip of a crack in a hyperelastic incompressible material is based on an asymptotic method, similar to William's expansion in linear materials. Here we focus on a plane stress crack in mode-I symmetric conditions, following the solution derived by Geubelle and Knauss [107] and recently revised by Long and co-workers [131–133]. This geometry correctly approximates the configuration that we have adopted in the experimental campaign on silicone rubbers.

The asymptotic method presented here is fully consistent with the non-linear theory summarised in the Appendix A.1. We start by considering a two-dimensional configuration with a crack embedded in a large sheet of hyperelastic material and a reference system X_1, X_2 centred at the tip, so that the crack faces are coincident with the line $X_1 < 0$, $X_2 = 0$ in the initial configuration (Fig.3.5a). Upon the application of load, the crack opens and the points in the deformed configuration can be identified with respect to the current coordinates of the translated crack tip (Fig.3.5b), defined as

$$y_i(\mathbf{X}) = x_i(\mathbf{X}) - x_i(\mathbf{X} = \mathbf{0}), \qquad i = 1, 2, \tag{3.21}$$

where $x_i(\mathbf{X})$ are the coordinates in the current configuration. Furthermore, we assume that the material is described by an elastic potential that is a smooth function of the first strain invariant

$$W(I_1) = A(I_1 - 3)^n + B(I_1 - 3)^{(n-1)}, \tag{3.22}$$

where A, B and n are material constants. Here we focus on the Generalised Neo-Hookean (GNH) strain energy density function, which is a particular case of Eq.(3.22). The strain energy density function of a GNH material is given by

$$W(I_1) = \frac{\mu}{2b}\left\{\left[1 + \frac{b}{n}(I_1 - 3)\right]^n - 1\right\}, \tag{3.23}$$

where μ is the initial shear modulus, and b and n are strain hardening parameters.

In hyperelastic materials, the nominal first Piola-Kirchoff stress tensor $\mathbf{P}$ is obtainable by derivation, according to

$$\mathbf{P} = \frac{\partial W(\mathbf{F})}{\partial \mathbf{F}}, \tag{3.24}$$

where $F_{ij} = \partial x_i/\partial X_j$ is the deformation gradient tensor. In the deformed configuration, the Cauchy true stress tensor $\boldsymbol{\sigma}$ is obtained as

$$\boldsymbol{\sigma} = J^{-1}\mathbf{P}\mathbf{F}^T, \tag{3.25}$$

where $J \equiv \det\mathbf{F} = 1$ is the volume ratio in incompressible materials.

The hypothesis of a symmetric opening crack (mode-I) is expressed by

$$y_1(X_1, X_2) = y_1(X_1, -X_2), \qquad y_2(X_1, X_2) = -y_2(X_1, -X_2). \tag{3.26}$$

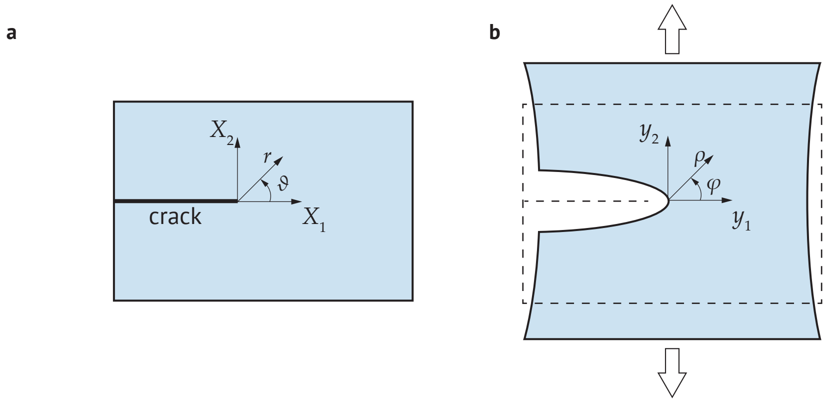

Figure 3.5 Sketch of the crack geometry. **a** Undeformed and **b** deformed configuration with local axes centred at the crack tip

The analytical solution assumes that the near-tip displacement field is given by

$$y_i = C_i r^{p_i} f_i(\vartheta), \tag{3.27}$$

where C_i are unknown constants, depending on the geometry and loading conditions, p_i is the order of the singularity and $f_i(\theta)$ are angular functions. Conditions of symmetry require that $f_1(\vartheta = 0) = 1$ and $f_2(\vartheta = 0) = 0$. Note that (r, ϑ) designate a polar coordinate system in the initial configuration, with $r = \sqrt{X_i X_i}$; the corresponding system in the deformed configuration is defined by (ρ, φ). The linear elastic solution is also a particular case of Eq.(3.27), with $p_1 = p_2 = 0.5$ and $f_1(\vartheta) = \sin^2(\vartheta/2)\cos(\vartheta/2)$, $f_2(\vartheta) = \sin^2(\vartheta/2)\sin(\vartheta/2)$.

From the solution of the crack boundary value problem, the leading order behaviour in the near-tip zone is determined. In the GNH case, we have[133]

$$y_1 = \begin{cases} C_1 r^c f_1(\vartheta, n) & \text{if } n < 1.46 \\ C_1 r^{(1+1/4n)} f_1(\vartheta, n) & \text{if } n \geq 1.46 \end{cases} ; \tag{3.28a}$$

$$y_2 = C_2 r^{(1-1/2n)} f_2(\vartheta, n), \tag{3.28b}$$

where the exponent $c < 1 + 1/4n$ was derived analytically by Geubelle and Knauss[107]. The solution depends on the strain-hardening exponent n, whose implications on the displacement field can be appreciated from the analysis of the results obtained from numerical simulations. The expression of y_1 has a bifurcation point for $n = n^* \approx 1.46$, which in the original solution was the limit to allow the separable form of Eq.(3.27)[107]. Moreover, n must always satisfy the requirement $n > 0.5$, which ensures the ellipticity of the equilibrium equations of the elastic problem. Situations with $n \leq 0.5$, while not common under ordinary deformations, might arise in particular situations leading to an unstable behaviour (for instance, the nominal stress during uniaxial extension decreases with the stretch ratio increasing) and the so-called equilibrium shocks[134].

The solution for a Neo-Hookean (NH) material is derived as a special case of the previous, taking $n = 1$. The near-tip displacement field is parabolic and is given by

$$y_1 = C_1 r \cos\vartheta, \qquad y_2 = C_2 r^{1/2} \sin(\vartheta/2). \tag{3.29}$$

Now we turn our attention to the stress fields in the vicinity of the crack tip, which are singular as expected. In particular, the Cauchy stress components in a GNH material are

$$\text{if } n < 1.46 \begin{cases} \sigma_{11} & \sim r^{(2c-3+1/n)} \\ \sigma_{22} & \sim r^{-1} \\ \sigma_{12} & \sim r^{(c-2+1/2n)} \end{cases} ; \tag{3.30}$$

$$\text{if } n \geq 1.46 \begin{cases} \sigma_{11} & \sim r^{(-1+3/2n)} \\ \sigma_{22} & \sim r^{-1} \\ \sigma_{12} & \sim r^{(-1+3/4n)} \end{cases} . \tag{3.31}$$

In a NH material we can write the closed form expression for the true stresses as follows

$$\begin{aligned} \sigma_{11} &= \mu C_1^{\,2}, \\ \sigma_{22} &= \frac{\mu}{4} C_2^{\,2} r^{-1}, \\ \sigma_{12} &= -\frac{\mu}{2} C_1 C_2 r^{-1/2} \sin\left(\frac{\vartheta}{2}\right), \end{aligned} \tag{3.32}$$

where C_2 is somehow analogous to the stress intensity factor of LEFM (see §3.2.4).

Comparing these singularities with those of the linear elastic solution, one can appreciate a first, fundamental difference: the stress components have different singularities, whereas in LEFM they all have the same inverse square root dependence with the crack-tip distance. For a GNH material, the singularity depends on the strain hardening exponent n, although the most severe is the -1 singularity displayed by the normal stress. Since the near-tip stress field is dominated by the strongest singular component, a material element in a hyperelastic materials experiences a condition of uniaxial tension. Some authors have suggested that this should be considered when studying the damage mechanisms in the crack-tip zone, for instance the phenomenon of cavitation[133].

In a NH material, we are able to write the stress components in the deformed coordinates (ρ, φ), by expressing the undeformed coordinates (r, ϑ) in terms of y_1 and y_2. The same method cannot be followed in a GNH material, because the angular functions $f_i(\vartheta, n)$ have no closed expression[133].

For $n = 1$, from Eq.(3.29) we find[131]

$$r = \frac{2}{C_2^2} y_1^2 + \frac{y_1}{C_1}, \qquad \cos\vartheta = \frac{C_2^2 y_1}{2C_1 y_2^2 + C_2^2 y_1} \tag{3.33}$$

and $y_1 = \rho\cos\varphi$, $y_2 = \rho\sin\varphi$. For $0 \le |\varphi| < \pi/2$ the stress have the following form

$$\begin{aligned} \sigma_{11} &= \mu {C_1}^2, \\ \sigma_{22} &= \frac{\mu}{4} C_1 {C_2}^2 \rho^{-1} f_{22}(\rho, \varphi), \\ \sigma_{12} &= \mu {C_1}^{3/2} C_2 \rho^{-1/2} f_{12}(\rho, \varphi), \end{aligned} \tag{3.34}$$

which shows that ahead of the crack tip, for $\vartheta = \varphi = 0$, the stress has the same singularity with respect to the undeformed or deformed crack tip, see Eq.(3.32). For $\varphi = \pi/2$ we have instead

$$\sigma_{22} = \frac{\mu C_2^4}{8} \rho^{-2}, \qquad \sigma_{12} = -\frac{\mu C_1 C_2^2}{4} \rho^{-1}. \tag{3.35}$$

The noticeable feature is that the singularity along the deformed crack face is different and larger than that ahead of the crack tip; in particular, the -2 exponent in the normal opening stress implies that along the deformed crack there are severe stress gradients, which might result in secondary crack initiation from the blunted surface[133].

3.2.3. Results of numerical analyses

Now we turn our attention to more complex strain hardening formulations, such as those presented in §3.2.1 for soft biological tissues. Unfortunately, asymptotic solutions beyond the GNH model are not easily obtainable, due to the difficulties arising in the determination of the leading order behaviour of y_1 and y_2. For this reason, we have employed detailed finite element (FE) analyses to compute the true stress fields in the crack tip region and determine the singularity of the various stress components. We have considered a pure shear specimen consisting of a thin long strip of height $2h$ and width $w = 10h$, with an edge crack $a = 2.5h$ (Fig.3.6a). The specimen thickness t is assumed to be much smaller than other dimensions, so that a condition of plane stress is enforced. A uniform displacement is imposed in the direction parallel to the short edges.

Crack-tip stress singularities

The model is implemented in the commercial finite element software SIMULIA Abaqus 2017 (Dassault Systèmes[135]), using eight-node plane stress elements with collapsed tip elements. The tip nodes were left free to move independently so that the typical blunting under load could

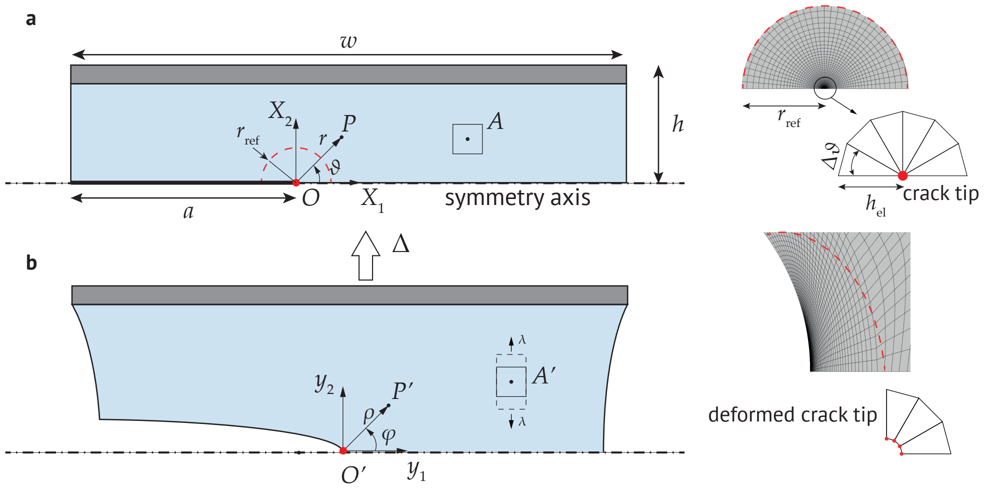

Figure 3.6 Schematic view of the specimen with an edge crack of length $a > 2h$. Due to the applied displacements Δ on the top and bottom edges, a point A far ahead from the crack tip is in a state of pure shear, with principal stretches $\lambda_1 = 1, \lambda_2 = \lambda$ and $\lambda_3 = \lambda^{-1}$. **a** Undeformed symmetric configuration. The enlarged view shows a detailed view of the finite element mesh in the crack tip region (not in scale). **b** Deformed configuration and detail of the finite element mesh

be modelled, and the mid-side nodes were not shifted to quarter-points. This choice was taken because the nature of the singularity is not of the regular types for linear elastic and elastic-plastic materials. For more details on the correct meshing in fracture mechanics, refer to the Appendix A.4. Due to symmetry, only half specimen was modelled and pertinent constraints were added to the lower edge of the specimen. A refined radial zone centred at the crack tip and with radius $r_{\text{ref}} = 0.1h$, was added, where the smallest element size is $h_{\text{el}} = 10^{-5}h$ and the angular span is $\Delta\vartheta = 5°$ (Fig.3.6a). The stresses are extracted from the integration points of elements ahead of the crack tip enclosed in the refined region, extrapolated to the nodes and plotted on a double logarithmic plot as a function of the distance ρ from the current position of the crack tip (Fig.3.6b).

In Fig.3.7 we show the normalised Cauchy true stress σ_{11} and σ_{22} ahead of the crack tip, i.e. for $\varphi = 0$, as a function of the deformed distance ρ from the tip, divided by the specimen half-height h. Four different values of the strain hardening exponent n are considered, specifically two cases where $n < n^*$ and two with $n > n^*$, being $n^* \approx 1.46$ the value for which the asymptotic solution has a discontinuity. In order to put in evidence the power of the singularity, results obtained from FE analyses are plotted on a log-log plot, with the slope of the linear trends included in the figure. Comparing these results with the theoretical values, we also have a mean to evaluate the accuracy of the numerical model. Note that the theoretical slopes shown in Fig.3.7 are referred to the undeformed coordinate r, except for the neo-Hookean case where deformed and undeformed configurations are the same. The dominant singular term is always the opening stress σ_{22}, whose singularity does not depend on the hardening parameter. In addition, our results confirm that for increasing strain hardening the singularity of σ_{11} stress component becomes larger and the crack tip fields tend to resume a biaxial stress state as in the linear elastic solution. If the hardening exponent is further increased beyond the values considered in Fig.3.7, the stress-strain curve is a reasonable approximation of exponential hardening models, and the stress σ_{11} tends to the same singularity

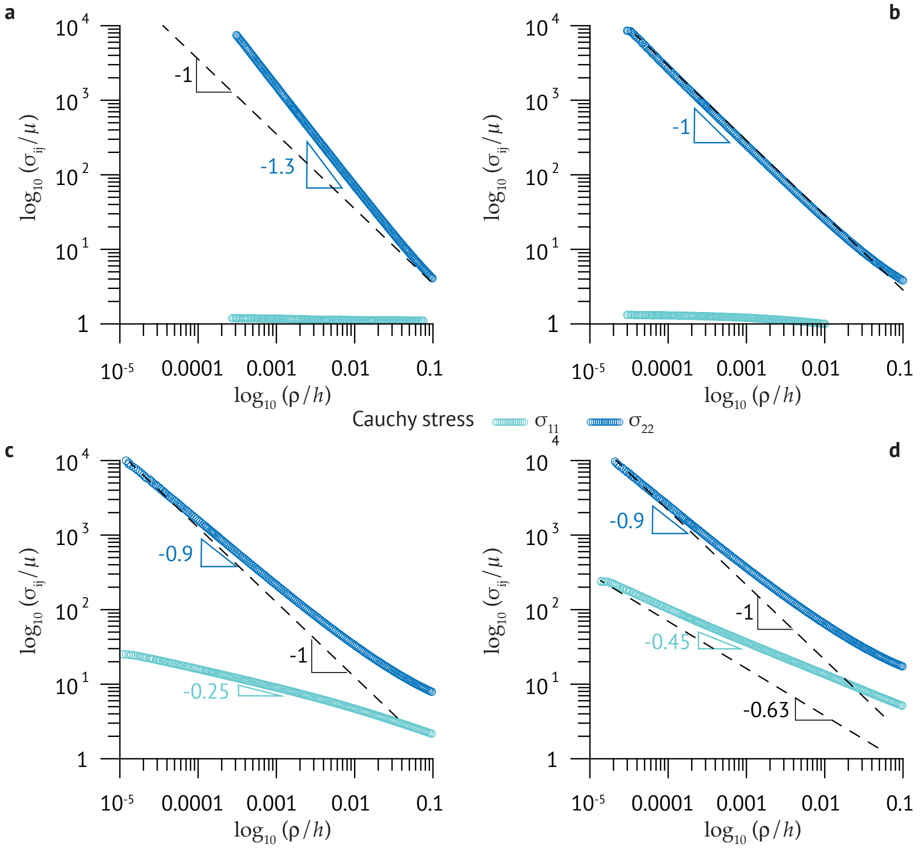

Figure 3.7 Cauchy stress σ_{11} and σ_{22} ahead of the crack tip in a GNH material, at an applied stretch $\lambda = 2$ (logarithmic plot). Power of the singularities with respect to the deformed radial coordinate ρ is compared with the values predicted by the analytical solution (dashed lines). **a** $n = 0.6$, **b** $n = 1$ (neo-Hookean), **c** $n = 2$ and **d** $n = 4$

of the normal stress (for instance, when $n = 20$ the singular exponent predicted by Eq.(3.30) is ~ -0.9). We also observe that for $n = 2$ and $n = 4$ (Fig.3.7c-d) the region dominated by the singular term seems to be reduced with respect to the neo-Hookean case (Fig.3.7a), a fact that confirms the shrinking of the large strain zone with increasing strain hardening. The opposite situation occurs for $n = 0.6$, which is close to the lower bound $n = 0.5$ below which the solution is unstable.

The results summarised in Fig.3.8 are related to the same pure shear geometry considered before, where Vito's hyperelastic model, Eq.(3.14), is chosen as representative of the exponential strain-hardening SED functions. By assuming different values of the calibration parameter α, we have explored the influence of the second strain invariant on the near-tip stress fields, with the notable case of $\alpha = 1$ corresponding to the Fung-Demiray model, Eq.(3.13). The curves seem to suggest that the effect of this parameter on the power of the singularities is somehow limited. More importantly, the trend already anticipated in GNH materials with large strain hardening is here

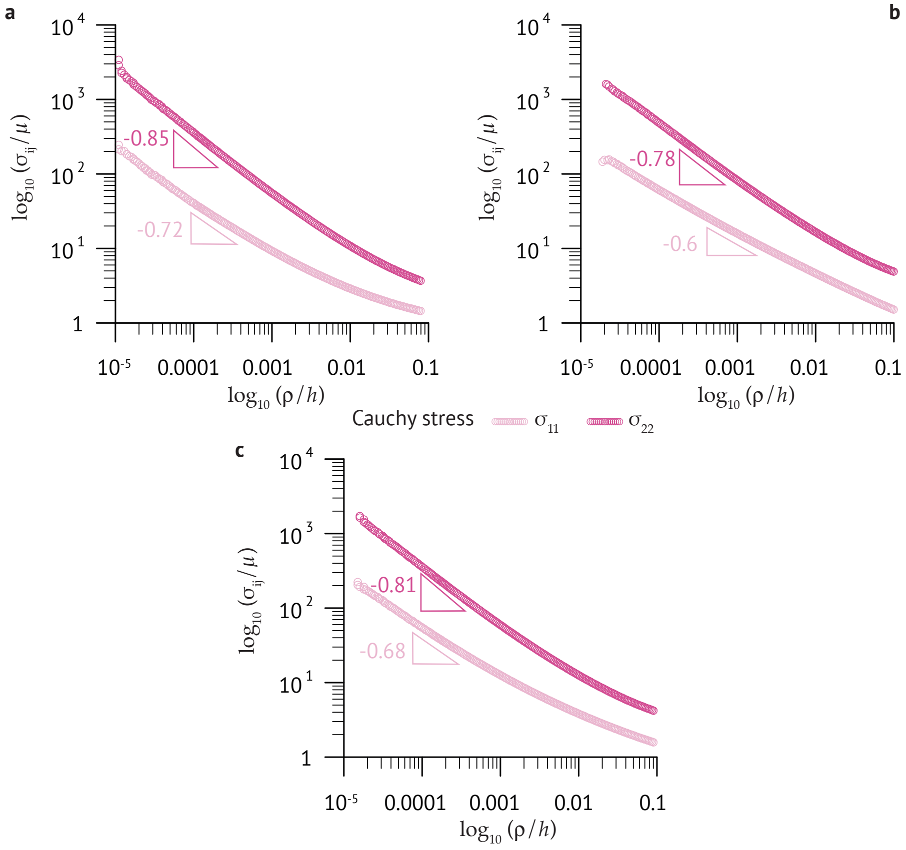

Figure 3.8 Cauchy stress σ_{11} and σ_{22} ahead of the crack tip in a hyperelastic soft tissue described by Vito's model, at an applied stretch $\lambda = 2$ (logarithmic plot). Power of the singularity with respect to the deformed radial coordinate ρ is indicated on the plots. **a** $\alpha = 0$, **b** $\alpha = 1$ (Fung) and **c** $\alpha = 0.5$

confirmed. The singularity exponent of the normal stress ahead of the crack tip is ~ -0.8, which is close to the value of the neo-Hookean material, but here also σ_{11} has a similar singular behaviour. In addition, we notice that the power law trend (linear in the logarithmic plots) only fits a small distance from the tip, approximately for $\rho/h \leq 10^{-3}$, confirming that in strain hardening materials the crack tip region consists of a localized zone of high stress gradients.

Deformed crack profile

We have already anticipated how the size of the large deformation zone, and hence the elastic blunting of the crack tip, is influenced by the degree of strain hardening of the material. Now we take a closer look at the deformed crack profiles for the previously considered cases and offer a local measure of elastic blunting by means of a radius of curvature at the crack tip. The geometry is exactly as above, with the only difference in the mesh of the crack-tip region: since the displacement field we are interested in is not singular, the tip is modelled as a blunted notch to obtain better deformed profiles. The initial radius of the blunted notch was set to $10^{-4}h$ and has been

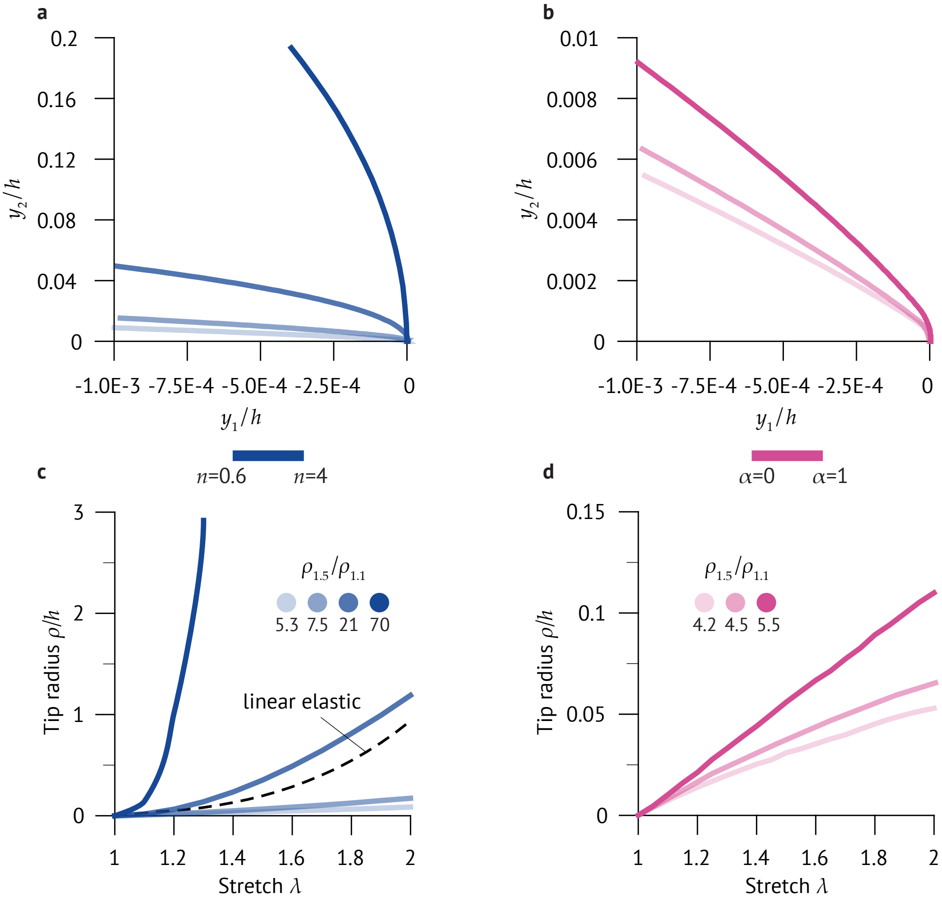

Figure 3.9 Deformed crack profiles at an applied stretch $\lambda = 2$, in GNH materials at various strain hardening (**a**), and in Vito's materials at different α (**b**). **c-d** Tip radius variation with the remote stretch in the same materials. Also shown is the increase at $\lambda = 1.5$ with respect to the tip radius at small deformations $\lambda = 1.1$

tested to be irrelevant on the resulting curvature upon deformation.

Figure 3.9 illustrates the deformed profiles of the near-tip region for the cases considered before. From Fig.3.9a we can appreciate the remarkable influence of the strain hardening parameter in GNH materials: in particular, for $n \rightarrow 0.5$ the phenomenon of crack blunting is greatly enhanced[107] and progressively mitigates at higher values. Vito's exponential hardening model is shown in Fig.3.9b. The normalised displacement y_2/h is notably different from that in GNH materials, approximately one order of magnitude lower, confirming that strain hardening has the effect of reducing the deformation in the crack-tip region. As in the stress curves, the variation of α seems to be of marginal importance.

Elastic blunting of the crack tip under loading can be quantified in terms of a local curvature. From the deformed coordinates y_1, y_2 of the crack profile (Fig.3.6b), we define the radius of curvature ρ as the radius of the best fitting circle, estimated using the hyper-circle algorithm[136]. This method assumes that the curvature of the crack flank is constant, at least within a certain distance from the tip, which we have taken approximately equal to $10^{-3}h$. The results summarised in Fig.3.9c-d confirm the role of strain hardening in diminishing the local deformation, with blunting markedly reduced in GNH materials with $n > 1$ and in Vito's model (please note the different scale in Fig.3.9d). The magnitude of crack blunting is put in evidence by considering the ratio between the tip radius $\rho_{1.5}$ under remote large stretch, defined as the radius for $\lambda = 1.5$, and the radius $\rho_{1.1}$ for small deformation (illustrated in the insets of Fig.3.9c-d). This ratio, approximately equal to 5 in strain hardening materials, rises up to $\sim$ 20 in a NH material and peaks at $\sim$ 70 when $n = 0.6$. Also plotted in Fig.3.9c is the solution for LEFM, which is obtained by employing the generalised linear elastic model (also known as Saint Venant-Kirchhoff model) and displays blunting similar to the NH case.

A further proof comes from the contours of the nominal opening strain ε_{22} in the crack-tip region, illustrated in Fig.3.10. For $n \leq 1$ the zone of high strains, defined as the region where the local strain exceeds the remote nominal strain ε by a factor of three, is large, whereas in Vito's material it seems to be very concentrated around the crack tip. Specifically, for $n = 0.6$ the crack appears severely blunted and the region with high strains covers a large area (in the red zone shown the local strains are up to 40 ε).

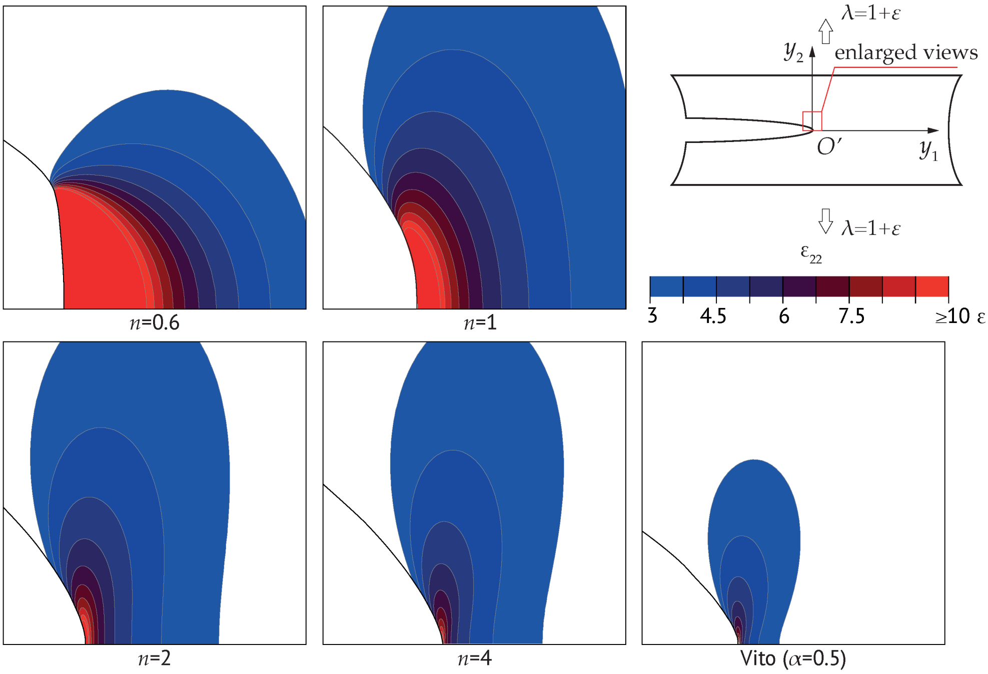

Figure 3.10 Contours of the opening strain ε_{22} in the crack-tip region, as a function of the remote nominal strain ε. GNH materials at various strain hardening and Vito's material are compared

3.2.4. Characterisation of the crack-tip fields

Based on the results of the numerical analyses, we have shown that strain hardening affects both the singular stress and the crack conformation conspicuously. But what are the implications? The ultimate goal of characterising the crack-tip fields in hyperelastic materials is to understand if a stress-based parameter, similar to the stress intensity factor K of LEFM, exists and can be used to investigate the critical condition for propagation. In other terms, with the energetic approach being a valid criterion for fracture in any elastic material when dissipative processes are not relevant, we look for a corresponding SIF-like stress parameter.

In hyperelastic materials the energy release rate G depends on the strain energy density $W(\lambda)$. In particular, for a pure shear configuration, Eq.(3.4), G is independent of the crack length and hence shows an increasing trend with the stretch λ in the same measure of W (Fig.3.11a). We notice that Vito's strain energy is similar to the GNH model for the calibration parameters here adopted, and is independent of the parameter α. This feature is peculiar of the pure shear configuration, because the first and second strain invariants turn out to be equal.

Let us begin by considering the NH material (i.e., taking $n = 1$ in the GNH strain energy density). The crack-tip stress field in the current configuration, Eq.(3.34), is dominated by the normal component σ_{22}. On the crack-line the angular function $f_{22}(\rho, \varphi)$ is equal to unity, so that we can write

$$\sigma_{22} = \frac{\mu}{4} C_1 C_2{}^2 \rho^{-1}, \tag{3.36}$$

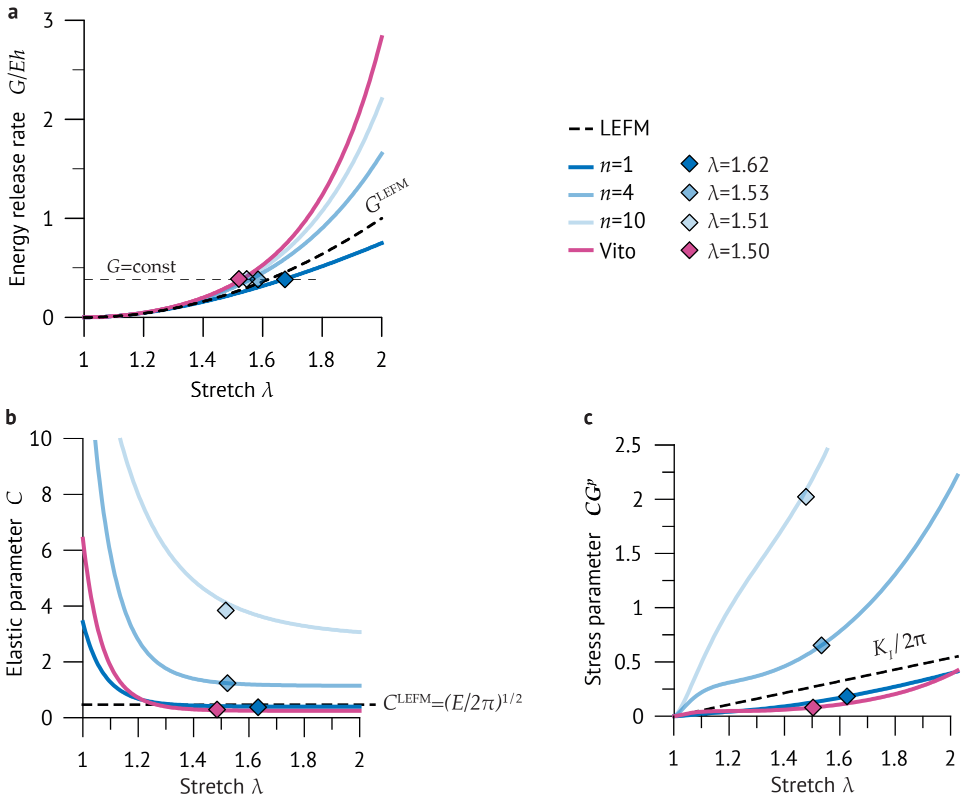

Figure 3.11 **a** Normalised energy release rate G/Eh as a function of the applied stretch λ for different strain hardening materials. **b** The elastic parameter C. **c** The SIF-like stress parameter CG^p. The dashed lines refer to the corresponding quantities in LEFM. Diamonds on the plots are obtained at constant strain energy

where C_1 and C_2 are two independent parameters governing the amplitude of the singular field. Recalling that the energy release rate is equal to $G = \pi/4\mu C_2^2$ [131], we rewrite Eq.(3.36) to obtain

$$\sigma_{22} = CG\rho^{-1}, \tag{3.37}$$

with $C = C_1/\pi$. We now generalise to other hyperelastic models and arrive at the following from of the singular normal stress

$$\sigma_{22} = CG^p\rho^{-p}, \tag{3.38}$$

where p is the power of the singularity. CG^p is a SIF-like stress parameter which characterises the magnitude of the singular stress field in any hyperelastic material. Note that now C has dimensions $F^{(1-p)}/L^{(2-2p)}$. A better understanding of the previous expression comes from considering the case of LEFM. Here the singular normal stress ahead of the crack tip, Eq.(3.19), is given by

$$\sigma_{22}{}^{\text{LEFM}} = \frac{K_I}{\sqrt{(2\pi)}}\rho^{-1/2}, \tag{3.39}$$

where the SIF is related to the energy release rate of LEFM through $G{=}K_I^2/E$. Moreover, in the pure shear configuration we can derive G from the strain energy in a linear elastic material and obtain

$$G^{\mathrm{LEFM}} = hE(\lambda - 1)^2. \tag{3.40}$$

Adopting the same formalism introduced above, $p = 1/2$ and

$$C^{\mathrm{LEFM}} = (E/2\pi)^{1/2}, \tag{3.41}$$

which shows that, in linear elastic materials, C is constant and proportional to the Young's modulus. On the contrary, in hyperelastic materials the parameter C changes with the applied stretch, as shown in Fig.3.11b. The parameter C was obtained from FE analyses, through a linear regression at zero intercept on the logarithmic plots of the stress σ_{22} versus the true distance from the tip. It appears that, regardless of the strain hardening behaviour, the curves follow a power-law decreasing trend with the applied stretch, tending towards a horizontal asymptote for large stretches. In Fig.3.11c we show the plots of the SIF-like stress parameter CG^p, increasing with stretch with different trends depending on the strain-hardening parameter n. The reference case of a linear elastic material is illustrated by the dashed linear trend of the stress intensity factor $K_I/2\pi$, where K_I is a linear function of the stretch according to

$$K_I = E\sqrt{h}(\lambda - 1). \tag{3.42}$$

In order to explore the implications on fracture, we consider an analysis at constant G. This could be the fracture toughness of a given material measured experimentally, but to retain general validity we prefer to denote it as a constant value of the energy release rate. Besides, we observe that constant values of G are related to equal areas in the stress-stretch plots, being G proportional to the strain energy density $W(\lambda)$ in the pure shear configuration. We can compare materials with different strain-hardening behaviour by extracting the corresponding stretch λ from the curves of G. The results are illustrated by coloured diamonds on the plots in Fig.3.11. The key to read this analysis is the following: while in LEFM any value of G has a univocal correspondence with K_I, which is also independent of the material properties, in hyperelastic materials we have a different scenario. Observing Fig.3.11c, we notice that the same strain energy release rate results in different values of the SIF-like parameter CG^p. Based on this observation and on the previous numerical analyses on the stress singularities, we are now able to sketch a unifying picture of crack-tip fields and fracture in hyperelastic strain-hardening materials. While the energetic approach is a valid criterion for fracture in any elastic material, the equivalent field approach, which employs a stress-based parameter, is limited to small scale yielding and hence to LEFM. In hyperelastic materials, the stress parameter CG^p defines the amplitude of the normal stress but does not provide an equivalent parameter to define a critical condition for crack

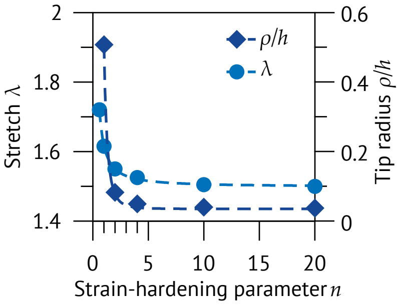

Figure 3.12 Effect of strain-hardening in GNH materials, on the stretch λ and the crack-tip radius ρ/h at constant strain energy release rate

propagation. Moreover, the normal stress dominates the crack-tip solution only at reduced strain hardening, because for increasing values of n the parallel stress σ_{11} also increases its singularity.

One last aspect which we have shown to be essential in characterising the crack-tip zone in strain hardening materials is elastic blunting. In different strain-hardening materials, equivalent values of G might occur at similar stretches but with drastically different blunting. This is illustrated in Fig.3.12, where we have plotted the variation of the stretch λ and the crack-tip radius ρ/h as a function of the strain-hardening parameter n of GNH materials, computed at constant strain energy. For $n > 5$ both the curves tend to a constant value, but below this limit we observe that moderate changes in the stretch (in the range $\lambda = 1.5-1.7$) correspond to a ten-fold increase in the tip radius, from $\rho/h \simeq 0.05$ to $\rho/h \simeq 0.5$. This is of no less importance, because crack propagation mechanisms can be influenced by the degree of blunting. Although these mechanisms are unique to a specific material and a detailed analyses was beyond the scope of the present thesis, we can try to suggest possible behaviours. The typical failure mechanism of elastomers is by growth of cavities inside the blunted region, which occur when the hydrostatic tension is of the order of the elastic modulus[108]. As observed during the analysis of the singular stress fields, a point close to the crack-tip is subjected to uniaxial tension in a neo-Hookean material but tends to recover the hydrostatic state with increasing strain hardening. Another possible mechanism consists in the formation of micro-cracks from the blunted crack-tip, where the local elastic modulus can be several order of magnitudes larger than the initial modulus[108]. Future experimental observations on elastomers and biological tissues would allow us to better understand how the failure process is affected by strain hardening.

3.3. The strength of soft solids: crack blunting and flaw tolerance

Crack blunting is among the most peculiar features of fracture in soft materials and adds a fundamental contribution to their remarkable toughness. Motivated by an extensive experimental campaign on thin silicone specimens[137–139], we have investigated the impact of crack blunting on the macroscopic mechanical response in relation to flaws of various severity and shape. In this section we collect some of the experimental results and propose an analytical model of crack blunting, based on a refinement of the formulation presented by Spagnoli et al.[115].

3.3.1. Experimental tests on thin flawed specimens

Here we focus on experimental tests carried out on thin plates containing cracks of different lengths, which were stretched under displacement control up to complete failure (Fig.3.13). The plates were subjected to tensile loading along the y-axis applied at a constant strain rate $\dot{\varepsilon} = 1.9-5.8\cdot 10^{-3}\mathrm{s}^{-1}$. The samples material consists of commercial silicone rubbers similar to those used in Chapter 2, with Young's modulus $E = 0.84-1.50\mathrm{MPa}$ and Poisson's ratio $\nu = 0.37-0.42$. A summary of the tests is presented in Table 3.1, reporting an identification code, the relevant geometry of the specimen and the ultimate stretch λ_c.

The response of the specimens during the experimental tests is monitored by measuring displacements and applied forces with a load cell, and using a Digital Image Correlation (DIC) technique to get full-field displacement and strain maps under load. Displacement and strain fields within the specimens were acquired through the freeware software Ncorr[89].

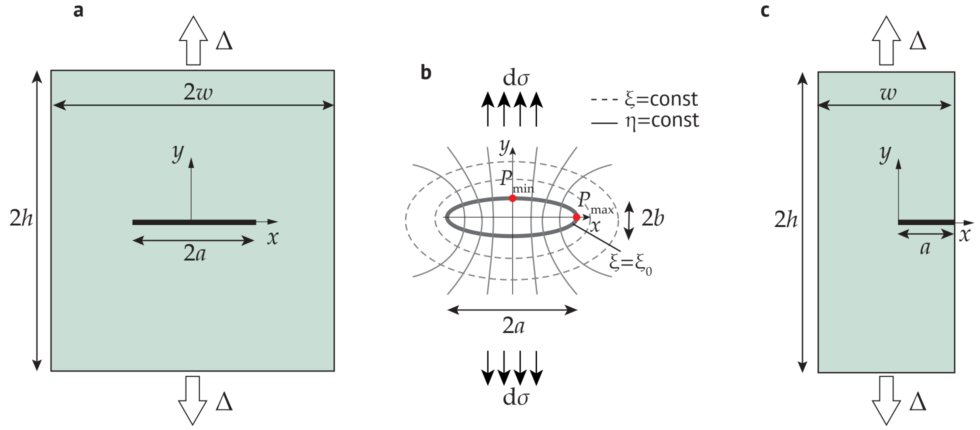

Figure 3.13 **a** Sketch of the sample containing a centred internal crack of length a. **b** Elliptic deformed configuration in curvilinear coordinates. **c** Sketch of the edge-cracked plates

Upon applying the tensile load, the initial crack-like defects tend to blunt progressively exhibiting a remarkable defect remodelling. In Fig.3.14a-b two specimens containing a centred crack are shown at increasing loads. In an intermediate stretch range, the DIC maps clearly show a strain concentration typical of an elliptical notch, where the maximum strain values occur in the locations corresponding to the original crack tips. At incipient failure ($\lambda = \lambda_c$), the strain maps exhibit a more complex distribution due to the failure mechanisms developing in the vicinity of the notch roots. At the same time, a compressed region can be noticed close to the crack flanks, due to the contraction effect arising in the direction normal to the applied displacement. Figures 3.14c-e are related to experiments on edge-cracked specimens, which failed noticeably earlier than centre-cracked samples and with limited crack tip blunting. The behaviour might depend on the different configuration, which causes an enhanced stress intensification that leads to a premature failure of the polymer network chains close to the crack tip.

An insightful representation of the experimental results is provided in Fig.3.15, which can be interpreted as a flaw-sensitivity map: each test is identified by a value of the ultimate stretch λ_c as a function of the characteristic length a of the initial crack-like defect. According to LEFM, the stretch at failure shows a decreasing power-law dependence on the crack length, given by the following equation

$$\lambda_c \sim \sqrt{\frac{\Gamma}{\pi E}}\, a^{-1/2}, \tag{3.43}$$

where Γ is the fracture toughness. This equation is obtained if we assume the condition of failure when $G = \Gamma$ and recalling that the remote stress $\sigma \sim \sqrt{GE/\pi a}$. While the experimental results of edge-cracked specimens seem to agree well with the LEFM prediction (dashed lines in Fig.3.15), centre-cracked samples behave differently. We speculate that the reason lies in the more pronounced blunting of the crack tip, which is not predicted by the linear elastic solution.

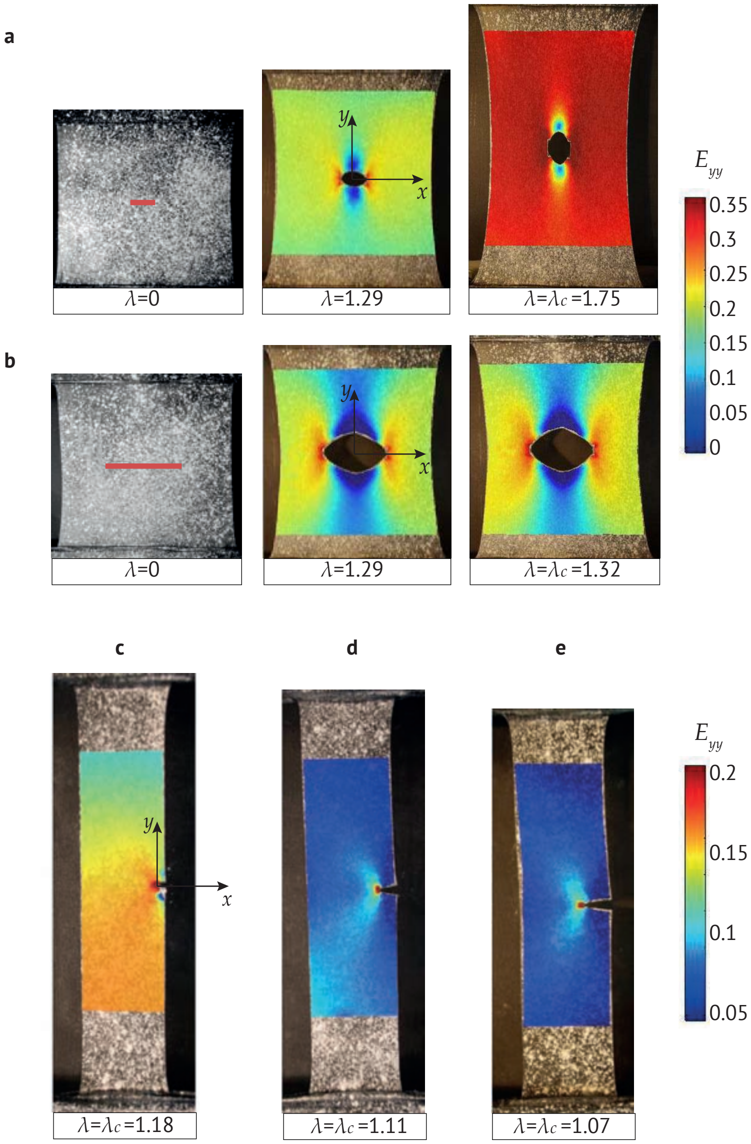

Figure 3.14 DIC maps of the Green-Lagrange strain E_{yy} in the pre-cracked specimens, at different loading (the applied stretch λ is shown below each plot). **a-b** Centre-cracked specimens CC1 and CC4. **c-e** Edge-cracked specimens EC2, EC3 and EC4

Table 3.1 Geometric characteristics of cracked specimens

Specimen ID	w (mm)	a (mm)	t (mm)	a/w	λ_c
CC1	56	10	2.75	0.179	1.75
CC2	56	15	3	0.268	1.61
CC3	56	20	2.75	0.357	1.55
CC4	56	25	2.85	0.446	1.32
EC1	26.3	1	3.5	0.038	1.26
EC2	26	2	3.2	0.077	1.18
EC3	26	5	2.9	0.192	1.11
EC4	26	8	2.9	0.308	1.07
EC5	25	1.8	4.2	0.072	1.42
EC6	25.5	3	4.2	0.118	1.36
EC7	26	4	4.3	0.154	1.28
EC8	25	5	4.6	0.202	1.26

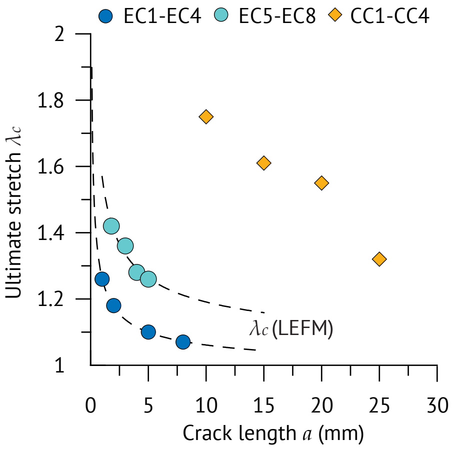

Figure 3.15 Ultimate remote stretches at failure λ_c as a function of the initial crack length a. The dashed lines correspond to best-fit curves with a the power law dependence of LEFM (Eq.3.43)

3.3.2. An analytical model for crack blunting

The DIC images of the silicone samples confirmed that crack-like defects become distorted under loading and assume an elliptic conformation. In terms of the crack-tip fields, this process causes a progressive mitigation of the stress concentration, which justifies the higher ultimate stretches observed in the samples with increased blunting. In particular, centre-cracked specimens failed at larger strains than those predicted by LEFM. We propose a simplified model of crack blunting in a linear elastic material to quantify the magnitude of blunting, and show its impact on the failure mechanism.

In a generic notched component subjected to uniform stress we can define the stress concentration factor K_t as

$$K_t = \sigma_{\max}/\sigma, \tag{3.44}$$

where $\sigma_{\max}$ is the maximum stress at the notch root and σ is the applied stress, measured with respect to a uniformly stressed section of the sample.

We assume that the deformed crack evolves into an elliptic shape, whose major and minor semi-axes are denoted by a and b, and obtain the local stress and displacements from the general solution of an elliptical hole in an infinite elastic plate (Fig.3.13b) [140]. In the curvilinear elliptical coordinates (ξ,η) the semi-axes are given by

$$a = c\cosh\xi_0, \qquad b = c\sinh\xi_0, \tag{3.45}$$

where $c = \sqrt{a^2 - b^2}$ is the focal distance and $\xi = \xi_0 = \operatorname{arccosh}(a/c)$ is the equation of the ellipse boundary. These expressions hold for an ellipse with $a > b$, otherwise a and b need to be exchanged. The complete solution is available in the literature [141].

The stress concentration factor K_t for an elliptical notch in an infinite plate is [113]

$$K_t = \left(1 + 2\sqrt{\frac{a}{\rho}}\right), \tag{3.46}$$

with $\rho = b^2/a$ being the minimum radius of curvature of the ellipse.

Let us consider the sketch of the elliptic crack shown in Fig.3.13b. In order to describe the change of K_t with increasing deformation, we need to consider the variation of the radius of curvature ρ under load. Adopting a step-by-step solution, external loading is applied in increments $\mathrm{d}\sigma^i$ and stress and displacements are computed in the points of intersection with the reference axes (x, y), denoted as $P_{\max} = P(x=a, y=0) = P(\xi_0, 0)$ and $P_{\min} = P(x=0, y=b) = P(\xi_0, \pi/2)$. The deformed configuration of the ellipse is obtained by updating the semi-axes according to the displacement increments

$$a^i = a^{i-1} + \mathrm{d}u^i_{\max}, \quad b^i = b^{i-1} + \mathrm{d}u^i_{\min}, \tag{3.47}$$

where $\mathrm{d}u^i_{\max}$ and $\mathrm{d}u^i_{\min}$ are, respectively, the increment of displacements obtained from the solution of the elliptical hole in the points $P_{\max}$ and $P_{\min}$. The solution is then updated with c and ξ_0, using Eq.(3.45). The tip radius and the stress concentration factor are obtained from

$$\rho^i = \frac{(b^i)^2}{a^i} \quad \text{and} \quad K^i_t = \frac{\sigma^i_{\max}}{\sigma^i} = 1 + 2\sqrt{\frac{a^i}{\rho^i}}. \tag{3.48}$$

The results are shown in Fig.3.16a. Here we compare our simplified analytic solution with numerical results obtained from a large strain FE analyses of the specimen CC1, where the tip radius is extracted as the radius of the best fitting circle to the deformed crack. Excellent agreement is obtained with the analytic model proposed, which is based on a linear elastic material but considers the geometric non-linearity through the configuration update of the ellipse. Also added to the plot is the model for elastic blunting proposed by Hui et al.[108]. It is based on a Dugdale cohesive zone near to the ellipse tip, characterised by a cohesive stress σ_c and fracture toughness Γ. The maximum notch root stress $\sigma_{\max}$ as a function of the applied stress σ is given by

$$\frac{\sigma_{\max}}{E} = \frac{2\frac{\sigma}{E}}{\frac{\sigma}{E} + B}, \tag{3.49}$$

where $B = \Gamma/(\sigma_{\max} a)$. The tip radius ρ was then obtained replacing $\sigma_{\max}$ in Eq.(3.44) and inverting Eq.(3.46).

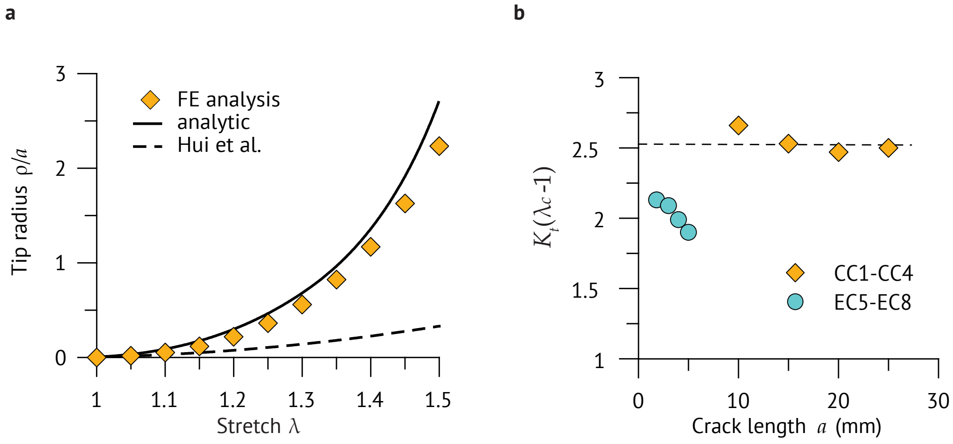

Figure 3.16 **a** Variation of the tip radius with the applied stretch: comparison between numerical results and analytical models. **b** Normalised notch root true stress at incipient failure. The effect of crack blunting is enhanced in specimens CC1–CC4, with the failure stress being approximately constant (dashed line)

Application to experimental data

We have applied the model proposed to the geometries tested during the experiments, to evaluate the magnitude of stress concentration corresponding to failure. If crack blunting anticipates rupture and mitigates the local crack tip stress, it is possible that failure could be predicted by a local stress rather than by a fracture mechanics related parameter. With this speculation we have obtained the quantity $K_t\,(\lambda_c - 1)$, which represents the normalised true stress at the notch root at incipient failure, and can therefore be considered a material property. In particular, λ_c is the ultimate stretch derived from the experiments (Table 3.1) and K_t is the stress concentration factor, corresponding λ_c, computed from the analytical model, Eq.(3.48). The results are shown in Fig.3.16b as a function of the initial length a of the crack-like defects. It appears that failure in the centre-cracked specimens CC1-CC4, where blunting is enhanced, occurs at a constant nominal stress independent on the length a, differently from the other cases.

We wish to point out that the aim of our analyses was not to provide a chart of flaw sensitivity in the canonical form; rather, we have focussed on the effect of blunting. Our results suggest that elastic crack blunting mitigates the stress intensification and promotes a flaw-tolerant failure in soft materials.

In the analyses we have not considered the effect of rate. It is known that viscoelastic dissipation may affect the deformed crack profile and impact on the elastic blunting of polymeric materials. Specifically, at lower strain rates, the material can be assumed in a relaxed state with the elastic modulus that is the modulus at zero rate. Increasing the rate, the deformation is governed by the instantaneous modulus which is much larger, hence elastic blunting could be reduced[108]. To generalise the observed behaviour to biological tissues, we would need to explore the role of strain hardening, which is expected to reduce the elastic blunting. Further analyses are required to shed light on these points.

3.4. Crack blunting and sharpness in cutting

When propagating a crack with an external tool, for instance during cutting with a blade or a wire, the interaction between the finite size of the tool and the crack tip must be accounted for. Hui et al.[108] suggested that a sharp knife exerts some sort of constraint on the elastic blunting of the crack, which might be limited by the fact that the crack opening displacement is determined by the knife geometry. Adopting a cohesive crack model, they speculated that such limiting effect occurs whenever the tip radius of the tool is smaller than the critical opening displacement of the crack. Following their idea, we have investigated the interaction between a rigid wire and a blunted crack, but instead of using the critical displacement of the cohesive law, we have computed a critical radius at the tip of the blunted crack. This is defined as the local radius of curvature when a pre-existing mode-I crack is in the condition of incipient propagation

$$\rho_c = \rho(G = \Gamma), \tag{3.50}$$

where Γ is the fracture toughness of the material.

We have analysed, by means of large strain FE analyses, various configurations of a specimen containing an open edge-crack of length a (Fig.3.17a). The material is an elastic, soft and brittle compound, described by Ogden's incompressible hyperelastic model, Eq.(A.52), where the elastic modulus E is in the order of 18 KPa. Due to symmetry, only half specimen is modelled, with 8-node plane strain elements suitably refined around the crack tip, which is artificially blunted by taking an initial small radius of curvature. The geometry does not correspond to the pure-shear type considered in previous analyses. Therefore, in order to compute the strain energy release rate G, we cannot employ Eq.(3.4). In a contour surrounding the crack tip, we have computed the J-integral, with respect to the undeformed configuration, defined as[101]

$$J = \int_C \left(W N_1 - \frac{\partial u_i}{\partial X_1} P_{ij} N_j \right) \mathrm{d}s, \tag{3.51}$$

where W is the elastic strain energy density function, N_1 is the unit vector in the direction of crack propagation and P_{ij} is the first Piola-Kirchoff stress. In elastic materials, the J-integral is path-independent and equal to the energy release rate G, so that the condition of crack propagation is

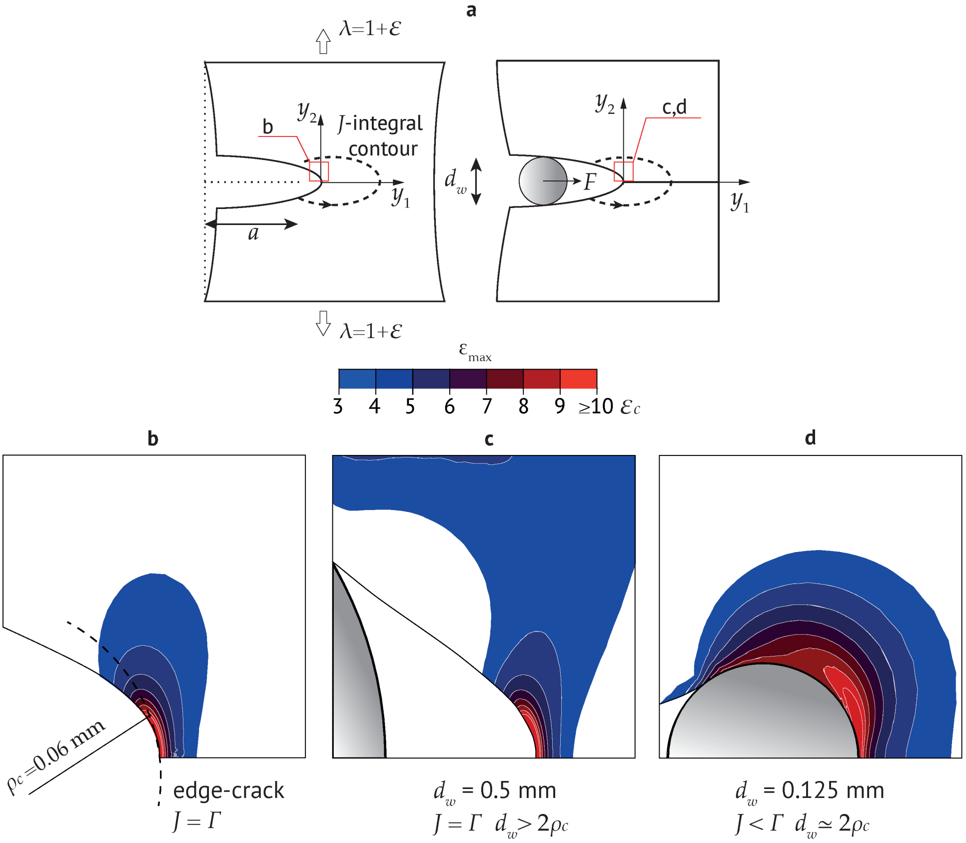

Figure 3.17 **a** Sketch of the edge-crack and wire-cutting. Contours of the in-plane maximum principal strain ε_{max} in the crack-tip region, as a function of the remote nominal strain ε_c at incipient propagation: **b** edge-crack configuration with remote mode-I loading; **c**-**e** wire cutting at different diameters d_w

attained when $J \equiv G = \Gamma$. The parameter Γ is the fracture toughness of the material obtained from experimental measures, in this specific case approximately equal to 1.1 Pa m.

Firstly, the case of an edge-crack subjected to far-field mode-I loading, by means of applied displacement in the direction perpendicular to the crack, is considered. Subsequently, we have analysed the same configuration with a rigid circular wire that is inserted and pushed forward, in the direction parallel to the crack, until the full length of the crack is covered. The critical condition is the same as before, having hypothesized that the resistance to cutting is equally defined by Γ. The relationship between the finite size of the tool and the crack tip is expressed in terms of the wire diameter d_w versus the critical radius ρ at the tip of the blunted crack. From the deformed coordinates (y_1, y_2) of the crack profile, ρ is determined as the radius of the circle fitting the profile within a distance equal to $10^{-3}a$ from the crack tip.

Results of the analyses are presented in Figs.3.17-3.18. In Fig.3.17 each frame shows the contours of the maximum principal strain ε_{max} at the condition of incipient propagation, that is when $J = \Gamma$. The effect of strain localisation around the crack tip is illustrated by scaling the contours with respect to ε_c, defined as the remote nominal strain in the edge-crack configuration, $\varepsilon_c = \lambda_c - 1$. The edge-crack configuration is shown in Fig.3.17b, with tip radius of the blunted crack ρ_c. By considering various wires with decreasing diameters, we are able to locate a transition to constrained blunting, where the critical condition is met when the wire touches the crack tip (Fig.3.17d). Further evidences of such a transition come from the plots of the deformed crack profile, in a region within a distance equal to $0.1a$ from the crack tip (Fig.3.18a). The curves obtained from the insertion of wires with different diameters are almost equivalent and similar to the profile of an edge-crack subjected to remote loading, with the exception of the diameter $d_w = 0.125$mm.

Our analyses contribute to shed light on the mechanism driving crack propagation during cutting, which is here treated as a two-dimensional steady state process. In general terms, cutting with a wire or a thin blade is considered analogous to propagate a crack in symmetric loading conditions, where the crack driving energy comes primarily from the external work performed by the wire. Differently from propagation of a crack under remote loading, the finite size of cutting tools adds an additional length scale to the fracture process. In the case of wire cutting here considered, it is the wire diameter d_w the relevant dimension that needs to be compared with a characteristic length of the fracture process. In an elastic material, such length is defined as the natural tip radius of the blunted crack $\rho_c \sim \Gamma/E$. By comparing analyses with wires of various diameters, we notice that the tip radius ρ is approximately equal to ρ_c when $d_w \geq 2\rho_c$ (Fig.3.18b). Below this limit, we hypothesise that the tip radius scales with the wire diameter (hence the slope 1/2 shown in the plots). The analyses here presented are consistent with the simplified model of cutting proposed in Chapter 2, where a sharpness parameter was introduced as point of transition between two different mechanisms of propagation for blunt and sharp tools. Here we illustrate a case where that simplified framework is discussed in relation to very soft elastic materials. Contrary to hard solids, the natural critical tip radius ρ is in the order of millimetres, hence the transition limit becomes attainable with commercial tools. The ratio between the wire diameter d_w and natural critical tip radius ρ_c is nothing else that a different form of the tip sharpness given in Eq.(2.36), and we can make analogous considerations by observing Figs.3.17b-d and Fig.3.18:

- for $d_w \geq 2\rho_c$, propagation of the cut happens as an autonomous process under symmetric mode-I conditions, with a certain distance between the wire and the crack tip. The crack tip radius is determined by its natural value Γ/E. This situation corresponds to what we have previously defined as cutting with 'blunt' tools.

- for $d_w < 2\rho_c$, the shape of the blunted crack is constrained by the wire, which touches the crack-tip. In this situation, the mechanism of propagation is different and requires a further input of external energy, since the condition $J = \Gamma$ cannot be attained (Fig.3.17d). This is the case of cutting with 'sharp' tools.

What we have not considered in the analyses is the effect of friction, which is known to add a relevant contribution to the applied force in cutting soft solids. However, there are two reasons which motivated our choice: firstly, the fact that cutting with wire minimises frictional dissipation because of the reduced contact area during the insertion; secondly, the assumption that friction does not influence the mechanism of propagation below the transition limit. With the latter statement we mean that when a wire or a straight blade is advanced steadily and rectilinearly in the material, frictional tangential stresses arise symmetrically along the edge, resisting motion but

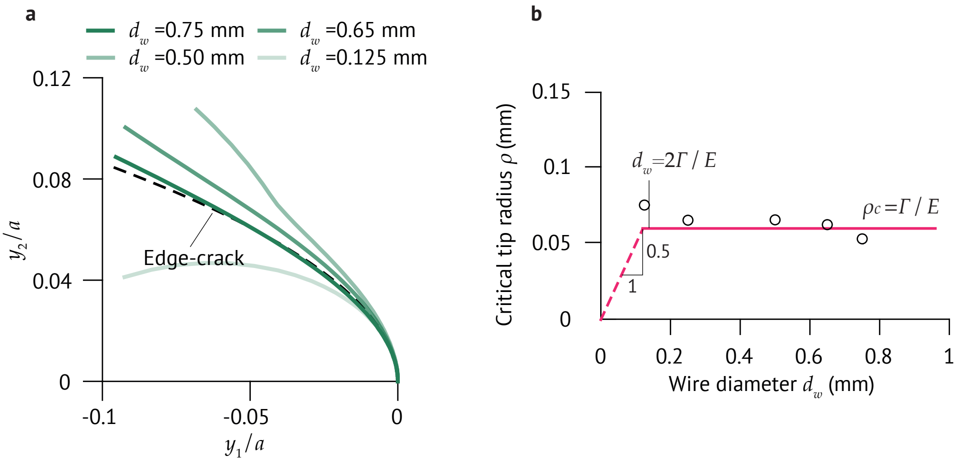

Figure 3.18 **a** Deformed crack profiles at incipient propagation, for an edge-crack (dashed line) and various wire diameters d_w. **b** Crack tip radius at incipient propagation ρ versus the wire diameter. The horizontal line is the natural crack tip radius $\rho_c \sim \Gamma/E$

not giving rise to any mode-II contribution to the crack driving energy. Below the limit $d_w = 2\rho_c$ the picture is likely to change, with the cutting force directly pushing the crack tip and generating additional frictional force, which might alter in an unknown fashion the crack driving energy. An example of a mixed-mode propagation during the insertion of bevel-tipped needles is considered in §5.3 of the present thesis.

4

Fracture in rate-dependent porous biomaterials

We should not overlook the importance of simplicity combined with depth of understanding, not only for its cultural value, but as a technological tool. Deeper physical insight combined with theoretical simplicity provides the short cuts leading immediately to the core of extremely complex problems and to straightforward solutions. Of course, formal knowledge is essential but, as for everything in life, the truth involves a matter of balance.

Maurice A. Biot

Many biological materials combine their soft elastic nature with a microstructure that resembles a soft sponge, where small pores can be permeated by fluids. The behaviour shown by such materials is complicated by the fact that, in addition to a non-linear elastic response, they usually show rate-dependent properties. Human brain is one relevant example. Results from laboratory tests reveal a non-linear stress-strain relationship and a complex rate-dependent nature, ascribable both to viscoelasticity and to the flow of cerebrospinal fluid during deformation[30]. Less is known experimentally about the fracture behaviour, partly because of the technical difficulties in realising proper fracture tests. In this chapter we address the topic of brain fracture indirectly, combining some available experimental results with numerical models of the fracture process in porous materials. Due to the complications in having reliable fracture data, we have also considered phantom tissues which are employed to mimic the behaviour of the human brain, in particular a biopolymeric gelatine and a viscoelastic soft hydrogel[44–47]. Moreover, we can take advantage of the known microstructure and predictable failure mechanisms of phantoms to investigate the rate-dependent behaviour of human brain more in detail. The content presented in this chapter is partly obtained through simplifying assumptions that might require to be verified experimentally in the future, and in this sense it offers a global view on the topic of fracture in rate-dependent materials, rather than a direct means of comparison with the experimental data.

The rate-dependent behaviour observed in fracture tests is due to the effect of energy dissipation. In porous materials, we need to consider two sources of dissipation, one connected to the viscoelastic relaxation of the solid network and the other one arising from the flow of fluid in the pores[142]. For the sake of completeness, we shall mention that rate-independent mechanisms, such as the well-known Mullins effect in rubber-like materials[143], have also been observed in biological tissues[28,144] and hydrogels[145–147]. However, here we restrict our analysis to rate-dependent phenomena that are predominant in porous biomaterials. In order to correctly describe the rate-dependent fracture, we need to link the sources of dissipation to the available energy for crack propagation. This topic is discussed in §4.1, where we introduce the relevant time and length scales of energy dissipation in soft porous materials and present the model employed in the numerical analyses of fracture.

When a porous network is swollen by fluid, mechanical and hydraulic responses are coupled, resulting in a complex non-linear behaviour. During fracture, fluid flows inside the crack surface with mechanical deformations, and at the same time fluid is exchanged between the fracture zone and the bulk material. Experimental evidences on physical hydrogels showed that the fracture energy is increased by the drainage of fluid in the crack-tip zone[44,148]. In addition, polymeric hydrogels swollen with fluid and subjected to subcritical loading, i.e. such that the elastic strain energy is not enough to cause instant failure, fail with a delay because fluid drainage increases the available energy for fracture[149]. A similar delayed mechanism has also been observed at slow loading rates in micro-indentation of cartilage[24]. Poroelastic theories, derived from the consolidation of soils by Biot[150,151], and mixture biphasic theories have been employed to study biological materials[23] and were shown to offer an equal description[152]. More complex approaches are required in case of large deformations, where the non-linear response of the solid matrix as well as the effect of swelling need to be considered. A few models have been proposed to study the effect of solvent diffusion in fracture of hydrogels[153,154]. With respect to the human brain, confined and unconfined compression have been investigated adopting the basic theory of consolidation[28]. A coupled poro-hyperelastic model has been proposed to model compression tests in biopolymeric gelatines[44] and recently applied on human brain to simulate the complex phenomenon of brain shift[31]. In Section §4.2 we present the poro-hyperelastic model and show the main results of numerical simulations on the effect of fluid.

Often, the flow-dependent dissipation is coupled with viscoelastic relaxation. Fracture in viscoelastic materials is reasonably well understood with respect to rubber-like materials[155–158], where experimental evidences showed a remarkable increase of fracture energy with rate due to the molecular friction[159–161]. The same mechanisms also applies to the failure of tough hydrogels with chemical cross-links[162,163], although other studies on dual cross-linked hydrogels with physical bonds showed a reversed behaviour[116]. A different mechanism of viscous fracture has been observed in physical hydrogels used for bioengineering applications[39,40,42,164]. With respect to the human brain, experimental evidences from compression and tensile tests showed clear signs of frequency-dependent stiffness, with the brain deforming differently at fast and slow rates. Brain tissue has been studied according both to linear and non-linear viscoelastic theory[26,27,165], but the resulting picture is far from being exhaustively investigated, and there are often controversial results coming from experiments. For hydrogels fracture, recent theories have been proposed, which account for the coupled effects of viscoelasticity, fluid diffusion and large deformations[142,166]. In Section §4.4 we attempt to consider the effect of viscoelasticity during fracture of brain tissue and mimicking hydrogels. A visco-hyperelastic model, proposed to model the unconfined compression of human brain[30], is used. Based on physical reasoning, we are also able to sketch a qualitative view of the possible interaction of viscoelasticity and fluid draining on crack propagation.

4.1. Toughness and energy dissipation

As anticipated, dissipative mechanisms occurring in the material during crack propagation might affect the available energy for fracture. We need to identify not only the different sources of dissipation but also if and in which measure they actually impact on crack propagation under cutting. After considering the possible sources of dissipation in soft porous materials, we present the approach adopted in the analyses of rate-dependent fracture included in this chapter.

4.1.1. Sources of rate-dependent fracture

In general we can assume that any material containing a crack experiences energy dissipation when loaded. Notice that this is relevant not only to cyclic loading but also to monotonic loads, because the stress state near the crack tip is inhomogeneous. Specifically, points ahead of the crack are first loaded and then unloaded as the crack extends, leaving behind two layers of the material going through hysteresis[167]. Although a certain amount of dissipation is inevitable, it is important to quantify the size of the regions affected and compare them with the finite dimensions of real bodies. Similarly to the schematic presented in Chapter 1, Fig.4.1 illustrates the region surrounding a propagating crack in a soft porous material. With respect to energy dissipation, we can identify the following three sources[49]:

- rate-dependent damage phenomena within the process zone (A);
- flow-independent dissipation due to the viscous relaxation in the material surrounding the crack tip (B);
- flow-dependent dissipation due to the drainage of fluid in the crack-tip region (B).

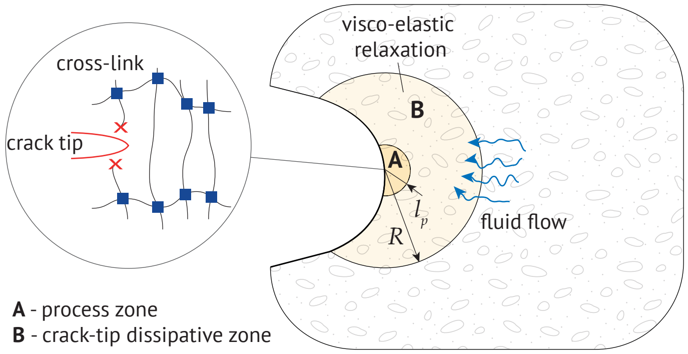

Figure 4.1 Illustrative sketch of a crack in a porous viscoelastic material. Shown in figure are the process zone (A) with radius l_p, and the crack-tip dissipative zone (B) with radius R. The enlarged view shows the chain scission mechanism typical of rubber-like polymers and chemical hydrogels

The process zone comprises rupture processes occurring at the molecular scale, which are peculiar of each material and account for an *intrinsic* toughness Γ_0. Dissipative processes occurring within this highly localised region, of radius l_p, might result in a toughening effect on Γ_0. In rate-dependent materials, such increase is proportional to the velocity of crack propagation. For instance, Baumberger et al.[39] observed a linear increase with crack velocity in gelatine pure-shear specimens, and linked such effect to a local process of viscoplastic disentanglement. Similarly, Forte et al.[44] noticed a rate-dependent toughening during wire cutting tests of biopolymeric gelatines. They proposed a mechanism of fluid draining in the pores within the process zone to explain the phenomenon. Their model is considered more in detail in Section §4.3.

The other dissipative terms are originated from the relaxation in the bulk material but might become relevant to crack propagation only if they affect the crack-tip region, of radius R. Viscoelasticity results from conformational changes of the molecular network and dominates the short-time range behaviour, while poroelasticity results from long-range motion of the fluid molecules, hence it requires longer times. Usually, they might affect fracture by preventing the external force from being fully delivered to the crack[147]. The effectiveness of each mechanism depends not only on the material properties but also on the loading conditions. Moreover, in soft materials these mechanisms are coupled with large deformations. In such conditions, boarders between the regions fade out and the very definition of typical fracture parameters such as G is questionable. While the resulting picture might appear daunting, we can formulate a few assumptions which make the foundation of our approach to fracture in soft porous materials, as explained in the next paragraph.

4.1.2. Analytical approach to rate-dependent fracture

We assume to split the fracture energy of a dissipative material in two terms: the intrinsic term Γ_0 originating from the process zone, and an additional term Γ_D due to energy dissipation in the crack-tip region affected by propagation[49], so that we have

$$\Gamma = \Gamma_0 + \Gamma_D \tag{4.1}$$

The purpose of this distinction is to identify that part of fracture energy that can unambiguously be related to crack propagation, and separate it from the source of bulk dissipation resulting from the deformation field surrounding the crack tip[158].

Unlike the intrinsic toughness Γ_0, Γ_D cannot be treated as a property of the material because it is affected by rate. For instance, in elastomers the dissipative term is related to the crack velocity v according to[157]

$$\Gamma_D = \Gamma_0 f(a_T v), \tag{4.2}$$

where f is a monotonically increasing function, which takes zero value when $v \to 0$, and a_T is a temperature dependent empirical parameter.

Similar relationships have also been proposed for hydrogels, derived from experimental fracture tests. However, to develop an approach which we can use in computational analyses is not trivial, as it requires to relate crack propagation velocity and energy dissipation, and compute the part of energy available for fracture. With respect to the latter, we recall that the energy release rate G is not obtainable from the strain energy density, as this includes dissipative terms. The J-integral definition has been modified in order to include the contribution from viscoelastic dissipation[155], but we cannot assume that it provides the energy release rate G. Moreover, the J-integral is path-dependent because the local strain rates are amplified in the crack-tip zone non-uniformly, so that different points within this zone do not follow a single stress-strain relationship[49].

The approach we follow, similar to that proposed by Wang and Hong[149] for the analysis of delayed fracture in hydrogels, is based on the separation of the fracture energies according to Eq.(4.1). We then consider a cohesive process zone for the intrinsic toughness Γ_0, whose size is assumed much smaller than that interested by dissipation coming from the bulk, that is we assume $l_p \ll R$ (Fig.4.1). Furthermore, we assume that the large strain zone and the crack-tip dissipative zone have the same length scales, and define such length as

$$R \equiv \rho_0 = \Gamma_0 / E, \tag{4.3}$$

where E is the instantaneous elastic modulus of the material. We are aware of the fact that an alternative definition, based on the ratio between the toughness Γ and the strain energy W, would allow to account for dissipative contributions on the length R. However, lacking experimental values of the toughness Γ we believe that the length in Eq.(4.3) is still a pertinent definition for the crack-tip zone.

Potential dissipative mechanisms which might affect crack propagation, such as viscoelastic relaxation or fluid draining, are condensed in the crack driving energy. Differently from an elastic material, G also depends on the strain rate $\dot{\varepsilon}$. Then, crack propagation occurs when

$$G(\dot{\varepsilon}) = \Gamma_0, \tag{4.4}$$

where the fracture toughness Γ_0 is provided by the cohesive energy, i.e. the area below the cohesive stress-displacement law. Notice that this corresponds to the energy that we could obtain from a path integral surrounding the cohesive zone, so that dissipation is excluded[116].

The practice to adopt a cohesive model for rate-dependent fracture processes is popular, in particular with polymeric materials. As a matter of fact, the rupture of polymers is accompanied by void growth ahead of a propagating crack, leading to strain softening and eventually material disintegration[156]. In the analyses presented in this chapter, the intrinsic toughness is considered rate-independent. Implicit in this formulation is the assumption that the rate dependence of the fracture process is derived primarily from the bulk[158]. However, the effect of rate within the process zone could be added to the model by considering a modification of the cohesive law according to the rate of loading. Relevant examples can be found in the literature for viscoelastic materials[168–172] and poroelastic gels[154].

Intrinsic toughness in hydrogels

The intrinsic toughness Γ_0 derives from molecular rupture mechanisms which take place right ahead of a propagating crack. In rubbery networks, Lake and Thomas[43] calculated the intrinsic fracture energy assuming that, at a load approaching the threshold, the extension of a crack only breaks polymer chains ahead of the crack tip (see the inset in Fig.4.1). Consequently, the energy is proportional to the areal density of the chains crossing the interface and the bond energy U_b of a single covalent bond. We obtain the following expression[43]

$$\Gamma_0 = N l \, n_0^{3/2} U_b, \tag{4.5}$$

where N is the number of cross-linked chains per unit volume, l is the length of each monomer and n_0 is the average number of monomers per chain. Curiously, the approach is analogous to the famous fracture mechanism in metals proposed by Griffith, where the energy is that required to break a single layer of atomic bonds[167]. Since the force to break covalent bonds does not vary much with rate, in many cases the intrinsic toughness is assumed constant while dissipation is related to what happens in the bulk[50].

The same mechanism has also been considered for hydrogels with covalent cross-links, where the areal density of the chains is proportional to the volume fraction of the polymer[173]. This explains why elastic hydrogels with the same number of monomers per chain are more brittle than elastomers. Moreover, it can be shown that the Young's modulus is inversely related to the fracture toughness[51]. To overcome the complexity in deriving a correct value of toughness from molecular models, some authors suggested to employ direct experimental measures in which dissipation is prevented[157]. Typically, this means performing a fracture test at very low loading rates, so that quasi-static conditions are assumed. Results from wire cutting tests at low loading rates are available for the biopolymeric gelatine[44], from which we have derived the toughness following the model presented in §3.1.2.

4.2. Fluid diffusion in brain tissue and mimicking hydrogels

4.2.1. Time and length scales in poroelastic fracture

When loads are applied to a saturated porous solid, fluid is trapped in the pores and the material is in an *undrained* state, where an excess pressure is generated in the pores. As time goes by, fluid is expelled from the solid (assuming that there is at least one free surface in contact with air) and pressure decreases until eventually it equilibrates the atmospheric. This situation is referred to as a *drained* state. The mathematical expressions of such conditions are

$$\begin{aligned} \zeta &= 0 \quad \text{(undrained)}, \\ p_F &= 0 \quad \text{(drained)}, \end{aligned} \tag{4.6}$$

where p_F is the fluid pressure and ζ the variation of fluid content.

The process of fluid draining is at the origin of the time-dependence observed in relaxation tests of porous material: from the initial undrained state the material equivalent stiffness decreases with time as draining progresses. We can define a characteristic time of poroelastic relaxation as

$$t_d = \frac{R^2}{D_F}, \tag{4.7}$$

where R is a characteristic length scale, function of the geometry of the specific problem, and D_F is a material parameter known as the diffusion coefficient, with dimensions L^2/T. Rather than a material property, the poroelastic time represents the actual time needed to complete the draining process. Comparing the poroelastic time with a typical observation time t, we can assume that the material is in undrained conditions if $t \ll t_d$ and in a drained state if $t \gg t_d$. When arranging experiments to evaluate the mechanical parameters of fluid diffusion, it is preferable to reduce the characteristic length making use of micron-size indenters and atomic force microscopy, in order to shorten the time required[174,175].

A subtle difference arises in problems with moving boundaries, as for instance in crack propagation. Assuming that there is always a region close to the crack-tip which is drained, we can relate the size R_d of this region to the crack propagation velocity v

$$R_d = \frac{D_F}{v} \tag{4.8}$$

and compare it with a typical observation length R. Then we can consider the region of size R to be in undrained conditions if $R_d \ll R$ and in a drained state if $R_d \gg R$.

4.2.2. Numerical analysis of poroelastic fracture

Numerical analyses were performed in order to understand the source of rate-dependence observed during fracture of human brain and mimicking materials. In particular, results from wire cutting experiments at different insertion velocities showed that the steady-state force is affected by rate[44,45]. In Fig.4.2 we report some results from wire cutting on gelatine (Fig.4.2a) and brain tissue (Fig.4.2b). Both materials show an increasing force with rate, although the evolution to steady-state cutting (yellow regions in the figures) is different. The transition to a constant force is not well marked in the brain tissue, probably due to the extreme softness and the inhomogeneous structure of the sample.

The presence of fluid in the region surrounding the crack tip might be one of the reasons behind the behaviour observed. Since the rate-dependent effect is predominant in the steady-state, when the external work is converted into fracture energy for crack propagation, we have decided to focus on the crack-tip zone only, leaving aside the whole process of contact and indentation. In this way, we can explore the influence of rate on fracture of porous materials without the complexity of contact interactions. However, we should recall that crack propagation in steady-state cutting can be treated as an equivalent fracture problem only in the case of autonomous propagation, which exists if the wire diameter is above a limit value. This aspect was explained and shown quantitatively in the quasi-static condition (elastic material) in §3.4, and here we consider that the same arguments apply with energy dissipation as well. The geometry is illustrated in Fig.4.3: it consists of a large rectangular plate of height $2h = 50$mm and width $w = 20$mm, containing an edge-crack of length $a = 1$mm. The normal displacement applied to the plate boundaries was defined such that the strain rate $\dot{\varepsilon}$ is constant

$$\Delta = \left(e^{\dot{\varepsilon}t} - 1\right)h, \tag{4.9}$$

where $\varepsilon = \ln[(h + \Delta)/h]$ is the true strain in the direction normal to the crack line.

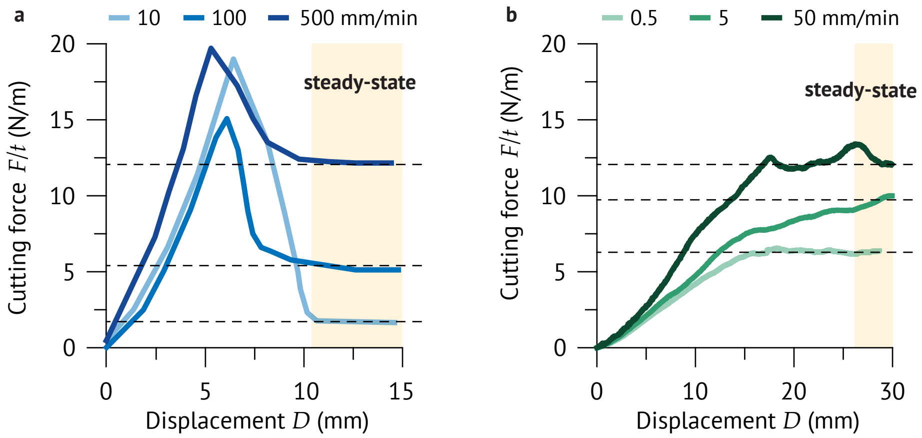

Figure 4.2 Experimental wire cutting force-displacement profiles, at different rates. **a** Results for a 10% w/w gelatine with a 0.05mm wire diameter (adapted from Forte et al. [Ref. 45]) and **b** for human brain tissue with a 0.16mm wire diameter

The poro-hyperelastic model

Both the brain tissue and the biopolymeric gelatine are considered as soft porous solids with fluid, whose constitutive behaviour is described by an hyperelastic model for the solid skeleton and fluid interaction is included by means of a law of fluid flow. The main ingredients of the poro-hyperelastic model are introduced below, limited to the aspects of interest for the numerical implementation. For a more detailed formulation of the poroelastic theory, the reader is referred to the Appendix A.2.

Following Biot's theory of poroelasticity at finite strains[151], the stress state in a porous solid in the reference configuration can be characterised by the second Piola-Kirchoff stress tensor $\mathbf{S}$ and the fluid pressure p_F. These are work conjugate with the Green-Lagrange strain tensor $\mathbf{E}$ and the variation of fluid content ζ. In this framework, it is common practice to introduce the notion of an *effective stress* tensor $\mathbf{S}'$ related to the elastic solid skeleton, defined by[176]

$$\mathbf{S}' = \mathbf{S} + J p_F \mathbf{C}^{-1}, \tag{4.10}$$

where a positive sign is included because the pressure p_F is treated as a compressive stress, i.e. $p_F \leq 0$.

A hyperelastic strain energy density function W' can be defined for the solid part, such that the effective stress $\mathbf{S}'$ is obtained by derivation. It should be noticed that any hyperelastic material formulation can be included, either given in terms of strain invariants or principal stretches, provided that it allows compressibility. Indeed, even if we consider both fluid and solid to be incompressible, volumetric deformation will derive from the process of fluid draining during structural deformation. One of the most used formulation to fit experimental data is the fractional Ogden model[177] proposed for hyperelastic compressible materials. We recall here the expression of the strain energy density function

$$W' = \sum_{i=1}^{N} \frac{2\mu_i}{{\alpha_i}^2} \left(\bar{\lambda}_1^{\alpha_i} + \bar{\lambda}_2^{\alpha_i} + \bar{\lambda}_3^{\alpha_i} - 3 \right) + \sum_{i=1}^{N} \frac{1}{D_i} (J-1)^{2i}, \tag{4.11}$$

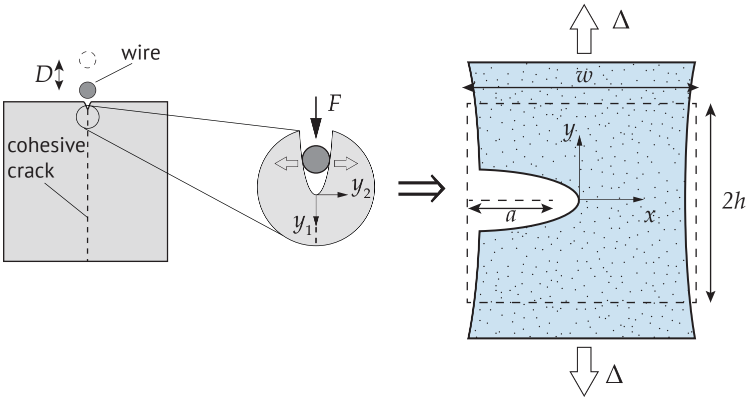

Figure 4.3 Sketch of the model employed to investigate the rate-dependent fracture process observed in wire cutting of a porous material. The equivalent geometry has an initial edge crack of length a and is subjected to an opening remote displacement Δ

where $\bar{\lambda}_i$ are the deviatoric principal stretches, μ_i, α_i and D_i are material parameters.

The fluid flow within the interstitial pores is governed by Darcy's law, which describes the motion of fluid relative to the solid. In an isotropic porous material, and conditions of fluid saturation, it is formulated as follows

$$\mathbf{w} = -\frac{k}{\gamma_F}\left(\nabla p_F + \gamma_F \nabla z\right), \tag{4.12}$$

where $\mathbf{w}$ is the specific discharge vector, defined as the volume of fluid crossing a unit area of porous medium, per unit time. k is the hydraulic conductivity (dimensions LT^{-1}), γ_F is the fluid specific weight, p_F is the fluid pressure and z is the elevation head. Notice that the hydraulic conductivity k is related to the fluid permeability K_F (dimension L^2) through

$$k = K_F \frac{\gamma_F}{\eta_F}, \tag{4.13}$$

where η_F is the fluid viscosity (dimensions $\mathrm{FL}^{-2}\mathrm{T}$).

The material parameters employed in the analyses are summarised in Table 4.1. In particular, those for the gelatine are related to a biopolymer concentration of 10% on the total weight.

Finite element model

The numerical analyses were performed using the commercial finite element (FE) software SIMULIA Abaqus 2017 (Dassault Systèmes[135]). Abaqus adopts an effective stress principle to describe the behaviour of a porous medium, in which the pore pressure p_F is treated as an additional nodal variable. A one-term hyperelastic Ogden model, Eq.(4.11), is used for the elastic response of the bulk material. In such a case, μ defines the shear modulus and the bulk modulus K is related to the parameter D by

$$K = \frac{2}{D} = \frac{2\mu(1+\nu)}{3(1-2\nu)} \tag{4.14}$$

where ν is the Poisson ratio.

Table 4.1 Mechanical parameters of the poro-hyperelastic model

Variable	Gelatine (10% w/w)[44]	Brain[30]
Shear modulus (Pa)	$6.21 \cdot 10^3$	$0.52 \cdot 10^3$
Ogden parameter α	2.64	-4.4
Poisson ratio	0.40	0.35
Ogden parameter D (1/Pa)	69	$1.3 \cdot 10^3$
Hydraulic conductivity k (m/s)	$1.25 \cdot 10^{-6}$	$1.57 \cdot 10^{-9}$
Fluid specific weight γ_F (kN/m^3)	9741	9741
Initial void ratio e (%)	9	2

The fluid flow is characterised by the hydraulic conductivity k, fluid specific weight γ_F and porosity n_F. The porosity n_F can be specified as an initial condition in the analyses through the void ratio e, which is related to the porosity by

$$n_F = \frac{e}{1+e} \tag{4.15}$$

We have assumed initial conditions of saturation and isotropic permeability. A transient fluid-stress diffusion analysis is required to simulate fluid flow through the porous material, where the accuracy of the solution is governed by the maximum pore pressure change allowed in an increment. Different values have been considered for the best compromise between accuracy and efficiency. 4-node quadrilateral plane strain hybrid elements, which include pore pressure, were employed for the bulk material. Boundary conditions were specified in terms of displacements (top and bottom forces are prevented from lateral motion), and in addition on the pore pressure degree of freedom. A condition of draining, enforced by setting the pore pressure equal to zero, is specified for the vertical free edges and the edge-crack surfaces in contact with atmospheric pressure. The FE model is illustrated in Fig.4.4a.

Fluid draining in the crack-tip region

The main purpose of the analyses is to understand if fluid draining affects the crack-tip region, when the critical condition corresponding to the onset of crack propagation is reached. With respect to the assumptions on energy dissipation and toughness introduced above (§4.1.2), we assume that the rate-dependence is due to fluid particles migrating from the bulk material towards the crack-tip. In other words, we are considering the effect of dissipation and of the loading rate on the crack driving energy $G(\dot{\varepsilon})$, whereas the fracture toughness is assumed equal to Γ_0. The critical condition of incipient propagation is then expressed by Eq.(4.4). A preliminary analysis on the elastic material is employed to investigate the critical condition for crack propagation. In such a case, the energy release rate can be evaluated through the J-integral in a contour surrounding the crack tip, and the critical condition is attained when $J = \Gamma_0$. At this point, we can also extract the critical stretch λ_0.

The results are illustrated in Fig.4.4b-c, where we show the contours of the fluid pressure p_F in the gelatine and in the brain tissue, for three different strain rates $\dot{\varepsilon}$, extracted at the stretch λ_0. The region considered is the crack-tip dissipative zone, whose radius, from Eq.(4.3), is in the order of 10^{-5}m in both materials. To this purpose, we must clarify that the gelatine intrinsic toughness Γ_0 was obtained from the wire cutting tests at quasi-static rate (see §3.1.2), which yielded a value of $\Gamma_0 \simeq 1.1 \mathrm{Pa\,m}$. Unfortunately, we did not have enough experimental data to obtain a reliable value of the same parameter in the brain tissue. In the analyses, Γ_0 of human brain was fixed arbitrarily such that the crack-tip dissipative regions in both materials had approximately the same extension.

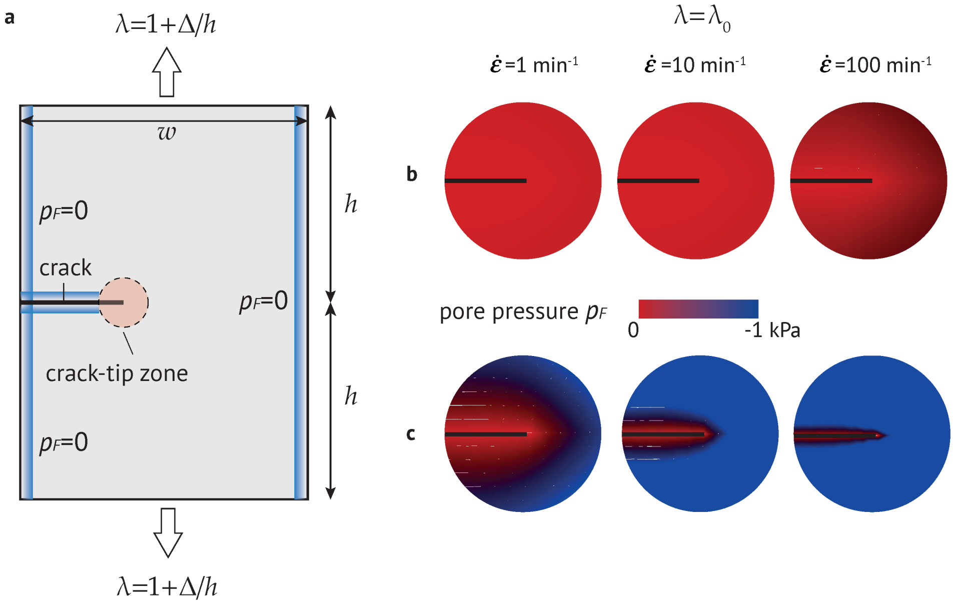

Figure 4.4 **a** Model of an edge-crack in a poroelastic solid. The blue edges are those with drained boundary conditions. Contours of the pore pressure p_F at constant stretch $\lambda = \lambda_0$ for different strain rates, in the gelatine (**b**) and the brain tissue (**c**)

The red regions correspond to the drained or relaxed condition ($p_F = 0$) whereas the blue regions are affected by fluid flowing in the pores. When loading is applied, in both cases the solid is saturated and there is only an infinitesimal zone close to the tip of the existing crack where the fluid pressure is zero. As time goes by, this region increases in extent until the critical condition is attained. It can be seen that, independently from the rate, the greater permeability of gelatines allows for a rapid draining of the whole crack-tip region. On the contrary, it appears that fluid takes a longer time to drain the same area in the brain tissue, where permeability is much lower.

To discuss the implications of dissipation due to fluid draining, we can assume that fracture is affected only if such process occurs within the crack-tip region in times comparable to those required for crack propagation. Let t denote the time measured from the instant of load application to the onset of crack propagation. By comparing it with the time of poroelastic relaxation t_d Eq.(4.7), we are able to distinguish the following cases:

- $t \ll t_d$: this situation occurs at very fast strain rates or reduced permeability, when fluid diffusion is too slow to be effective. We have undrained conditions in the crack-tip region, so that the material behaves as an incompressible solid. It applies to the brain tissue at high strain rates;

- $t \simeq t_d$: this case corresponds to intermediate situations when fluid drains the crack-tip region in a time range comparable to that leading to crack propagation. It applies to the brain tissue at moderate strain rates;

- $t \gg t_d$: finally we have the limit case of slow strain rates or very permeable materials. As draining is fast, the drained region is large compared to the crack-tip zone so that relaxation is ineffective with respect to fracture. We can assume that the material behaves as an elastic solid. This is the condition that we find in the gelatine.

In Eq.(4.7) the material permeability enters indirectly through the diffusion coefficient D_F, which in hydrogels is usually very small[166]. In the absence of experimental measures, we can use the following definition derived from the linear theory of poroelasticity[178]

$$D_F = \frac{2\mu(1-\nu)}{(1-2\nu)}\frac{K_F}{\eta_F}, \tag{4.16}$$

where D_F represents a generalised consolidation coefficient in the spirit of Terzaghi's formulation, that is, in the case of uniaxial strain with the assumption of both fluid and solid incompressibility. Approximate values are $D_F \sim 10^{-6}\mathrm{m}^2/\mathrm{s}$ in the gelatine and $D_F \sim 10^{-10}\mathrm{m}^2/\mathrm{s}$ in the brain tissue.

Since fluid draining is a dissipative process, it is reasonable to assume that crack propagation is affected by the phenomenon, at least in the brain tissue. The known effect of dissipation is an enhancement of the material toughness, which is reflected for instance in an increased value of the stretch corresponding to fracture[32]. With respect to the poroelastic model considered, in regions with fluid the effective stress is smaller than the same areas in drained conditions, Eq.(4.10). At the onset of crack propagation, this results in a lower value of the crack-driving energy, which is therefore also affected by rate. There is a further step, though, that is far from trivial: even if we can compute the strain energy per unit area within the crack-tip region (for instance, through the J-integral), this does not represent the real fracture energy because of the dissipation[49]. One way to overcome this problem would be to include crack propagation analysis within the FE model through cohesive elements deployed ahead of the existing crack, so that the critical condition given by Eq.(4.4) is automatically verified by the cohesive law. Unfortunately, when we have tried to employ cohesive elements with coupled fluid-stress analyses, we could not obtain any acceptable result, probably due to the lack of a pore pressure variable in the formulation of the cohesive elements adopted. Interface elements with a dedicated pressure degree of freedom[179] might be considered in future analyses of poroelastic fracture.

With these limitations, what we present below are the results obtained from the FE analyses where the strain energy per unit of crack surface is computed from the J-integral in a contour surrounding the crack-tip region, and hence includes dissipation. In Fig.4.5a, the normalised J-integral in the crack-tip region is obtained at the constant stretch λ_0 for different strain rates. In Fig.4.5b we have considered the situation when $J = \Gamma_0$, and plotted the critical stretch λ normalised with respect to the quasi-static value λ_0. As expected, no difference with respect to the elastic quasi-static situation is observed in the gelatine, which therefore behaves as an elastic relaxed material. The situation looks different in the brain tissue, where both the strain energy and the critical stretch are affected by rate. Since J does not provide the correct value of the energy release rate $G(\dot{\varepsilon})$, we cannot consider these stretches as the real ultimate stretches of the material. However, our results point out the effect of fluid draining in the crack-tip region of porous materials with reduced permeability.

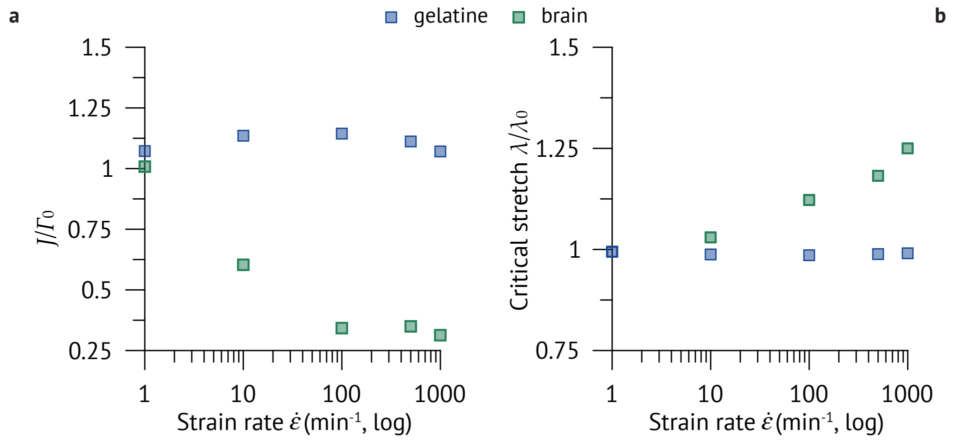

Figure 4.5 Fracture in a poro-hyperelastic material. **a** Strain energy per unit area in the crack-tip region, normalised by the fracture toughness Γ_0, and **b** applied stretch, normalised by the critical stretch in quasi-static conditions λ_0. Both are plotted as a function of the strain rate $\dot{\varepsilon}$ (logarithmic plot)

A direct confrontation with the experimental wire cutting is not viable. Firstly, brain tissue showed evident signs of viscoelastic behaviour during compression and indentation-relaxation tests[45,46], so that a contribution on the crack-related dissipative region coming from bulk viscoelasticity might also exist. This point is addressed in §4.4. Moreover, our analyses have considered the effect of the strain rate on the onset of crack propagation and not the relationship between the measured fracture toughness and the crack velocity during propagation, which is what it is normally measured in experiments[39]. It is reasonable to assume that the bulk behaviour is the same at the onset and during crack propagation (typically, once a crack is initiated it takes fractions of a second for tearing to complete[116]), particularly in pure shear specimens where the results are independent on the crack length. Still, we have no means of establishing an analytical relationship between the strain rate and the crack propagation velocity. As the mechanism of propagation is governed locally by the number of cross-links that fail in front of the crack tip, the obvious effect is that higher strain rates result in a faster propagation. However, this holds true below a certain limit, above which the crack velocity stays constant irrespectively of the strain rate[116]. It should also be noticed that the crack propagation velocity is not constant in a specimen of the type used in our analysis, whereas during steady-state cutting the crack velocity is controlled by the rate of insertion, and can be treated as constant.

4.3. Process zone model for biopolymeric gelatines

Although the numerical analyses employing the poro-hyperelastic model could not directly link fracture toughening to the crack propagation velocity, they seem to suggest that fracture of gelatines is not affected by rate. The reader might object that this is not consistent with the experimental wire cutting (Fig.4.2a), where the steady-state force (hence, the fracture toughness) seemed to increase with the insertion rate. Among the sources of energy dissipation in porous materials (§4.1.1), bulk viscoelasticity cannot be considered for gelatines, which show almost no sign of viscoelastic relaxation in compression and indentation tests, and loss angles measured from the rheometric curves are below 0.1 [44]. The only possibility is that rate-dependence is inside the local process zone. Here we recall a model of fluid draining of the process zone, which was presented in Forte et al. [44]. While the existence of a similar mechanism in the brain tissue, and possibly in other mimicking hydrogels, cannot be ruled out, this model is related to the specific rate-dependence observed in gelatines. An illustrative sketch is provided in Fig.4.6.

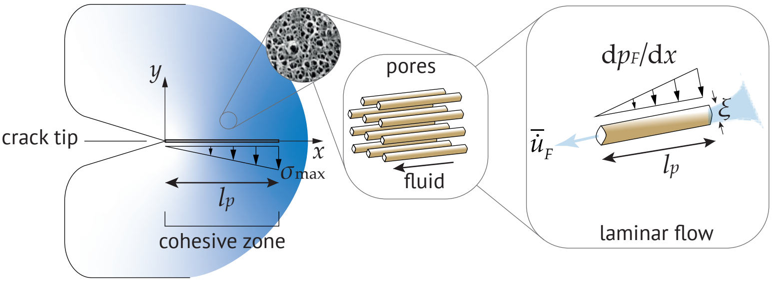

Figure 4.6 Sketch of the process zone model showing the rate-dependent cohesive zone l_p. During crack propagation, fluid flows through the circular pores of diameter ξ with a pressure gradient which is equal to $\sigma_{\max}/l_p$. The enlarged microstructure of a 10% w/w gelatine is adapted from Djabourov [36]

The model is based on the following assumptions:

- the process zone is drained by fluid flow in the pores of the solid matrix, which are considered as circular pipes of diameter ξ;
- the draining region is represented by a single pipe and assumed equal to a cohesive zone of length l_p;
- the flow of fluid is driven towards the crack-tip by the pressure gradient $-\mathrm{d}p_F/\mathrm{d}x$;
- steady-state conditions are assumed, so that the crack velocity v and the fluid average velocity $\bar{u}_F$ are equal;
- the cohesive stress $\sigma_{\max}$ and the fracture energy Γ change with rate but the crack-tip opening displacement δ_c is constant.

Under the assumption of plane strain conditions, the motion of fluid within the process zone is approximated with a one-dimensional laminar flow through a circular pipe of diameter ξ. The mean fluid velocity is

$$\bar{u}_F = -\frac{\xi^2}{32\eta_F}\left(\frac{\mathrm{d}p_F}{\mathrm{d}x}\right). \tag{4.17}$$

The fracture process is governed by a linear cohesive law within the process zone, relating the fracture energy $\Gamma(v)$ to the cohesive stress $\sigma_{\max}(v)$

$$\Gamma(v) = \frac{1}{2}\sigma_{\max}(v)\delta_c, \tag{4.18}$$

Table 4.2 Parameters of the cohesive zone model in quasi-static conditions

Variable	Gelatine (10% w/w)[44]
Cohesive stress $\sigma_{\max}$ (Pa)	$7.4 \cdot 10^3$
Fracture toughness Γ_0 (Pa m)	1.1
Cohesive critical displacement δ_c (mm)	0.30
Fluid viscosity η_F (Pa s)	$1 \cdot 10^{-3}$
Average pore size ξ (nm)	80

while the length of the cohesive process zone is given by[180]

$$l_p(v) = \frac{1}{6\pi} \frac{\Gamma(v) E}{\sigma_{\max}(v)^2}. \tag{4.19}$$

In steady-state crack propagation we assume that the total stress within the process zone is constant, $\sigma_{\max} + p_F = \text{const}$, so that the pressure gradient driving the fluid flow and the cohesive stress gradient are equal and opposite

$$\frac{\sigma_{\max}}{l_p} = -\frac{\mathrm{d}p_F}{\mathrm{d}x}. \tag{4.20}$$

Combining Eqs.(4.17)-(4.20) and assuming that the crack propagation velocity v is the same as the fluid mean velocity $\bar{u}_F$, we obtain the expression of the rate-dependent fracture energy

$$\Gamma(v) = \frac{4}{\xi} \left(\frac{E {\delta_c}^3 \eta_F}{3\pi} \right)^{0.5} v^{0.5}. \tag{4.21}$$

The previous equation describes a toughening power-law with the crack velocity, the value of the power being 0.5 which agrees with the experimental findings[44]. Figure 4.7 shows the fracture energy $\Gamma(v)$ in the gelatine 10% w/w, together with the size of the cohesive process zone $l_p(v)$. The relevant parameters are reported in Table 4.2, while the results are shown in Fig.4.7

It is evident that this model is incorrect below certain velocities (in the limit of $v \to 0$, one needs to recover the quasi-static toughness Γ_0). According to the poroelastic theory, at low crack velocities the size of the drained region R_d, Eq.(4.8), gets larger and completely surrounds the process zone, so that the fluid flow does not affect fracture (region A in Fig.4.7). We propose to correct the curves by considering the crack velocity at which $\Gamma(v) = \Gamma_0$, which for this material corresponds approximately to $v_0 = 3.5\text{mm/min}$. Below this value, the material is assumed to be in a drained state and the cohesive properties are those of the elastic material in quasi-static conditions. According to Eq.(4.19), increasing the velocity of crack propagation reduces the size of the cohesive process zone with respect to the quasi-static value l_{p0} (dashed line in Fig.4.7). In this range of propagation velocities, the flow of fluid in the pores explains the enhanced fracture toughness (region B in Fig.4.7). The phenomenon becomes inefficient when the size of the process zone is smaller than the characteristic size ξ of the polymeric material[148] (chain spacing), which sets an upper limit to the crack velocity.

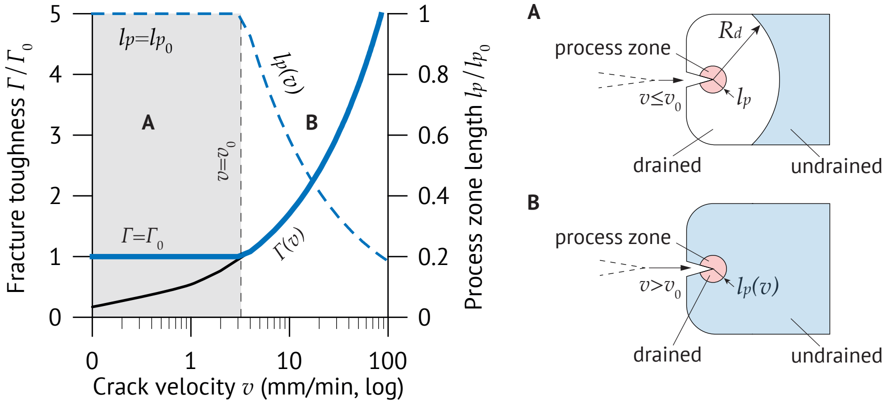

Figure 4.7 Rate-dependent fracture toughness $\Gamma(v)$ (thick line) and cohesive process zone length $l_p(v)$ (dashed line). The continuous black line is obtained from Eq.(4.21) when $v \leq v_0$. The shaded region in the plot shows the quasi-static condition (**a**) whereas the remaining part (**b**) is for velocities $v > v_0$ when the fluid draining mechanism is effective

4.4. On the effect of viscoelasticity

In the previous sections we have provided a theoretical and numerical explanation to the effect of fluid draining as a dissipative phenomenon in fracture of soft porous materials. We still need to discuss the role played by bulk viscoelasticity. In particular, human brain displays evidences of viscoelastic relaxation during compression tests and hysteresis when loaded and unloaded[45]. The contribution of viscoelastic relaxation during fracture might therefore be relevant.

4.4.1. Numerical analysis of viscoelastic fracture

We have performed FE analyses on the brain tissue using the same model shown in Fig.4.3 and described in Section §4.2.2. Although viscoelastic relaxation might be coupled with fluid diffusion, we have considered them separately in the numerical analyses. This choice was partly motivated by the will to separate the effect of different dissipative mechanisms on the fracture energy.

The visco-hyperelastic model

The model her employed is derived from the theory of viscoelasticity at finite strains (see the Appendix A.3). The instantaneous elastic response is assumed to follow the Ogden hyperelastic compressible model, Eq.(4.11). Stress relaxation is described by a generalised Maxwell model, given in terms of a normalised Prony series

$$g(t) = g_\infty + \sum_{i=1}^{N} g_i e^{-t/t_i}, \tag{4.22}$$

where g_i are the Prony constants, with g_∞ representing the long-term normalised shear modulus, and t_i are the relaxation times.

Table 4.3 Parameters of viscoelastic relaxation of human brain

Human brain tissue[30]					
g_1	g_2	g_3	t_1 (s)	t_2 (s)	t_3 (s)
0.6	0.1	0.16	0.5	20	200

Furthermore, we assume that only the deviatoric part of the stress is affected by relaxation. With respect to the reference configuration, the second Piola-Kirchoff stress tensor **S** is split according to

$$\mathbf{S} = Jp\mathbf{C}^{-1} + \bar{\mathbf{S}}, \tag{4.23}$$

where p is the hydrostatic pressure and $\bar{\mathbf{S}}$ is the deviatoric stress, defined in Eq.(A.57).

The deviatoric stress changes in time according to

$$\bar{\mathbf{S}}(t) = g_\infty \bar{\mathbf{S}}(t) + \sum_{i=1}^{N} g_i \bar{\mathbf{S}}_i(t), \tag{4.24}$$

where $\bar{\mathbf{S}}_i(t)$ is the deviatoric viscous stress in each term of the Prony series, according to Eq.(A.88).

Numerical results

The numerical analyses were performed using the commercial finite element software SIMULIA Abaqus 2017 (Dassault Systèmes[135]).

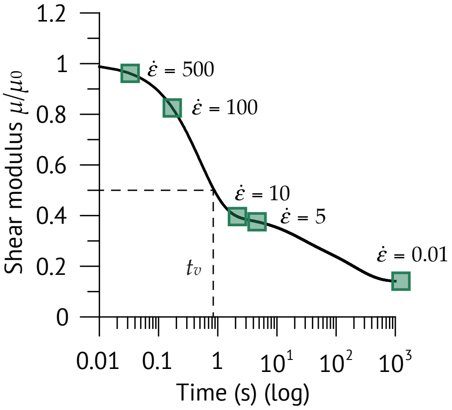

Figure 4.8 Relaxation of the shear modulus $\mu(t)$ with respect to the instantaneous modulus μ_0. The coloured squares are related to the brain tissue, with different strain rates $\dot{\varepsilon}$ (in min^{-1}). The characteristic times correspond to crack propagation in the FE analyses

A transient quasi-static analysis is required to simulate time-dependent material behaviour neglecting inertia effects. 4-node quadrilateral plane strain hybrid elements were employed for the bulk material. Boundary conditions were specified in terms of displacements (top and bottom forces are prevented from lateral motion). The viscoelastic properties of the material are taken from the experimental measures on human brain reported in Forte et al.[30]. The relaxation constants g_i and t_i, obtained by a third-order Prony series function fitting the rheological data, are shown in Table 4.3. The resulting variation of the shear modulus $\mu(t)$ is illustrated by the black line in Fig.4.8.

Following the same logic of the previous analyses with the poro-hyperelastic material, we have computed the J-integral in a contour surrounding the crack-tip dissipative region. The results are shown in Fig.4.9a and in Fig.4.9b, in terms of the ratios J/Γ_0 and λ/λ_0. At lower strain rates, it seems that the strain energy within the crack-tip region is modified with respect to the elastic reference case, but surprisingly this does not result in a substantial effect in terms of the critical stretch when $J = \Gamma_0$. We might need to explore the role played by stress relaxation, and to this purpose we have computed the times required to achieve the condition $J = \Gamma_0$ in the FE analyses. By plotting them on the relaxation curve of Fig.4.8, we can appreciate that the coloured squares corresponding to low strain rates ($\dot{\varepsilon} < 10\text{min}^{-1}$) fall in the region with $\mu/\mu_0 < 0.5$. In other terms, the material has a considerably lower shear modulus with respect to the elastic response. On the contrary, at higher strain rates the material complies to its instantaneous elastic behaviour, and it is reasonable to assume that the onset of crack propagation is not altered with respect to the elastic case.

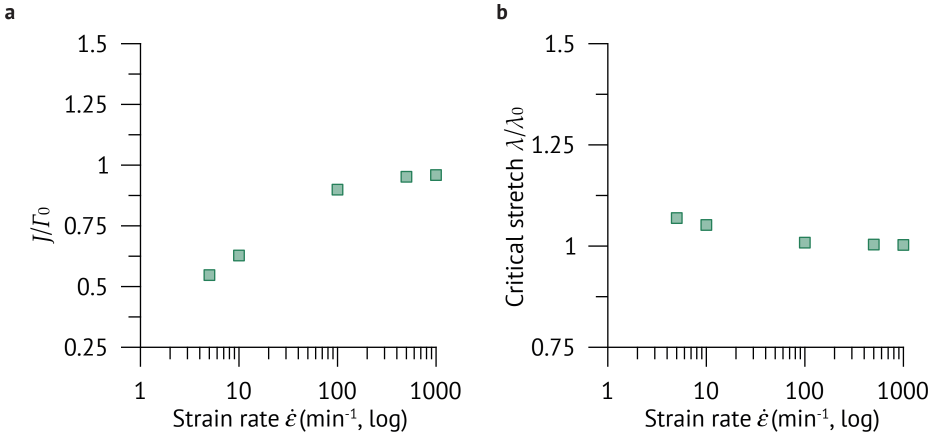

Figure 4.9 Fracture in a visco-hyperelastic material. **a** Strain energy per unit area in the crack-tip region, normalised by the fracture toughness Γ_0, and **b** applied stretch, normalised by the critical stretch in quasi-static conditions λ_0. Both are plotted as a function of the strain rate $\dot{\varepsilon}$ (logarithmic plot)

4.4.2. Interaction of viscoelastic and poroelastic relaxation

We have not performed FE analyses using a coupled poro- and visco-hyperelastic material model. Instead, we prefer to bring forward a physically based reasoning to explore the interaction of viscoelastic relaxation and fluid draining in the fracture process, each contribution being identified by a characteristic time. Viscoelastic relaxation results from conformational changes of the material network and is characterised by a time t_v which, contrary to the characteristic time of poroelastic relaxation t_p, is a material parameter. For instance, in a simple Maxwell model the time of viscoelastic relaxation is given as the ratio between the viscosity coefficient and the elastic modulus. Comparing the viscoelastic time with a typical observation time t we can distinguish two limit conditions: when $t \ll t_v$ the material is unrelaxed, whereas for $t \gg t_v$ relaxation is completed. In both cases, the material is elastic, although in the latter case the long-term modulus might be much smaller than the instantaneous modulus.

Let us introduce an observation time t and a characteristic length R. We still define t as the time measured from the instant of load application to the onset of crack propagation. The characteristic length R is the radius of the crack-tip dissipative region, Eq.(4.3) (Fig.4.1). If we compare the observation time with the viscoelastic relaxation time t_v and the poroelastic relaxation time t_p, Eq.(4.7), we can derive a qualitative chart of the interaction in crack propagation. The results are shown in Fig.4.10. A similar chart was developed by Hu and Suo[181] for general processes not related to crack propagation. The observation time t is compared with the viscoelastic relaxation time on the horizontal axis and with the poroelastic relaxation time on the vertical axis. According to our definition, t_p is the time needed to drain the crack-tip zone. The coloured bands are those where dissipation might affect the process of crack propagation, whereas in the corners we have the limiting conditions. In particular we can distinguish:

- $t \gg t_v$ and $t \gg t_p$ (V2-P2 in the chart): both the viscoelastic and poroelastic relaxation are completed when crack propagation begins. The material behaviour is elastic with the long-term modulus and drained conditions;
- $t \gg t_v$ and $t \ll t_p$ (V2-P1 in the chart): the viscoelastic relaxation is completed but poroelastic relaxation has not yet started when crack propagation begins. The material behaviour is elastic with the long-term modulus and undrained conditions;
- $t \ll t_v$ and $t \ll t_p$ (V1-P1 in the chart): both the viscoelastic relaxation and poroelastic relaxation have not yet started when crack propagation begins. The material behaviour is elastic with the instantaneous modulus and undrained conditions;
- $t \ll t_v$ and $t \gg t_p$ (V1-P2 in the chart): the viscoelastic relaxation has not yet started but poroelastic relaxation is completed when crack propagation begins. The material behaviour is elastic with the instantaneous modulus and drained conditions;

Some of the limiting conditions might be purely theoretical. To check the implications on real situations, we have explored the scenario in the brain tissue and in the biopolymeric gelatine. To this purpose, we have obtained the observation time t from the finite element analyses reported in the previous sections. The characteristic time of poroelastic relaxation t_p is obtained through Eq.(4.7), where R is computed in the elastic material through Eq.(4.3) and D_F is given by Eq.(4.16). In the brain tissue, the characteristic time of viscoelastic relaxation t_v is taken from the relaxation curve, as that corresponding to a reduction of 50 % of the initial modulus. From the Prony series (Fig.4.8), we find $t_v \simeq 1$s. We have not characterised the viscoelastic behaviour of the gelatine, but it is reasonable to assume its relaxation time t_v three orders of magnitude larger than that of the brain, so that the response is always elastic.

Six points are shown in Fig.4.10, obtained at different loading rates. Firstly, we observe that only one is related to the gelatine. Gelatines display an elastic behaviour with negligible viscoelastic effects. The rate-dependent failure observed in the experiments is due to the local process zone, whereas with respect to the bulk dissipation here considered they showed no effect. More specifically, they reasonably behave as elastic materials in drained conditions. With respect to the brain tissue we find five points at various strain rates falling within the plot. At low strain rates (green dot in the upper-right corner) the behaviour is elastic, with both viscoelastic and poroelastic relaxations completed at the onset of crack propagation. Increasing the rate of loading, crack propagation begins when both the relaxation processes are happening, and it is reasonable to assume that both result in energy dissipation affecting the crack-tip region.

The above discussion is grounded on the assumption that rate-dependence originates from bulk dissipation, and that a single relaxation time might describe the viscoelastic response. A more refined quantitative evaluation of the interaction of viscoelasticity and fluid draining is not

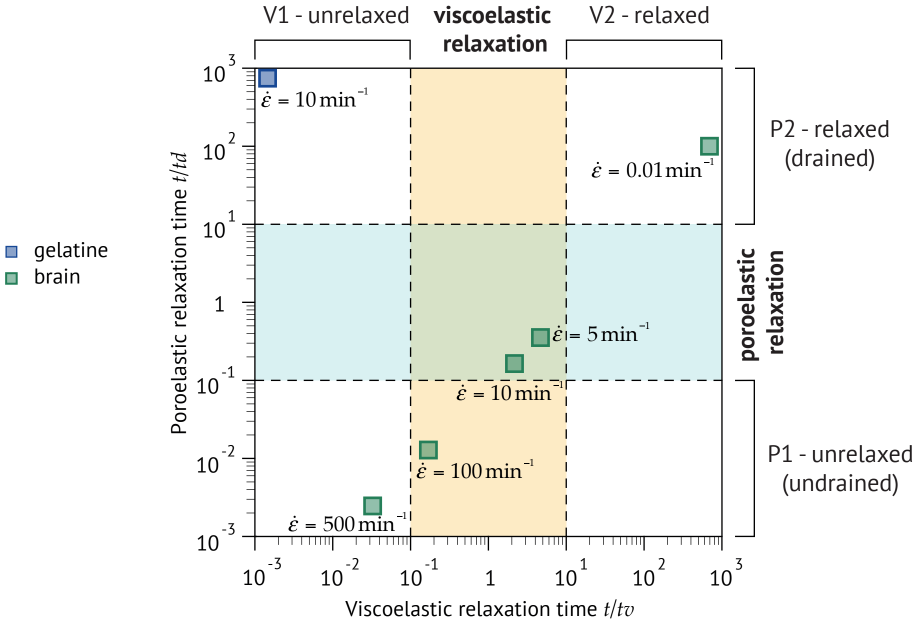

Figure 4.10 Graphic representation of limiting conditions and interaction in crack propagation of viscoelastic porous biomaterials, where both the time t_p for poroelastic relaxation of the crack-related zone and the time t_v of viscous relaxation are shown. The coloured dots are related to numerical results in the gelatine and the brain tissue. The strain rate $\dot{\varepsilon}$ (min^{-1}) is displayed below each dot

trivial. With respect to the role of fluid on the fracture process, we are confident that the poro-hyperelastic model implemented in the finite element analyses (Section §4.2.2) provides a reliable explanation of the fluid-induced toughening. The fact that poroelastic relaxation requires longer times with respect to viscoelastic relaxation has sometimes led to the conclusion that fluid draining can be neglected, at least for medium-high loading rates. While this holds true when considering the response of a material in compression, the characteristic length of the poroelastic process during fracture is much smaller. As a consequence, fluid draining might occur in times which are comparable to those typical of viscoelastic relaxation. With respect to the role played by viscoelasticity, it is not clear if neglecting the rate-sensitivity of the process zone is the more appropriate description of the viscoelastic behaviour during fracture. In other terms, while the relaxation observed in compression tests on human brain and similar mimicking hydrogels[45] is the result of bulk dissipation, crack propagation might require to consider ad-hoc models for the disintegrating material ahead of the crack tip[158]. This might help to explain while the numerical analyses did not provide any meaningful result with respect to the viscoelastic dissipation.

5

Detailed numerical analyses of cutting

I have been led to some elementary conclusions about research itself. Firstly, the fact that a theory appears to work does not mean that it is true. Secondly, even simple, carefully-selected, systems are often difficult to understand.

Alan N. Gent

Cutting simulations in complex materials, such as the biological tissues and mimicking compounds analysed in this thesis, requires refined numerical models capable of describing the material behaviour and the interactions with great accuracy[182–184]. Among several alternatives, high resolution finite element analyses can provide a reliable means to understand, analyse, and predict the processes occurring during indentation and cutting. In this chapter we consider two different problems, both of interest in the field of bioengineering, materials science and robotics: wire cutting and needle insertion in soft biological tissues. The results presented in this chapter are limited to the non-linear elastic behaviour without rate-dependence, due to the inherent complexities of numerical implementation.

A promising approach for accurate simulations of damaging and failure of materials, including biological tissues, is the cohesive zone model, used in combination with the finite element method[185,186]. There are two major techniques of implementing a cohesive zone in a numerical finite element model: a smeared approach and a discrete element-based one. The latter, which is adopted in this thesis, consists of inserting cohesive interface elements between the standard continuum elements. Since cohesive and regular bulk elements share common nodes, the damage process described by the cohesive model is coupled to deformation occurring in the bulk material[187]. Cohesive elements have been used extensively in delamination and crack propagation analyses, with specific techniques to allow for random propagation paths[188–190], and less frequently applied to cutting[191–194]. The purpose of §5.1 is to delineate the main features of the cohesive zone model, with emphasis on its application to cutting. We should also mention that many other computational techniques, dealing with damage and rupture of soft tissues, are available[195]: among them, the extended finite element method (XFEM)[196,197], meshless methods[198], CutFEM[199] and crack phase-field approaches (CPFA)[200]. Limitations exist when contact constraints, in the form of prescribed displacements, are enforced on the crack surface, as actually happens in cutting simulations.

In §5.2 we consider the problem of wire cutting in a soft elastic material. Cutting with a wire is part of the methods devised to reduce cutting forces and global deformation in the material, and is well-established in the food processing industry and to measure material parameters in soft materials[191] and biological tissues. Due to the reduced contact area offered by the wire, a significant drop of the cutting forces is obtainable with respect to the traditional techniques. The mechanics of wire cutting is simpler with respect to other techniques, therefore it is the best candidate to analyse and model the various stages occurring in the indentation and penetration of a soft material. Working within a two-dimensional framework, the initial deformation is followed by crack propagation driven by a symmetric opening mode, with limited effects of friction. Motivated by some experimental results of wire cutting on brain tissue and mimicking hydrogels[44,45], we have performed detailed FE analyses of the whole process. Firstly, we consider the indentation stage adopting a contact mechanics approach derived from the solution of a half-space with normal line loading[201]. The effects of large strain are observed in this and other indentation problems of highly compliant solids[70,96,202,203] and are discussed with respect to their role on crack initiation. The subsequent stage of crack propagation is treated with the cohesive zone model approach.

In §5.3 we consider the problem of deep needle penetration in a soft elastic material. Needle insertion is a common process in several fields of biology and medicine. Minimally invasive procedures are gaining widespread use in surgical applications, such as endoscopy, laparoscopy, percutaneous surgery and robot-assisted surgery. The small size of the incisions is possible thanks to the use of needles and catheters which are inserted in soft tissues. This has significant benefits, in terms of a reduction in the healing times, reduced risk of infection and a global containment of the overall cost of treatment and care. However, needle insertions in delicate organs need to be precise and accurate, and reaching a specific location may involve complex trajectories instead of straight paths. The solution comes from needle steering, which can be achieved through different techniques, including magnetic control, heating using optical fibres, external manipulation, pre-curved and nested cannulas, flexible devices with asymmetric tips[204]. A recent alternative consists in the so-called Programmable Bevel-tip Needles (PBNs), flexible probes possessing four interlocked segments and a bevel tip. Thanks to the asymmetric tip and a programmable offset between the segments, PBNs are capable of 3D steering in brain and similar mimicking materials[205–207]. Our purpose was to develop a refined algorithm to model the two-dimensional insertion of needles in soft materials, with an accurate description of the contact interaction and the damaging process. The main novelty is related to an iterative procedure to simulate crack propagation along unknown paths, which has allowed us to consider in detail the steering capability of PBNs. In addition, the technique provides an alternative to low resolution models of tool-tissue interaction[208–212], with cohesive elements used to model damaging and propagation in the soft tissue[213–215].

5.1. Modelling crack propagation with the cohesive zone model

The condition for crack propagation in cutting of elastic materials is formulated following the energetic approach presented in Chapter §2. As long as other sources of dissipation are neglected, cutting and crack propagation in fracture mechanics are energetically equivalent. The energy required for crack propagation in elastic materials is defined by the strain energy release rate G, that in the steady-state cutting is provided by Eq.(2.6).

Differently from standard fracture mechanics problems, cutting requires material failure to be captured in a way that enables tool-material interactions, taking into account not only the properties of the substrate but also the tool geometry. With respect to the mechanism of propagation, we have assumed that a fundamental role is played by the tip sharpness, related to a characteristic size of the tool. Focusing on the autonomous crack propagation, which happens in what we have defined blunt conditions (§2.2), a crack is propagated in front of the tool under a symmetric opening mode. Among the available numerical methods to simulate crack propagation, we focus on the Cohesive Zone Model (CZM), which is suitable for linear and non-linear materials and can be used in combination with the contact constraints imposed during cutting. A two-dimensional illustration of the CZM in a cutting problem is presented in Fig.5.1, where (n,t) characterise a local reference system centred at the crack tip.

According to cohesive models, the process zone is lumped into a line ahead of the crack tip and includes the damaging mechanisms through a stress-displacement relationship (Fig.5.1b). The size of the cohesive process zone l_{coh} in quasi-brittle materials is given by[180]

$$l_{\mathrm{coh}} = \frac{E\Gamma}{\sigma_{\mathrm{max}}^2}, \tag{5.1}$$

where E, σ_{max} and Γ are, respectively, the Young's modulus, the maximum cohesive stress and the fracture toughness of the material. An additional length l_{add} is embedded in the numerical formulation of CZMs, because a finite stiffness K prior to the onset of cracking is required for mathematical convergence. While of no physical meaning, an initial finite stiffness gives rise to elastic deformations which modify the system compliance[186].

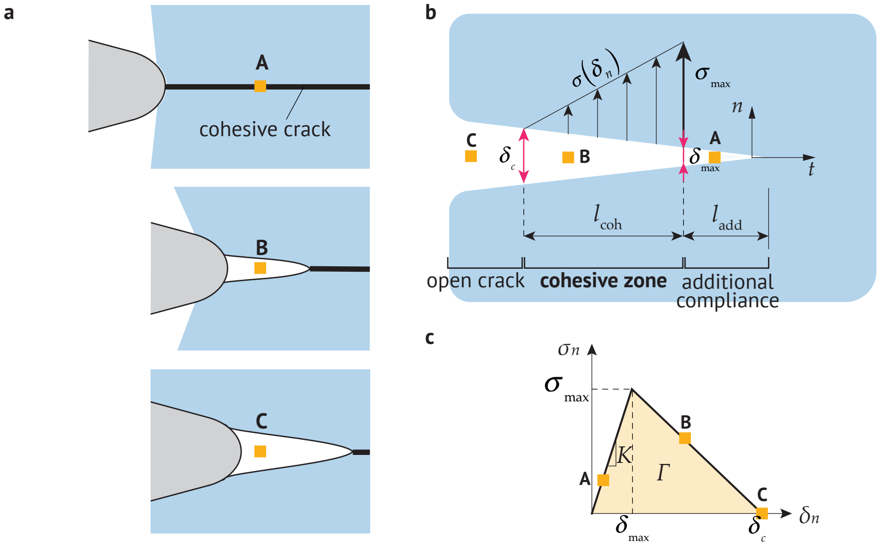

Figure 5.1 **a** The cohesive zone model applied to cutting. A single point on the crack line is shown in three consecutive stages of insertion. **b** Sketch of the CZM concept. The cohesive stress σ decreases from $\sigma_{\max}$ to zero along the process zone length l_{coh}, with the crack opening displacement δ_n rising from $\delta_{\max}$ to δ_c, at which the crack opens. The initial length l_{add} corresponds to an additional compliance introduced in numerical implementations of the cohesive model. **c** Bilinear cohesive stress-displacement relationship for quasi-brittle materials, which is assumed equal in both normal and tangential directions

The stress-displacement law relates the traction σ_n to the relative opening displacement δ_n between the upper and the lower crack surface (Fig. 5.1b). A similar relationship could also be employed for the tangential direction, in case that the material failure occurs with a shearing mechanism. The choice of a proper stress-displacement law depends on the type of damaging mechanism occurring in the material. In quasi-brittle materials, one of the most common is the bilinear model, where the onset of damage is followed by a linear softening down to complete failure (Fig. 5.1c). The stress-displacement relationship of the bilinear model, in both normal and tangential directions, is written as[216]

$$\sigma_i = \begin{cases} K_{ij}\,\delta_j & \delta_j \leq \delta_{\max} \\ \sigma_{\max}\frac{(\delta_c - \delta_j)}{(\delta_c - \delta_{\max})} & \delta_{\max} < \delta_j \leq \delta_c \\ 0 & \delta_j > \delta_c \end{cases} \qquad i,j = t,n\,. \tag{5.2}$$

The bilinear cohesive law has three independent parameters. Both the fracture energy Γ and the cohesive stress $\sigma_{\max}$ should be obtained from proper fracture experiments. The third parameter is the initial elastic stiffness K, which in principle should be kept as high as possible in order to minimise the effects of the additional compliance. The fracture resistance Γ represents the cohesive energy of the material and in the bilinear model it is given by

$$\Gamma = \frac{1}{2}\sigma_{\max}\delta_c. \tag{5.3}$$

With respect to a point ahead of the cutting tool illustrated in Fig. 5.1, initially the crack is closed and the relative displacement is null or limited to the fictitious elastic part (point A). Once that the stress reaches the tensile strength $\sigma_{\max}$, the crack is initiated and the softening part of the cohesive law describes the progressive damaging of the material (point B). Finally, when the critical displacement δ_c is reached the damage process is completed and the crack is fully open (point C). Notice that when we refer to the crack tip, we mean the point where $\delta_i \to 0$, not the point corresponding to δ_c.

5.1.1. Cohesive elements in finite element simulations of cutting

With respect to other available methods to simulate crack propagation, cohesive elements are versatile and easy to implement, since it is sufficient to define the stress-displacement law without any additional fracture criterion. There are, however, some specific aspects to consider when implementing the cohesive zone model to simulate a cutting process. Differently from a conventional crack propagation problem, cutting imposes additional constraints on the cohesive parameters. Specifically, the critical displacement δ_c is limited by a maximum dimension of the tool, for instance the diameter in wire cutting or needle penetration. Lacking this condition, one would simulate the unrealistic situation of penetrating into the material without achieving a complete cut. Moreover, there is one important limitation connected to the mechanics of indentation. When a tool is brought into contact and deforms the substrate material, a state of compression generally exists in the region immediately below. Standard normal cohesive laws describe a relationship between tensile stresses σ_n and opening displacements δ_b, therefore it is essential to ensure that the stress state is not compressive in front of the crack tip. For this reason, cohesive models cannot be used to simulate fracture initiation after the stage of indentation, unless an artificial tensile state is created in the material. In the analyses presented in this chapter, this is achieved through a small notch inserted at the point of contact of the tool with the material.

For a realistic simulation of crack propagation, cohesive elements need to be deployed along the expected path. When such path is predictable, as for instance in simple geometries or in delamination problems, cohesive elements can be pre-inserted between the bulk mesh elements. This solution is adopted in wire cutting simulations (§5.2). When the crack path is unknown a priori, a different strategy is required. Cohesive elements can be placed everywhere in the model so that the crack might follow the proper path of propagation. Downturns of this method are increased computational times, poor quality of the resulting crack constrained by the mesh boundaries and a remarkable reduction of the system stiffness[217]. Alternatively, cohesive elements are inserted adaptively based on a proper criterion[190]: this is the approach adopted in the simulation of needle insertion presented in §5.3.

One last point is related to the interaction between the cohesive elements and the cutting tool in simulations with very deformable materials. In particular, when the critical cohesive opening displacement δ_c is comparable to the characteristic size of the tool tip, the presence of the tool can interfere with the cohesive element and lead to imprecisions[218]. While this aspect has not been directly addressed here, we ensure that the minimum size of the tool tip is sufficiently large to keep the interaction minimal.

Table 5.1 Parameters of the hyperelastic model in the gelatine and the brain tissue/CH

Variable	Gelatine (10% w/w)[44]	Brain[30]
Shear modulus (Pa)	$6.21 \cdot 10^3$	$0.52 \cdot 10^3$
Ogden parameter α	2.64	-4.4
Poisson ratio	0.40	0.35
Ogden parameter D (1/Pa)	69	$1.3 \cdot 10^3$

5.2. Wire cutting in soft elastic materials

5.2.1. Numerical model of wire cutting

The analysis of wire cutting, involving deformation, friction and fracture, can be split in an initial stage of indentation followed by crack initiation and separation. A typical force-displacement profile begins with the force rising with increasing deformation until the point of failure, which corresponds to a peak followed by a sudden drop. Typical experimental curves were reported in Fig.4.2 on samples made of brain tissue and gelatine. Following the point of failure we observe that the force tends to stabilise at a constant value. The latter stage, denoted as steady-state cutting, involves crack propagation and is employed to derive the experimental measures of fracture toughness. In addition to numerical models of steady-state crack propagation, we have also considered the initial indentation in the sound material. We have built two different FE models to simulate the initial indentation (§5.2.2) and the subsequent stage of crack propagation (§5.2.3). Only a rate-independent analysis of elastic wire cutting is considered.

An illustrative sketch of the model geometry is shown in Fig.5.2a. The sample is a rectangular block of height h = 20mm, width w = 30mm and thickness t = 20mm. Rigid wires of various diameters d_w are inserted at low velocities, so that quasi-static conditions can be assumed. The depth of insertion is at least equal to $D = 10d_w$ and in any case enough for the achievement of the steady-state. Two different materials have been considered: an elastic gelatine and a sample of human brain tissue, both modelled as hyperelastic compressible solids. The model adopted is a one-term Ogden strain energy density, whose parameters were tuned on the results from compression tests on gelatine and human brain (see Table 5.1). The strain energy density function is given by[177]

$$W = \frac{2\mu}{\alpha^2}\left(\bar{\lambda}_1^\alpha + \bar{\lambda}_2^\alpha + \bar{\lambda}_3^\alpha - 3\right) + \frac{1}{D}(J-1)^2, \tag{5.4}$$

where $\bar{\lambda}_i$ are the deviatoric principal stretches, μ is the initial shear modulus, α and D are material parameters.

Finite element implementation

All the simulations are performed with the commercial FE software SIMULIA Abaqus 2017 (Dassault Systèmes[135]). We have considered a symmetric opening mode of crack propagation and plane strain conditions, which are justified if we take the wire length much larger than its diameter and the material transversal dimension. Four-node plane strain elements with reduced integration are employed for the bulk material, whereas the wire is modelled as a rigid surface. The indentation model is essentially a plane contact analysis at large strains, where we simulate the elastic deformation and stress concentration leading up to failure. Contact interaction is modelled with the implicit finite-sliding surface-to-surface formulation, based on contact pairs definition. Frictional interaction between the wire and the material is defined with a standard Coulomb law and implemented with a stiffness penalty method. The crack propagation model employs four-node cohesive elements, which are pre-inserted along the propagation path for the whole depth of wire insertion. As pointed out in §5.1.1, the cohesive model requires tensile opening stresses and for this reason we had to create an artificial notch on the top surface, without which the stress state below the wire is compressive (Fig.5.2b-c). We have tested different shapes and notch angles and found out that they only marginally affect the steady-state force. On the contrary, the force-displacement profile before crack initiation is inevitably altered.

Convergence of the combined contact-crack propagation problem was the most critical issue during the analyses. The initial large strain contact requires a regular and well refined mesh on the top surface where the wire is expected to indent the material. The minimum size of the elements with respect to the wire diameter, in the range $h_{\mathrm{el}}/d_w = 0.05 - 0.2$, was chosen as a compromise between accuracy and efficiency. In particular, this size is kept constant along the whole cohesive interface for smoother propagation, so that further increasing the mesh refinement led to prohibitive computational costs. Cohesive elements add additional complexity to the convergence due to the softening part of the stress-displacement curve. In order to speed-up convergence, time incrementation was tuned manually and larger-than-default tolerances on the force and displacement norms were required. We have tried small modifications of these parameters to check the reliability of the results.

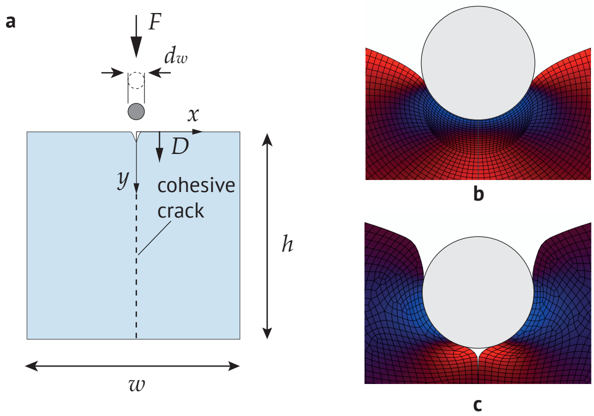

Figure 5.2 **a** Sketch of the plane model of wire cutting employed in the FE analyses. **b** Deformed configuration in the indentation model and **(c)** in the model for crack propagation. The normal opening stress contours are also shown (a blue region corresponds to compressive opening stresses σ_{xx})

5.2.2. Wire indentation

Let us consider the initial part of wire cutting, when the rigid wire indents the material. If we assume that frictional forces develop only during the stage of separation, this initial stage of indentation can be seen as a process of strain energy cumulation which eventually leads to failure.

In particular, from the energetic balance of cutting, Eq.(2.3), we have

$$F\mathrm{d}D = \mathrm{d}U_s, \tag{5.5}$$

where the term on the left is the work of the cutting force for an increment dD of wire insertion depth and dU_s is the strain energy variation in the elastic solid.

There are two key aspects to consider: firstly, what is the local stress state in the material during indentation, if we assume an elastic behaviour until the occurrence of failure. Secondly, we need to discuss the mechanism that generates fracture and how it is influenced by the tool geometry. Both these points are discussed here with respect to the specific geometry of wire cutting, but the results could be generalised to other plane problems.

Plane contact problem

We start by considering the problem of a thin wire which is pressed against a large elastic block under the action of a normal force, applied slowly enough so that quasi-static conditions are retained. Let the wire diameter d_w be the relevant size in this problem, which is much smaller than the wire length and the sample size. Then we can treat the block as an elastic half-space and assume plane small strain conditions, so that the solution is provided by the classical Flamant's problem[201] (Fig.5.3).

The stress at the point of load application is singular so that a proper stress function for this problem is given in polar coordinates (r, ϑ) as

$$\phi\left(r, \vartheta\right) = -\frac{P}{\pi} r\vartheta \sin\theta, \tag{5.6}$$

where $P = F/t$ is the load per unit wire length.

Using partial derivatives in polar coordinates we obtain the stress state of a generic point in the half space. In particular, the only non-zero stress component is

$$\sigma_{rr} = \frac{1}{r}\frac{\partial\phi}{\partial r} + \frac{1}{r^2}\frac{\partial^2\phi}{\partial\vartheta^2} = -\frac{2P\cos\vartheta}{\pi r}. \tag{5.7}$$

Into rectangular coordinates (x, y), the stress state at a point located at a depth c from the free surface is

$$\sigma_{xx} = \sigma_{rr}\sin^2\vartheta = -\frac{2P}{\pi c}\sin^2\vartheta\cos^2\vartheta, \tag{5.8a}$$

$$\sigma_{yy} = \sigma_{rr}\cos^2\vartheta = -\frac{2P}{\pi c}\cos^4\vartheta, \tag{5.8b}$$

$$\sigma_{xy} = \sigma_{rr}\sin\vartheta\cos\vartheta = -\frac{2P}{\pi c}\sin\vartheta\cos^3\vartheta, \tag{5.8c}$$

and the non-zero principal stress is

$$\sigma_1 = -\frac{2P}{\pi c}\cos^2\vartheta. \tag{5.9}$$

We can see that the principal stress is compressive everywhere and moreover the stress state is concentrated below the axis of loading and becomes vanishingly small moving away from the point

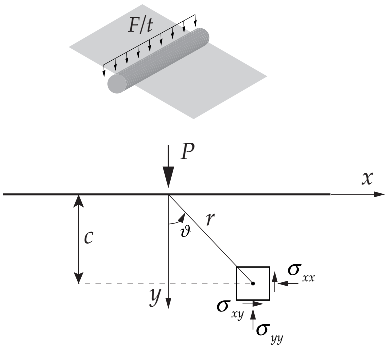

Figure 5.3 Schematic of the plane indentation of a rigid wire into an elastic material, which is treated as the line loading on an half-space, where $P = F/t$

of load application. This suggests that failure occurs with a compression mechanism that is highly localised, while the bulk material remains elastic and relatively little deformed. However, the effect of large deformation is not considered, and the contact mechanics solution requires the radii of the contacting bodies to be relatively well separated. These conditions fail when the penetration depth approximately exceeds the wire diameter d_w. In such a case, the principal stress becomes positive starting from the wire edges and shifting towards the middle with increasing loads[70]. This is confirmed from the results large strain numerical analyses, as shown in Fig.5.4.

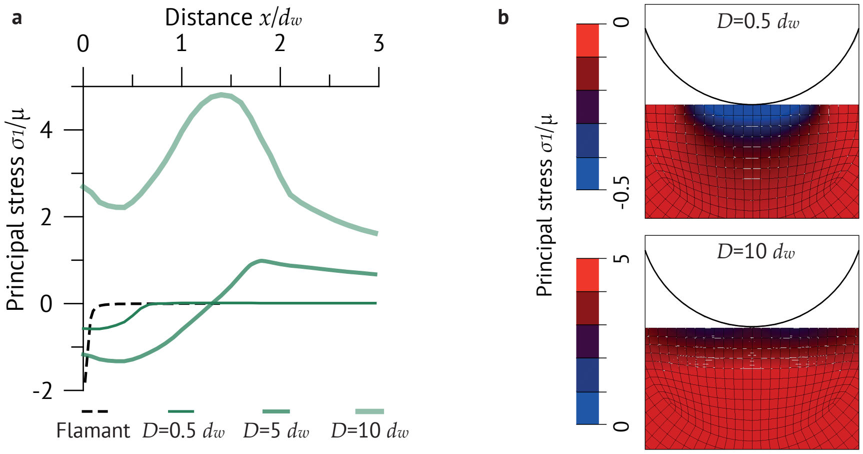

Figure 5.4 Indentation of a wire ($d_w = 1\mathrm{mm}$) into a compliant elastic solid. **a** Maximum principal stress right below the wire at different indentation depths. The dashed line is the analytical Flamant solution, Eq.(5.9), for $c = 0.01d_w$. **b** Contours from the large strain FE model (shown on the undeformed configuration)

What we notice from the numerical results is that the wire is required to indent deeply to reach a large tensile stress that can initiate a crack. This is considered to be a typical feature of the indentation of materials with low elastic modulus. Some authors have also modelled an additional action of slicing, which allows to reach the same critical stress at reduced indentation depths[70].

Initial indentation and the role of wire diameter

During the indentation stage, the deformation below the wire continues to increase until eventually a critical barrier is reached. At this point, a crack is initiated and the wire starts to cut through the material. In the experiments this moment corresponds to a peak in the cutting force, which is referred to as the critical force for puncturing P_c. In cutting of elastic materials, failure is a process where the only relevant dimension is a characteristic size of the tip. In the case of wire cutting here considered, such a dimension is the wire diameter d_w. We discuss here the results of large strain FE analyses, where we have changed the wire diameter over a wide range and observed how the force profile and the local region below the wire were affected.

In Fig.5.5 we show the cutting force F/t with wires of various diameters as a function of the relative indentation depth D/d_w. The results derive from the model of indentation at large strains, without any failure mechanism considered. With respect to the indentation depth, it seems that the force increases linearly in smaller wires but tends to follow a steeper gradient for larger diameters. This might be connected to the influence of the diameter on the elastic strain energy cumulated during the deformation. In the plots we have also included the value of the force when the wire indents the material for a depth $D = 10d_w$, which varies almost linearly with the wire diameter. The trend is confirmed in both materials, although the cutting force is almost one order of magnitude lower in the brain with respect to the gelatine. This agrees with the difference between the Young's moduli of the materials.

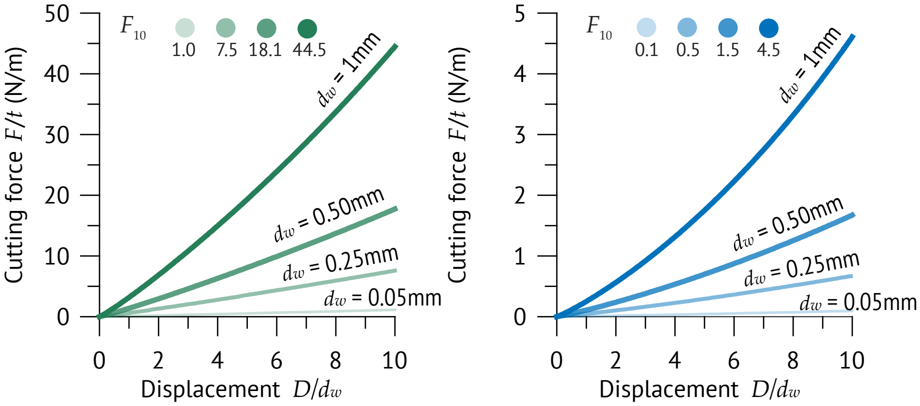

Figure 5.5 Indentation of a wire into a compliant elastic solid: cutting force F/t as a function of the indentation depth, in the gelatine (**a**) and the brain tissue (**b**). Also shown is the force when $D = 10d_w$ with different wire diameters

In order to understand the real influence of the wire diameter, we need to investigate failure. Crack initiation relies on the stress-concentrating capability of the indenter, that is, the local stress distribution in the material right below the wire. We have seen that it is quite complicated to predict the stress state in a very compliant material, therefore we do not investigate the stress distribution in detail. Instead, we focus on the cumulation of strain energy leading to crack initiation, which also depends on the wire diameter[96]. We can adopt an approach similar to those used for crack propagation, assuming that the volume of material whose strain energy participates in crack initiation is contained in a fracture process zone below the wire of length l_{coh}, Eq.(5.1). In the critical condition, the fracture initiation energy Γ_{in} is given by the strain energy per unit area $l_{\text{coh}}t$, whereas the force per unit area provides the critical stress σ_{in}. A recurring issue in fracture mechanics is how to define the fracture initiation energy and if it is related to the energy for crack propagation, what it is usually considered as the fracture toughness of a material. In our analyses we have assumed that Γ_{in} is equal to the fracture toughness Γ_0. Then we have computed the fracture energy from FE models in a contour surrounding the fracture process zone. However, in a purely elastic material the choice of the contour is not important. This approach is analogous to the J-integral computation, although in the absence of a crack it describes the simple cumulation of strain energy rather than a real fracture energy.

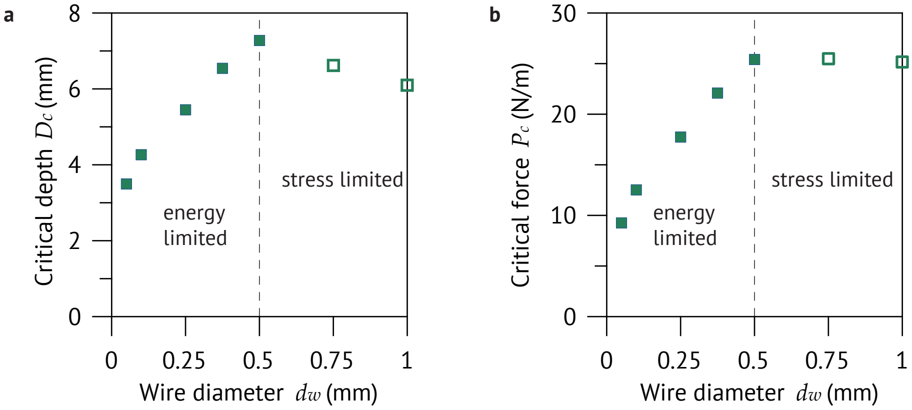

Figure 5.6 Crack initiation in the gelatine material. **a** Critical depth D_c and **b** critical force per unit thickness P_c as a function of the wire diameter

We show the results in Fig.5.6, in terms of critical depth D_c as a function of the wire diameter, in the gelatine material. The critical depth is obtained from the numerical analyses when the strain energy per unit area equals Γ_{in}. From the numerical analyses we could obtain the curves of the strain energy with respect to the insertion depth, with wires of various diameters. In order to find the exact value of D_c, we first interpolated each curve with a second-order polynomial and then extracted the exact value at Γ_{in}. The results of Fig.5.6a are illuminating in showing an evident transition in the critical depth for a specific wire diameter $\bar{d}_w$. Following Fakhouri et al.[96], we assume that the wire diameter affects the size of the fracture process zone, and in particular we distinguish the following two situations:

- when $d_w \leq \bar{d}_w$ the critical depth increases with a power-law dependence with the wire diameter. This is the so-called *energy limited* failure. At small diameters the stress is highly concentrated around the wire but failure cannot occur until there is enough strain energy in the fracture process zone, that is, until the strain energy per unit area reaches Γ_{in};
- when $d_w > \bar{d}_w$ fracture initiation occurs at an almost constant depth. This is the so-called *stress limited* failure. With larger wires, the process zone is larger too and so is the strain energy per unit area; however, failure requires that the local stress rises up to the initiation value σ_{in}.

Figure 5.6b confirms the transition with respect to the critical force, which increases almost linearly with the wire diameter in the energy limited region. To further validate our assumptions we would need experimental values of the critical force at crack initiation, in particular to check the fracture initiation energy that we have considered equal to Γ_0. Fakhouri et al.[96] obtained a higher value of Γ_{in} with respect to Γ_0 taken from a conventional fracture test. They motivated this difference as an increased energy needed to initiate a crack with respect to that needed in the stage of crack propagation.

5.2.3. Crack propagation in the steady-state

Following the point of failure, we assume that a crack is propagated below the wire in steady-state conditions under symmetric opening displacements. The fracture energy per unit of area is given by Eq.(2.6) of steady-state cutting, and assuming that the strain energy is negligible due to the small size of the wire we obtain

$$G = \frac{F}{t} - \frac{\mathrm{d}U_f}{t\mathrm{d}a} \tag{5.10}$$

Crack propagation is described by a cohesive zone model with a bilinear curve for the normal stress-opening displacement relationship. Reliable experimental values of the rate-independent fracture toughness Γ_0 and the cohesive stress σ_{max} derive from wire cutting experiments at low insertion rates and small diameters, as explained in §3.1. These were available for the gelatine[44] but not for the brain, which therefore is not considered in the simulations of crack propagation. The cohesive parameters are reported in Table 5.2.

Notice that the validity of the model is limited to the elastic behaviour of the material. In such framework, the critical condition for crack propagation is correctly defined by $G = \Gamma_0$. Moreover, crack propagation occurs under a symmetric opening mode only when the wire diameter is larger than a threshold value. An approximate value is obtained from the natural radius of an elastically blunted crack $\rho_c = \Gamma_0/E$, from which the threshold wire diameter is $d_w \geq 2\rho_c = 0.12$mm in the gelatine. As pointed out in the analysis of the crack-tip zone (§3.4), wire diameters smaller than the threshold exert a constraint on the elastic crack blunting. The cohesive zone model is feasible only when a crack propagates under tensile tractions, so the simulations are limited to wire diameters larger than the threshold.

Results obtained from the FE model are presented in Fig.5.7. The stress contours in the material near to the wire are shown at three different insertion depths (Fig.5.7a), for a wire of diameter $d_w = 0.5$mm. The normal opening stress σ_{xx} is tensile in front of the wire from the very beginning, as consequence of the artificial notch. After the indentation (B and C in the plots), the tensile stress ahead of the wire increases while the sides are compressed in the same measure, approximately two times the shear modulus of the gelatine. Due to this high compressive stress, it is reasonable to expect a relevant contribution of friction on the cutting force after the

Table 5.2 Parameters of the cohesive zone model in the gelatine

Variable	Gelatine (10% w/w)[44]
Fracture toughness Γ_0 (Pa m)	1.1
Cohesive stress σ_{max} (Pa)	$7.4 \cdot 10^3$
Cohesive critical displacement δ_c (mm)	0.30

initial indentation. Moreover, once that the steady-state is reached the stress distribution remains approximately unchanged for increasing depths. The force-displacement curves in Fig.5.7b have the typical shape of experimental wire cutting, with the initial increase followed by relaxation and the horizontal section of the steady-state. The values of the steady-state force are in the range observed during experiments on the gelatine at low rates of insertion[44]. However, the depth of indentation and the force drop following cut initiation are much smaller due to the artificial notch. With respect to the wire diameter, we notice that both the indentation force and the steady-state force increase at larger values. The latter seems to follow a linear trend with the diameter, although for smaller wire it deviates from linearity, contrary to what was noticed in the experiments (Fig.5.7c). At the moment of writing, the reasons of such a discrepancy remain unknown.

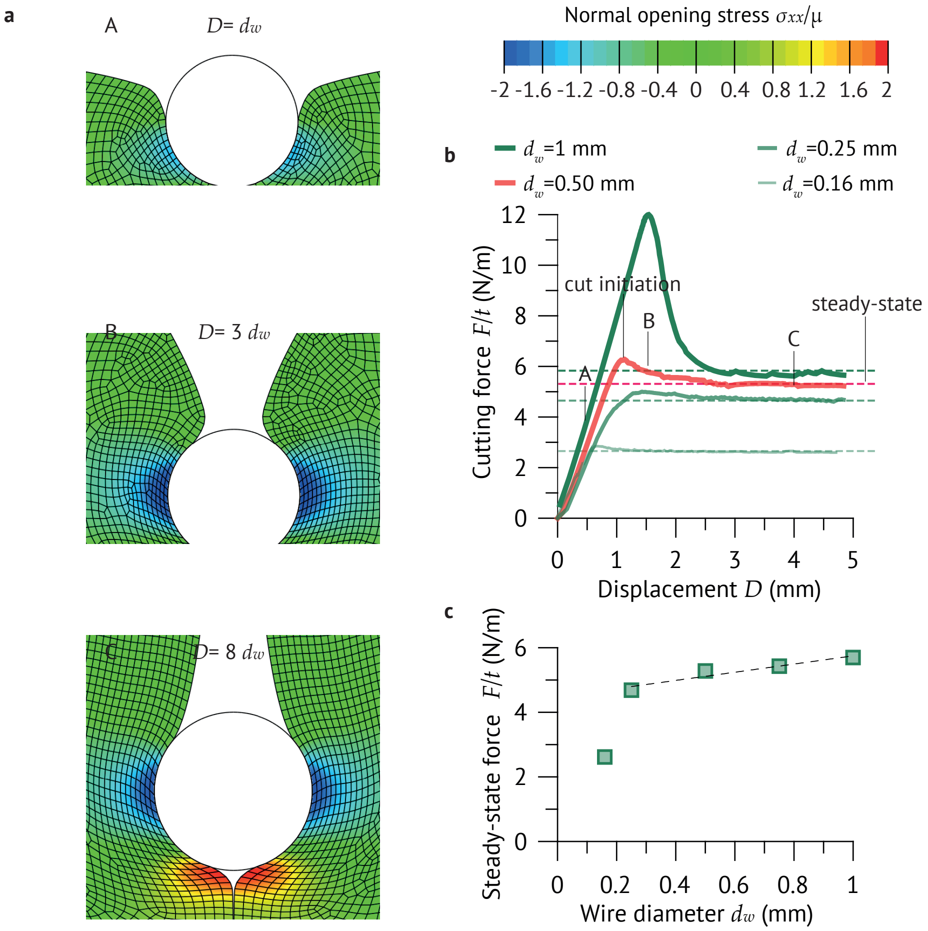

Figure 5.7 FE results of wire cutting in the elastic gelatine. **a** Normal opening stress contours at various depths, for a wire of diameter $d_w = 0.5\text{mm}$. **b** Force-displacement curves at various diameters. The dashed lines are the average steady-state cutting force. Letters and description are related to $d_w = 0{,}5\text{mm}$ (red line). **c** Steady-state cutting force as a function of wire diameter

5.3. Deep insertion of needles

In this section we present the detailed modelling of needle insertion in soft mimicking tissues, achieved through a finite element algorithm where the penetration path is obtained through consecutive insertions of cohesive elements[219]. It can be applied to needles of various geometries and materials, but here we have specifically considered the programmable bevel-tip needles (PBNs)[205–207]. The model is limited to a two-dimensional configuration. A sketch is shown in Fig.5.8a.

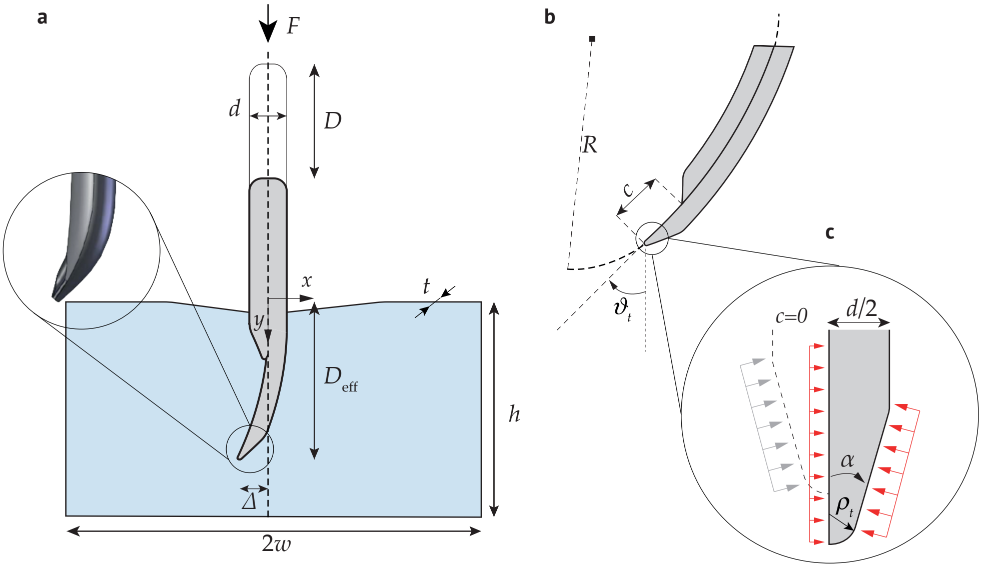

Figure 5.8 **a** Two-dimensional sketch of the needle insertion in a soft elastic tissue. **b** Enlarged view of the tip region, with the programmable offset c, the radius of curvature R and the tip angle ϑ_t. **c** Detail of the bevel tip with the asymmetric force distribution causing steering (the dashed configuration is for $c = 0$)

5.3.1. Mechanics of needle insertion

Deep penetration of needles in an elastic material is considered analogous to a cutting process and described adopting the energetic approach derived in Eqs.(2.1)-(2.6). Accordingly, we can distinguish three-main stages, which are listed below and shown in the schematic of Fig.5.9.

- *Initial indentation:* $W_{\mathrm{ext}} = U_s$
  The external work is converted into elastic energy due to the deformation of the material under the action of the indenter (region 1). The stage ends when the strain energy is sufficient to initiate a crack, at a critical depth D_c.
- *Cut propagation until full penetration:* $W_{\mathrm{ext}} = U_s + U_f + U_G$
  Once a crack is initiated, the external work is also consumed by frictional dissipation and work of fracture. A drop in the force is observed, due to a relaxation in the elastic strain

energy (region 2a) and the stage of stable crack propagation under increasing force begins (region 2b).

- *Sliding after full penetration:* $W_{\text{ext}} = U_f$
  When the needle has penetrated the material for the whole depth and breaks through the other end, another stage of relaxation is observed, with frictional work being the only contribution left (region 3).

Let us focus our attention on the stage of stable propagation, which according to the generic cutting model presented in §2.1 is described by Eq.(2.4). The relevant longitudinal extent of the needle implies that a great part of propagation occurs with increasing force. Indeed, when the needle is longer than the sample height h the steady-state cutting cannot be attained. When the needle is itself deformable, we might take into account its contribution to the energetic balance of cutting, through an elastic strain energy U_{sN} (due to axial and bending deformation). To a first approximation, we can correlate it to the difference between the imposed displacement D and the effective vertical displacement at the tip D_{eff}. Typically, during the experiments it is the vertical displacement D that is monitored, and only in the case of rigid symmetrical needles we can assume $D \simeq D_{\text{eff}}$ and $U_{sN} \simeq 0$.

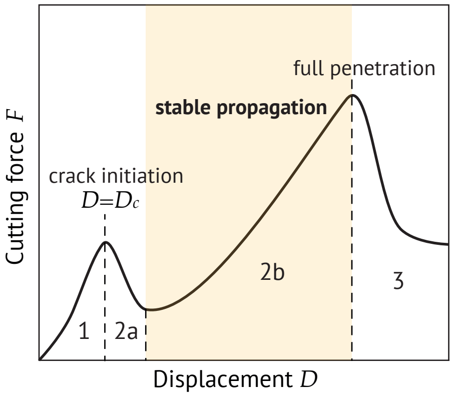

Figure 5.9 The main stages of through-and-through needle penetration into a soft elastic solid, where the needle is longer than the sample

Needle insertion is often treated as an axisymmetric problem with respect to the needle insertion axis, with fracture causing the formation of a ring crack[34]. However, the complex geometry of the PBN and the curved propagation trajectories might require a full three-dimensional model. We make a simplifying hypothesis to restrict the insertion process to the plane, so that we can adopt a two-dimensional plane strain formulation. The relevant sizes affecting the in-plane crack propagation and steering are illustrated in Fig.5.8b-c: these are the needle diameter d, the programmable offset c, the bevel angle α and the tip radius ρ_t. In general, needles advance into the target material propagating a crack under a combination of mode I and mode II fracture, with a tangential contribution coming from the sliding forces due to friction. Only if the tip is symmetric the opening mode I is predominant and the needle follows an approximately straight path. The first reason why needles with bevel tips follow curved paths is because of the asymmetric force distribution at the tip, as illustrated in Fig. 5.8c. In PBNs, the resulting tip deflection Δ and the radius of curvature R of the needle tip trajectory also depend on the offset c between the two segment pairs. In practice, this amount of unsupported length behaves as a cantilever beam.

5.3.2. Description of the finite element adaptive model

The simulation of deep needle penetration has been carried out with a finite element (FE) model. The propagation path followed by PBNs is not predictable a-priori: on the contrary, the path itself and its curvature constitute one of the major outputs of the analyses. For this reason, we have designed a specific iterative procedure to subdivide the insertion simulation in a number of steps, and insert cohesive elements to simulate an extension of the crack at each step. A detailed description of the algorithm is presented in this section and illustrated in Fig.5.10.

In summary, the iterative procedure consists of two main parts: the FE analysis and a stage of post-processing. Each iteration describes the penetration of the needle from the initial configuration ($D = 0$) to a certain displacement $D^{(i)}$. At this point, the FE analysis is interrupted because a further extension of the crack requires the definition of a new direction of propagation. During the post-processing, the local fields are employed to implement a proper fracture criterion proposed for mixed-mode propagation[213]. Subsequently, the mesh is updated in order to allow for the extension of the crack and to include new cohesive elements. We wish to point out that each iteration must start from the initial configuration ($D = 0$), because the insertion of new cohesive elements alters the global stiffness of the system. These steps are repeated until the planned depth of insertion is achieved.

Finite element analysis: initial mesh and solution

A finite element model of the initial configuration of the system is built, as shown in Fig.5.11a. Both the needle and the substrate are modelled with plane strain linear triangular elements, with refined areas in the contact regions. The minimum element size, in relation to the tip radius of the needle, was set to $h_{\mathrm{el}}/\rho_t = 0.5$. The element size and mesh configuration have been tested for convergence in comparison with considerably more refined meshes, in terms of the reaction force measured at the needle tip. A notch is introduced on the top surface, in order to give rise to a tensile stress state at the contact point and trigger the opening of the first cohesive elements (Fig.5.11b-c). The shape of this notch has been carefully designed with respect to the profile of the needle tip, and its effect was found to be negligible on the force-displacement profiles of the crack propagation stage and the resulting path of penetration. A radial mesh is designed around the initial crack tip, where the elements are employed to extract the internal fields needed to implement the fracture criterion in the post-processing stage. Triangular elements were adopted because of the excellent flexibility in meshing complex boundaries, although less accurate than higher order elements when used in regions with complex stress gradients. During the development of the algorithm, we have employed the freeware mesh generator DistMesh[220], which provides fast and accurate meshing tools within a Matlab environment.

Cohesive elements with zero thickness and a bilinear stress-displacement curve, Eq.(5.2), are employed to simulate crack propagation. In the case of the needle with the symmetric tip ($c = 0$), a line of ten cohesive elements with reduced strength is initially inserted along the needle longitudinal axis. With asymmetric bevel tips, only one cohesive element, aligned with the bisector of the bevel angle α, is inserted to facilitate the penetration. Boundary conditions are applied to replicate a typical experimental set-up as closely as possible. Specifically, the lateral surfaces of the substrate are constrained with respect to horizontal motion and the bottom nodes are restrained along the vertical direction. The needle is prevented from buckling by moving between two rigid vertical surfaces, which are fixed and frictionless. Vertical displacements are imposed on the top surface of the needle. A finite strain contact algorithm with Lagrange multipliers is employed to model the frictional interaction between the needle and the substrate. The full solution of the system is obtained using the large strain implicit solver of the commercial FE software SIMULIA Abaqus 2017 (Dassault Systèmes[135]). In each iteration, the FE analysis is interrupted when the penetration displacement $D^{(i)}$ of the needle is such that a critical condition is attained, and further displacement requires the computation of a new direction of crack propagation.

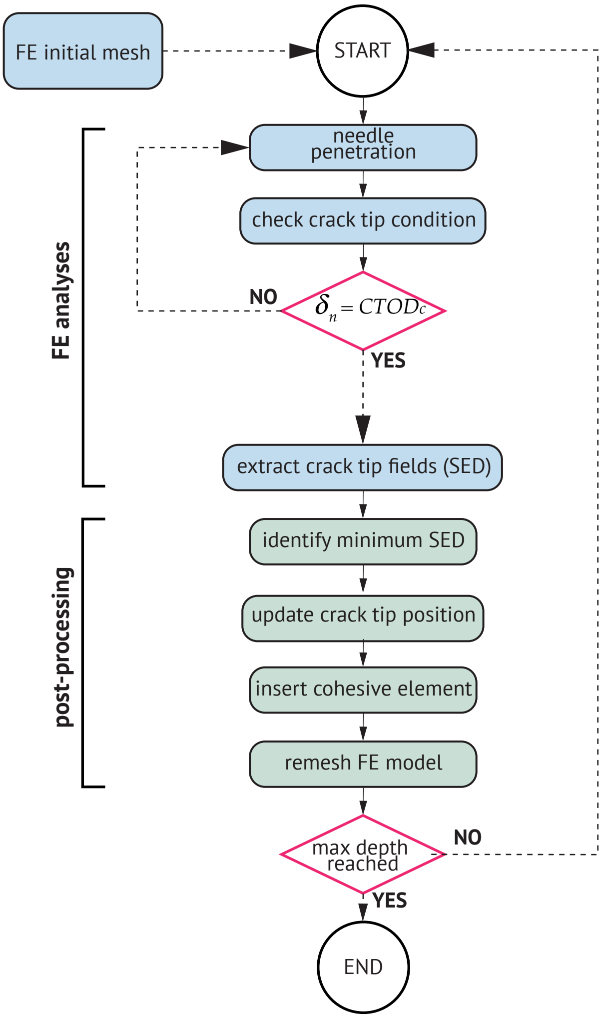

Figure 5.10 Flow-chart showing the key steps of the needle insertion algorithm. Each iteration is divided in the stages of FE analysis and post-processing

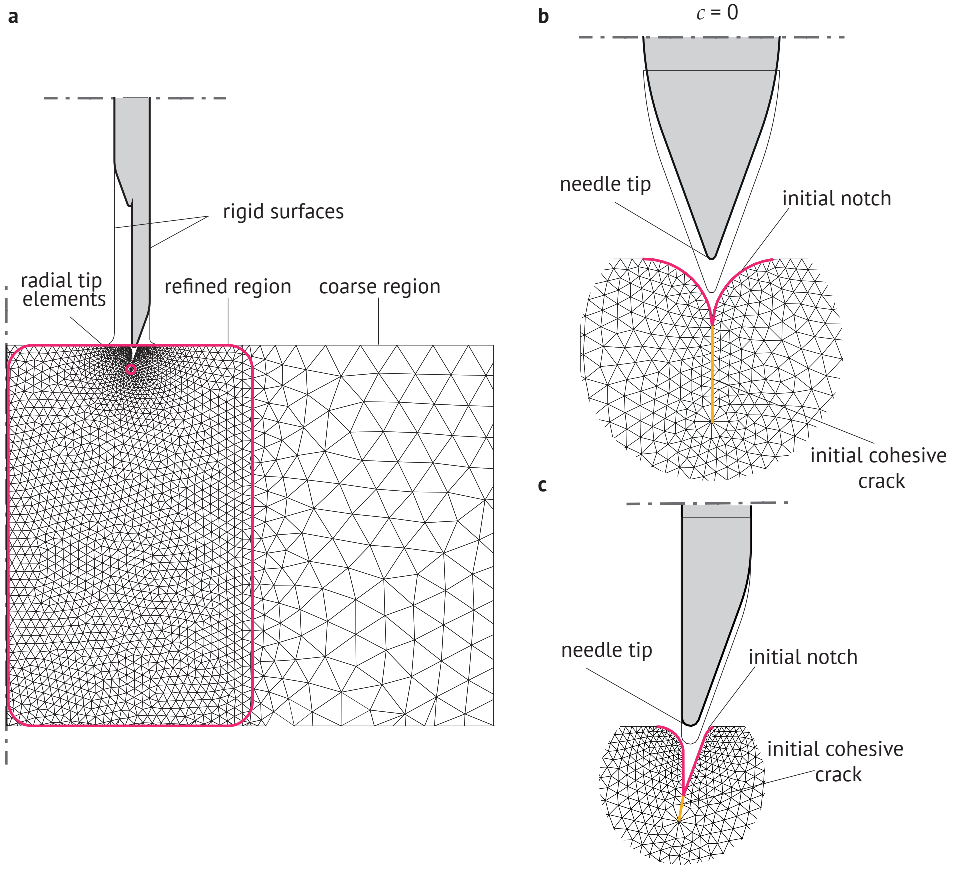

Figure 5.11 **a** General view of the initial configuration of the mesh (for clarity, the mesh of the needle is not shown). **b** Detail ot the near-tip region in the case of a needle with a symmetric tip ($c = 0$) and in the bevel-tip needle (**c**)

Post-processing: fracture criterion and re-meshing

When the needle is inserted into the material, existing cohesive elements are first damaged and then removed completely, allowing for an extension of the crack. However, to be displaced further the needle path needs to be determined and hence a proper fracture criterion is required. In particular, we should define both a critical condition for propagation and the crack kinking angle.

The fracture criterion is based on the crack-tip opening displacement (CTOD). This has been defined as the relative opening between the crack faces at a fixed distance $\bar{l}$ behind the current crack tip. Such distance is related to the material properties and the needle geometry (Fig. 5.12) through

$$\bar{l} = \frac{\rho_t}{\tan\alpha}, \tag{5.11}$$

where α is the bevel angle and ρ_t is the tip radius. As a reasonable assumption, we link the CTOD to the role played by the tip radius ρ_t in crack propagation by considering $2\rho_t = \delta_{\max}$. Equation

(5.11) is modified in

$$\bar{l} = \frac{\delta_{\max}}{2\tan\alpha} = \frac{\sigma_{\max}}{2K\tan\alpha}. \tag{5.12}$$

The critical condition is formulated as

$$\delta_n\left(\bar{l}\right) \equiv CTOD = CTOD_c, \tag{5.13}$$

where $CTOD_c$ is the critical crack-tip opening displacement. In this way we are indirectly relating the tip radius ρ_t to the cohesive law of the material. The importance of this step is peculiar of the simultaneous presence of cohesive elements and a cutting tool with unknown propagation path. With respect to other adaptive methods proposed for crack propagation[190], the use of a displacement-based parameter in place of an effective stress allows us to consider the relevant influence of the tip radius and sharpness on the condition of propagation (see §3.4).

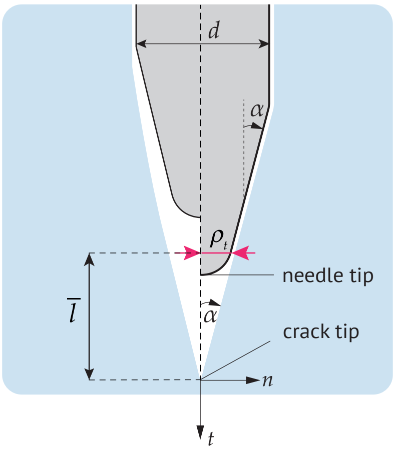

Figure 5.12 Schematic of the needle tip geometry to determine the length $\bar{l}$ and the CTOD

The crack propagation direction can be determined using different crack growth criteria. Specifically, various energy-based or stress-based approaches suitable for non-linear materials can be implemented in the algorithm[221]. Here we describe the minimum Strain Energy Density (SED) criterion[222], which employing the energy fields is less sensible to the error in the stress evaluation connected to the use of low-order elements. The kinking angle ϑ_c is found from the direction that minimises the strain energy density W

$$\begin{cases} \left(\frac{\partial W}{\partial \vartheta}\right)_{\vartheta=\vartheta_c} & = 0 \\ \left(\frac{\partial^2 W}{\partial \vartheta^2}\right)_{\vartheta=\vartheta_c} & \geq 0 \end{cases}, \tag{5.14}$$

where the second condition states that the point must be a point of minimum of the function $W(\vartheta)$.

During the post-processing stage, strain energy densities are extracted from the Gauss points of the ring elements and interpolated on an admissible angular range for propagation, based on the limit in pure-shear loading[223] (Fig.5.13a). Adopting an angular resolution of 1°, the angle corresponding to the local minimum of the SED is determined without any constraint on the existing mesh. Considering the SED contours illustrated in Fig.5.13b, we can appreciate the effect of the asymmetric tip with respect to a symmetric configuration. When the segment offset c is null, the force distribution on the needle is symmetric with respect to the insertion axis. The strain energy density distribution is also symmetric and the critical direction corresponds to a pure mode-I propagation. On the contrary, in bevel tip needles the SED contours are strongly asymmetric, reflecting the asymmetric distribution of the tip forces.

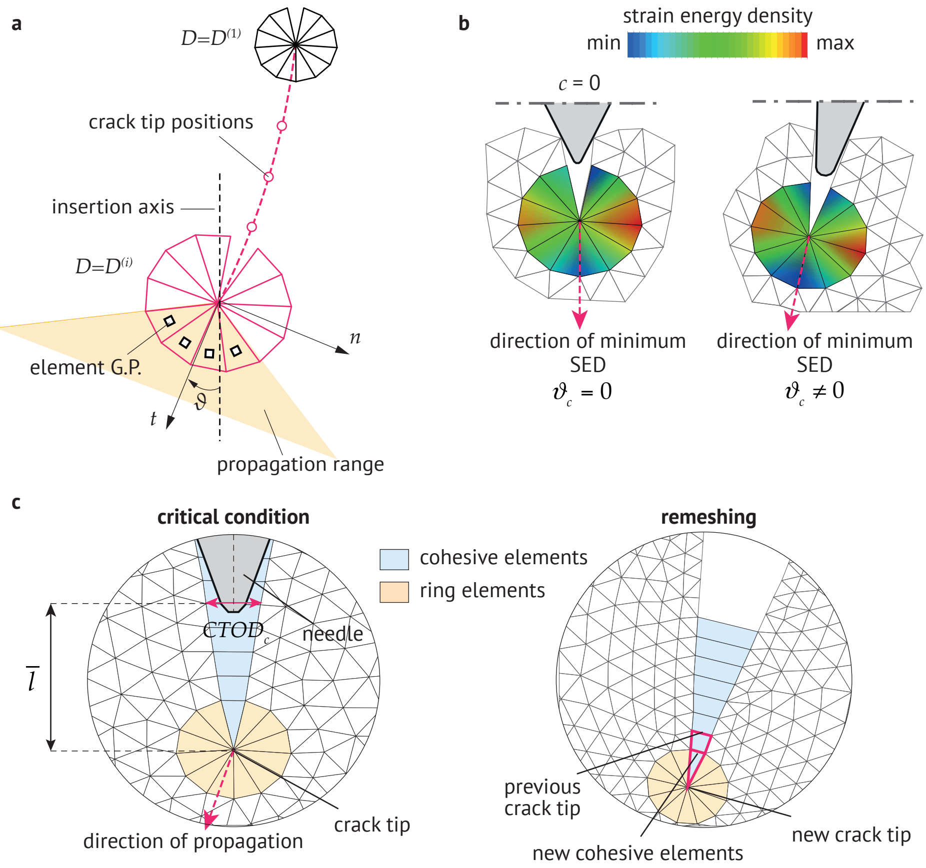

Figure 5.13 Illustration of the post-processing stage. **a** Implementation of the crack growth criterion, based on the local fields extracted at the Gauss points of the ring elements. The kinking angle ϑ is measured with respect to the needle insertion axis. **b** Schematic contours of the strain energy density in the ring elements, in the case of a needle with a symmetric tip $c = 0$ and for the bevel tip needle. **c** View of the crack-tip mesh at the onset of crack propagation and during the re-meshing stage, when new cohesive elements are added (for clarity, we show the deformed configuration)

Once that the kinking angle is determined, the surrounding mesh needs to be updated to include the new cohesive elements along the critical direction and adapt to the new position of the crack tip (Fig.5.13c). The ring of radial elements is shifted with the new crack tip and reoriented according to the kinking angle, so that two element edges are always aligned with the current direction of propagation. The path of propagation, i.e. the coordinates of the nodes along the crack path, are stored at each iteration for the next one, so that in the last iteration the needle travels along a defined path down to the prescribed depth. In summary, it is only the last iteration that we consider for the analysis output, with the propagation path determined by the increments in the crack length that occurred in all the previous iterations. The change of the system compliance due to the cohesive elements is minimised, although it is not completely avoided. What we have observed is a small difference in the slope of the force-displacement curves obtained from early iterations with respect to the last.

Table 5.3 Parameters of the model geometry and materials

Geometry	
Needle diameter d (mm)	8
Needle offset c (mm)	0-50
Bevel angle α (deg)	10
Tip radius ρ_t (mm)	0.5
Sample height h (mm)	245
Sample width $2w$ (mm)	235
Materials	
Needle Young modulus E_N (Pa)	$0.1 - 1 \cdot 10^6$
Gelatine Young modulus E_G (Pa)	$14.8 \cdot 10^3$
Poisson coefficient $\nu_\mathrm{G} = \nu_\mathrm{N}$ (-)	0.475

5.3.3. Results: force and steering prediction

The finite element model is based on the experimental setup adopted by Burrows et al.[224], where two adjacent segments of the programmable bevel-tip needle were advanced equally to create a fixed offset that was maintained throughout the experiment. The needle is inserted in a large rectangular block of soft gelatine with a concentration of 10% by weight, the same material employed for wire cutting simulations in §5.2 and in Chapter 4. To speed-up the analyses, gelatine was modelled here as a generalised linear elastic and nearly incompressible material, although the algorithm is equally valid for any non-linear elastic model. The needle is itself elastic and almost incompressible. The relevant parameters related to the geometry and the materials are summarised in Table 5.3. Contact interactions between the needle and the surrounding gelatine are represented by a coefficient of Coulomb's friction equal to $f = 0.3$, taken from similar cutting experiments[215]. Cohesive elements were assigned a bilinear stress-displacement relationship, Eq.(5.2), both for the normal and the tangential direction ($K_{ij} = K$ for $i = j$, with $i, j = t, n$), without any coupling ($K_{ij} = 0$ for $i \neq j$). The initial stiffness K was set three order of magnitude larger than the elastic modulus of the gelatine to minimise the elastic opening. The critical value of the CTOD was set equal to the displacement δ_max corresponding to the cohesive strength of the material. The cohesive parameters are summarised in Table 5.4.

Several analyses were performed, in order to predict the cutting force and the steering capability of the needle, and examine deformations and stresses caused in the substrate during the insertion. Each simulation was run sufficiently long to fully develop the condition of propagation and obtain a stable curvature of the penetration path (notice that the depth reached falls within the region 2b of Fig. 5.9). In the light of an optimisation of the needle design and insertion procedure, two parameters were changed between the simulations: the programmable offset c and the needle material, in terms of its Young's modulus E_N. A third parameter, the bevel angle α, is also known to affect the cutting force[192] but is not addressed, since the focus was the peculiar steering mechanism of PBNs. The main results are presented and discussed below.

Table 5.4 Parameters of the cohesive model

Variable	*Value*
Fracture toughness Γ_0 (Pa m)	1.1
Cohesive stress $\sigma_{\max}$ (Pa)	$1.5 \cdot 10^3$
Cohesive displacement $\delta_{\max}$ (mm)	1.0
Cohesive critical displacement δ_c (mm)	1.5
Initial stiffness K (Pa/m)	$1.5 \cdot 10^6$

Symmetrical needle configuration

A symmetrical needle configuration, obtained by setting the offset c to zero, is initially considered. As already observed, a symmetric needle under the action of a vertical force propagates a crack in pure mode-I, therefore the penetration path consists of a straight line along the insertion axis. This configuration is employed to test whether a straight path could also be achieved with the iterative algorithm.

The cutting force, derived from the reaction force extracted from the top nodes of the needle, is plotted against the applied displacement D in Fig.5.14a. The needle was inserted for a total displacement $D = 65$mm but we notice that after approximately $D = 20$mm the stable propagation is achieved. In this configuration, the initial deformation is relevant and the peak force is followed by a sudden drop corresponding to the crack initiation. In Fig.5.14b we might appreciate that the path is a straight line as expected, although at a closer look there is a minor bend to the right, probably due to small inaccuracies in the numerical approximation. The contours of the normal opening stress σ_{xx} (normalised by the shear modulus μ) reflect the symmetry of the cutting process (Fig.5.14c). During the stage of propagation there is a localised region of compressive stresses, of magnitude comparable to the elastic modulus of the material, at the transition between the tip and the needle shaft. Ahead of the needle, a symmetric tensile region ensures that the path propagation follows the needle insertion axis.

In Fig.5.15 we show the contour plots of the nominal strain in the region surrounding the needle tip, when $D = D_{\max} = 65$mm. The asymmetric behaviour is again dependent on minor imprecisions affecting the algorithm at deep insertion lengths. Figure 5.15a is related to the opening strain ε_{xx}, which as expected is tensile ahead of the crack tip while it is compressive near the edges. In Fig.5.15b we show the effective stress, a measure often associated to damage in biological tissues[46], which is defined as

$$\varepsilon_{\text{eff}} = \sqrt{2/3\,(\varepsilon_{\max}^2 + \varepsilon_{\min}^2)}, \tag{5.15}$$

where $\varepsilon_{\max}$ and $\varepsilon_{\min}$ are, respectively, the maximum and minimum principal strains. The largest value, not exceeding 20%, provides good arguments for our assumption of a generalised linear material, as it is reasonable to consider the difference with other more refined hyperelastic formulations to be negligible.

Force-displacement curves

The offset drastically modifies the insertion process, and this is reflected in both the force-displacement curve and the stress state surrounding the needle. Figure 5.16 illustrates the results for a PBN, with offset $c = 32$mm and stiffness ratio $E_N/E_G = 16$, where E_N and E_G are, respectively, the needle and gelatine Young's moduli. Each simulation with the PBN was carried on until $D = 2c$, a length which we have considered sufficient to develop stable propagation and attain a stable curvature of the propagation path.

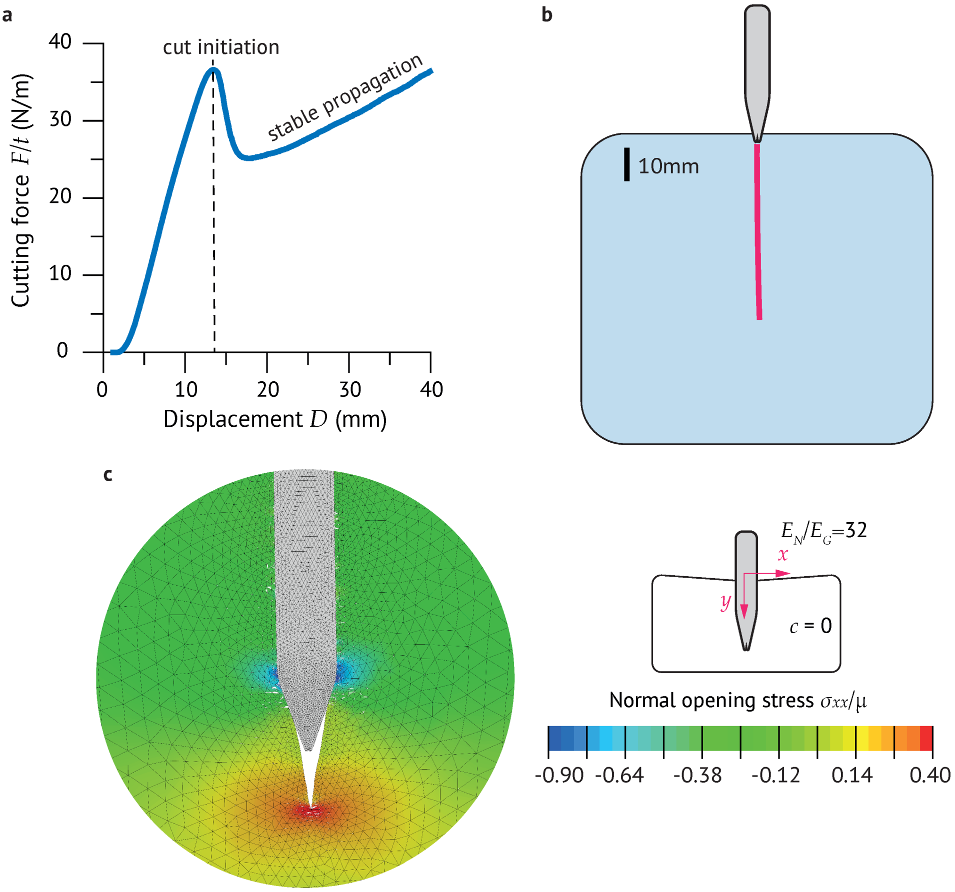

Figure 5.14 Needle in the symmetric configuration ($c = 0$, $E_N/E_G = 32$). **a** Cutting force as a function of the imposed displacement D. **b** Schematic showing the penetration path. **c** Contours of the normal opening stress σ_{xx}/μ at the maximum depth of insertion $D = 65\text{mm}$

Compared to the overall characteristic shape of the symmetric needle insertion, the force-displacement curve in Fig.5.16a shows additional detailed features. The shape of the initial notch in the gelatine mesh (Fig. 5.11c) is in this case responsible for the lack of an evident indentation stage. After an initial linear increase of the cutting force, the small relaxation corresponds to the completion of the bevel penetration. The curve now enters a first stage of stable propagation, in which a crack is propagated ahead of the needle tip. The length of this stage is determined by the offset c and ends when the offset has penetrated for its whole length, i.e. when $D = c$. The subsequent part is peculiar of the PBN insertion. When the thicker part of the needle begins to enter into the material, the cutting force rises with a steep gradient to a maximum, corresponding to the complete tip-shaft transition. Afterwards, a strong relaxation is followed by a second stage of stable propagation, which is believed to continue with increasing force until full penetration.

The transition from the needle tip to the thicker shaft is the most critical aspect to consider, in terms of deformations and stresses induced in the material. In Fig.5.16b we take a closer look to

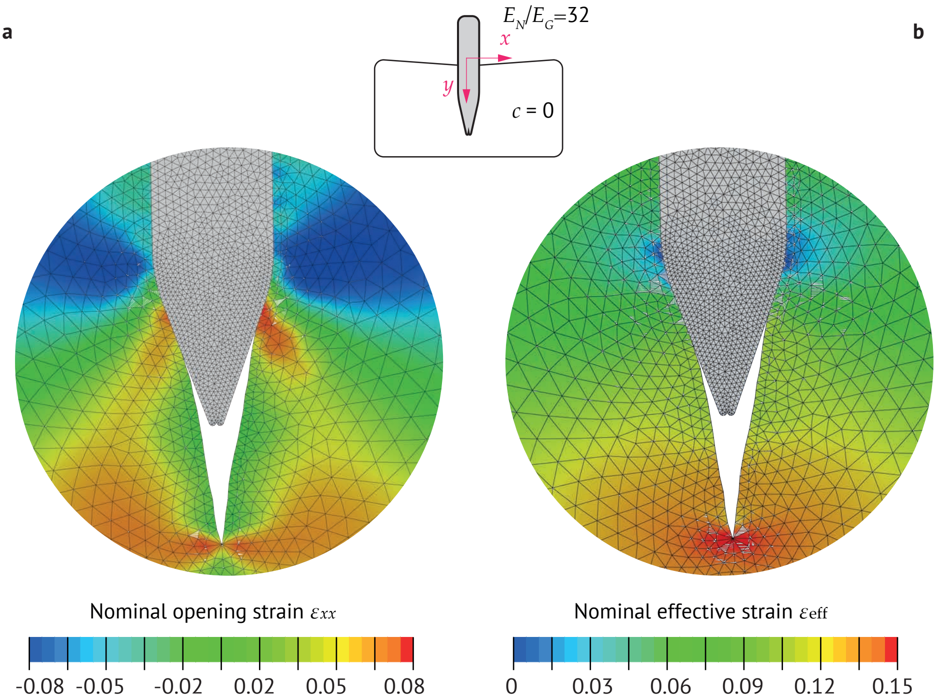

Figure 5.15 Needle in the symmetric configuration (c = 0, E_N/E_G = 32). **a** Contour plot of the nominal opening strain ε_{xx} and **b** and of the effective strain $\varepsilon_{\mathrm{eff}}$

the normal stress σ_{xx} in the material surrounding the needle, during three consecutive stages of the insertion (which are also indicated with numbers on the force-displacement curve). The tensile stress state ahead of the needle tip is similar in the three frames, and the largest value is of the same order to that observed in the symmetric configuration (Fig.5.14b). However, the distribution is strongly asymmetric, reflecting the uneven forces acting on the needle tip. A closer look to the compressed regions provides an insight into the effect of needle insertion, which could not have been possible with other less refined simulations. For the part of propagation in which only the tip with the offset is inserted, a compressed region with stresses in the order $0.5 - 0.7\mu$ exist near the tip-bevel transition. Comparing frames 1 and 2 in Fig.5.16b, it appears that the stresses tend to relax with ongoing penetration. In the third frame we focus on the critical point corresponding to the peak cutting force. Here the region of compressive stresses is located on the side of the thicker section of the needle. Such a high compression, together with the resulting frictional stresses, is feature which needs to be considered carefully with respect to possible damages in the tissue.

Other results are shown in Fig.5.17, where the force-displacement curves are obtained from the insertion of needles with different offset lengths c and various ratios of the relative stiffness E_N/E_G. The bold numbers in the figures are related to the three stages considered in Fig.5.16. Notice that the displacement D is normalised with respect to the offset, a choice adopted to obtain a clearer view of the results. With respect to the needle-gelatine stiffness ratio, (Fig.5.17a) the effect is rather limited: the curves are simply shifted upwards with stiffer needles. The effect in early stages (points 1-2) is totally negligible but becomes more evident with ongoing insertion; however,

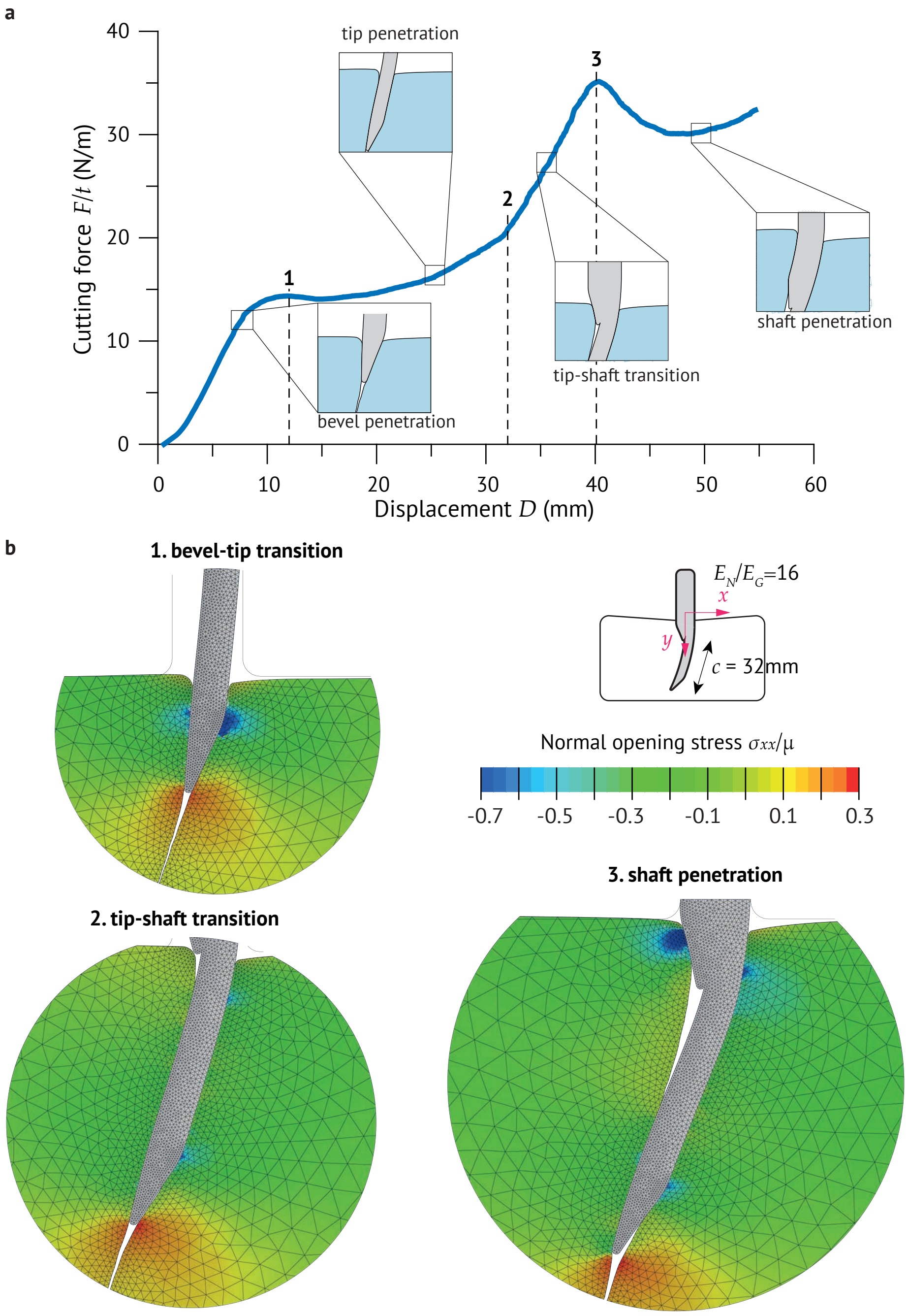

Figure 5.16 Programmable bevel tip needle ($c = 32\mathrm{mm}$, $E_N/E_G = 16$). **a** Cutting force as a function of the imposed displacement D. Insets on the plot are taken from the FE model. **b** Contours of the normal opening stress σ_{xx}/μ at three different insertion depths D

at the moment of shaft penetration (point 3) an eightfold growth of the needle Young's modulus results in a mere 40 % increase in the cutting force. This point corresponds to approximately $D/c \simeq 1.3$. In Fig.5.17b we show the effect of the offset, at a constant stiffness ratio $E_N/E_G = 16$. Contrary to the previous case, now the curves are also translated horizontally. The cutting force is almost unaffected by changing the needle offset, with only minor differences in the slope with respect to the relative displacement. It appears that the cutting force may not be the most pertinent variable to monitor when optimising the design of PBNs. Instead, we should consider the effect of the same parameters on the propagation path.

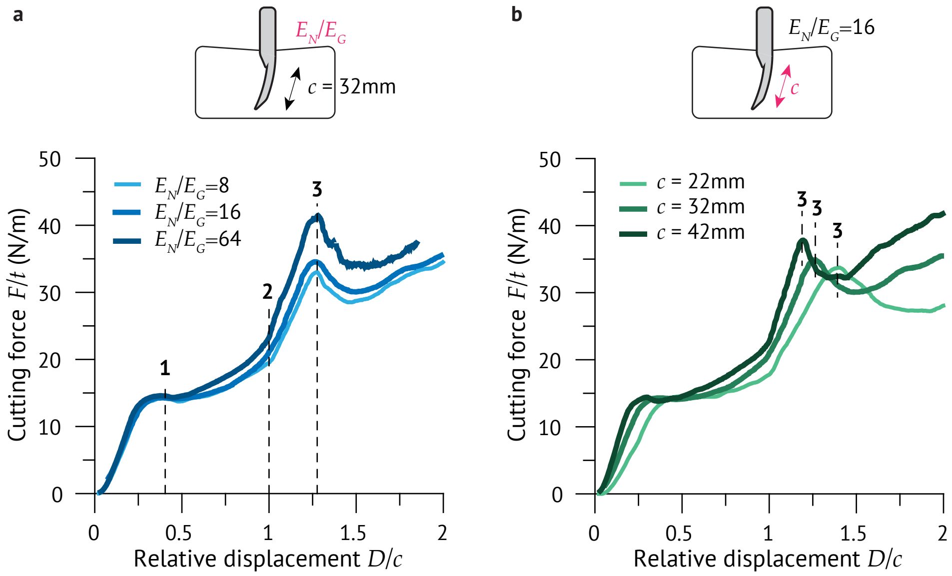

Figure 5.17 Force–displacement curves of the programmable bevel tip needle. **a** Effect of the stiffness ratio E_N/E_G, at constant offset $c = 32\text{mm}$. **b** Influence of the offset c, at constant stiffness $E_N/E_G = 16$. Dashed lines and numbers are related to three relevant stages of the penetration

Needle path and curvature

The main feature of PBNs is the curved propagation path followed by the needle during the insertion, which can be controlled by the programmable offset c. During the simulations, we have recorded the trajectory taken by the needle tip node. The examples shown in Fig. 5.18 are obtained from the last iteration of each simulation, when the imposed displacement reached the maximum depth $D_{\text{max}} = 2c$. It seems that the needle follows an initial linear path before the occurrence of a deflection point, after which the trajectory assumes a slightly higher curvature.

This fact is further confirmed in Fig.5.19, where the effective tip displacement D_{eff} is plotted against the tip deflection Δ, both normalised with respect to the offset c. Specifically, these plots explore the influence of the offset c and the relative stiffness E_N/E_G, and reflect the force-displacement curves presented in Fig.5.17. Figure 5.19a shows the needle paths for $c = 32\text{mm}$ and different values of relative stiffness. The deflection (point D) is observed in all the cases considered at the same relative depth $D_{\text{eff}}/c \simeq 1.25$. On the contrary, when different offsets are considered (Fig.5.19b), the same point is noticed at various depths. This point corresponds to the completed

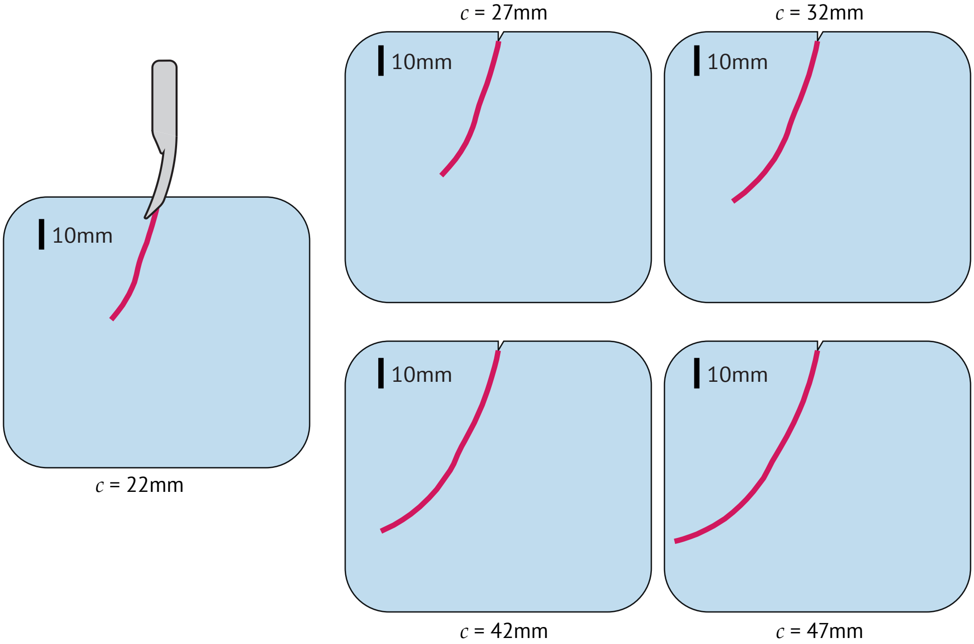

Figure 5.18 Paths of PBNs with different offsets c. The red lines are the paths taken by the needle tip node at completed penetration $D = D_{\max}$

transition from the needle tip to the thicker shaft (point 3 in Fig.5.17), with an increase in the bending stiffness of the needle.

A better insight is gained if we consider the curvature $1/R$ of the needle path, calculated from the trajectory followed by the needle tip node. The presence of a deflection point, which is not easily detectable during the experiments, suggests that there is a transient stage during the insertion. In other terms, the evolution to a stable and constant curvature might require a certain depth to complete. We have obtained the radius of curvature R from the best fitting circle to the needle trajectory, estimated using a hyper-circle algorithm[136]. The results are illustrated in Fig.5.20 for three simulations with different offset c and same stiffness ratio. To smooth out the resulting trends, we have applied the hyper-circle fitting to a depth span of 5 mm. It is found that initially the curvature decreases sharply, until the needle has penetrated for a length approximately equal to the offset c. More importantly, the curvature appears to reach a minimum value at $D \simeq 2c$ before attaining a stable trend. It appears that the curvature starts to increase again at deeper penetration but this aspect has not been explored during the simulations because of prohibitive computational costs. Moreover, it might be that the the behaviour depends on the effect of free boundaries and a reduced system compliance when the cohesive elements increase in number. In all the simulations, the points are approximately fitted by a power-law decreasing curve (dashed lines in Fig.5.20). Here, we retain that the curvature $1/R$ when $D = 2c$ is the stable value to consider.

The stable curvature is plotted against the stiffness ratio E_N/E_G in Fig.5.21a and as a function of the offset c in Fig.5.21b. Additionally, we also provide the value of the tip angle ϑ_t formed by the local tangent direction and the needle insertion axis, computed from the first derivative of the

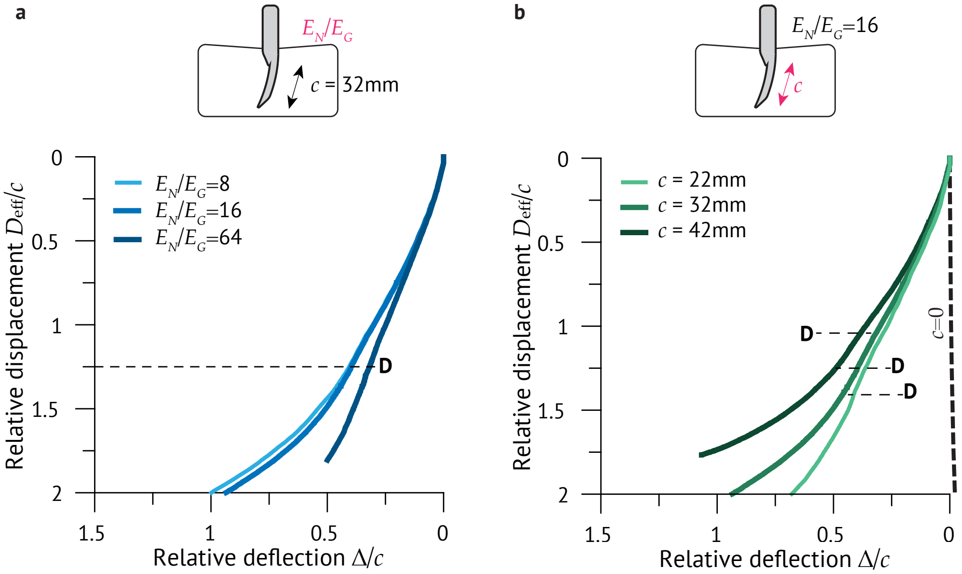

Figure 5.19 Paths of the programmable bevel tip needle. **a** Effect of the stiffness ratio E_N/E_G, at constant offset $c = 32\text{mm}$. **b** Influence of the offset c, at constant stiffness $E_N/E_G = 16$. Dashed lines mark the deflection point D in the trajectories

hyper-circle. The trends seem to suggest a linear dependence of both the curvature and the tip angle with the stiffness ratio and the needle offset. Specifically, increasing the needle stiffness leads to smaller values of curvature and tip angle (with a reduction of 83% for both at the extremes considered). The results obtained in terms of offset dependence confirm the fundamental role played by such a parameter: for instance, changing the offset from $c = 22\text{mm}$ to $c = 42\text{mm}$ leads to a double value of curvature and a five-fold increase in the tip angle.

Overall, the needle steering capacity seems to be altered by both the relative stiffness and the offset, confirming similar experimental findings[212,224]. In particular, the linear increase of the curvature with the offset c is in good agreement with trends extrapolated from experimental insertions[224] and confirms the validity of the computational model. However, there are still some limitations that can be observed and should be considered with care during the design. The penetration of flexible needles is more complex than other cutting processes considered in the thesis, because of the coupling between the cutting force, the penetration path and the influence this path has on the overall profile of the needle as it passes through. The limits of the model are clearly visible when extrapolating the linear relationship between stiffness and curvature (Fig. 5.21a) to the extreme values of E_N/E_G. In practical terms, the presence of a bevel tip results in a curved trajectory even in the case of a rigid needle ($E_N \to \infty$). On the other hand, when the relative stiffness becomes very low, buckling prevents an efficient insertion of the needle in the material. Similarly, the offset-curvature relationship in Fig. 5.21b breaks down for a zero offset (which results in a straight path with $R \to \infty$). At small offsets it is reasonable to assume that a more complex relationship between curvature and offset is established.

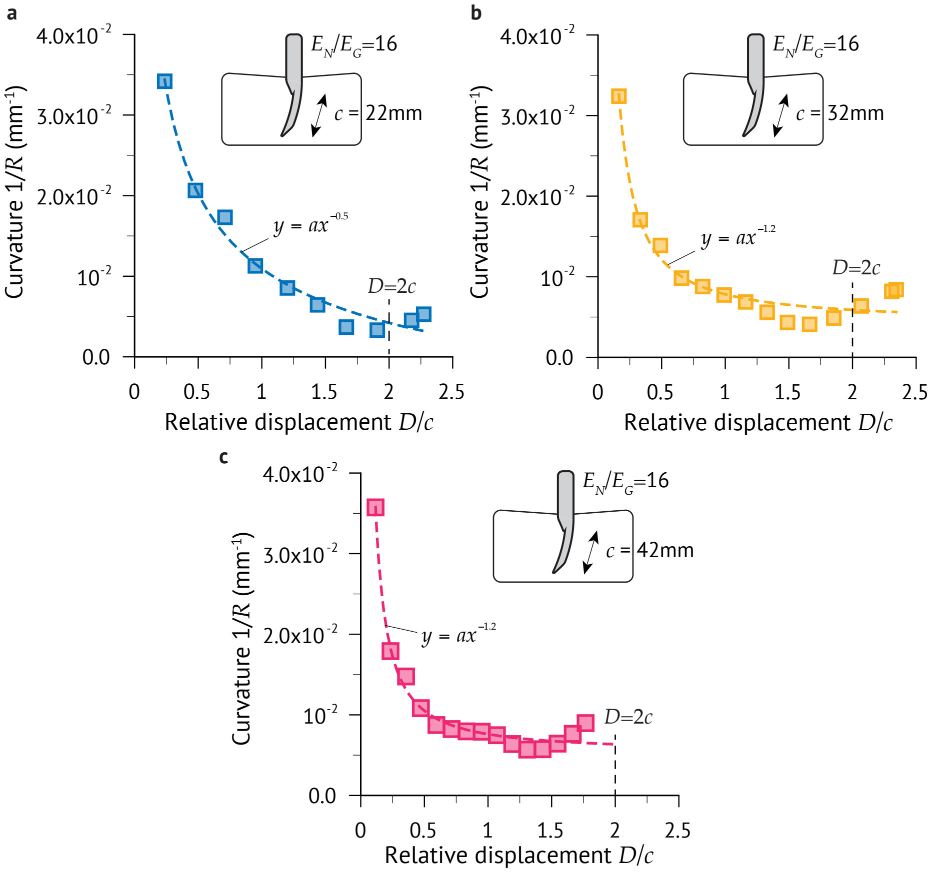

Figure 5.20 Variation of the curvature $1/R$ as a function of the relative displacement D/c, for **a** $c = 22\mathrm{mm}$, **b** $c = 32\mathrm{mm}$ and **a** $c = 42\mathrm{mm}$

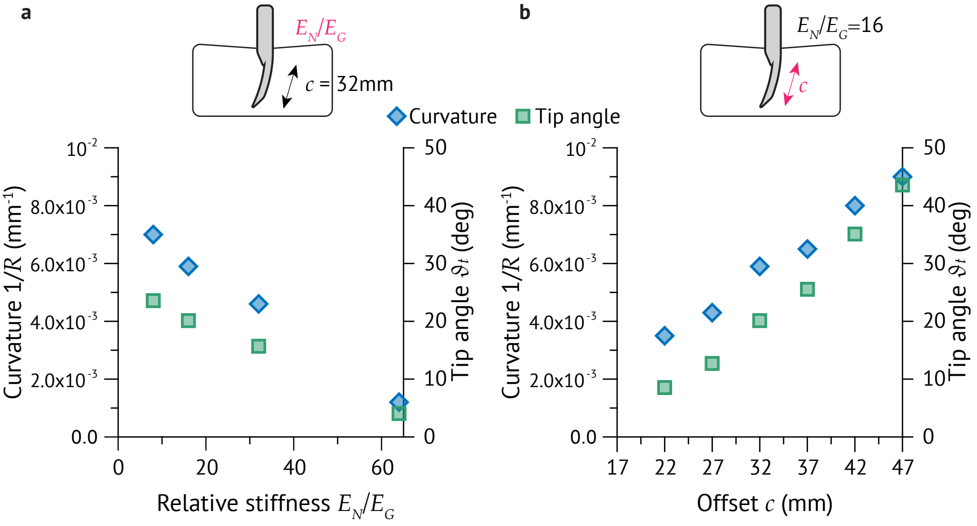

Figure 5.21 Stable values of the curvature $1/R$ and the tip angle ϑ_t, extracted through a hyper-circle fit when $D = 2c$. **a** Effect of the stiffness ratio E_N/E_G and **b** the needle offset c

6

Conclusions

The work presented in this thesis is related to the topic of cutting in soft materials, with relevant examples in materials science, bioengineering, healthcare and the food processing industry. Alongside its industrial applications, cutting-based methods are being increasingly used to test the mechanical response of materials with a soft nature.

In order to develop efficient and reliable computational tools to simulate the process of cutting in various situations, we have examined the mechanics of cutting in general terms. In particular, it has been observed that a remarkable importance might be ascribed to the fracture process connected to the separation of elastic materials. This is the foremost reason which motivated us to centre our dissertation on fracture mechanics, combining theory, experiments and numerical simulations. Although the behaviour of the materials considered generalises a response typical of a large group of natural and synthetic soft solids, the applications are oriented towards cutting and fracture in the brain tissue and similar porous materials.

Human brain shows a complex mechanical behaviour. The response during fracture entails a relevant influence of large deformations and rate-dependent effects, due both to its biphasic nature and viscoelastic relaxation. Each aspect has been considered individually in the thesis and its influence on the fracture process has been discussed in the relevant sections. In this concluding chapter we summarise the main findings using bullet points for an improved readability, trying to establishing useful connections among the various part of the thesis.

- The mechanics of cutting in materials with an elastic nature is governed in large part by the energy required to initiate and propagate a crack. In this sense, the basic assumptions do not differ from classical fracture mechanics and ordinary variables can be used to derive the analytical models of cutting;

- an example of the previous statement is provided by the steady-state of cutting in a linear elastic material. Within the small scale yielding hypothesis of linear elastic fracture mechanics, the region where cutting separation occurs is autonomous from any material property or geometry, save for the stress intensity factor. In such a case, the cutting force may be related to the stress concentration caused by the tool and the fracture toughness of the material;

- the influence of the tool on the mechanism of crack propagation is arguably a relevant point in elastic cutting. More specifically, we have shown how a tool sharpness parameter can be employed to discriminate two different propagation mechanisms. The first, that we have defined as 'blunt' propagation, is an autonomous process, in which the crack extends ahead of the cutting tool under symmetric mode-I conditions. The second, denoted as 'sharp' propagation, is a constrained process which requires the cutting tool to compress the material in order to provide enough energy to advance the crack;

- a corollary of the previous statement is that the definition of sharpness depends both on a characteristic size of the cutting tool and the material properties. To this purpose, we have presented experimental results of cutting in two different types of polymeric materials, showing that the same commercial blade can produce a cut accordingly to the two distinct mechanisms discussed above. In defining sharpness for linear elastic materials, the relevant mechanical parameter is the fracture toughness. The characteristic size depends on the tool geometry, and it might be reasonably correlated to a local radius of curvature at the tool tip;

- friction is another feature of cutting worth to be considered, which has a direct effect on the forces required in practical applications. In this thesis we have focused on the technique of oblique cutting, in which typically a blade is inclined during the insertion into the material in order to induce a slicing action which reduces the cutting force;

- when cutting is applied to soft materials, large deformations affect the whole process, starting from the stage of indentation. Focusing on the technique of wire cutting, we have shown how large strains modify the initial contact solution that can be derived in small strains. The consequence is that the mechanism of fracture initiation is affected by a characteristic size of the tool, e.g. the radius in wire cutting, similarly to the subsequent stage of crack propagation;

- in order to investigate the role of large strains, we have considered the fracture mechanics of hyperelastic materials. The crack-tip stress fields show different singularities from those in linear elastic solids and the deformed configuration of cracks is affected by the strain hardening of the stress-strain law, particularly relevant for soft biological tissues. We have also proposed to extend the concept of tool sharpness, previously introduced for linear elasticity, to the framework of finite strains. An approximation of the relevant mechanical parameter distinguishing blunt and sharp propagation in cutting is provided by the natural tip radius of a blunted crack, defined as the ratio between the fracture resistance and the elastic modulus of the material;

- crack-tip blunting has been identified as a peculiarity of crack propagation in highly deformable materials. Combining experimental observations with a numerical model of a blunted crack, we have clarified the contribution of blunting leading to the enhanced flaw tolerance displayed by soft materials;

- a rate-dependent behaviour observed during wire cutting of human brain and synthetic mimicking materials suggested that fracture is coupled with energy dissipation. We have identified two possible sources of rate-dependence in materials with a soft porous nature. One is related to a volumetric relaxation due to the flow of interstitial fluid within the porous skeleton. The second mechanism is linked to conformational changes in the elastic network, resulting in a volume preserving viscoelastic relaxation. We have developed a computational framework based on the separation of two length scales related to energy dissipation in the presence of a crack. Namely, these are a process zone at the crack tip and a larger region, where dissipation originated in the bulk material affects crack propagation. The process zone has been described adopting a cohesive model, in which the energy derived from a cohesive stress-displacement relationship along the crack provides the intrinsic toughness of the material;

- in order to evaluate the role of fluid draining, we have firstly considered a rate-independent process zone and a poro-hyperelastic model to simulate the behaviour of human brain and of a biopolymeric gelatine. The results obtained seem to correlate fluid draining within the crack-related region to energy dissipation, although its effect in terms of the fracture energy depends on material properties, such as the permeability. In the gelatine material, analyses and experiments have suggested that the fracture process is highly localised at the crack-tip. Therefore, we have suggested that the observed rate effects is the consequence of rate-dependence in the process zone only;

- with respect to the viscoelastic relaxation, an approach similar to that described at the previous point has been adopted, with the bulk material modelled as a visco-hyperelastic solid. The impact of viscoelasticity seems to be minimal, at least in the range of loading rates which can be found in typical cutting or fracture tests. A quantitative assessment of the interaction between both forms of dissipation has not been carried out. We have proposed a qualitative view of the combined rate-dependence based on physical arguments, showing that fluid draining and viscoelastic relaxation might interfere for particular combinations of material properties and loading rates;

- the use of cohesive models within a non-linear elastic bulk material has been proposed to model two different problems: the penetration of a rigid wire and the deep insertion of a flexible needle with an asymmetric, bio-inspired configuration. In the latter example, the model has proved capable of describing with great detail the complex interaction between needle and sample material. In particular, a curved propagation path observed in experiments has been reproduced thanks to an adaptive finite element algorithm.

We believe that this dissertation provides an overall picture on the topic of cutting applied to soft biomaterials, leading towards the development of refined computational tools. Although we have introduced a simplification by considering separately different effects, we have proposed a unifying treatment of the cutting process by applying the cohesive zone model, which has proved capable of describing the complexity of the mechanical response found in biomaterials.

There are, however, specific points that need to be further investigated in the future. With respect to the rate-dependent behaviour observed in the brain tissue, a better understanding of the fracture mechanism in terms of its microstructure is desirable. Together with new experimental tests, this could lead to a precise assessment of the role played by fluid and viscosity during fracture and, potentially, should allow a reliable evaluation of the fracture toughness of human brain.

With respect to the computational aspects, limitations in the actual model are related to the mechanism of propagation. Specifically, the numerical simulations are limited to the case that we have defined as ‘blunt’ propagation, because a damage criterion in the presence of compressive stress states in the crack-tip region has not been developed yet. In addition, the algorithm proposed for needle insertion simulations could be improved by allowing for a rate-dependent behaviour of the fracture process. The implementation of a full three-dimensional model could be the last step to achieve an even more accurate computational tool for cutting simulations.

A

Appendices

A.1. Formulation of finite strain elasticity

We here present a concise review of the standard formulation of finite strain mechanics and non-linear elasticity, limited to the aspects of interest for the present thesis. This section is mainly taken from standard books on elasticity, such as the monograph by Holzapfel[225] and others which the author believes to stand out for easiness of comprehension[126,226,227].

A.1.1. Fundamentals of non-linear mechanics

Let us consider a continuum body, which at a time instant $t = 0$ occupies the region Ω_0 and at a generic time instant t assumes the configuration Ω. With respect to a fixed origin O, a point P in the continuum body is identified by the vector $\mathbf{X}$ in the region Ω_0, which is called the initial or *reference* configuration of the body. The same point, at the generic time instant t, is identified by the vector $\mathbf{x}$ in the current or *deformed* configuration Ω (Fig.A.1a). On the grounds of this definition, it is common practice to distinguish the material or *Lagrangian* description, which observes the motion of a point with respect to the reference coordinates, from the spatial or *Eulerian* description, which follows the motion of a point during its evolution in terms of the current coordinates.

We introduce the vector field $\Phi(\mathbf{X}, t)$ which transforms points $\mathbf{X}$ on the reference configuration to places $\mathbf{x}$ in the deformed configuration, so that we can write

$$\mathbf{x} = \Phi(\mathbf{X}, t) = \mathbf{X} + \mathbf{U}(\mathbf{X}, t), \tag{A.1}$$

where $\mathbf{U}(\mathbf{X}, t)$ is the displacement field in the reference configuration, while we denote $\mathbf{u}(\mathbf{x}, t)$ the displacement field in the current configuration, with $\mathbf{u}(\mathbf{x}, t) = \mathbf{U}(\mathbf{X}, t)$. For future use we also define the velocity fields $\mathbf{V}(\mathbf{X}, t) = \dot{\mathbf{U}}$ and $\mathbf{v}(\mathbf{x}, t) = \dot{\mathbf{x}} = \dot{\mathbf{u}}$, where the dot is used for the material time derivative.

Under the compatibility assumption that the transformation occurs without lacerations or penetrations, $\Phi(\mathbf{X}, t)$ is a one-to-one continuously differentiable function representing the *motion* of the continuum body. Considering an infinitesimal length $\mathrm{d}\mathbf{X}$ in the reference configuration, the transformation due to motion is given by

$$\mathrm{d}\mathbf{x} = \mathbf{F}(\mathbf{X}, t)d\mathbf{X}, \tag{A.2}$$

where $\mathbf{F}(\mathbf{X}, t)$ is a second-order tensor denoted as *deformation gradient*, having nine components in three-dimensional problems, which represent the material derivatives of the motion Φ

$$F_{ij} = \frac{\partial \Phi_i}{\partial X_j} = \frac{\partial x_i}{\partial X_j}. \tag{A.3}$$

In general, $\mathbf{F}$ includes both deformations and rigid body rotations. The determinant of the deformation gradient is known as the *volume ratio* or Jacobian determinant J, and due to the impenetrability of matter is a positive quantity defined as

$$\det\mathbf{F} \equiv J > 0. \tag{A.4}$$

The relevant case of $J = 1$ corresponds to isochoric deformations, i.e. where volume is preserved.

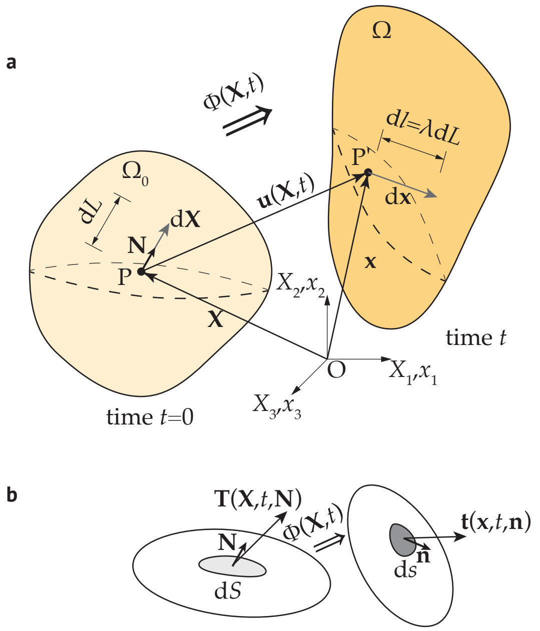

Figure A.1 **a** Reference undeformed and current deformed configuration of a continuum body. **b**, Stress vectors acting on an infinitesimal surface element within the body

Stress and strain measures

Here we present the derivation of strain which is commonly followed in non-linear mechanics. In the neighbourhood of P, let us consider a line vector $\mathrm{d}\mathbf{X}$ in the reference configuration, whose orientation is determined by the unit vector $\mathbf{N}$

$$\mathrm{d}\mathbf{X} = \mathrm{d}L\mathbf{N}, \tag{A.5}$$

where dL is the initial length of the unit vector. As a consequence of motion, the vector d$\mathbf{X}$ is transformed into d$\mathbf{x}$, having length dl in the deformed configuration. The squared lengths are

$$\mathrm{d}L^2 = \mathrm{d}\mathbf{X}^T\mathrm{d}\mathbf{X} \qquad \text{and} \qquad \mathrm{d}l^2 = \mathrm{d}\mathbf{x}^T\mathrm{d}\mathbf{x}. \tag{A.6a}$$

The ratio

$$\lambda = \frac{\mathrm{d}l}{\mathrm{d}L} = \sqrt{\frac{\mathrm{d}\mathbf{x}^T\mathrm{d}\mathbf{x}}{\mathrm{d}\mathbf{X}^T\mathrm{d}\mathbf{X}}} \tag{A.7}$$

is known as the *stretch ratio* and measures how much the line element is extended or compressed along the direction of $\mathbf{N}$, whereby the deformed length of the element is simply derived as dl = λdL. Notice that $\lambda > 1$ corresponds to an elongation, while rigid body motions are identified by $\lambda = 1$.

A recurring measure of strain within the material framework follows from the change in square lengths. From Eq.(A.6) we have

$$\mathrm{d}l^2 - \mathrm{d}L^2 = \mathrm{d}\mathbf{x}^T\mathrm{d}\mathbf{x} - \mathrm{d}\mathbf{X}^T\mathrm{d}\mathbf{X} = \mathrm{d}\mathbf{X}^T(\mathbf{F}^T\mathbf{F} - \mathbf{I})d\mathbf{X}, \tag{A.8}$$

where $\mathbf{I}$ is the second-order identity tensor. The quantity in brackets in Eq.(A.8) defines the second-order tensor $\mathbf{E}$, which is known as *Green-Lagrange* strain tensor

$$\mathbf{E} = \frac{1}{2}(\mathbf{F}^T\mathbf{F} - \mathbf{I}) = \frac{1}{2}(\mathbf{C} - \mathbf{I}). \tag{A.9}$$

The normalisation factor 1/2 is introduced for compatibility with the infinitesimal strain theory and the term $\mathbf{C}$ is known as the *right* Cauchy-Green tensor. Notice that $\mathbf{E}$ is a symmetric tensor, whose components are expressed in terms of the displacement field as follows (Einstein's summation rule on repeated indices is adopted)

$$E_{ij} = \frac{1}{2}\left(\frac{\partial u_i}{\partial X_j} + \frac{\partial u_j}{\partial X_i} + \frac{\partial u_k}{\partial X_i}\frac{\partial u_k}{\partial X_j}\right), \tag{A.10}$$

where we recognise the conventional engineering definition of the infinitesimal strain

$$\varepsilon_{ij} = \frac{1}{2}\left(\frac{\partial u_i}{\partial X_j} + \frac{\partial u_j}{\partial X_i}\right). \tag{A.11}$$

Combining Eqs.(A.7)-(A.9), we obtain

$$\lambda = \sqrt{1 + 2\mathbf{N}^T\mathbf{E}\mathbf{N}}. \tag{A.12}$$

To complete the presentation of the strain measures, we also introduce a spatial measure of strain, the *left* Cauchy-Green tensor $\mathbf{b} = \mathbf{F}\mathbf{F}^T$, which is often used in the formulation of the stress-strain relationships.

Now we move on to introduce some measures of stress. For an infinitesimal spatial surface element on the deformed configuration ds with normal vector $\mathbf{n}$, and the corresponding quantities dS and $\mathbf{N}$ with respect to the reference configuration, we introduce the stress vectors (Fig.A.1b)

$$\mathbf{t}(\mathbf{x}, t, \mathbf{n}) = \sigma(\mathbf{x}, t)\mathbf{n}, \tag{A.13a}$$

$$\mathbf{T}(\mathbf{X}, t, \mathbf{N}) = \mathbf{P}(\mathbf{X}, t)\mathbf{N}, \tag{A.13b}$$

where $\boldsymbol{\sigma}$ is the Cauchy or *true* stress tensor, related to the deformed configuration, whereas $\mathbf{P}$ is known as the first Piola-Kirchoff or *nominal* stress tensor, which refers to the force per unit surface area in the reference configuration. The two are related by

$$\mathbf{P} = J\boldsymbol{\sigma}\mathbf{F}^{-T}. \tag{A.14}$$

Contrary to the Cauchy stress tensor, $\mathbf{P}$ is not symmetric and for convenience of use we introduce the symmetric second Piola-Kirchoff stress tensor $\mathbf{S}$, which is related to the previous by

$$\mathbf{S} = J\mathbf{F}^{-1}\boldsymbol{\sigma}\mathbf{F}^{-T} = \mathbf{F}^{-1}\mathbf{P}. \tag{A.15}$$

Within the linear theory of small strain elasticity, the different definitions of strain and stress are equivalent, i.e. $\boldsymbol{\varepsilon} \approx \mathbf{E}$ and $\boldsymbol{\sigma} \approx \mathbf{P} \approx \mathbf{S}$.

Balance equations

We recall here the well-known principles of mass conservation and balance of linear momentum for the continuum body. Firstly, we introduce the mass densities with respect to the reference $\rho_0(\mathbf{X})$ and current configuration $\rho(\mathbf{x}, t)$. The total mass of the system is defined as

$$m = \int_{\Omega_0} \rho_0(\mathbf{X})\, \mathrm{d}V = \int_{\Omega} \rho(\mathbf{x}, t)\, \mathrm{d}v, \tag{A.16}$$

where $\mathrm{d}v$ is an infinitesimal volume element in the current configuration, related to the reference state through $\mathrm{d}v = J(\mathbf{X}, t)\mathrm{d}V$. The conservation of mass requires that the total mass is constant, so that we may write

$$\frac{d}{dt}\int_{\Omega} \rho(\mathbf{x}, t)\mathrm{d}v = 0, \tag{A.17}$$

from which we also have

$$\rho_0(\mathbf{X}) = J\,\rho(\mathbf{x}, t). \tag{A.18}$$

Now we consider a control volume Ω_c and suppose that mass and energy can be exchanged through the system boundary. At a certain time t, the total mass in the region is

$$m(t) = \int_{\Omega_c} \rho(\mathbf{x}, t)\, \mathrm{d}v. \tag{A.19}$$

The conservation of mass for an open system is written as

$$\frac{d}{dt}\int_{\Omega_c} \rho(\mathbf{x}, t)\mathrm{d}v = -\int_{\partial\Omega_c} \rho(\mathbf{x}, t)\, \mathbf{v}(\mathbf{x}, t) \cdot \mathbf{n}\, \mathrm{d}s, \tag{A.20}$$

where the right-hand term represents the flux of mass entering the control volume through the boundary $\partial\Omega_c$.

Let us now consider a system of forces acting on the continuum body, and denote with $\mathbf{f} = \mathbf{f}(\mathbf{x}, t)$ the body forces acting per unit volume $\mathrm{d}v$ in the configuration Ω. Moreover, the boundary $\partial\Omega$ is subjected to surface tractions $\mathbf{t}(\mathbf{x}, t, \mathbf{n})$ per unit area $\mathrm{d}s$. The corresponding variables in the reference configuration are denoted by $\mathbf{F}(\mathbf{X},t) = J\mathbf{f}(\mathbf{x},t)$ and $\mathbf{T}(\mathbf{X},t,\mathbf{N})$. The balance of linear momentum is written as

$$\frac{d}{dt}\int\limits_{\Omega} \rho \mathbf{v} \mathrm{d}v = \int\limits_{\Omega} \mathbf{f} \mathrm{d}v + \int\limits_{\partial\Omega} \mathbf{t} \mathrm{d}s, \tag{A.21a}$$

$$\frac{d}{dt}\int\limits_{\Omega_0} \rho_0 \mathbf{V} \mathrm{d}V = \int\limits_{\Omega_0} \mathbf{F} \mathrm{d}V + \int\limits_{\partial\Omega_0} \mathbf{T} \mathrm{d}S. \tag{A.21b}$$

By using the divergence theorem and Cauchy's stress theorem (Eq.A.13), and neglecting inertia, we obtain the well-known equilibrium equations

$$\nabla_x \cdot \boldsymbol{\sigma} + \mathbf{f} = 0, \tag{A.22a}$$

$$\nabla_X \cdot \mathbf{P} + \mathbf{F} = 0, \tag{A.22b}$$

where the symbol ∇ denotes the gradient vector and the operation $\nabla \cdot (\bullet)$ computes the divergence of $(\bullet)$, in the current or reference configuration.

A.1.2. Isotropic hyperelastic behaviour

To represent the material behaviour of soft matter, non-linear constitutive theories are formulated within the framework of finite strains. Among the most popular theories, hyperelasticity is based on the existence of a strain energy density function, representing a Helmholtz free-energy per unit volume $W = W(\mathbf{F})$. The first Piola-Kirchoff stress tensor is obtained by derivation as

$$\mathbf{P} = \frac{\partial W(\mathbf{F})}{\partial \mathbf{F}}, \tag{A.23}$$

and the Cauchy true stress can be derived from the inverse of Eq.(A.14)

$$\boldsymbol{\sigma} = J^{-1}\frac{\partial W(\mathbf{F})}{\partial \mathbf{F}}\mathbf{F}^T. \tag{A.24}$$

A more convenient formulation might be derived in isotropic materials, for which the strain energy density can be written in terms of the strain invariants. Let us consider the right Cauchy-Green strain tensor $\mathbf{C}$, whose invariants are expressed by

$$I_1(\mathbf{C}) = \mathrm{tr}\mathbf{C}, \tag{A.25a}$$

$$I_2(\mathbf{C}) = \frac{1}{2}[(\mathrm{tr}\mathbf{C})^2 - \mathrm{tr}(\mathbf{C}^2)], \tag{A.25b}$$

$$I_3(\mathbf{C}) = \det\mathbf{C} = J^2. \tag{A.25c}$$

Because the left Cauchy-Green strain tensor $\mathbf{b}$ has the same eigenvalues of $\mathbf{C}$, i.e. the squares of the principal stretches λ_α, $\alpha = 1,2,3$, the invariants for $\mathbf{b}$ and $\mathbf{C}$ are equivalent, and in terms of the principal stretches are

$$I_1(\mathbf{C}) = I_1(\mathbf{b}) = \lambda_1^2 + \lambda_2^2 + \lambda_3^2, \tag{A.26a}$$

$$I_2(\mathbf{C}) = I_2(\mathbf{b}) = \lambda_1^2\lambda_2^2 + \lambda_1^2\lambda_3^2 + \lambda_2^2\lambda_3^2, \tag{A.26b}$$

$$I_3(\mathbf{C}) = I_3(\mathbf{b}) = \lambda_1^2\lambda_2^2\lambda_3^2. \tag{A.26c}$$

The strain energy density for an isotropic hyperelastic material is a function of the strain invariants $W = W(I_1, I_2, I_3)$, from which the second Piola-Kirchhoff stress is computed as

$$\begin{aligned}\mathbf{S} &= 2\left[\frac{\partial W}{\partial I_1}\frac{\partial I_1}{\partial \mathbf{C}} + \frac{\partial W}{\partial I_2}\frac{\partial I_2}{\partial \mathbf{C}} + \frac{\partial W}{\partial I_3}\frac{\partial I_3}{\partial \mathbf{C}}\right] = \\ &= 2\left[\left(\frac{\partial W}{\partial I_1} + I_1\frac{\partial W}{\partial I_2}\right)\mathbf{I} - \frac{\partial W}{\partial I_2}\mathbf{C} + I_3\frac{\partial W}{\partial I_3}\mathbf{C}^{-1}\right], \end{aligned} \tag{A.27}$$

and its spatial counterpart Cauchy stress tensor follows from the transformation in Eq.(A.15)

$$\sigma = 2J^{-1}\left[\left(\frac{\partial W}{\partial I_1} + I_1\frac{\partial W}{\partial I_2}\right)\mathbf{b} - \frac{\partial W}{\partial I_2}\mathbf{b}^2 + I_3\frac{\partial W}{\partial I_3}\mathbf{I}\right]. \tag{A.28}$$

Note that the strain energy density functions must satisfy the normalisation condition, i.e. $W(\mathbf{F} = \mathbf{I}) = 0$, so that zero initial stress is assumed and the strain invariants are $I_1 = I_2 = 3$ and $I_3 = 1$. Moreover, strain energy densities increase with deformation, so that $W(\mathbf{F}) \geq 0$.

An additional formulation of the hyperelastic strain energy density function is given in terms of the Green-Lagrange strain tensor $\mathbf{E}$, which is work conjugate to the second Piola-Kirchoff stress tensor. In this case we may directly obtain

$$\mathbf{S} = \frac{\partial W(\mathbf{E})}{\partial \mathbf{E}}. \tag{A.29}$$

The Saint Venant–Kirchhoff model is an example of this formulation. Basically, it is a simple extension of the Hooke linear model to the non-linear regime. Although not suitable to describe the large strain behaviour of materials, we report here its expression for consistency with the linear theory, and because it is used in computational mechanics when a linear elastic material is modelled in the framework of finite strains. The strain energy density function for a *Saint Venant–Kirchhoff* material is given by

$$W = W(\mathbf{E}) = \frac{\lambda}{2}(\mathrm{tr}\mathbf{E})^2 + \mu\mathrm{tr}(\mathbf{E})^2, \tag{A.30}$$

where λ and μ are the Lamé's constants.

Basic homogeneous deformations

It might be useful to derive explicitly the expression of principal stretches, strain invariants and Cauchy stress components for basic deformations that are recurrent in experiments, namely uniaxial extension, equibiaxial extension and pure shear. These three categories are sketched in Fig.A.2, with respect to an element whose edges are aligned with the unit normals $\mathbf{N}_1 = [1, 0, 0]^T$ and $\mathbf{N}_2 = [0, 1, 0]^T$. For simplicity, an incompressible behaviour is assumed, i.e. $J = \lambda_1\lambda_2\lambda_3 = 1$.

Uniaxial extension (or compression) is characterised by a stretch ratio λ in the direction of $\mathbf{N}_1$. The principal stretches are

$$\lambda_1 = \lambda, \quad \lambda_2 = \lambda_3 = \lambda^{-1/2}, \tag{A.31}$$

whereas the strain invariants, from Eq.(A.26), are

$$I_1 = \lambda^2 + 2\lambda^{-1}, \quad , I_2 = \lambda^{-2} + 2\lambda, \quad I_3 = 1. \tag{A.32}$$

The Green-Lagrange strain, from Eq.(A.12), is

$$E_{11} = \frac{\lambda^2 - 1}{2} = \varepsilon_{11} + \frac{1}{2}\varepsilon_{11}^2, \tag{A.33}$$

where $\varepsilon_{11} = \lambda - 1$ is the *nominal* strain. The only non-zero component of the Cauchy stress tensor is derived from Eq.(A.28)

$$\sigma_{11} = 2(\lambda^2 - \lambda^{-1})\left(\frac{\partial W}{\partial I_1} + \lambda^{-1}\frac{\partial W}{\partial I_2}\right). \tag{A.34}$$

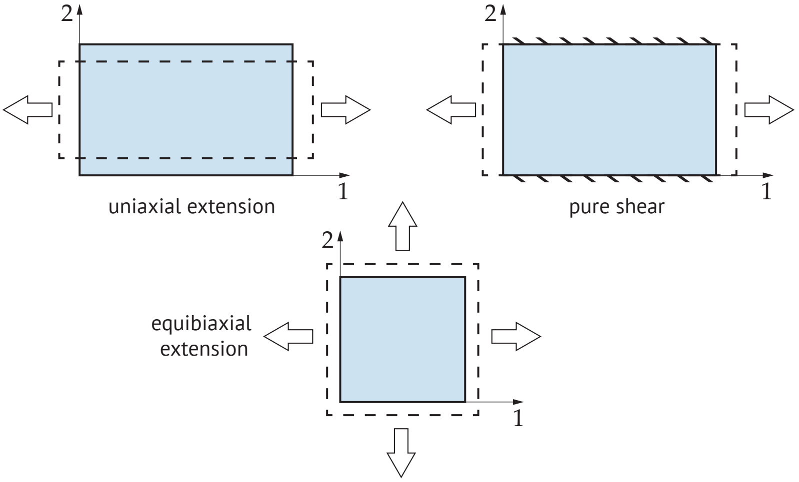

Figure A.2 Sketches of basic deformations of a hyperelastic solid

In an *equibiaxial extension*, the same stretch ratio λ is applied in the direction of $\mathbf{N}_1$ and $\mathbf{N}_2$. The principal stretches are

$$\lambda_1 = \lambda_2 = \lambda, \quad \lambda_3 = \lambda^{-2}, \tag{A.35}$$

whereas the strain invariants are

$$I_1 = 2\lambda^2 + 2\lambda^{-4}, \quad I_2 = \lambda^4 + 2\lambda^{-2}, \quad I_3 = 1. \tag{A.36}$$

The non-zero components of the Cauchy stress tensor are

$$\sigma_{11} = \sigma_{22} = 2(\lambda^2 - \lambda^{-4})\left(\frac{\partial W}{\partial I_1} + \lambda^2\frac{\partial W}{\partial I_2}\right). \tag{A.37}$$

A long strip of material which is constrained along the edges parallel to $\mathbf{N}_1$ and stretched along the same direction results in a plane deformation known as *pure shear*. Therefore the principal stretches are

$$\lambda_1 = \lambda, \quad \lambda_2 = 1, \quad \lambda_3 = \lambda^{-1}, \tag{A.38}$$

whereas the strain invariants are

$$I_1 = I_2 = \lambda^2 + 2\lambda^{-2} + 1, \quad I_3 = 1. \tag{A.39}$$

The non-zero components of the Cauchy stress tensor are

$$\sigma_{11} = 2(\lambda^2 - \lambda^{-2})\left(\frac{\partial W}{\partial I_1} + \frac{\partial W}{\partial I_2}\right), \tag{A.40}$$

$$\sigma_{22} = 2(1 - \lambda^{-2})\left(\frac{\partial W}{\partial I_1} + \lambda^2\frac{\partial W}{\partial I_2}\right). \tag{A.41}$$

Isotropic incompressible hyperelasticity

A large number of polymeric materials, and to some extent biological soft tissues, can sustain large strains without relevant volume change. For this reason, hyperelastic models that are based on the assumption of an isochoric deformation have found large use in continuum and computational mechanics. In order to derive the hyperelastic models for incompressible materials, the strain energy density is written as

$$W = W(\mathbf{F}) - p(J-1), \tag{A.42}$$

where p is the scalar hydrostatic pressure and the volume ratio is subjected to the incompressibility constraint $J = 1$. Similarly, we can obtain the expression for isotropic hyperelasticity in terms of the strain invariants

$$W = W(I_1, I_2) - \frac{p}{2}(I_3 - 1), \tag{A.43}$$

where the strain energy density function depends on two invariants, the third one enforcing the incompressibility constraint as $I_3 = \det\mathbf{C} = \det\mathbf{b} = 1$. Equations (A.27)-(A.28) for incompressible materials take the form

$$\mathbf{S} = 2\left[\left(\frac{\partial W}{\partial I_1} + I_1\frac{\partial W}{\partial I_2}\right)\mathbf{I} - \frac{\partial W}{\partial I_2}\mathbf{C} - \frac{p}{2}\mathbf{C}^{-1}\right], \tag{A.44}$$

$$\boldsymbol{\sigma} = 2\left[\left(\frac{\partial W}{\partial I_1} + I_1\frac{\partial W}{\partial I_2}\right)\mathbf{b} - \frac{\partial W}{\partial I_2}\mathbf{b}^2 - \frac{p}{2}\mathbf{I}\right]. \tag{A.45}$$

For strain energy densities formulated in terms of principal stretches, we report below the expression of the principal second Piola-Kirchoff stress

$$S_i = -\frac{1}{{\lambda_i}^2}p + \frac{1}{\lambda_i}\frac{\partial W}{\partial \lambda_i}, \tag{A.46}$$

whereas the Cauchy stress is given by

$$\sigma_i = -p + \lambda_i\frac{\partial W}{\partial \lambda_i}. \tag{A.47}$$

Among the most common hyperelastic incompressible models are those derived for the behaviour of rubbers, which under isothermal conditions (above the glass temperature) show very small volume changes under a large hydrostatic pressure. The *neo-Hookean* (NH) is one of the simplest available models[228], whose strain energy density is given by

$$W(I_1) = \frac{\mu}{2}(I_1 - 3), \tag{A.48}$$

where the initial shear modulus μ is the only parameter and is directly connected to the Young modulus E by the relation $\mu = E/3$ (with the implicit condition $\nu = 0.5$ from the incompressibility assumption).

A slight more general formulation is obtained with the introduction of the second strain invariant, whose influence has been clarified in the theory of elasticity[128,229]. In brief, deformations that involve a single stress or strain component, as uniaxial extension or simple shear, can be reasonably well approximated by a strain energy density function of the form $W(I_1)$, whereas biaxial deformations might require the introduction of the second invariant. The simplest two-invariant formulation is the *Mooney-Rivlin* (MR) model[228,230], for which the strain energy density is assumed to be a linear function of the first and second invariant

$$W(I_1, I_2) = \frac{\mu}{2}\left[\alpha(I_1 - 3) + (1 - \alpha)(I_2 - 3)\right] \tag{A.49}$$

, where α is a non-dimensional parameter lower than 1.

It has been observed that the stress-strain behaviour described by the simpler formulations becomes inaccurate at large stretches (usually, above $\lambda = 1.2 - 1.3$ in rubber-like materials). Specifically, the increasing slope of the stress curve due to the strain hardening phenomenon, which occurs at large stretches in rubbers but considerably earlier in some biological materials, cannot be described properly. Phenomenological models for strain hardening materials are those which reflect the limited chain extensibility of the molecular chains within their formulation. A famous example is given by *Gent* model[231]

$$W(I_1) = -\frac{\mu J_m}{2}\ln\left(1 - \frac{I_1 - 3}{J_m}\right), \tag{A.50}$$

where J_m is a dimensionless parameter that reflects the maximum allowable strain connected to the limited extensibility, and takes different values depending on the specific material. Although initially devised to model the strain crystallisation of rubbers, it has also been applied to biological materials such as the arterial tissue, which typically have low values of the limiting parameter J_m (0-1 as opposed to 10-100 for rubber)[232].

Another well-known strain-hardening model is the *Generalised neo-Hookean* (GNH) model, proposed by Knowles[104]. The strain energy density function of the GNH model is

$$W(I_1) = \frac{\mu}{2b}\left\{\left[1 + \frac{b}{n}(I_1 - 3)\right]^n - 1\right\}, \tag{A.51}$$

where μ, b and n are three calibration parameters. In particular, $n > 0$ controls the influence of strain hardening.

Finally, we introduce a model which is often employed for its accurate description of the elastic behaviour of strain hardening polymers and biological tissues: the *Ogden* model. Instead of using strain invariants, where only integer powers of the principal stretches appear, Ogden's strain energy density is directly formulated in terms of stretches with fractional powers[233]

$$W(\lambda_1, \lambda_2, \lambda_3) = \sum_{i=1}^{N} \frac{\mu_i}{\alpha_i}\left(\lambda_1^{\alpha_i} + \lambda_2^{\alpha_i} + \lambda_3^{\alpha_i} - 3\right), \tag{A.52}$$

where N is a positive integer, μ_i are the shear moduli and α_i are dimensionless constants that can be fractional.

Isotropic compressible hyperelasticity

Some materials, although characterised by a bulk modulus much larger than their shear modulus, cannot be treated as perfectly incompressible. We show here the main equations for compressible hyperelasticity, which is based on the split between deviatoric (volume-preserving) and volumetric deformation. The deviatoric component of the deformation gradient and the corresponding right Cauchy-Green strain tensor are defined as

$$\begin{aligned}\bar{\mathbf{F}} &= J^{-1/3}\mathbf{F},\\ \bar{\mathbf{C}} &= J^{-2/3}\mathbf{C}.\end{aligned} \tag{A.53}$$

Similarly, the modified principal stretches and strain invariants can be derived

$$I_1(\bar{\mathbf{C}}) = \mathrm{tr}\bar{\mathbf{C}} = J^{-2/3}I_1, \tag{A.54a}$$

$$I_2(\bar{\mathbf{C}}) = \frac{1}{2}[(\mathrm{tr}\bar{\mathbf{C}})^2 - \mathrm{tr}(\bar{\mathbf{C}}^2)] = J^{-4/3}I_2, \tag{A.54b}$$

$$I_3(\bar{\mathbf{C}}) = \det\bar{\mathbf{C}} = J^2. \tag{A.54c}$$

The strain energy density function in isotropic materials is decomposed as

$$W(I_1, I_2, J) = U(J) + \bar{W}\left(\bar{I}_1, \bar{I}_2\right), \tag{A.55}$$

where U describes the volumetric elastic response and $\bar{W}$ the isochoric deformation. Stress tensors are obtained by derivation; in particular, the second Piola-Kirchoff stress is given by

$$\mathbf{S} = \frac{\partial U(J)}{\partial \mathbf{C}} + \frac{\partial \bar{W}\left(\bar{I}_1, \bar{I}_2\right)}{\partial \mathbf{C}}, \tag{A.56}$$

where the first term represents the volumetric stress and the second term is the deviatoric part $\bar{\mathbf{S}}$. The latter is written explicitly as

$$\bar{\mathbf{S}} = J^{-2/3}\mathrm{Dev}\left(2\frac{\partial \bar{W}(\bar{I}_1, \bar{I}_2)}{\partial \bar{\mathbf{C}}}\right), \tag{A.57}$$

where we have introduced the deviatoric operator (in the reference configuration), defined by

$$\mathrm{Dev}(\bullet) = (\bullet) - \frac{1}{3}[(\bullet) : \mathbf{C}]\,\mathbf{C}^{-1}. \tag{A.58}$$

Finally we obtain

$$\mathbf{S} = Jp\mathbf{C}^{-1} + \bar{\mathbf{S}}, \tag{A.59}$$

where $p = \mathrm{d}U/\mathrm{d}J$ is the hydrostatic pressure. Equation (A.59) is also employed in constitutive models of polymeric materials and soft tissues with time-dependent behaviour, characterised by different relaxation functions for the deviatoric and volumetric parts of the deformation.

A.2. Formulation of poroelasticity

The foundations of poroelasticity derive from the pioneering studies in the mechanics of soils and the consolidation theory developed by Terzaghi and Biot[150,234]. We start this section from the general finite strain framework, introduced by Biot himself[151], and then show the simpler case of linear poroelasticity as a specific case of this formulation. The main concepts are taken from the monograph on poroelasticity by Cheng[235] and the work by Simon[152,176] on the poro-hyperelastic model.

Let us consider a granular material, characterised by a solid matrix and interstitial pores, and isolate an elementary representative volume V, distinguishing the solid part V_S from that occupied by the pores V_P. If fluid is entrapped in the pores and occupies a volume V_F, the condition of saturation is identified by $V_P = V_F$. We also define the porosity n_F as the volumetric fraction of the fluid component on the total volume, so that we have

$$n_F = \frac{V_F}{V}. \tag{A.60}$$

In the current configuration Ω (Fig.A.1), we denote with $\mathbf{u}_F(\mathbf{x}, t)$ and $\dot{\mathbf{u}}_F(\mathbf{x}, t)$ the displacement and velocity fields of the fluid, where the dot denotes time derivation. A relative fluid velocity, also known as specific discharge vector, is defined by

$$\mathbf{w}(\mathbf{x}, t) = n_F(\dot{\mathbf{u}}_F - \dot{\mathbf{u}}), \tag{A.61}$$

and represents the rate of fluid volume passing through a unit area of porous medium, per unit time, in the direction normal to that area.

Now we need to derive the balance equations of the porous material. Neglecting internal sources of fluid in the representative volume, the conservation of mass requires that the rate of variation of fluid content is balanced by the fluid exchange between the volume and the outside. We can express this statement as

$$\frac{d}{dt}\int\limits_{\Omega_c} \zeta \mathrm{d}v = -\int\limits_{\partial\Omega_c} \mathbf{w}\,(\mathbf{x}, t) \cdot \mathbf{n}\,\mathrm{d}s, \tag{A.62}$$

where the left-hand integral is the rate of change in fluid content ζ (defined as the variation of fluid volume per unit volume of porous medium), whereas the right-hand term accounts for the volume of fluid passing through the boundary $\partial\Omega_c$ in the normal direction.

The equilibrium equation of the porous material is analogous to that given in Eq.(A.22a), whereas to derive the fluid equilibrium we need to consider a law governing the fluid flow within the pores. Biot's theory is based on Darcy's law, which was derived empirically and describes a thermodynamic irreversible process controlled by a pressure gradient driven viscous flow. Neglecting inertia, we can write

$$\mathbf{w} = -\frac{\mathbf{K}_F}{\eta_F}\nabla_x p_F, \tag{A.63}$$

where p_F is the fluid pressure, $\mathbf{K}_F$ is the permeability tensor and η_F is the fluid viscosity.

Although fluid mechanics makes large use of the Eulerian framework, it is more convenient for porous materials to shift to the Lagrangian approach, in which the material properties can be measured more easily. Variables and balance equations are referred to the reference configuration Ω_0 by means of a correspondence principle[152]. In particular, we define the relative fluid velocity $\mathbf{W}(\mathbf{X}, t)$ such that the fluid mass flow rate $\dot{m}_F$ is the same as in the current configuration. In mathematical terms we can express this condition according to the following equivalence

$$\dot{m}_F = \int_{\partial\Omega} \rho_F \mathbf{w} \cdot \mathbf{n} \mathrm{d}s = \int_{\partial\Omega_0} \rho_{0_F} \mathbf{W} \cdot \mathbf{N} \mathrm{d}S, \tag{A.64}$$

where $\mathbf{W}(\mathbf{X}, t) = J\mathbf{F}^{-1}\, \mathbf{w}(\mathbf{x}, t)$ with the assumption of fluid incompressibility ($\rho_F = \rho_{0F}$).

The equilibrium equation of the porous material is analogous to that given in Eq.(A.22b), whereas Darcy's law in Eq.(A.63) needs to be replaced by

$$J\mathbf{F}^{-1}\mathbf{w} = -\frac{\mathbf{K}_{0F}}{\eta_F} \nabla_X p_F, \tag{A.65}$$

with $\mathbf{K}_{0F}$ representing the permeability tensor in the reference configuration. This can be related to the spatial definition of permeability by[176]

$$\mathbf{K}_{0F} = J\mathbf{F}^{-1}\mathbf{K}_F\mathbf{F}^{-T}. \tag{A.66}$$

A constitutive relationship needs to be specified for both the solid and the fluid. For materials characterised by a hyperelastic behaviour, suitable strain energy densities W can be written in terms of the Green-Lagrange strain tensor $\mathbf{E}$ and the variation of fluid content ζ. Specifically, we may write[152]

$$W(\mathbf{E}, \zeta) = W'(\mathbf{E}) + \frac{1}{2} M(\zeta + J - 1)^2, \tag{A.67}$$

where $\zeta = \nabla_X \mathbf{W}$ and M is Biot's modulus. $W'(\mathbf{E})$ is the hyperelastic strain energy density for the elastic material in a drained state, i.e. when $p_F = 0$. The stress-strain relationship is given by the following equations

$$\mathbf{S}' = \frac{\partial W'(\mathbf{E})}{\partial \mathbf{E}}, \tag{A.68a}$$

$$p_F = M(\zeta + J - 1), \tag{A.68b}$$

where $\mathbf{S}'$ is known as the *effective* stress tensor, whereby the total stress $\mathbf{S}$ is obtained by adding the stress in the fluid

$$\mathbf{S} = \mathbf{S}' + \mathbf{S}_F = \frac{\partial W'(\mathbf{E})}{\partial \mathbf{E}} - Jp_F\mathbf{C}^{-1}. \tag{A.69}$$

Linear poroelasticity

The original Biot's theory[150] was derived under the assumption of infinitesimal deformations. As in the theory of linear elasticity, we can write the strain energy density of a linear poroelastic material as

$$W(\varepsilon_{ij}, \zeta) = \frac{1}{2}\left(K_u - \frac{2\mu}{3}\right)\varepsilon_{kk}^2 + \mu\varepsilon_{ij}\varepsilon_{ji} + \frac{1}{2}M\left(\zeta^2 - 2\alpha\zeta\varepsilon_{kk}\right), \tag{A.70}$$

where K_u is the undrained bulk modulus. Similarly to Eq.(A.68), the stress-strain relationships are obtained by derivation as

$$\sigma'_{ij} = 2\mu\varepsilon_{ij} + \left(K - \frac{2\mu}{3}\right)\delta_{ij}\varepsilon_{kk}, \quad \text{with} \quad \sigma'_{ij} = \sigma_{ij} + \alpha\delta_{ij}p_F, \tag{A.71a}$$

$$p_F = M\left(\zeta - \alpha\varepsilon_{kk}\right), \tag{A.71b}$$

where K is the elastic bulk modulus, with $K = K_u - \alpha^2 M$, and α is Biot's effective stress coefficient. When the solid deformation is null, Biot's modulus is the constant of proportionality between the fluid pressure and the variation of fluid content ζ

$$p_F = M\zeta, \tag{A.72}$$

with the inverse $1/M$ measuring the change in fluid content due to a variation of fluid pressure. Biot's effective stress coefficient α is included in the definition of the effective stress tensor $\boldsymbol{\sigma}'$ to account for the solid skeleton compressibility (in the limit of $\alpha = 1$ we assume an incompressible solid skeleton).

Darcy's law, Eq.(A.63), combined with Eq.(A.71b), allows us to derive the following diffusion equation

$$\frac{1}{M}\frac{\partial p_F}{\partial t} - \frac{K_F}{\eta_F}\nabla^2 p_F = -\alpha\frac{\partial\varepsilon_{kk}}{\partial t}, \tag{A.73}$$

where we recognise a structure similar to the equation of thermoelasticity, with the pore pressure field coupled to the hydrostatic deformation of the gel. Notice that in Eq.(A.73) we have considered an isotropic material, so that $\mathbf{K}_F = K_F\mathbf{I}$.

A.3. Formulation of viscoelasticity

Viscoelastic materials exposed to a fixed stain are characterised by an instantaneous elastic response and a time-dependent behaviour defined by a stress relaxation function, or a creep function if subjected to a fixed stress. The mathematical formulation of viscoelasticity summarised here and adopted in the thesis can be found in standard textbooks (for instance, see Simo[236] and Christensen[237]). We first introduce the fundamental equations in the limits of linear viscoelasticity, as they are easier to manage, and then move to the finite strain formulation which is suitable for large strain analyses and non-linear viscoelastic materials.

The time-dependent stress-strain relationship is written as

$$\boldsymbol{\sigma}(t) = \int_0^t \mathbf{G}(t-\tau)\dot{\boldsymbol{\varepsilon}}(\tau)\mathrm{d}\tau, \tag{A.74}$$

where $\mathbf{G}(t)$ is a tensor-valued stress relaxation function and ε is the strain tensor, where the dot superscript denotes time derivation. The stress tensor $\boldsymbol{\sigma}$ and the strain tensor $\boldsymbol{\varepsilon}$ are decomposed in a deviatoric and a volumetric part as follows

$$\boldsymbol{\sigma} = \mathbf{s} + p\mathbf{I}, \quad \text{with} \quad p = \frac{1}{3}\mathrm{tr}\,\boldsymbol{\sigma}; \tag{A.75a}$$

$$\boldsymbol{\varepsilon} = \mathbf{e} + \phi\mathbf{I}, \quad \text{with} \quad \phi = \frac{1}{3}\mathrm{tr}\,\boldsymbol{\varepsilon}. \tag{A.75b}$$

Introducing the assumption of isotropy, the stress can be written in terms of two independent relaxation functions as shown below

$$\boldsymbol{\sigma}(t) = \int_0^t G_1(t-\tau)\,\dot{\mathbf{e}}(\tau)\,\mathrm{d}\tau + \frac{1}{3}\mathbf{I}\int_0^t G_2(t-\tau)\,\dot{\phi}(\tau)\,\mathrm{d}\tau\,, \tag{A.76}$$

where $\mathbf{e}$ and ϕ are, respectively, the deviatoric strain tensor and the volumetric strain. It is common practice to express $G_1(t)$ and $G_2(t)$ in terms of the bulk and the shear moduli of the material, where

$$\mu(t) = G_1(t)/2 \quad \text{and} \quad K(t) = G_2(t)/3. \tag{A.77}$$

A common formulation writes the isotropic relaxation functions in terms of a series of exponentials known as the Prony series

$$K(t) = K_\infty + \sum_{i=1}^{N} K_i e^{-t/t_i}, \tag{A.78a}$$

$$\mu(t) = \mu_\infty + \sum_{i=1}^{N} \mu_i e^{-t/t_i}, \tag{A.78b}$$

where K_∞ and μ_∞ are the long-term bulk and shear moduli. Notice that this description represents a generalisation of the standard Maxwell model with N elements arranged in parallel. For convenience, we can derive a normalised form; with respect to the shear modulus relaxation, for instance, we may write

$$g(t) = \frac{\mu(t)}{\mu_0} = g_\infty + \sum_{i=1}^{N} g_i e^{-t/t_i}, \tag{A.79}$$

where g_i are the normalised relaxation parameters and μ_0 is the instantaneous shear modulus given by

$$\mu_0 = \mu_\infty + \sum_{i=1}^{N} \mu_i. \tag{A.80}$$

Focusing on the deviatoric component, the stress response is derived from Eqs.(A.76)-(A.78b) combined with the definitions in Eqs.(A.79)-(A.80)

$$\mathbf{s}(t) = 2\mu_0\left(g_\infty \mathbf{e}(t) + \sum_{i=1}^{N} g_i \mathbf{e}_i(t)\right), \tag{A.81}$$

where $\mathbf{e}_i(t)$ is the deviatoric viscous strain in each term of the Prony series defined by

$$\mathbf{e}_i(t) = \int_0^t e^{(\tau-t)/t_i}\,\dot{\mathbf{e}}(\tau)\,\mathrm{d}\tau. \tag{A.82}$$

To derive the formulation of viscoelasticity in finite strains, we start from an alternative expression of the stress in Eq.(A.81), given by

$$\mathbf{s}(t) = \mathbf{s}_0(t) - \sum_{i=1}^{N} \mathbf{h}_i(t), \tag{A.83}$$

where $\mathbf{h}_i$ are internal stress variables and $\mathbf{s}_0$ denotes the instantaneous elastic response. The internal variables are obtained from the solution of rate equations for a single Maxwell element, written in the following form

$$\begin{cases} \dot{\mathbf{h}}_i + \frac{1}{t_i}\mathbf{h}_i = g_i \dot{\mathbf{s}}_0 \\ \lim\limits_{t\to\infty} \mathbf{h}_i = 0 \end{cases}. \tag{A.84}$$

With respect to the reference configuration, the second Piola-Kirchoff stress is split according to Eq.(A.59), and following Eq.(A.83) the deviatoric stress response is written as

$$\bar{\mathbf{S}} = \bar{\mathbf{S}}_0 - \sum_{i=1}^{N} \mathbf{H}_i(t), \tag{A.85}$$

where $\mathbf{H}_i$ are internal stress variables governed by rate equations analogous to Eq.(A.84)

$$\begin{cases} \dot{\mathbf{H}}_i + \frac{1}{t_i}\mathbf{H}_i = g_i \dot{\bar{\mathbf{S}}}_0 \\ \lim\limits_{t\to\infty} \mathbf{H}_i = 0 \end{cases}. \tag{A.86}$$

Omitting the complete mathematical derivation, the deviatoric stress is written similarly to Eq.(A.81) as

$$\bar{\mathbf{S}}(t) = g_\infty \, \bar{\mathbf{S}}(t) + \sum_{i=1}^{N} g_i \bar{\mathbf{S}}_i(t), \tag{A.87}$$

where $\bar{\mathbf{S}}_i(t)$ is the deviatoric viscous stress in each term of the Prony series, defined by

$$\bar{\mathbf{S}}_i(t) = \int_0^t e^{(\tau - t)/t_i} \frac{\partial \bar{\mathbf{S}}(t)}{\partial \tau} \mathrm{d}\tau. \tag{A.88}$$

Similar equations can be derived in the case of time-dependent bulk behaviour.

A.4. Finite elements applied to fracture mechanics

Finite element (FE) analysis is nowadays a standard computational method in fracture mechanics. Here we collect some guidelines for a correct use of the FE method, that have been followed in the numerical examples presented in this thesis in order to ensure a good accuracy of the results[238].

The design of a high-quality finite element mesh is the first essential ingredient. In problems involving the presence of a crack, a fundamental difficulty is posed by the singularities in the strain and stress fields, which can be poorly approximated by conventional finite elements. With respect to the type of element, in two-dimensional problems we have several possibilities. Constant strain triangles are those less suitable to reproduce the large gradients in proximity of the crack tip, therefore they should not be used when the aim of the analyses is to compute stress singularities or the stress intensity factors. Isoparametric elements (linear or quadratic) provide superior performances in approximating complex and irregular boundaries, however they also have limitations due to the crack singularity, which cannot be overcome with a refinement of the mesh. This led to the development of special crack-tip elements, to be used to discretise the surroundings of the crack tip while regular elements can be used elsewhere in the model.

One of the simplest type is derived from a modification of the isoparametric elements through nodal distorted shape functions that can approximate the crack-tip fields. In quarter-point elements, the isoparametric quadratic shape functions are modified by shifting the mid-side nodes to the quarter-point position along the edges of elements pointing to the crack tip. The emergence of a $-1/2$ power dependence with the distance from the tip reproduces the singularity displayed by the strain and stress components in linear elastic materials. In this case, the crack-tip mesh can consist of refined layers of quadratic eight-node elements and quarter-point elements connected to the crack tip (Fig.A.3a). However, this configuration reproduces the angular dependence of the near-field solution poorly, so that the recommended choice is to adopt six-node quadratic elements or distorted eight-node elements arranged in a fan shape around the tip. One side of the element is collapsed to a point so that the nodes have identical coordinates (Fig.A.3b).

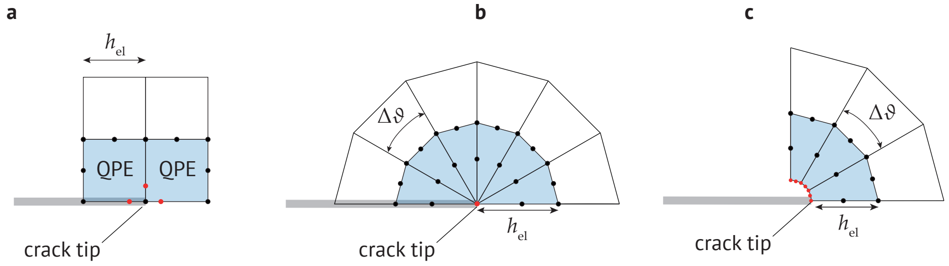

Figure A.3 Finite element mesh at the crack tip. **a** Isoparametric eight-node elements and quarter-point elements (QPE) at the crack tip. **b** Isoparametric eight-node elements with collapsed tip elements. **c** Isoparametric eight-node elements with blunted tip for large strain analyses

Various combinations, using collapsed eight-node elements and mid-side node shifting, are employed to model different material behaviours:

- *linear elastic materials*. The strain singularity is $-1/2$. Recommended choice: eight-node elements with collapsed coincident nodes and mid-side nodes shifted to quarter-point positions;
- *perfectly plastic materials*. The strain singularity is -1. Recommended choice: eight-node elements with collapsed nodes, left free to move independently;
- *strain-hardening materials*. The strain singularity is proportional to $-n/(n+1)$ (n is the strain-hardening parameter). Recommended choice: eight-node elements with collapsed nodes, free to move independently and mid-side nodes shifted to quarter-point positions.

In large strain analyses where singular crack-tip fields are not required, it is advisable to model the crack tip as a blunted notch with a small radius of curvature, the presence of which should not influence the results (Fig.A.3c).

The solution accuracy depends on the mesh refinement through the characteristic size of the tip elements h_{el} and the angular span $\Delta\vartheta$. As general indications we can assume to be satisfactory elements with h_{el} comprised between 1/100 and 1/20 of the crack length and an angular span $\Delta\vartheta$ not larger than 30°. The element size might need to be decreased further if the purpose is to describe the near-tip singularities under small applied loads, where the zone dominated by the asymptotic solution is extremely concentrated around the tip.

Stress intensity factors

The stress intensity factor (SIF) in linear elastic fracture mechanics may be obtained from finite elements analyses employing the expressions of the near field solution, either in terms of stresses or displacements. With respect to the coordinates (r, ϑ) we have the following expressions (in mode-I)

$$K_I(r,\vartheta) = 2\mu\sqrt{\frac{2\pi}{r}}\,\frac{u_i(r,\vartheta)}{g_i(\vartheta)}, \tag{A.89a}$$

$$K_I(r,\vartheta) = \sqrt{2\pi r}\,\frac{\sigma_{ij}(r,\vartheta)}{f_{ij}(\vartheta)}, \tag{A.89b}$$

where $i, j = 1, 2$ are, respectively, the tangential and normal directions to the crack, and $g_i(\vartheta)$, $f_{ij}(\vartheta)$ are the angular functions.

The best precision is achieved using the expression in terms of displacements, which are nodal variables instead of stresses, which are given at the integration points. In particular, using the opening displacements of nodes located along the crack face we may write

$$K_I = \lim_{r\to 0} u_2(r, \vartheta = \pi)\frac{\kappa}{2\mu}\sqrt{\frac{2\pi}{r}}, \tag{A.90}$$

where κ is the Kolosov's constant. Because the results too close to the crack tip might be inaccurate, it is usual practice to obtain K_I through a linear extrapolation from the mid-range nodes towards $r \to 0$, provided that these are still within the K-dominated region (Fig.A.4a). Notice that if we use quarter-point elements, an alternative expression can be derived directly from the nodal displacements of the quarter-point element[238].

J-integral computation

The J-integral is a line integral that can be applied both to linear and non-linear problems to evaluate the strain energy per unit of crack surface area. In elastic materials, i.e. when energy dissipation is negligible, the J-integral is path independent and provides a measure of the crack driving energy, in the form of the strain energy release rate G. The numerical computation of the J-integral is based on the energy domain integral methodology[239], which is implemented in most commercial FE software.

A standard definition of the J-integral in quasi-static conditions can be written as[239]

$$J = \int_C \left(W n_1 - \frac{\partial u_i}{\partial x_1}\sigma_{ij} n_j \right) \mathrm{d}s, \tag{A.91}$$

where W is the strain energy density and n_j is the unit vector normal to the contour C.

If the contour C becomes vanishingly small, the numerical solution is problematic, and a modified definition of J might be introduced. In practice, we consider an area A enclosed by an inner contour C_0 and an outer contour C_1 (Fig.A.4b). Equation (A.91) is transformed into

$$J = \int_A \left(\frac{\partial u_i}{\partial x_1} \sigma_{ij} - W \delta_{1i} \right) \frac{\partial q}{\partial x_i} \mathrm{d}A, \tag{A.92}$$

where q is a smooth function that is equal to unity on C_0 and vanishes on C_1.

In FE analyses, the inner contour C_0 is shrunk onto the crack tip and the unit normal vector is defined to specify the virtual crack extension direction. The boundary of the outer contour C_1 should coincide with the mesh edges, and the function q is specified at the nodes of the element boundaries and interpolated using the element shape functions.

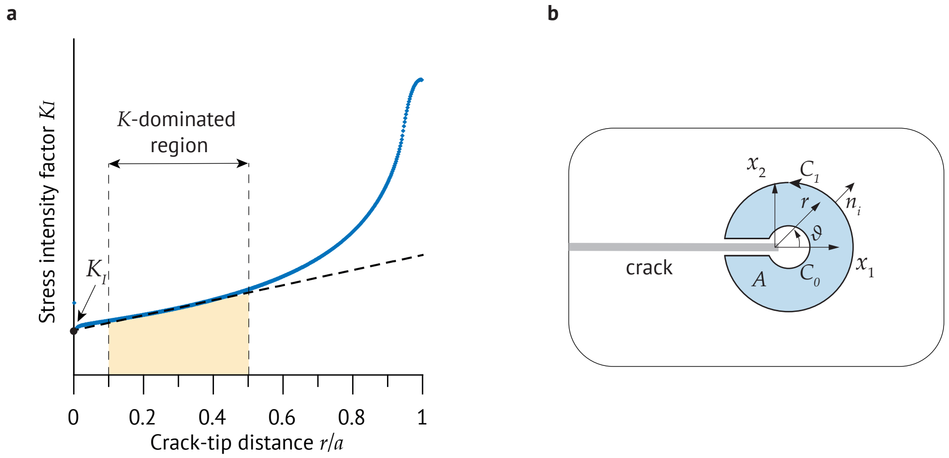

Figure A.4 **a** FE computation of the stress intensity factor K_I, showing the optimal range of the crack-tip distance r/a where to extrapolate the results from. **b** Sketch of the closed region in which the J-integral is evaluated, according to the domain integral method

Bibliography

[1] Bruck, H., Evans, J. and Peterson, M. (2002) The Role of Mechanics in Biological and Biologically Inspired Materials. *Experimental Mechanics*, **42**(4), 361–371.

[2] Bao, G. and Suresh, S. (2003) Cell and molecular mechanics of biological materials. *Nature Materials*, **2**(11), 715–725.

[3] Buehler, M.J. (2010) Multiscale mechanics of biological and biologically inspired materials and structures. *Acta Mechanica Solida Sinica*, **23**(6), 471–483.

[4] Wegst, U.G.K., Bai, H., Saiz, E., Tomsia, A.P. and Ritchie, R.O. (2015) Bioinspired structural materials. *Nature Materials*, **14**(1), 23–36.

[5] Lee, K.Y. and Mooney, D.J. (2001) Hydrogels for Tissue Engineering. *Chemical Reviews*, **101**(7), 1869–1880.

[6] Hollister, S.J. (2005) Porous scaffold design for tissue engineering. *Nature Materials*, **4**(7), 518–524.

[7] Calvert, P. (2009) Hydrogels for Soft Machines. *Advanced Materials*, **21**(7), 743–756.

[8] Hoffman, A.S. (2012) Hydrogels for biomedical applications. *Advanced Drug Delivery Reviews*, **64**, 18–23.

[9] Suo, Z. (2012) Mechanics of stretchable electronics and soft machines. *MRS Bulletin*, **37**(3), 218–225.

[10] Dimas, L.S. and Buehler, M.J. (2014) Modeling and additive manufacturing of bio-inspired composites with tunable fracture mechanical properties. *Soft Matter*, **10**(25), 4436.

[11] Shang, J. and Theato, P. (2018) Smart composite hydrogel with pH-, ionic strength- and temperature-induced actuation. *Soft Matter*, **14**(41), 8401–8407.

[12] Jia, Z., Yu, Y. and Wang, L. (2019) Learning from nature: Use material architecture to break the performance tradeoffs. *Materials & Design*, **168**, 107650.

[13] Baik, S., Lee, H.J., Kim, D.W., Kim, J.W., Lee, Y. and Pang, C. (2019) Bioinspired Adhesive Architectures: From Skin Patch to Integrated Bioelectronics. *Advanced Materials*, **31**(34), 1803309.

[14] Zhu, Y., Zhang, Q., Shi, X. and Han, D. (2019) Hierarchical Hydrogel Composite Interfaces with Robust Mechanical Properties for Biomedical Applications. *Advanced Materials*, **1804950**, 1804950.

[15] Ritchie, R.O. (2011) The conflicts between strength and toughness. *Nature Materials*, **10**(11), 817–822.

[16] Yang, W., Sherman, V.R., Gludovatz, B., Schaible, E., Stewart, P., Ritchie, R.O. and Meyers, M.A. (2015) On the tear resistance of skin. *Nature Communications*, **6**(1), 6649.

[17] Holzapfel, G.A. (2005) Similarities between soft biological tissues and rubberlike materials. In *Constitutive Models for Rubber IV*. Routledge, Leiden.

[18] Yang, W., Meyers, M.A. and Ritchie, R.O. (2019) Structural architectures with toughening mechanisms in Nature: A review of the materials science of Type-I collagenous materials. *Progress in Materials Science*, **103**(January), 425–483.

[19] Storm, C., Pastore, J.J., MacKintosh, F.C., Lubensky, T.C. and Janmey, P.A. (2005) Nonlinear elasticity in biological gels. *Nature*, **435**(7039), 191–194.

[20] Gordon, J.E. (1978) *Structures, or why things don't fall down*. Springer US, New York.

[21] Mai, Y.W. and Atkins, A.G. (1989) Further comments on J-shaped stress-strain curves and the crack resistance of biological materials. *Journal of Physics D: Applied Physics*, **22**(1), 48–54.

[22] Horgan, C.O. and Smayda, M.G. (2012) The trousers test for tearing of soft biomaterials. *International Journal of Solids and Structures*, **49**(1), 161–169.

[23] Mow, V.C., Kuei, S.C., Lai, W.M. and Armstrong, C.G. (1980) Biphasic Creep and Stress Relaxation of Articular Cartilage in Compression: Theory and Experiments. *Journal of Biomechanical Engineering*, **102**(1), 73–84.

[24] Han, G., Eriten, M. and Henak, C.R. (2019) Rate-dependent crack nucleation in cartilage under microindentation. *Journal of the Mechanical Behavior of Biomedical Materials*, **96**, 186–192.

[25] Kaczmarek, M. (1997) The hydromechanics of hydrocephalus: Steady-state solutions for cylindrical geometry. *Bulletin of Mathematical Biology*, **59**(2), 295–323.

[26] Miller, K. (1999) Constitutive model of brain tissue suitable for finite element analysis of surgical procedures. *Journal of Biomechanics*, **32**(5), 531–537.

[27] Miller, K. and Chinzei, K. (2002) Mechanical properties of brain tissue in tension. *Journal of Biomechanics*, **35**(4), 483–490.

[28] Franceschini, G. (2006) *The mechanics of human brain tissue*. Ph.D. thesis, University of Trento.

[29] Budday, S., Sommer, G., Birkl, C., Langkammer, C., Haybaeck, J., Kohnert, J., Bauer, M., Paulsen, F., Steinmann, P., Kuhl, E. and Holzapfel, G.A. (2017) Mechanical characterization of human brain tissue. *Acta Biomaterialia*, **48**, 319–340.

[30] Forte, A.E., Gentleman, S.M. and Dini, D. (2017) On the characterization of the heterogeneous mechanical response of human brain tissue. *Biomechanics and Modeling in Mechanobiology*, **16**(3), 907–920.

[31] Forte, A.E., Galvan, S. and Dini, D. (2018) Models and tissue mimics for brain shift simulations. *Biomechanics and Modeling in Mechanobiology*, **17**(1), 249–261.

[32] Zhao, X. (2014) Multi-scale multi-mechanism design of tough hydrogels: building dissipation into stretchy networks. *Soft Matter*, **10**(5), 672–687.

[33] Shergold, O.A. and Fleck, N.A. (2004) Mechanisms of deep penetration of soft solids, with application to the injection and wounding of skin. *Proceedings of the Royal Society of London. Series A: Mathematical, Physical and Engineering Sciences*, **460**(2050), 3037–3058.

[34] Shergold, O.A. and Fleck, N.A. (2005) Experimental Investigation Into the Deep Penetration of Soft Solids by Sharp and Blunt Punches, With Application to the Piercing of Skin. *Journal of Biomechanical Engineering*, **127**(5), 838–848.

[35] Roberts, J.J., Earnshaw, A., Ferguson, V.L. and Bryant, S.J. (2011) Comparative study of the viscoelastic mechanical behavior of agarose and poly(ethylene glycol) hydrogels. *Journal of Biomedical Materials Research Part B: Applied Biomaterials*, **99B**(1), 158–169.

[36] Djabourov, M. (1991) Gelation—A review. *Polymer International*, **25**(3), 135–143.

[37] Luyten, H. and Van Vliet, T. (1995) Fracture properties of starch gels and their rate dependency. *Journal of Texture Studies*, **26**(3), 281–298.

[38] Van Vliet, T. and Walstra, P. (1995) Large deformation and fracture behaviour of gels. *Faraday Discussions*, **101**, 359–370.

[39] Baumberger, T., Caroli, C. and Martina, D. (2006) Fracture of a biopolymer gel as a viscoplastic disentanglement process. *The European Physical Journal E*, **21**(1), 81–89.

[40] Baumberger, T., Caroli, C. and Martina, D. (2006) Solvent control of crack dynamics in a reversible hydrogel. *Nature Materials*, **5**(7), 552–555.

[41] Seitz, M.E., Martina, D., Baumberger, T., Krishnan, V.R., Hui, C.Y. and Shull, K.R. (2009) Fracture and large strain behavior of self-assembled triblock copolymer gels. *Soft Matter*, **5**(2), 447–456.

[42] Kwon, H., Rogalsky, A.D. and Kim, D.W. (2011) On the measurement of fracture toughness of soft biogel. *Polymer Engineering & Science*, **51**(6), 1078–1086.

[43] Lake, G.J. and Thomas, A.G. (1967) The strength of highly elastic materials. *Proceedings of the Royal Society of London. Series A. Mathematical and Physical Sciences*, **300**(1460), 108–119.

[44] Forte, A.E., D'Amico, F., Charalambides, M.N., Dini, D. and Williams, J.G. (2015) Modelling and experimental characterisation of the rate dependent fracture properties of gelatine gels. *Food Hydrocolloids*, **46**, 180–190.

[45] Forte, A.E., Galvan, S., Manieri, F., Rodriguez y Baena, F. and Dini, D. (2016) A composite hydrogel for brain tissue phantoms. *Materials & Design*, **112**, 227–238.

[46] Leibinger, A., Forte, A.E., Tan, Z., Oldfield, M.J., Beyrau, F., Dini, D. and Rodriguez y Baena, F. (2016) Soft Tissue Phantoms for Realistic Needle Insertion: A Comparative Study. *Annals of Biomedical Engineering*, **44**(8), 2442–2452.

[47] Tan, Z., Dini, D., Rodriguez y Baena, F. and Forte, A.E. (2018) Composite hydrogel: A high fidelity soft tissue mimic for surgery. *Materials & Design*, **160**, 886–894.

[48] Shull, K.R. (2006) Fracture and adhesion of elastomers and gels: Large strains at small length scales. *Journal of Polymer Science Part B: Polymer Physics*, **44**(24), 3436–3439.

[49] Long, R. and Hui, C.Y. (2016) Fracture toughness of hydrogels: measurement and interpretation. *Soft Matter*, **12**(39), 8069–8086.

[50] Creton, C. and Ciccotti, M. (2016) Fracture and adhesion of soft materials: a review. *Reports on Progress in Physics*, **79**(4), 046601.

[51] Creton, C. (2017) 50th Anniversary Perspective: Networks and Gels: Soft but Dynamic and Tough. *Macromolecules*, **50**(21), 8297–8316.

[52] Tanaka, Y., Fukao, K. and Miyamoto, Y. (2000) Fracture energy of gels. *The European Physical Journal E*, **3**(4), 395–401.

[53] Zhang, T., Lin, S., Yuk, H. and Zhao, X. (2015) Predicting fracture energies and crack-tip fields of soft tough materials. *Extreme Mechanics Letters*, **4**, 1–8.

[54] Zhang, T., Yuk, H., Lin, S., Parada, G.A. and Zhao, X. (2017) Tough and tunable adhesion of hydrogels: experiments and models. *Acta Mechanica Sinica*, **33**(3), 543–554.

[55] Gong, J.P., Katsuyama, Y., Kurokawa, T. and Osada, Y. (2003) Double-Network Hydrogels with Extremely High Mechanical Strength. *Advanced Materials*, **15**(14), 1155–1158.

[56] Gong, J.P. (2010) Why are double network hydrogels so tough? *Soft Matter*, **6**(12), 2583.

[57] Sun, J.Y., Zhao, X., Illeperuma, W.R.K., Chaudhuri, O., Oh, K.H., Mooney, D.J., Vlassak, J.J. and Suo, Z. (2012) Highly stretchable and tough hydrogels. *Nature*, **489**(7414), 133–136.

[58] Zhang, Z., Liu, J., Li, S., Gao, K., Ganesan, V. and Zhang, L. (2019) Constructing Sacrificial Multiple Networks to Toughen Elastomer. *Macromolecules*, **52**(11), 4154–4168.

[59] Chen, C., Wang, Z. and Suo, Z. (2017) Flaw sensitivity of highly stretchable materials. *Extreme Mechanics Letters*, **10**, 50–57.

[60] Li, W. (2016) Damage Models for Soft Tissues: A Survey. *Journal of Medical and Biological Engineering*, **36**(3), 285–307.

[61] Czerner, M., Fasce, L.A., Martucci, J.F., Ruseckaite, R. and Frontini, P.M. (2016) Deformation and fracture behavior of physical gelatin gel systems. *Food Hydrocolloids*, **60**, 299–307.

[62] Atkins, A.G. (2009) *The Science and Engineering of Cutting*. Butterworth-Heinemann/Elsevier, Oxford.

[63] Hill, R., Lee, E.H. and Tupper, S.J. (1947) The theory of wedge indentation of ductile materials. *Proceedings of the Royal Society of London. Series A. Mathematical and Physical Sciences*, **188**(1013), 273–289.

[64] Lundberg, B. (1974) Penetration of rock by conical indenters. *International Journal of Rock Mechanics and Mining Sciences & Geomechanics Abstracts*, **11**(6), 209–214.

[65] Atkins, A.G. (2003) Modelling metal cutting using modern ductile fracture mechanics: quantitative explanations for some longstanding problems. *International Journal of Mechanical Sciences*, **45**(2), 373–396.

[66] Atkins, A.G. (2005) Toughness and cutting: a new way of simultaneously determining ductile fracture toughness and strength. *Engineering Fracture Mechanics*, **72**(6), 849–860.

[67] Truman, C.E., Sackfield, A. and Hills, D.A. (1995) Contact mechanics of wedge and cone indenters. *International Journal of Mechanical Sciences*, **37**(3), 261–275.

[68] Ciavarella, M., Hills, D.A. and Monno, G. (1998) Contact problems for a wedge with rounded apex. *International Journal of Mechanical Sciences*, **40**(10), 977–988.

[69] Shull, K.R. (2002) Contact mechanics and the adhesion of soft solids. *Materials Science and Engineering: R: Reports*, **36**(1), 1–45.

[70] Reyssat, E., Tallinen, T., Le Merrer, M. and Mahadevan, L. (2012) Slicing Softly with Shear. *Physical Review Letters*, **109**(24), 244301.

[71] Liu, J., Chen, Z., Liang, X., Huang, X., Mao, G., Hong, W., Yu, H. and Qu, S. (2018) Puncture mechanics of soft elastomeric membrane with large deformation by rigid cylindrical indenter. *Journal of the Mechanics and Physics of Solids*, **112**, 458–471.

[72] Spagnoli, A., Terzano, M., Brighenti, R., Artoni, F. and Ståhle, P. (2018) The fracture mechanics in cutting: A comparative study on hard and soft polymeric materials. *International Journal of Mechanical Sciences*, **148**, 554–564.

[73] Terzano, M., Spagnoli, A. and Ståhle, P. (2018) A fracture mechanics model to study indentation cutting. *Fatigue & Fracture of Engineering Materials & Structures*, **41**(4), 821–830.

[74] Dunn, P.D., Burton, J.D., Xu, X. and Atkins, A.G. (2007) Paths swept out by initially slack flexible wires when cutting soft solids; when passing through a very viscous medium; and during regelation. *Proceedings of the Royal Society A: Mathematical, Physical and Engineering Sciences*, **463**(2077), 1–20.

[75] Reilly, G., McCormack, B.A.O. and Taylor, D. (2004) Cutting sharpness measurement: a critical review. *Journal of Materials Processing Technology*, **153-154**(1-3), 261–267.

[76] McCarthy, C., Hussey, M. and Gilchrist, M. (2007) On the sharpness of straight edge blades in cutting soft solids: Part I – indentation experiments. *Engineering Fracture Mechanics*, **74**(14), 2205–2224.

[77] Frick, T., Marucci, D., Cartmill, J., Martin, C. and Walsh, W. (2001) Resistance forces acting on suture needles. *Journal of Biomechanics*, **34**(10), 1335–1340.

[78] McGorry, R.W., Dowd, P.C. and Dempsey, P.G. (2005) The effect of blade finish and blade edge angle on forces used in meat cutting operations. *Applied Ergonomics*, **36**(1), 71–77.

[79] Atkins, A.G., Xu, X. and Jeronimidis, G. (2004) Cutting, by 'pressing and slicing,' of thin floppy slices of materials illustrated by experiments on cheddar cheese and salami. *Journal of Materials Science*, **39**(8), 2761–2766.

[80] Deibel, K.R., Raemy, C. and Wegener, K. (2014) Modeling slice-push cutting forces of a sheet stack based on fracture mechanics. *Engineering Fracture Mechanics*, **124-125**, 234–247.

[81] Spagnoli, A., Brighenti, R., Terzano, M. and Artoni, F. (2019) Cutting resistance of soft materials: Effects of blade inclination and friction. *Theoretical and Applied Fracture Mechanics*, **101**, 200–206.

[82] Rivlin, R.S. and Thomas, A.G. (1953) Rupture of rubber. I. Characteristic energy for tearing. *Journal of Polymer Science*, **10**(3), 291–318.

[83] Lake, G.J. and Yeoh, O.H. (1978) Measurement of rubber cutting resistance in the absence of friction. *International Journal of Fracture*, **14**(5), 509–526.

[84] Anderson, T.L. (2005) *Fracture Mechanics: Fundamentals and Applications*. CRC Press/Taylor & Francis, Boca Raton (Fla.), third edition.

[85] Spagnoli, A., Carpinteri, A. and Terzano, M. (2018) Near-tip stress fields of rough and frictional cracks under mixed-mode loading. *Fatigue & Fracture of Engineering Materials & Structures*, **41**(10), 2099–2109.

[86] Hills, D.A., Kelly, P.A., Dai, D.N., Korsunsky, A.M. and Keer, L.M. (1996) *Solution of Crack Problems: The Distributed Dislocation Technique*. Springer Netherlands, Heidelberg.

[87] Hui, C.Y., Ruina, A., Creton, C. and Kramer, E.J. (1992) Micromechanics of crack growth into a craze in a polymer glass. *Macromolecules*, **25**(15), 3948–3955.

[88] Kono, R. (1960) The Dynamic Bulk Viscosity of Polystyrene and Polymethyl Methacrylate. *Journal of the Physical Society of Japan*, **15**(4), 718–725.

[89] Blaber, J., Adair, B. and Antoniou, A. (2015) Ncorr: Open-Source 2D Digital Image Correlation Matlab Software. *Experimental Mechanics*, **55**(6), 1105–1122.

[90] Cotterell, B. (2010) *Fracture and life*. Imperial College Press, London.

[91] Griffith, A.A. (1921) The Phenomena of Rupture and Flow in Solids. *Philosophical Transactions of the Royal Society A: Mathematical, Physical and Engineering Sciences*, **221**(582-593), 163–198.

[92] Thomas, A.G. (1955) Rupture of rubber. II. The strain concentration at an incision. *Journal of Polymer Science*, **18**(88), 177–188.

[93] Vincent, J.F., Jeronimidis, G., Khan, A.A. and Luyten, H. (1991) The wedge fracture test a new method for measurement of food texture. *Journal of Texture Studies*, **22**(1), 45–57.

[94] Doran, C.F., McCormack, B.A.O. and Macey, A. (2004) A Simplified Model to Determine the Contribution of Strain Energy in the Failure Process of Thin Biological Membranes during Cutting. *Strain*, **40**(4), 173–179.

[95] Azar, T. and Hayward, V. (2008) Estimation of the Fracture Toughness of Soft Tissue from Needle Insertion. In F. Bello and P.J.E. Edwards, editors, *Biomedical Simulation*, pages 166–175. Springer Berlin Heidelberg, Berlin, Heidelberg.

[96] Fakhouri, S., Hutchens, S.B. and Crosby, A.J. (2015) Puncture mechanics of soft solids. *Soft Matter*, **11**(23), 4723–4730.

[97] Barney, C.W., Zheng, Y., Wu, S., Cai, S. and Crosby, A.J. (2019) Residual strain effects in needle-induced cavitation. *Soft Matter*, **15**(37), 7390–7397.

[98] Kamyab, I., Chakrabarti, S. and Williams, J.G. (1998) Cutting cheese with wire. *Journal of Materials Science*, **33**(11), 2763–2770.

[99] Patel, Y., Blackman, B. and Williams, J.G. (2009) Determining fracture toughness from cutting tests on polymers. *Engineering Fracture Mechanics*, **76**(18), 2711–2730.

[100] Irwin, G. (1957) Analysis of Stresses and Strains Near the End of a Crack Traversing a Plate. *Journal of Applied Mechanics*, **24**, 361–364.

[101] Rice, J.R. (1968) A Path Independent Integral and the Approximate Analysis of Strain Concentration by Notches and Cracks. *Journal of Applied Mechanics*, **35**(2), 379–386.

[102] Knowles, J.K. and Sternberg, E. (1973) An asymptotic finite-deformation analysis of the elastostatic field near the tip of a crack. *Journal of Elasticity*, **3**(2), 67–107.

[103] Knowles, J.K. and Sternberg, E. (1974) Finite-deformation analysis of the elastostatic field near the tip of a crack: Reconsideration and higher-order results. *Journal of Elasticity*, **4**(3), 201–233.

[104] Knowles, J.K. (1977) The finite anti-plane shear field near the tip of a crack for a class of incompressible elastic solids. *International Journal of Fracture*, **13**(5), 611–639.

[105] Stephenson, R.A. (1982) The equilibrium field near the tip of a crack for finite plane strain of incompressible elastic materials. *Journal of Elasticity*, **12**(1), 65–99.

[106] Knowles, J.K. and Sternberg, E. (1983) Large deformations near a tip of an interface-crack between two Neo-Hookean sheets. *Journal of Elasticity*, **13**(3), 257–293.

[107] Geubelle, P.H. and Knauss, W.G. (1994) Finite strains at the tip of a crack in a sheet of hyperelastic material: I. Homogeneous case. *Journal of Elasticity*, **35**(1-3), 61–98.

[108] Hui, C.Y., Jagota, A., Bennison, S.J. and Londono, J.D. (2003) Crack blunting and the strength of soft elastic solids. *Proceedings of the Royal Society of London. Series A: Mathematical, Physical and Engineering Sciences*, **459**(2034), 1489–1516.

[109] Mao, Y., Talamini, B. and Anand, L. (2017) Rupture of polymers by chain scission. *Extreme Mechanics Letters*, **13**, 17–24.

[110] Yang, C., Yin, T. and Suo, Z. (2019) Polyacrylamide hydrogels. I. Network imperfection. *Journal of the Mechanics and Physics of Solids*, **131**, 43–55.

[111] Gao, H., Ji, B., Jager, I.L., Arzt, E. and Fratzl, P. (2003) Materials become insensitive to flaws at nanoscale: Lessons from nature. *Proceedings of the National Academy of Sciences*, **100**(10), 5597–5600.

[112] Mirzaeifar, R., Dimas, L.S., Qin, Z. and Buehler, M.J. (2015) Defect-Tolerant Bioinspired Hierarchical Composites: Simulation and Experiment. *ACS Biomaterials Science & Engineering*, **1**(5), 295–304.

[113] Inglis CE (1913) Stresses in a plate due to the presence of cracks and sharp corners. *Transactions of the Institution of Naval Architects*, **55**, 219–230.

[114] Creager, M. and Paris, P.C. (1967) Elastic field equations for blunt cracks with reference to stress corrosion cracking. *International Journal of Fracture Mechanics*, **3**(4), 247–252.

[115] Spagnoli, A., Terzano, M., Brighenti, R., Artoni, F. and Carpinteri, A. (2019) How Soft Polymers Cope with Cracks and Notches. *Applied Sciences*, **9**(6), 1086.

[116] Mayumi, K., Guo, J., Narita, T., Hui, C.Y. and Creton, C. (2016) Fracture of dual crosslink gels with permanent and transient crosslinks. *Extreme Mechanics Letters*, **6**, 52–59.

[117] Sawyers, K. and Rivlin, R.S. (1974) The trousers test for rupture. *Engineering Fracture Mechanics*, **6**(3), 557–562.

[118] Greensmith, H.W. (1963) Rupture of rubber. X. The change in stored energy on making a small cut in a test piece held in simple extension. *Journal of Applied Polymer Science*, **7**(3), 993–1002.

[119] Roucou, D., Diani, J., Brieu, M. and Mbiakop-Ngassa, A. (2019) Critical strain energy release rate for rubbers: single edge notch tension versus pure shear tests. *International Journal of Fracture*, **216**(1), 31–39.

[120] Pereira, B.P., Lucas, P.W. and Swee-Hin, T. (1997) Ranking the fracture toughness of thin mammalian soft tissues using the scissors cutting test. *Journal of Biomechanics*, **30**(1), 91–94.

[121] Fung, Y.C. (1967) Elasticity of soft tissues in simple elongation. *American Journal of Physiology*, **213**(6), 1532–1544.

[122] Demiray, H. (1972) A note on the elasticity of soft biological tissues. *Journal of Biomechanics*, **5**(3), 309–311.

[123] Vito, R. (1973) A note on arterial elasticity. *Journal of Biomechanics*, **6**(5), 561–564.

[124] Gambarotta, L., Massabò, R., Morbiducci, R., Raposio, E. and Santi, P. (2005) In vivo experimental testing and model identification of human scalp skin. *Journal of Biomechanics*, **38**(11), 2237–2247.

[125] Tong, P. and Fung, Y.C. (1976) The stress-strain relationship for the skin. *Journal of Biomechanics*, **9**(10), 649–657.

[126] Amabili, M. (2018) *Nonlinear Mechanics of Shells and Plates in Composite, Soft and Biological Materials*. Cambridge University Press, Cambridge.

[127] Horgan, C.O. and Saccomandi, G. (2003) A description of arterial wall mechanics using limiting chain extensibility constitutive models. *Biomechanics and Modeling in Mechanobiology*, **1**(4), 251–266.

[128] Horgan, C.O. and Smayda, M.G. (2012) The importance of the second strain invariant in the constitutive modeling of elastomers and soft biomaterials. *Mechanics of Materials*, **51**, 43–52.

[129] Westergaard, H.M.W. (1939) Bearing Pressures and Cracks. *Journal of Applied Mechanics*, **6**, 49–53.

[130] Williams, M.L. (1956) On the Stress Distribution at the Base of a Stationary Crack. *Journal of Applied Mechanics*, **24**(1), 109–114.

[131] Krishnan, V.R., Hui, C.Y. and Long, R. (2008) Finite Strain Crack Tip Fields in Soft Incompressible Elastic Solids. *Langmuir*, **24**(24), 14245–14253.

[132] Long, R., Krishnan, V.R. and Hui, C.Y. (2011) Finite strain analysis of crack tip fields in incompressible hyperelastic solids loaded in plane stress. *Journal of the Mechanics and Physics of Solids*, **59**(3), 672–695.

[133] Long, R. and Hui, C.Y. (2015) Crack tip fields in soft elastic solids subjected to large quasi-static deformation - A review. *Extreme Mechanics Letters*, **4**, 131–155.

[134] Abeyaratne, R.C. (1980) Discontinuous deformation gradients in plane finite elastostatics of incompressible materials. *Journal of Elasticity*, **10**(3), 255–293.

[135] Dassault Systèmes, SIMULIA (2017). Abaqus 2017, Documentation.

[136] Chernov, N. (2010) *Circular and Linear Regression: Fitting Circles and Lines by Least Squares*. CRC Press, Boca Raton (Fla.).

[137] Brighenti, R., Spagnoli, A., Carpinteri, A. and Artoni, F. (2016) Notch effect in highly deformable material sheets. *Thin-Walled Structures*, **105**, 90–100.

[138] Brighenti, R., Spagnoli, A., Carpinteri, A. and Artoni, F. (2017) Defect tolerance at various strain rates in elastomeric materials: An experimental investigation. *Engineering Fracture Mechanics*, **183**, 79–93.

[139] Brighenti, R., Carpinteri, A., Artoni, F. and Domenichelli, I. (2018) Defect sensitivity of highly deformable polymeric materials with different intrinsic qualities at various strain rates. *Fatigue & Fracture of Engineering Materials & Structures*, **41**(4), 806–820.

[140] Timoshenko, S. and Goodier, J.N. (1951) *Theory of elasticity*. McGraw-Hill, New York.

[141] Gao, X.L. (1996) A general solution of an infinite elastic plate with an elliptic hole under biaxial loading. *International Journal of Pressure Vessels and Piping*, **67**(1), 95–104.

[142] Wang, X. and Hong, W. (2012) A visco-poroelastic theory for polymeric gels. *Proceedings of the Royal Society A: Mathematical, Physical and Engineering Sciences*, **468**(2148), 3824–3841.

[143] Bueche, F. (1961) Mullins effect and rubber–filler interaction. *Journal of Applied Polymer Science*, **5**(15), 271–281.

[144] Muñoz, M., Bea, J., Rodríguez, J., Ochoa, I., Grasa, J., Pérez del Palomar, A., Zaragoza, P., Osta, R. and Doblaré, M. (2008) An experimental study of the mouse skin behaviour: Damage and inelastic aspects. *Journal of Biomechanics*, **41**(1), 93–99.

[145] Webber, R.E., Creton, C., Brown, H.R. and Gong, J.P. (2007) Large Strain Hysteresis and Mullins Effect of Tough Double-Network Hydrogels. *Macromolecules*, **40**(8), 2919–2927.

[146] Long, R., Mayumi, K., Creton, C., Narita, T. and Hui, C.Y. (2014) Time Dependent Behavior of a Dual Cross-Link Self-Healing Gel: Theory and Experiments. *Macromolecules*, **47**(20), 7243–7250.

[147] Qi, Y., Caillard, J. and Long, R. (2018) Fracture toughness of soft materials with rate-independent hysteresis. *Journal of the Mechanics and Physics of Solids*, **118**, 341–364.

[148] Naassaoui, I., Ronsin, O. and Baumberger, T. (2018) A poroelastic signature of the dry/wet state of a crack tip propagating steadily in a physical hydrogel. *Extreme Mechanics Letters*, **22**, 8–12.

[149] Wang, X. and Hong, W. (2012) Delayed fracture in gels. *Soft Matter*, **8**(31), 8171.

[150] Biot, M.A. (1941) General theory of three dimensional consolidation. *Journal of Applied Physics*, **12**(2), 155–164.

[151] Biot, M.A. (1972) Theory of Finite Deformations of Porous Solids. *Indiana University Mathematics Journal*, **21**(7), 597–620.

[152] Simon, B.R. (1992) Multiphase Poroelastic Finite Element Models for Soft Tissue Structures. *Applied Mechanics Reviews*, **45**(6), 191–218.

[153] Bouklas, N., Landis, C.M. and Huang, R. (2015) Effect of Solvent Diffusion on Crack-Tip Fields and Driving Force for Fracture of Hydrogels. *Journal of Applied Mechanics*, **82**(8), 081007.

[154] Noselli, G., Lucantonio, A., McMeeking, R.M. and DeSimone, A. (2016) Poroelastic toughening in polymer gels: A theoretical and numerical study. *Journal of the Mechanics and Physics of Solids*, **94**, 33–46.

[155] Schapery, R.A. (1984) Correspondence principles and a generalized J integral for large deformation and fracture analysis of viscoelastic media. *International Journal of Fracture*, **25**(3), 195–223.

[156] Knauss, W.G. and Losi, G.U. (1993) Crack Propagation in a Nonlinearly Viscoelastic Solid With Relevance to Adhesive Bond Failure. *Journal of Applied Mechanics*, **60**(4), 793–801.

[157] Persson, B.N.J., Albohr, O., Heinrich, G. and Ueba, H. (2005) Crack propagation in rubber-like materials. *Journal of Physics: Condensed Matter*, **17**(44), 1071–1142.

[158] Knauss, W.G. (2015) A review of fracture in viscoelastic materials. *International Journal of Fracture*, **196**(1-2), 99–146.

[159] Gent, A.N. and Lai, S.M. (1994) Interfacial bonding, energy dissipation, and adhesion. *Journal of Polymer Science Part B: Polymer Physics*, **32**(8), 1543–1555.

[160] Gent, A.N. (1996) Adhesion and Strength of Viscoelastic Solids. Is There a Relationship between Adhesion and Bulk Properties? *Langmuir*, **12**(19), 4492–4496.

[161] de Gennes, P.G. (1996) Soft Adhesives. *Langmuir*, **12**(19), 4497–4500.

[162] Brown, H.R. (2007) A Model of the Fracture of Double Network Gels. *Macromolecules*, **40**(10), 3815–3818.

[163] Guo, J., Liu, M., Zehnder, A.T., Zhao, J., Narita, T., Creton, C. and Hui, C.Y. (2018) Fracture mechanics of a self-healing hydrogel with covalent and physical crosslinks: A numerical study. *Journal of the Mechanics and Physics of Solids*, **120**, 79–95.

[164] Lefranc, M. and Bouchaud, E. (2014) Mode I fracture of a biopolymer gel: Rate-dependent dissipation and large deformations disentangled. *Extreme Mechanics Letters*, **1**, 97–103.

[165] Budday, S., Sommer, G., Holzapfel, G.A., Steinmann, P. and Kuhl, E. (2017) Viscoelastic parameter identification of human brain tissue. *Journal of the Mechanical Behavior of Biomedical Materials*, **74**, 463–476.

[166] Mao, Y. and Anand, L. (2018) A theory for fracture of polymeric gels. *Journal of the Mechanics and Physics of Solids*, **115**, 30–53.

[167] Zhang, W., Liu, X., Wang, J., Tang, J., Hu, J., Lu, T. and Suo, Z. (2018) Fatigue of double-network hydrogels. *Engineering Fracture Mechanics*, **187**, 74–93.

[168] Bažant, Z.P. and Li, Y.N. (1997) Cohesive crack with rate-dependent opening and viscoelasticity: I. Mathematical model and scaling. *International Journal of Fracture*, **86**(3), 247–265.

[169] Landis, C.M., Pardoen, T. and Hutchinson, J.W. (2000) Crack velocity dependent toughness in rate dependent materials. *Mechanics of Materials*, **32**(11), 663–678.

[170] Allen, D.H. and Searcy, C.R. (2001) A micromechanical model for a viscoelastic cohesive zone. *International Journal of Fracture*, **107**(2), 159–176.

[171] Geißler, G. and Kaliske, M. (2010) Time-dependent cohesive zone modelling for discrete fracture simulation. *Engineering Fracture Mechanics*, **77**(1), 153–169.

[172] Zreid, I., Fleischhauer, R. and Kaliske, M. (2013) A thermomechanically coupled viscoelastic cohesive zone model at large deformation. *International Journal of Solids and Structures*, **50**(25-26), 4279–4291.

[173] Tang, J., Li, J., Vlassak, J.J. and Suo, Z. (2017) Fatigue fracture of hydrogels. *Extreme Mechanics Letters*, **10**, 24–31.

[174] Kalcioglu, Z.I., Mahmoodian, R., Hu, Y., Suo, Z. and Van Vliet, K.J. (2012) From macro- to microscale poroelastic characterization of polymeric hydrogels via indentation. *Soft Matter*, **8**(12), 3393.

[175] Lai, Y. and Hu, Y. (2017) Unified solution for poroelastic oscillation indentation on gels for spherical, conical and cylindrical indenters. *Soft Matter*, **13**(4), 852–861.

[176] Simon, B.R., Kaufmann, M.V., McAfee, M.A. and Baldwin, A.L. (1996) Porohyperelastic theory and finite element models for soft tissues with application to arterial mechanics. In A.P.S. Selvadurai, editor, *Mechanics of Poroelastic Media*, pages 245–261. Springer Netherlands, Dordrecht.

[177] Ogden, R.W. (1972) Large Deformation Isotropic Elasticity: On the Correlation of Theory and Experiment for Compressible Rubberlike Solids. *Proceedings of the Royal Society A: Mathematical, Physical and Engineering Sciences*, **328**(1575), 567–583.

[178] Hui, C.Y., Lin, Y.Y., Chuang, F.C., Shull, K.R. and Lin, W.C. (2006) A contact mechanics method for characterizing the elastic properties and permeability of gels. *Journal of Polymer Science Part B: Polymer Physics*, **44**(2), 359–370.

[179] Pervaiz Fathima, K. and de Borst, R. (2019) Implications of single or multiple pressure degrees of freedom at fractures in fluid-saturated porous media. *Engineering Fracture Mechanics*, **213**(February), 1–20.

[180] Hillerborg, A., Modéer, M. and Petersson, P.E. (1976) Analysis of crack formation and crack growth in concrete by means of fracture mechanics and finite elements. *Cement and Concrete Research*, **6**(6), 773–781.

[181] Hu, Y. and Suo, Z. (2012) Viscoelasticity and poroelasticity in elastomeric gels. *Acta Mechanica Solida Sinica*, **25**(5), 441–458.

[182] Abolhassani, N., Patel, R. and Moallem, M. (2007) Needle insertion into soft tissue: A survey. *Medical Engineering and Physics*, **29**(4), 413–431.

[183] van Gerwen, D.J., Dankelman, J. and van den Dobbelsteen, J.J. (2012) Needle–tissue interaction forces – A survey of experimental data. *Medical Engineering & Physics*, **34**(6), 665–680.

[184] Takabi, B. and Tai, B.L. (2017) A review of cutting mechanics and modeling techniques for biological materials. *Medical Engineering & Physics*, **45**, 1–14.

[185] Cornec, A., Scheider, I. and Schwalbe, K.H. (2003) On the practical application of the cohesive model. *Engineering Fracture Mechanics*, **70**(14), 1963–1987.

[186] de Borst, R. (2003) Numerical aspects of cohesive-zone models. *Engineering Fracture Mechanics*, **70**(14), 1743–1757.

[187] Rahul-Kumar, P., Jagota, A., Bennison, S.J., Saigal, S. and Muralidhar, S. (1999) Polymer interfacial fracture simulations using cohesive elements. *Acta Materialia*, **47**(15-16), 4161–4169.

[188] Xu, X.P. and Needleman, A. (1994) Numerical simulations of fast crack growth in brittle solids. *Journal of the Mechanics and Physics of Solids*, **42**(9), 1397–1434.

[189] Camacho, G. and Ortiz, M. (1996) Computational modelling of impact damage in brittle materials. *International Journal of Solids and Structures*, **33**(20-22), 2899–2938.

[190] Geißler, G., Netzker, C. and Kaliske, M. (2010) Discrete crack path prediction by an adaptive cohesive crack model. *Engineering Fracture Mechanics*, **77**(18), 3541–3557.

[191] Goh, S., Charalambides, M. and Williams, J.G. (2005) On the mechanics of wire cutting of cheese. *Engineering Fracture Mechanics*, **72**(6), 931–946.

[192] Misra, S., Reed, K.B., Douglas, A.S., Ramesh, K.T. and Okamura, A.M. (2008) Needle-tissue interaction forces for bevel-tip steerable needles. In *2008 2nd IEEE RAS & EMBS International Conference on Biomedical Robotics and Biomechatronics*, pages 224–231.

[193] Tai, B.L., Wang, Y. and Shih, A.J. (2013) Cutting Force of Hollow Needle Insertion in Soft Tissue. In *2013 International Manufacturing Science and Engineering Conference*.

[194] Lan, G.J. and Lin, C.L. (2017) A Computational Approach Using Surface-Based Cohesive Behavior to Study Tissue Cutting With Rotation in Vacuum-Assisted Biopsy. In *2017 Design of Medical Devices Conference*.

[195] Gültekin, O. and Holzapfel, G.A. (2018) A Brief Review on Computational Modeling of Rupture in Soft Biological Tissues. In *A Brief Review on Computational Modeling of Rupture in Soft Biological Tissues*, volume 46, pages 113–144. Springer.

[196] Agathos, K., Chatzi, E., Bordas, S.P.A. and Talaslidis, D. (2016) A well-conditioned and optimally convergent XFEM for 3D linear elastic fracture. *International Journal for Numerical Methods in Engineering*, **105**(9), 643–677.

[197] Wan, D., Hu, D., Natarajan, S., Bordas, S.P.A. and Yang, G. (2017) A fully smoothed XFEM for analysis of axisymmetric problems with weak discontinuities. *International Journal for Numerical Methods in Engineering*, **110**(3), 203–226.

[198] Cheng, Q., Liu, P.X., Lai, P., Xu, S. and Zou, Y. (2018) A Novel Haptic Interactive Approach to Simulation of Surgery Cutting Based on Mesh and Meshless Models. *Journal of Healthcare Engineering*, **2018**, 1–16.

[199] Bui, H.P., Tomar, S. and Bordas, S.P.A. (2019) Corotational cut finite element method for real-time surgical simulation: Application to needle insertion simulation. *Computer Methods in Applied Mechanics and Engineering*, **345**, 183–211.

[200] Gültekin, O., Hager, S.P., Dal, H. and Holzapfel, G.A. (2019) Computational modeling of progressive damage and rupture in fibrous biological tissues: application to aortic dissection. *Biomechanics and Modeling in Mechanobiology*, pages 1–22.

[201] Johnson, K.L. (1987) *Contact Mechanics*. Cambridge University Press, Cambridge.

[202] Zhou, D. and McMurray, G. (2010) Modeling of blade sharpness and compression cut of biomaterials. *Robotica*, **28**(2), 311–319.

[203] Rattan, S. and Crosby, A.J. (2018) Effect of far-field compliance on local failure dynamics of soft solids. *Extreme Mechanics Letters*, **24**, 14–20.

[204] van de Berg, N.J., van Gerwen, D.J., Dankelman, J. and van den Dobbelsteen, J.J. (2015) Design Choices in Needle Steering—A Review. *IEEE/ASME Transactions on Mechatronics*, **20**(5), 2172–2183.

[205] Frasson, L., Ko, S.Y., Turner, A., Parittotokkaporn, T., Vincent, J.F. and Rodriguez y Baena, F. (2010) STING: a soft-tissue intervention and neurosurgical guide to access deep brain lesions through curved trajectories. *Proceedings of the Institution of Mechanical Engineers, Part H: Journal of Engineering in Medicine*, **224**(6), 775–788.

[206] Ko, S.Y., Frasson, L. and Rodriguez y Baena, F. (2011) Closed-Loop Planar Motion Control of a Steerable Probe With a "Programmable Bevel" Inspired by Nature. *IEEE Transactions on Robotics*, **27**(5), 970–983.

[207] Ko, S.Y. and Rodriguez y Baena, F. (2013) Toward a Miniaturized Needle Steering System With Path Planning for Obstacle Avoidance. *IEEE Transactions on Biomedical Engineering*, **60**(4), 910–917.

[208] DiMaio, S. and Salcudean, S. (2003) Needle insertion modeling and simulation. *IEEE Transactions on Robotics and Automation*, **19**(5), 864–875.

[209] Okamura, A.M., Simone, C. and O'Leary, M. (2004) Force Modeling for Needle Insertion Into Soft Tissue. *IEEE Transactions on Biomedical Engineering*, **51**(10), 1707–1716.

[210] DiMaio, S. and Salcudean, S. (2005) Interactive Simulation of Needle Insertion Models. *IEEE Transactions on Biomedical Engineering*, **52**(7), 1167–1179.

[211] Webster, R.J., Kim, J.S., Cowan, N.J., Chirikjian, G.S. and Okamura, A.M. (2006) Nonholonomic Modeling of Needle Steering. *The International Journal of Robotics Research*, **25**(5-6), 509–525.

[212] Misra, S., Reed, K.B., Schafer, B., Ramesh, K.T. and Okamura, A.M. (2010) Mechanics of Flexible Needles Robotically Steered through Soft Tissue. *The International Journal of Robotics Research*, **29**(13), 1640–1660.

[213] Oldfield, M.J., Dini, D. and Rodriguez y Baena, F. (2012) Predicting failure in soft tissue phantoms via modeling of non-predetermined tear progression. In *2012 Annual International Conference of the IEEE Engineering in Medicine and Biology Society*, pages 6305–6308.

[214] Oldfield, M.J., Dini, D., Giordano, G. and Rodriguez y Baena, F. (2013) Detailed finite element modelling of deep needle insertions into a soft tissue phantom using a cohesive approach. *Computer Methods in Biomechanics and Biomedical Engineering*, **16**(5), 530–543.

[215] Oldfield, M.J., Dini, D., Jaiswal, T. and Rodriguez y Baena, F. (2013) The significance of rate dependency in blade insertions into a gelatin soft tissue phantom. *Tribology International*, **63**, 226–234.

[216] Zhang, Z. and Paulino, G.H. (2005) Cohesive zone modeling of dynamic failure in homogeneous and functionally graded materials. *International Journal of Plasticity*, **21**(6), 1195–1254.

[217] Tabiei, A. and Zhang, W. (2017) Cohesive element approach for dynamic crack propagation: Artificial compliance and mesh dependency. *Engineering Fracture Mechanics*, **180**, 23–42.

[218] Pagani, M. and Perego, U. (2015) Explicit dynamics simulation of blade cutting of thin elastoplastic shells using “directional” cohesive elements in solid-shell finite element models. *Computer Methods in Applied Mechanics and Engineering*, **285**, 515–541.

[219] Terzano, M., Dini, D., Rodriguez y Baena, F., Spagnoli, A. and Oldfield, M.J. An Adaptive Finite Element Model for Steerable Needles (submitted). *Biomechanics and Modeling in Mechanobiology*.

[220] Persson, P.O. and Strang, G. (2004) A Simple Mesh Generator in MATLAB. *SIAM Review*, **46**(2), 329–345.

[221] Bouchard, P., Bay, F. and Chastel, Y. (2003) Numerical modelling of crack propagation: automatic remeshing and comparison of different criteria. *Computer Methods in Applied Mechanics and Engineering*, **192**(35-36), 3887–3908.

[222] Sih, G.C. and Macdonald, B. (1974) Fracture mechanics applied to engineering problems-strain energy density fracture criterion. *Engineering Fracture Mechanics*, **6**(2), 361–386.

[223] Sih, G.C. (1974) Strain-energy-density factor applied to mixed mode crack problems. *International Journal of Fracture*, **10**(3), 305–321.

[224] Burrows, C., Secoli, R. and Rodriguez y Baena, F. (2013) Experimental characterisation of a biologically inspired 3D steering needle. In *2013 13th International Conference on Control, Automation and Systems (ICCAS 2013)*, pages 1252–1257.

[225] Holzapfel, G.A. (2000) *Nonlinear Solid Mechanics: A Continuum Approach for Engineering Science*. Wiley, Chichester.

[226] Corradi Dell’Acqua, L. (1992) *Meccanica delle strutture-2*. McGraw Hill, Milano.

[227] Zienkiewicz, O.C., Taylor, R.L. and Fox, D. (2014) *The Finite Element Method for Solid and Structural Mechanics: Seventh Edition*. Elsevier Science, Amsterdam.

[228] Rivlin, R.S. (1948) Large Elastic Deformations of Isotropic Materials. I. Fundamental Concepts. *Philosophical Transactions of the Royal Society A: Mathematical, Physical and Engineering Sciences*, **240**(822), 459–490.

[229] Wineman, A. (2005) Some results for generalized neo-Hookean elastic materials. *International Journal of Non-Linear Mechanics*, **40**(2-3), 271–279.

[230] Mooney, M. (1940) A Theory of Large Elastic Deformation. *Journal of Applied Physics*, **11**(9), 582–592.

[231] Gent, A.N. (1996) A New Constitutive Relation for Rubber. *Rubber Chemistry and Technology*, **69**(1), 59–61.

[232] Horgan, C.O. (2015) The remarkable Gent constitutive model for hyperelastic materials. *International Journal of Non-Linear Mechanics*, **68**, 9–16.

[233] Ogden, R.W. (1972) Large Deformation Isotropic Elasticity - On the Correlation of Theory and Experiment for Incompressible Rubberlike Solids. *Proceedings of the Royal Society A: Mathematical, Physical and Engineering Sciences*, **326**(1567), 565–584.

[234] Terzaghi, K. (1923) Die Berechnung der Durchlässigkeitsziffer des tones aus dem verlauf der hydrodynamischen. *Sitzungsberichte der Akademie der Wissenschaften in Wien, Mathematisch-Naturwissenschaftliche Klasse, Abteilung IIa*, **132**, 125–138.

[235] Cheng, A.H.D. (2016) *Poroelasticity*. Theory and Applications of Transport in Porous Media. Springer International Publishing, New York.

[236] Simo, J.C. and Hughes, T.J.R. (2000) *Computational inelasticity*. Interdisciplinary Applied Mathematics. Springer US, New York.

[237] Christensen, R.M. (1982) *Theory of viscoelasticity of fluids*. Academic Press, New York.

[238] Kuna, M. (2013) *Finite elements in fracture mechanics: Theory - Numerics - Applications*. Solid Mechanics and Its Applications. Springer Netherlands, Heidelberg.

[239] Shih, C.F., Moran, B. and Nakamura, T. (1986) Energy release rate along a three-dimensional crack front in a thermally stressed body. *International Journal of Fracture*, **30**(2), 79–102.